UNIVERSITY OF CALGARY

Processing and Interpretation of Time-Lapse Seismic Data from a Heavy Oil Field, Alberta, Canada

by

Byron Matthew Kelly

A THESIS

SUBMITTED TO THE FACULTY OF GRADUATE STUDIES

IN PARTIAL FULFILMENT OF THE REQUIREMENTS FOR THE

DEGREE OF MASTER OF SCIECNE

DEPARTMENT OF GEOSCIENCE

CALGARY, ALBERTA

NOVEMBER, 2012

Abstract

The monitoring of a SAGD heavy oil reservoir is commonly executed through time-lapse 3D seismic surveying, focused on identifying areas of steam stimulation by tracking the movement of a steam front, and identifying areas of bypassed reserves. In this thesis, we processed and interpreted a 4D - 3C seismic dataset, identified time-lapse amplitude anomalies and isochron time-delays associated with the injection of high volumes of steam into a McMurray Formation reservoir. Through processing, and the application of a novel calibration procedure, non-production related differences between the baseline and monitor seismic surveys were minimized. Production-related differences were analyzed through a variety of geophysical techniques, and were projected into a map display to delineate the spatial position of the reservoir steam zones. It was interpreted that the observed amplitude anomalies corresponded to steam injection, while concurrent time-delays represent reservoir heating above pre-injection ambient temperatures.

Acknowledgements

First and foremost, I would like to thank my supervisor, Dr. Don Lawton for providing me with the opportunity to work under his supervision and advisory on this thesis. Thank you for the support, patience, and knowledge throughout the last two years.

I would like to thank the CREWES, students, staff and professors for their support. Especially, I thank Helen Isaac for all of her help, support and input during processing of the data. Without her help I would not have achieved the end result to which I am happy to present in this thesis. Thank you to my office mates Andrew Nicol and Jessie Arthur for their support and opinions. Thank you to Dave Cho for his help and input, Peter Gagliardi for his support, Chris Bird and Steve Kim for their help with Matlab, and Adam Fraser for his geological knowledge.

Thank you to the CREWES sponsors for funding this research, and to the donor of the data for this thesis, who would like to remain anonymous.

Thank you to Dr. Larry Lines and Dr. Harvey Yarranton for serving as members of my defense committee.

I would like to thank my Mom and Dad for their continued support through the entirety of my university experience.

Finally, thank you to my girlfriend for her endless support during the entirety of my time at the University of Calgary.

Dedication

To my mom, dad, my family and Cassandra Frosini.

Table of Contents

List of Tables

List of Figures and Illustrations

List of Symbols, Abbreviations and Nomenclature

Symbol	Definition
°C	Degree Celsius
≥	Greater Than or Equal to
2D	Two Dimensional
3C	Three Component
3D	Three Dimensional
4D	Four Dimensional
API	American Petroleum Institute Gravity Measurement
CMP	Common Midpoint
CP	Centipoises
CCP	Common Conversion Point
FFID	Field File Identification Number
Hz	Hertz
kPa	Kilopascal
M	Meter(s)
m/s	Meters per second
Ma	Million years
Md	Millidarcy
Ms	Milisecond(s)
NMO	Normal Moveout
NRMS	Normalized Root-mean-squared
PSPT	Phase-Shift Plus Interpolation
RMS	Root-mean-squared
SAGD	Steam Assisted Gravity Drainage
S:N	Ratio of Signal to Noise
TVSPW	Time Variant Spectral Whitening
Vp	Velocity of the Compressional-Wave
Vs	Velocity of the Shear-Wave
Vp:Vs	Ratio of Compressional-Wave Velocity to Shear-Wave Velocity

Chapter One: **Introduction and Background**

1.1 Introduction

Canada is the sixth largest oil producer in the world, extracting an average of 3.5 million barrels of crude oil per day in 2011 (BP Global, 2012). The production of bitumen from Alberta's oil sands accounted for 49.5% of total Canadian production, with the remainder coming from conventional crude oil (45%) and natural gas (5.5%) (BP Global, 2012). The oil sand reserves in Canada are currently the primary focus of many energy companies, both locally and internationally, with the majority of bitumen reserves being extracted through in-situ methods such as steam assisted gravity drainage (SAGD).

To ensure the optimal recovery of bitumen reserves, time-lapse 3D seismic monitoring is employed in an effort to track steam front movements and delineate zones of reservoir heating. It has been shown that 4D seismic monitoring is an effective technique for monitoring the steam injection recovery processes (Smith & Perepelecta, 2002; Watson, 2004; McGillivray, 2005; Nakayama, 2005), providing insightful information regarding the efficiency of steam injection and identifying zones of bypassed reserves.

For this thesis, a 4D seismic dataset from an Athabasca bitumen deposit was processed and interpreted to provide a detailed understanding of time-lapse changes within the McMurray Formation reservoir over a span of nine years. The detailed interpretation employed an assortment of geophysical interpretation techniques, including time-lapse difference volumes and seismic attributes, as well as the integration of geological well log data. Through such efforts, the spatial location of reservoir steam and heat distributions were identified, which correlated with horizontal well pair locations. Also, baffles to steam flow and reservoir thief zones were interpreted, providing an explanation to the inefficiency of steam stimulation in some areas.

1.2 Steam Assisted Gravity Drainage

In-situ extrication methods are used to produce Alberta's bitumen resources which lie at a depth greater than that accessible via surface mining. The two primary methods commonly employed are active and passive stimulation. The active method utilizes high pressure steam to heat a reservoir, reducing the viscosity of the bitumen (Watson, 2004). The passive method, most commonly known as Steam Assisted Gravity Drainage (SAGD), employs two horizontal well bores, one for steam injection and a second for oil production, each drilled within a few meters of vertical separation from one another. Steam is continually injected into the reservoir via the upper wellbore at a low pressure, heating the bitumen and reducing its viscosity to a point that allows for the downward gravitational flow into the lower production well. The continued injection of steam forms a steam chamber within the reservoir which grows both horizontally and vertically along the porous and permeable reservoir sands.

To ensure the effective recovery of reservoir hydrocarbons, seismic monitoring of an active steam zone is essential in delineating the location of stimulated reserves. The concept of time-lapse seismic monitoring has been readily employed through Alberta's oil sand deposits in an attempt to constrain the effectiveness of the SAGD extraction technique through the identification of changes in the seismic characteristics of a reservoir before and after steam injection (Watson, 2004; Bianco, et al., 2008).

The introduction of steam into a reservoir reduces the P-wave velocity due to the elevation of reservoir temperatures, creating a time-delay for wave propagating through the reservoir as well as an amplitude anomaly within a time-lapse difference volume (see Section 1.3) Hence, through the identification of seismic changes over time, steam chamber development can be identified and investigated to provide insight into the effectiveness of a reservoir steam flood.

In this study, a time-lapse data set was processed and the McMurray Formation reservoir was identified and analyzed for steam induced changes through the following techniques:

- Identical processing of baseline and monitor P-wave volumes for a shallow heavy oil reservoir.
- Calibration of the monitor P-wave data to match the baseline in terms of amplitudes, statics and phase.
- Comparison of isochrons amplitude Sections for the baseline and monitor P-wave volumes.
- Reflectivity differencing for the monitor and baseline P-wave volumes.
- Analysis of complex seismic trace attributes for the P-wave baseline, monitor and difference volumes.
- Integration of geological well logs and production information to time-lapse reservoir changes.
- Projection of amplitude anomalies into a spatial display.
- Analysis of Vp/Vs for the baseline multicomponent data.

The results of each of these approaches were compared, contrasted and correlated as a means of delineating the spatial and temporal location of steam and heat zones within the McMurray Formation reservoir.

Through the application of the above techniques, this thesis provided three main contributions to academia: (1) processing modifications for the robust imaging of a shallow, highly attenuative bitumen reservoir (2) the novel calibration procedure using reflections underlying the zone of interest and (3) the interpretation process using both geophysical and geological information for the detailed analysis of reservoir steam zones.

1.3 Reservoir Monitoring

1.3.1 Changes in P-wave Velocity

Seismic wave velocities within a rock are dependent upon the elastic constraints of the rock including porosity, pore fluid, consolidation, temperature and effective pressure (Hicks & Berry, 1956; Isaac, 1996). A deviation in these parameters will result in changes in the seismic wave velocity through the rock. Steam injection into a reservoir may alter some of the elastic constraints, resulting in decreases in the P-wave velocity. Some of the earliest work investigating the reduction of P-wave velocity associated with altered elastic constraints was performed by Huges and Kelly (1952), and Wyllie et al, (1956) studying the effect of heavy oil saturation and effective pressure on compressional wave velocity. They observed lower P-wave velocities in water-saturated rocks at high pressure than in non-saturated equivalents. Hicks and Berry (1956) furthered this work, reporting that decreasing the differential pressure of reservoir rocks resulted in a decrease in P-wave velocity. The increase in differential pressure can be related to SAGD production, where the injection of steam into a reservoir increases the pore fluid pressure, thus reducing the differential pressure between the pore fluid pressure and overburden pressure (Wang & Nur, 1988; Isaac, 1996).

Tosaya et al. (1984) and Nur et al. (1984) studied the effect of increasing temperatures on heavy oil saturated rocks. At a temperature of 125-150^{O}C, they observed significant decreases in P-wave velocities, as large as 50%. This work was followed by Wang and Nur (1988) and Eastwood (1993), reporting that higher bitumen saturation levels lead to greater velocity sensitivity to temperature. Using rocks representing typical bitumen saturated reservoir sands, temperatures in the range of 100-250^{O}C lead to a 30% reduction in P-wave velocity. This reduction in P-wave velocity was attributed to the increased compressibility of heavy oil with increasing temperature. Decreases in shear-wave velocities were also observed, although to a lesser extent than the decrease in P-wave velocity. Lastly, Tosaya et al., (1987) proposed that, for high saturation levels, P-wave velocity can serve as a highly accurate reservoir thermometer for enhanced oil recovery projects. However, Paulsson et al. (1994) negated this, cautioning that actual temperatures cannot be derived from seismic velocities. The velocity response to temperature is dependent upon several factors, including bitumen saturation, which varies throughout the reservoir (Paulsson, et al., 1994; Isaac, 1996).

More recently, Bianco (2008) investigated the rock properties of heavy oil reservoirs subject to SAGD recovery processes through rock physics modeling, suggesting that seismic monitoring depends on both thermal and mechanical changes, as well as the size of the steam anomaly.

1.3.2 Time-Lapse Monitoring of Heavy Oil

Bitumen reservoirs have been actively monitored through time-lapse seismic for several years. Initial time-lapse monitoring concepts were developed by Nur (1982) and Wang (1988), where increasing reservoir temperatures were related to the reduction of P-wave velocities. The work by Nur and Wang led to furrther invesitgations into the seismic monitoring method. Britton et al. (1983) observed velocity anomolies within seismic data associated with steam injection wells. Matthews et al. (1987) used 3D seismic to image an Athabasca oil reservoir with the ultimate goal of locating and imaging the progress of in-situ steam movememt. Lines et al. (1990) used time-lapse reflection and borehole data to derive time variant velocity models, displaying low velocity values representing steam injecdtion. Isaac (1996) used time-lapse multicomponent data to observed P-wave and S-wave reservoir changes and used Vp/Vs to distinguish heated and non-heated reservoir zones in the Cold Lake oil field, and Sun (1999) used time-lapse seismic and VSP data at Cold Lake for reservoir monitoring and characterization.

More recently, time-lapse seismic monitoring have been actively employed and investigated at the Pikes Peak field (Watson, 2004), the Cold Lake field (Smith & Perepelecta, 2002), the Peace River field (McGillivray, 2005) and the Athabasca field (Kendall, 2010). .

1.4 Data

1.4.1 Geophysical Data

The geophysical dataset comprised of a 3D-3C time-lapse seismic survey. The baseline data was recorded in 2002, prior to reservoir recovery processes. Conversely, the 2011 monitor survey was recorded after nine years of production and steam injection in an effort to gain an understanding of the reservoir changes since the recording of the baseline survey.

The baseline 3D survey was recorded over an area of approximately 9.0 km^2 with an inline and crossline separation of 50 m and a geophone separation of 10 m. Source lines were oriented N - S while receiver lines were oriented NE – SW. The three-component geophones were oriented towards magnetic north.

The monitor 3D survey was recorded over a subset of the baseline survey area, covering approximately 3.8 km^2. Inline, crossline and geophone separations were the same as the baseline survey, as were the orientation of the source lines, receiver lines and geophones. However, the monitor survey was recorded using accelerometers, while the baseline survey was recorded using conventional geophones (velocity). This difference is observable on raw records, as discussed in Chapter 3 (Section 3.2). Source and receiver locations were reoccupied via GPS X and Y surface coordinate locations, allowing for good repeatability.

1.4.2 Geological Data

An assortment of geological well log data was provided with the geophysical data for this thesis. However, only a subset of wells was utilized in conjunction with the time-lapse interpretation. The well logs were used to provide cross- Sectional views of the reservoir, intersecting both zones of steam injection and areas without a steam anomaly. Primarily, gamma ray logs were used to aid the geophysical interpretation, providing structural views of the McMurray Formation reservoir and the identification of sand and mud/shale zones. However, temperature logs were also analyzed where available to provide temperature information in areas containing steam anomalies.

Sonic and density logs were used to construct synthetic seismograms, generated by the convolution of the reflectivity series with an Ormsby wavelet extracted from the geophysical data. Geological well tops identified on the well logs were related to seismic reflections of interest through the correlation of the well tops to the synthetic seismograms.

1.5 Software and Hardware

The processing of the time-lapse data set was dominantly performed in Halliburton's ProMAX Processing software, in conjunction with Gedco's Vista 2D/3D Processing software to a lesser extent.

Hampson-Russell's Pro4D module was used to calibrate the monitor seismic survey to match the baseline data, to construct a reflectivity difference volume and was used to perform data interpretation including isochron analysis and seismic attributes. Seismic well ties and well log analysis was completed in Hampson Russell's Geoview application.

Charts, figures and thesis manuscripts were generated in Microsoft PowerPoint, Excel and Word applications.

Chapter Two: **Geology and Reservoir Characterization**

2.1 Regional Overview

Alberta is home to one of the largest oil sands deposits in the world, contained within three development areas: Athabasca, Cold Lake and Peace River (Figure 2-1). The Athabasca deposit is the largest Cretaceous oil deposit in Alberta, covering an area of 140,000 km^2 and containing in excess of 270 billion cubic meters of bitumen (1.7 trillion barrels), primarily within the Lower Cretaceous McMurray-Wabiskaw interval (Hein & Cotterill, 2006; Mossop, 1980; Flach, 1984; Hien, et al., 2008; Gingras & Rokosh, 2004).

The majority of the bitumen is hosted in a north-south trend along the eastern margin of the Athabasca region (Figure 2-2) (Hein & Cotterill, 2006). Approximately 20% of reserves occur within the upper 75 m of the subsurface, accessible via surface mining in the northern region of the Athabasca, while the remaining 80% is recoverable from in-situ methods such as steam assisted gravity drainage (SAGD).

The main source rocks for the Athabasca deposit are the Exshaw Shales, located approximately 100 km to the southwest (Hien, et al., 2008). Hydrocarbon generation occurred during the Tertiary in conjunction with the Laramide orogeny. Oil migration and biodegradation began towards the end of the Laramide orogeny and ended in coincidence with the orogeny termination (Hien, et al., 2008). The migration and deposition of oil into the Athabasca region was largely influenced by the variable topography of the Pre-Cretaceous unconformity, as well as regional salt-dissolution features including extensive valley systems, karstification, and salt roll-over and anticlinal structures (Hien, et al., 2008; Schneider, et al., 2012). The underlying Devonian and Mississippian carbonates of the Athabasca region also contain bitumen reservoirs, but these are beyond the scope of this thesis.

2.1.1 Study Area and Reservoir

The study area for this thesis is located within the Athabasca region. The name and exact location of the study area is confidential as per requested by the operating company, and thus is referred to as only the study area.

The reservoir of interest is the McMurray Formation, a bitumen saturated reservoir lying at a maximum depth of ~200 m below the surface. Stimulation of bitumen reserves is ongoing via SAGD extraction methods through a series of horizontal injection and production wells penetrating the McMurray Formation reservoir at different depths. The bitumen sands are hosted within stacked channel deposits, separated by silty or muddy intervals.

Bitumen of the Athabasca region is heavy and largely immobile due to extensive biodegradation, containing a viscosity of 100,000-1,000,000 CP and an API of 5-10°, in comparison to conventional oil with an API of 24-40° (Mossop, 1980). The sand of the bitumen reservoir is hydrophilic, a key element when considering the effectiveness of the SAGD extraction method (Mossop, 1980). Oil saturation levels vary, where deposits contain as much as 18% bitumen by weight (36% by volume).

Average effective reservoir porosities are on the order of 30%, with an average volume of shale of 11% and permeability in the range of 4800-6300 mD. Water saturation levels average 32%, and ambient reservoir temperatures are 6-10 $^{\circ}$C at a pressure of 1000-1100 kPa.

2.2 Stratigraphy

The stratigraphy of interest are the Cretaceous siliciclastics and the Devonian carbonates.

Figure 2-3 is a simplified stratigraphic column for the Athabasca region illustrating the three intervals of interest: the Beaverhill Lake Group, the McMurray Formation, and the Clearwater Formation. All formations overlying the Clearwater Formation are referred to as overburden.

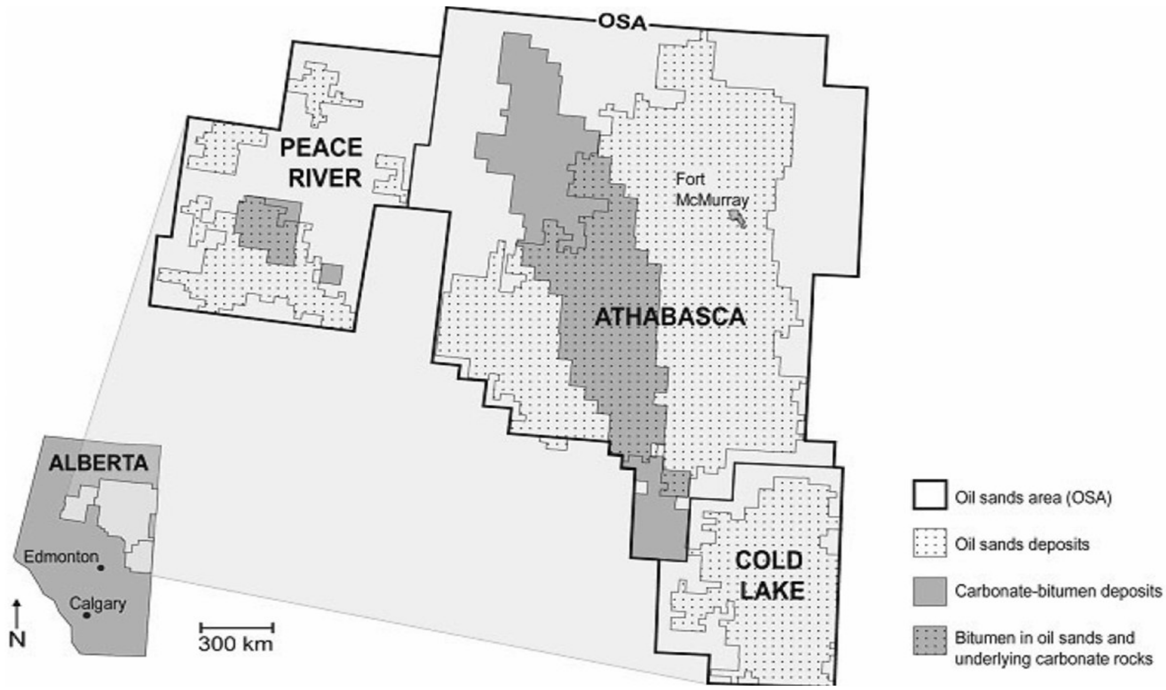

Figure 2-1 Regional map of the Alberta oil sands deposits (Hien, et al., 2008)

2.2.1 Beaverhill Lake Group

The lower stratigraphic limit of our study area is defined by the Beaverhill Lake Group. The Beaverhill Lake Group consists of Devonian age dolomites, limestones, shales and evaporates (Buschkuehle, 2003). The carbonates of the Beaverhill Lake Group are characterized by a high degree of deformation and karstification due to the dissolution of the Prairie Evaporite Formation, resulting in a complex surface with variable topographic highs and lows (Schneider, et al., 2012). The upper boundary of the Beaverhill Lake Group is defined by the Pre-Cretaceous unconformity, an angular unconformity of ~250Ma, during which extensive erosion, non-deposition and karstification occurred. This unconformity represents an ancient and mature paleotopographic erosional surface containing escarpments, faults, linear erosion, sinkholes and collapse features (Gingras & Rokosh, 2004). The topography of the Pre-Cretaceous unconformity is an important feature of the Beaverhill Lake Group due to its influence on the deposition of the overlying McMurray Formation sediments.

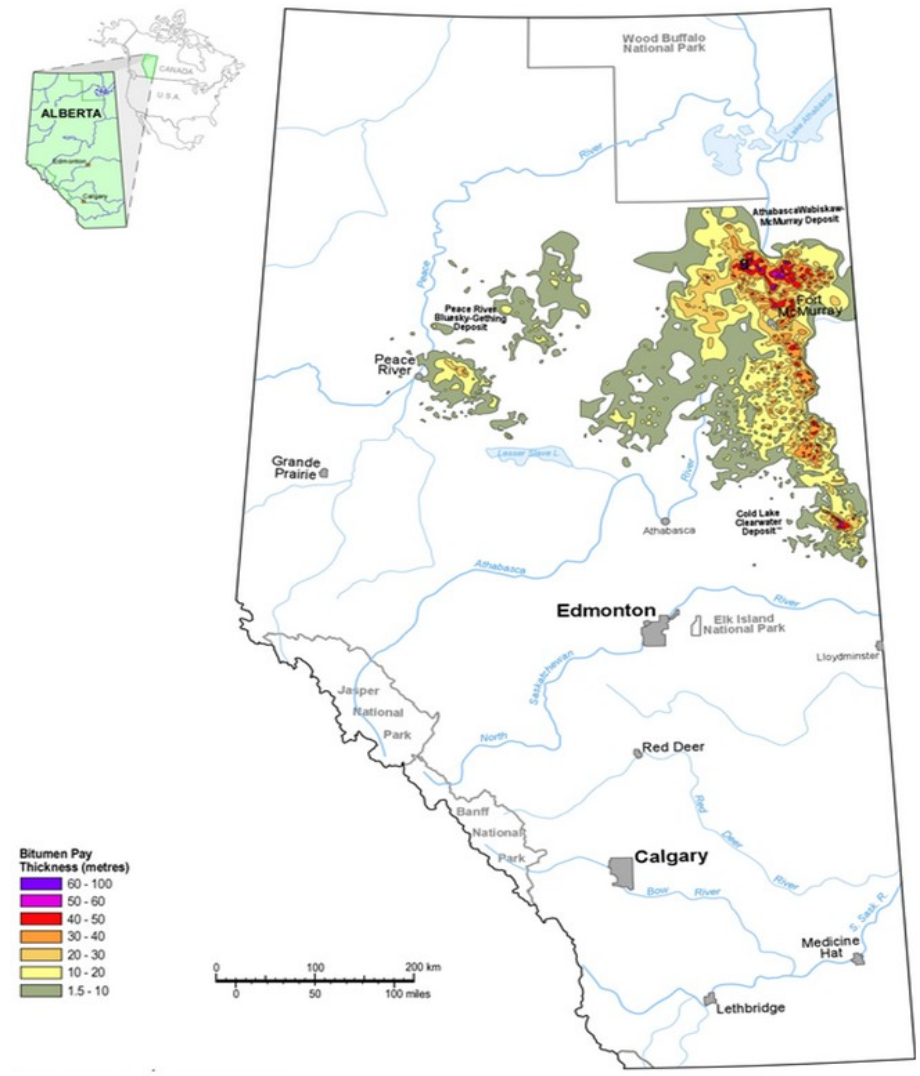

Figure 2-2 Bitumen pay thickness map of the Athabasca region. Modified from ERCB 2012.

Seismically, the Beaverhill Lake Group is represented by a positive high amplitude peak due to the strong impedance created by unconsolidated McMurray Formation sands directly overlying the Devonian carbonates (Figure 2-5). P-wave RMS velocities for events within the Devonian carbonates are on the order of 2500 - 3000m/s (5000m/s interval velocity).

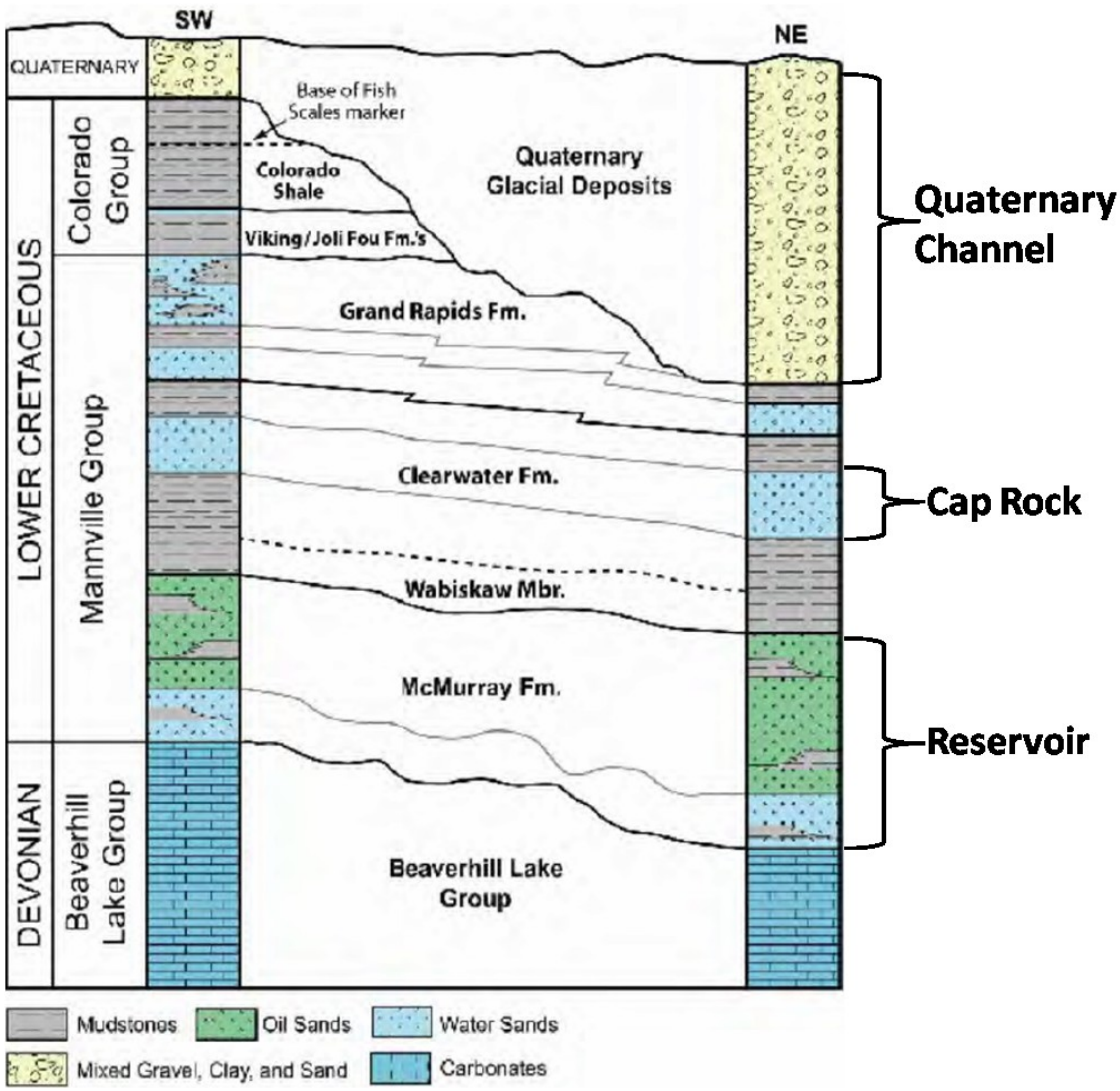

Figure 2-3 Stratigraphic Chart for the McMurray reservoir and overlying stratigraphy (modified from 2011 Nexen ERCB report)

2.2.2 McMurray Formation

The Lower Cretaceous McMurray Formation is the main bitumen reservoir in the region, and was the focus of SAGD production and reservoir interpretations for this thesis. The McMurray Formation is comprised dominantly of continental successions of fine to very fine grained sands with interspersed conglomerates and shales, deposited in incised valleys directly on the angular Pre-Cretaceous unconformity of the Beaverhill Lake Group (Flach, 1984; Mossop, 1980). The McMurray Formation was deposited in a north-south trending depression on the pre-Cretaceous erosional surface, created from the dissolution of the Prairie Evaporite and subsequent collapse of overlying formations. During Cretaceous time, a large fluvial system occupied this depression, shaping the limestone into a series of structural highs and lows (Flach, 1984). These structural lows played a key role in the distribution of McMurray Formation reserves, where the paleotopography controlled the deposition of McMurray Formation sediments and subsequently host the bulk of bitumen in the Athabasca region. The thicknesses of the McMurray Formation sediments differ as a function of Devonian relief, varying from 150 m thick in the center of deposition to zero in the west where it pinches out against a ridge of Devonian age limestone (Flach, 1984).

The McMurray Formation is commonly separated into the Lower and Upper McMurray, a classification which was adopted for this discussion. Lower McMurray fluvial successions are primarily sand-dominated channel-and-bar complexes with high porosities and permeabilities, and are often water saturated (Hein & Cotterill, 2006). The Upper McMurray succession is comprised of amalgamated estuarine channels and point bar complexes with lower porosities and permeabilities than the Lower McMurray deposits (Hein & Cotterill, 2006). These channels contain a mixture of mud beds and point bar sands, which are often bitumen rich (Hein & Cotterill, 2006). Mudstones are commonly present in the form of inclined heterolithic stratification (IHS) and are typically thick and discontinuous fills of abandoned channels, acting as baffles to steam flow (Hein & Cotterill, 2006). Due to the lack of burial, diagenesis and cementation is largely absent and thus the sands of the McMurray Formation are unconsolidated (Mossop, 1980). Figure 2-4 is a stratigraphic model for the McMurray Formation.

Seismically, the McMurray Formation lacks a single strong and coherent reflection. It is thus identified as the package of reflectors contained above the Devonian reflection and beneath the Clearwater C cap rock reflection (Figure 2-5). P-wave RMS velocities for the McMurray Formation range from 2000 - 2200m/s (2400m/s interval velocity).

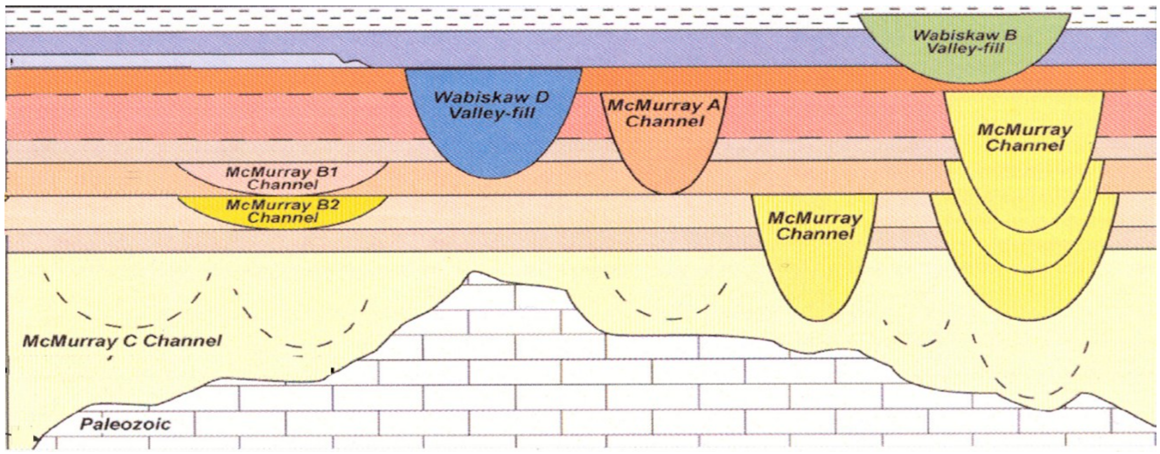

Figure 2-4 Stratigraphic model for the Wabiskaw Member and McMurray Formation (modified from Hein & Cotterill, 2006)

2.2.3 Clearwater Formation

The Early Cretaceous Clearwater Formation overlies the McMurray Formation reservoir throughout the Athabasca region. The Clearwater Formation is largely heterogeneous, consisting of marine siliciclastics of Albian age, primarily mudstones with intermingled silts and shales (Chou, 2011; Parks, 2001). The fine grained mud and shales of the Clearwater Formation form the cap rock for the McMurray Formation reservoir, where it provides a vertical seal for the entrapped oil prior to biodegradation and presently acts as a vertical barrier to SAGD steam migration. Average cap rock thickness is on the order of 50 m (Uwiera-Gartner, et al., 2011).

The base of the Clearwater Formation contains the Wabiskaw Member, a glauconitic sand and sandy shale unit which directly overlies the McMurray Formation (Flach, 1984). The Wabiskaw Member has hydrocarbon potential within the Athabasca region; however, this was not be addressed in this thesis.

The cap rock for the reservoir is defined on a type log as the interval ranging from the top of the Clearwater B to the top of the Wabiskaw sand (Figure 2-6). Seismically, the

Clearwater Formation can be divided into the Clearwater B and the Clearwater C reflections with the aid of geological well tops and synthetic seismograms. The Clearwater C reflection was designated as the cap rock reflection within the seismic data. The Clearwater C reflection is a laterally coherent trough spanning the entirety of the data set (Figure 2-5). P-wave RMS velocities for the Clearwater Formation and overburden range from 1400m/s - 1800m/s (2000m/s interval velocity).

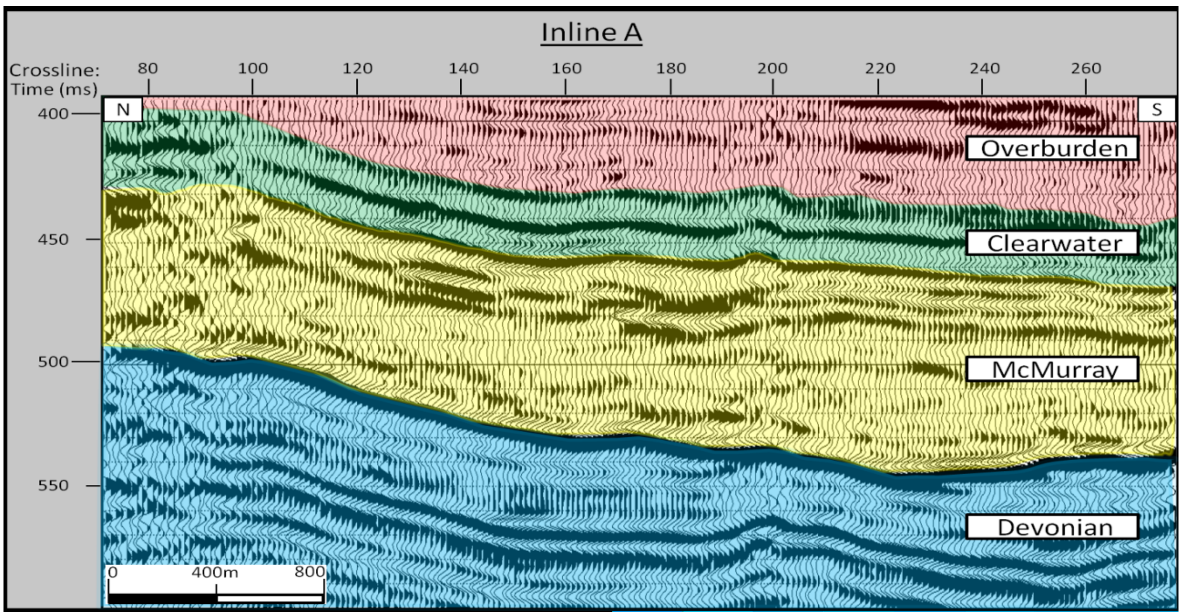

Figure 2-5: Seismic Section along Inline 155 displaying the seismic character for the Devonian Carbonates, McMurray Formation Reservoir and the Clearwater C and Clearwater B.

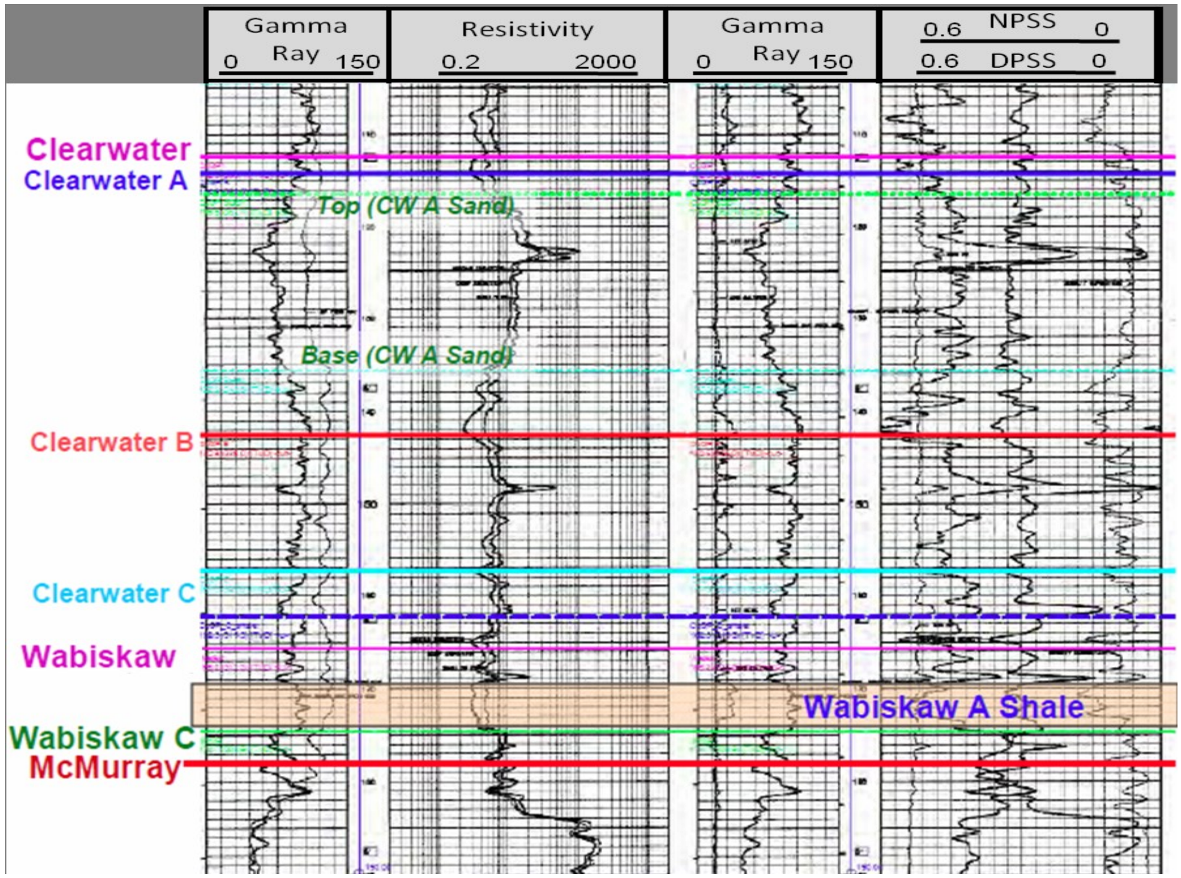

Figure 2-6 Type log displaying the Clearwater B, Clearwater C and Wabiskaw sands (cap rock) (modified from 2011 Nexen ERCB report).

2.3 Thief Zones

Water saturated and/or gas saturated sediments commonly have permeabilities thousands of times greater than those of bitumen sands (Flach, 1984). These highly permeable sands are hazardous to drilling operations and act as thief zones for steam when injection pressures exceed those of the reservoir (O'Rourke & Anderson, 1999; Pooladi-Darvish & Mattar, 2002). Thief zones commonly occur within the Athabasca region, often identified above the reservoir within the Clearwater Formation (gas in the Wabiskaw sands), or as a basal water lag within or beneath the Lower McMurray sediments where water saturation levels are high (Collins, 2005). A number of thief zones have been identified in this study area.

2.3.1 Quaternary Channel

One thief zone of major concern is a large channel comprised of Quaternary age sediments. The Quaternary channel is comprised of glacial deposits of coarse grained sands, pebbles and cobbles, is water saturated, and may breach the McMurray Formation reservoir in the eastern region of the study area. The pressure within the Quaternary channel is hydrostatic, while the pressure within the McMurray Formation reservoir is under-pressured due to the outcropping of McMurray sediments river valleys to the North. Therefore, operating horizontal SAGD wells below the Quaternary channel pressure allows for safe operations, where fluids will move into the under-pressured reservoir. However, drilling into the Quaternary channel at elevated pressures would result in excessive loss of circulating fluids and steam, posing a hazard to reservoir production.

Seismically, the Quaternary channel can be observed as a large Section of low quality seismic signal contaminating the eastern side of the data, as observed along a crossline (Figure 2-7). Due to the highly unconsolidated and pebbly nature of the Quaternary channel infill, the sediments are highly attenuative, preventing clear imaging of the channel boundaries and the underlying reflections. Thus, the Quaternary channels can be located from the seismic data, but lacks coherent reflections and thus its lower boundary in time cannot be easily delineated. Seismic data within the vicinity of the Quaternary channel is low quality and unreliable data, and therefore should not be used when performing an analysis of the reservoir (Figure 2-7). All SAGD well pairs terminate prior to the inter Section of the Quaternary channel, restricted by a production boundary of 150 meters offset from the Quaternary channel edge.

2.3.2 Gas Charged Sands

Gas charged sands are present within the McMurray Reservoir, primarily within the upper McMurray Formation. Figure 2-8 is a type log from the study area displaying gas charged sands within the upper McMurray reservoir, as identified on resistivity and density logs. Gas charged sands are also present within the Wabiskaw Member (Lower Clearwater Formation). These gas sands are clearly observable as high amplitude anomalies within the upper McMurray reflections, as well as crossover on the density logs in Figure 2-8.

2.3.3 Water Saturated Sands

Lastly, thief zones are present within the McMurray reservoir. Figure 2-9 displays water saturated sands underlying the gas charged sands of the upper McMurray reservoir, as identified by low resistivity values. For production purposes, horizontal wells penetrating the underlying bitumen reservoir maintain a 5 m stand-off from water saturated sands when the water saturated sands are in direct contact with bitumen, and a 3 m stand-off when the water is separated from the bitumen by $\geq$ 2 m of shale. Figure 2-9 is type log displaying thief zones of high water saturation within the bitumen pay zone. Thief zones such as this may prevent heat within the lower channel sands from reaching the overlying sands, thus bypassing bitumen reserves.

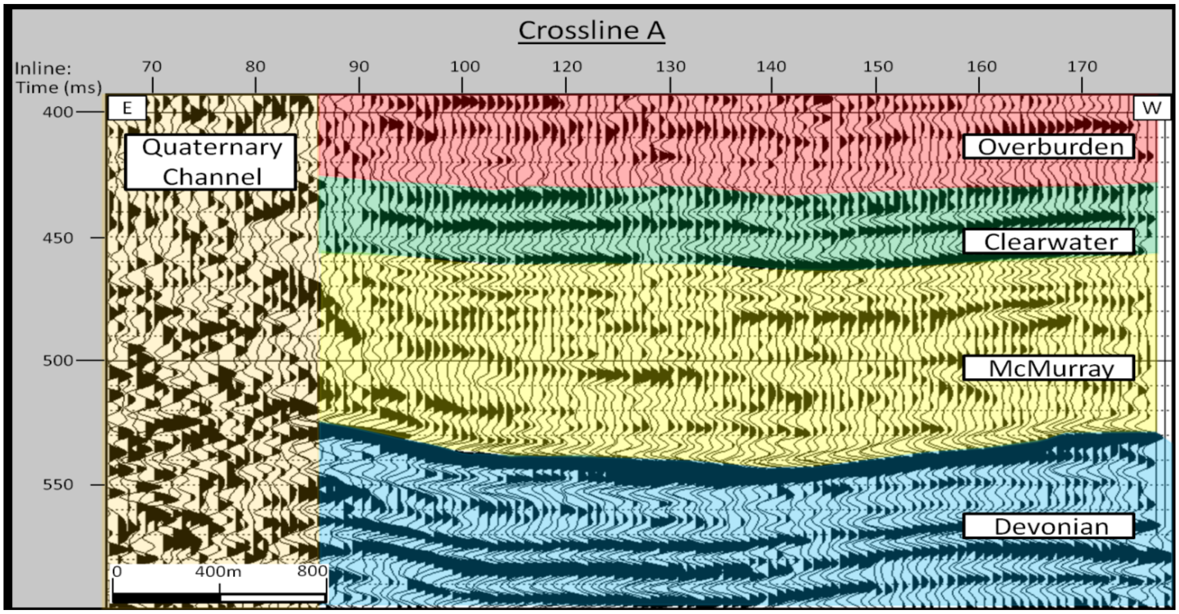

Figure 2-7 An East-West crossline displaying data contamination from the Quaternary channel

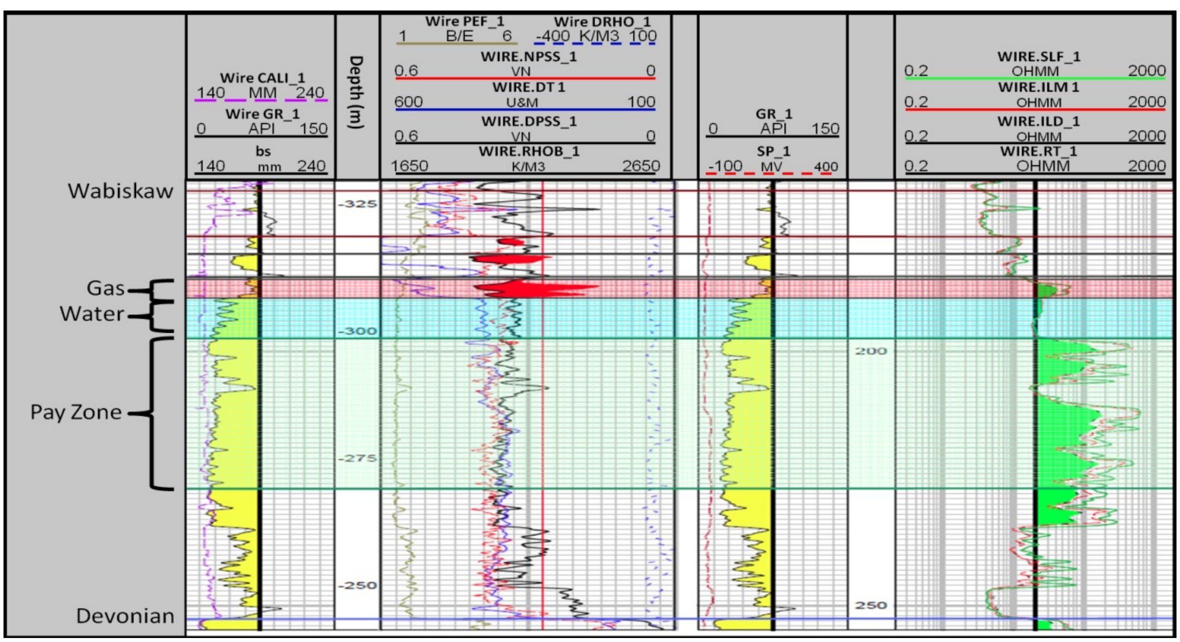

Figure 2-8 Type Log displaying thief zones and bitumen pay interval. Gas and water saturated sands overlie the reservoir (modified from 2011 Nexen ERCB report)

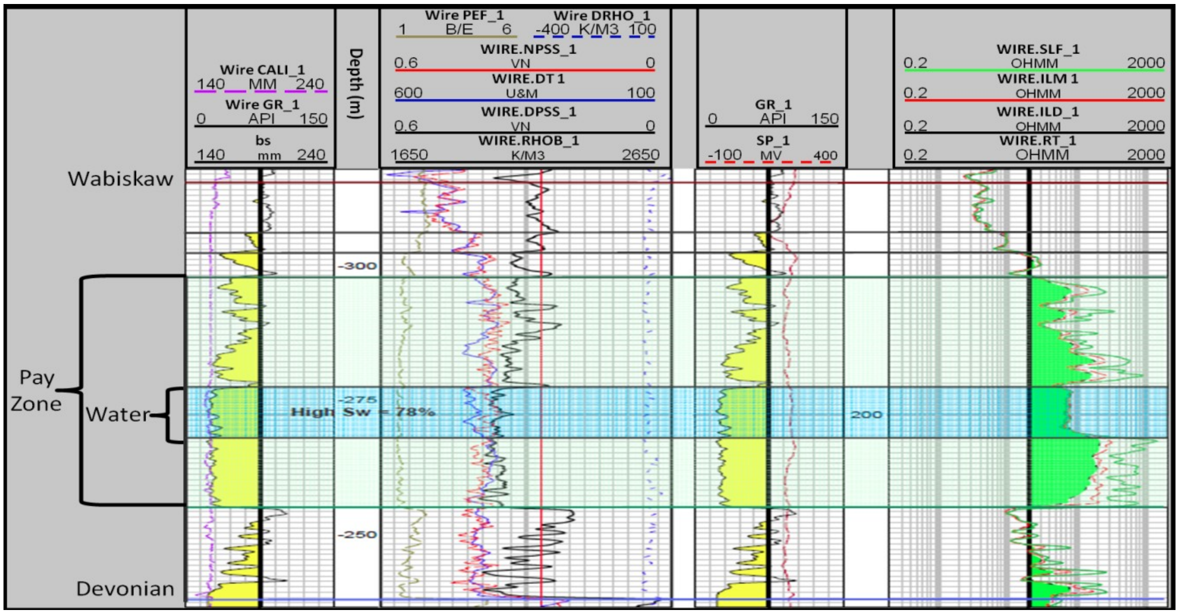

Figure 2-9 Type log displaying a thief zone within the bitumen pay interval (modified from 2011 Nexen ERCB report)

Chapter Three: **Data Processing**

The processing of the 4D geophysical data was focused on repeatable imaging of the McMurray Formation reservoir, a shallow bitumen reservoir lying at a depth of ~200 meters. This shallow, unconsolidated reservoir unconformably overlies the Beaverhill Lake Group carbonates, as discussed in Chapter 2. The pre-Cretaceous unconformity separates the low velocity and highly attenuative sand from underlying high velocity carbonates and shales. Seismically, these carbonates exhibit a high amplitude peak, created by the positive impedance contrast from unconsolidated bitumen sands over carbonates (Li, 2001). Thus, the images of the data is dominated by this high-amplitude reflection.

The complete processing of the geophysical data was carried out in <u>Halliburton's ProMAX geophysical processing software</u>. The processing was focused on the repeatable imaging of the McMurray Formation reservoir in a time-lapse sense. To accomplish this, identical processing flows were applied to the baseline and monitor data sets to preserve production induced changes within the reservoir, and to minimize differences due to acquisition, processing or other non-production induced changes.

The processing flow of the data sets was comprised of 7 steps as follows: (1) common data decimation, (2) data conditioning, (3) Gabor deconvolution, (4) velocity analysis and stack, (5) static corrections, (6) post stack migration, and (7) post migration conditioning. Figure 3-1 is a schematic chart of the processing flow applied to both the 2002 and 2011 P-wave data sets.

This chapter of the thesis discusses the repeatable processing of the 4D P-wave data. I will discuss the challenges of, and innovations for, generating robust images of a highly attenuative shallow reservoir.

3.1 Common Data Decimation

As mentioned previously in Chapter 1, the 2002 survey contained a greater number of source and receiver locations than the 2011 survey. Table 3-1 is a comparison of sources and receivers between the two surveys. The 2002 survey extends over a much

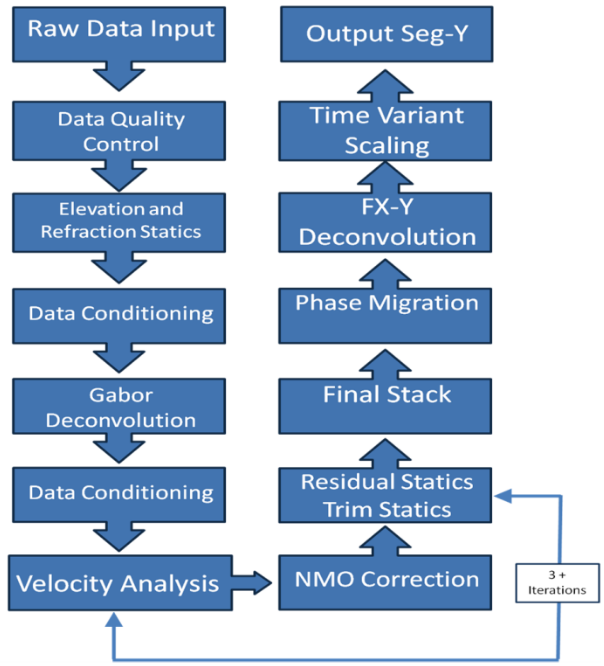

Figure 3-1 Processing flow applied to the baseline and monitor P-wave surveys.

larger area than the 2011 survey and hence contains data non-common to both surveys, as displayed in Figure 3-2. For repeatable analysis, all non-common sources and receivers were removed from the two data sets, leaving only common source and receivers. To decimate the dataset, a Matlab algorithm was developed to match common source and receiver locations through the identification of common X and Y coordinates. Source and receiver X and Y coordinates were matched within a 10 m criterion, allowing for a negligible difference of source and receiver locations between the baseline and monitor surveys. Differences between monitor and baseline positions greater than 10 m no longer represented an accurate reoccupation of source or receiver locations and thus did not satisfy our criteria of highly repeatable receiver reoccupation. As a result, the 2002 survey was reduced from 8900 source locations and 9300 receiver location to 2420 common source locations and 2250 common receiver locations, a reduction of 73% and 76% respectively. The 2011 survey was reduced from 2450 source locations and 2500 receiver locations to 2420 common source locations and 2250 common receiver locations, a reduction of 1.3% and 10% respectively (Table 3.1). Figure 3-3 is the final source locations for the 2002 and 2011 surveys after decimation. Figure 3-4 and Figure 3-5 are the original and matched receivers for the 2002 and 2011 survey.

Survey	Source	Receiver	Decimated Source	Decimated Receivers
2002	8900	9300	2420	2250
2011	2450	2500	2420	2250

Table 3-1 Source and receiver numbers for the 2002 and 2011 surveys

3.2 Data Conditioning

Before data processing, quality control checks were performed to remove dead or noisy traces and to ensure that the remaining data was consistent and of high quality. Figure 3-6 is a raw shot record from the 2011 survey containing a number of noisy and dead traces. Through manual interaction, all traces were inspected for the presence of dead (zero amplitude) traces, traces with a reversed polarity, or traces with a signal character significantly different from that of the remainder of the data. Such traces were flagged through an interactive trace killing routine, removing them from the data set (setting their amplitude to zero). Four iterations of the manual trace inspection were performed on each data set to ensure that all bad traces have been flagged. To certify that the same data was processed in both data sets, any traces removed in one survey had its equivalent trace removed in the other survey. Hence, the removal of such traces guarantees that the same traces were processed in both surveys (Figure 3-6).

The next step in quality control was to compare raw records from the 2002 survey against those from the 2011. Figure 3-7 is a comparison of a raw record from both surveys. It is quite evident that the two raw records are not visually the same. The 2011 survey was recorded with accelerometers, while the 2002 data was recorded as velocity. The 2011 data was integrated to move from acceleration to velocity. Figure 3-8 is a comparison of the same shot records after integration.

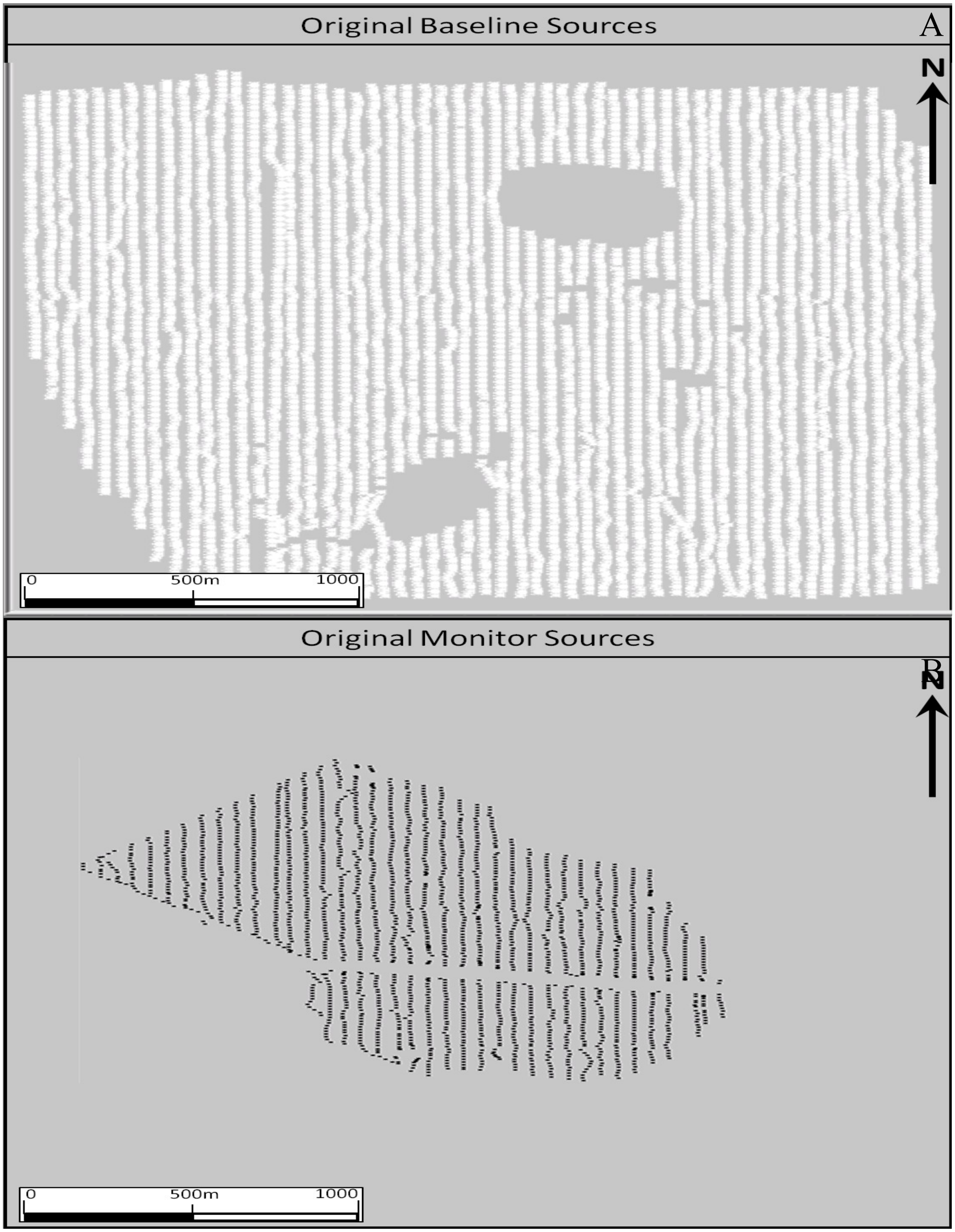

Figure 3-2 Original source locations for the 2002(a) and 2011(b) surveys

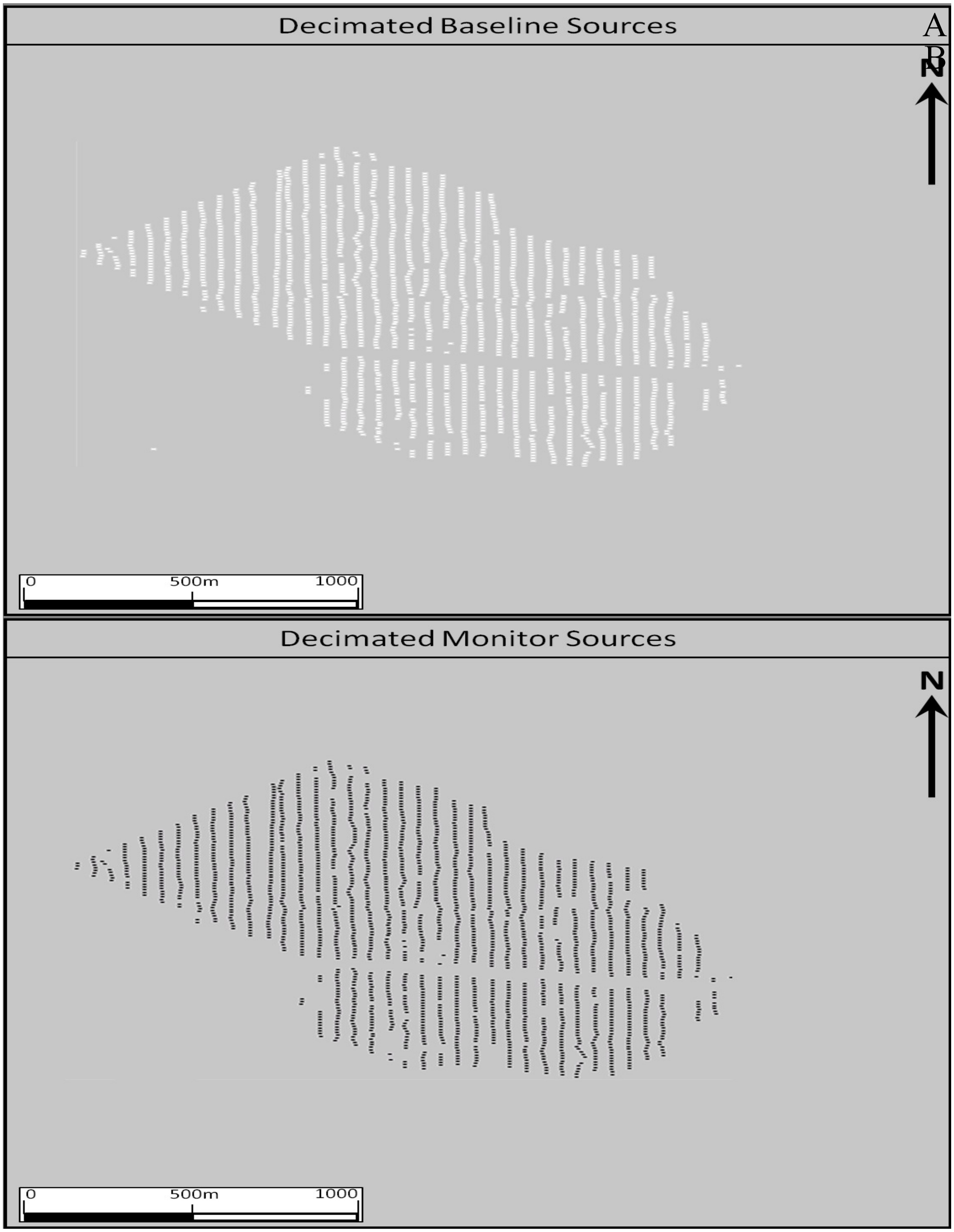

Figure 3-3 Decimated source locations for the (a) 2002 and (b) 2011 surveys

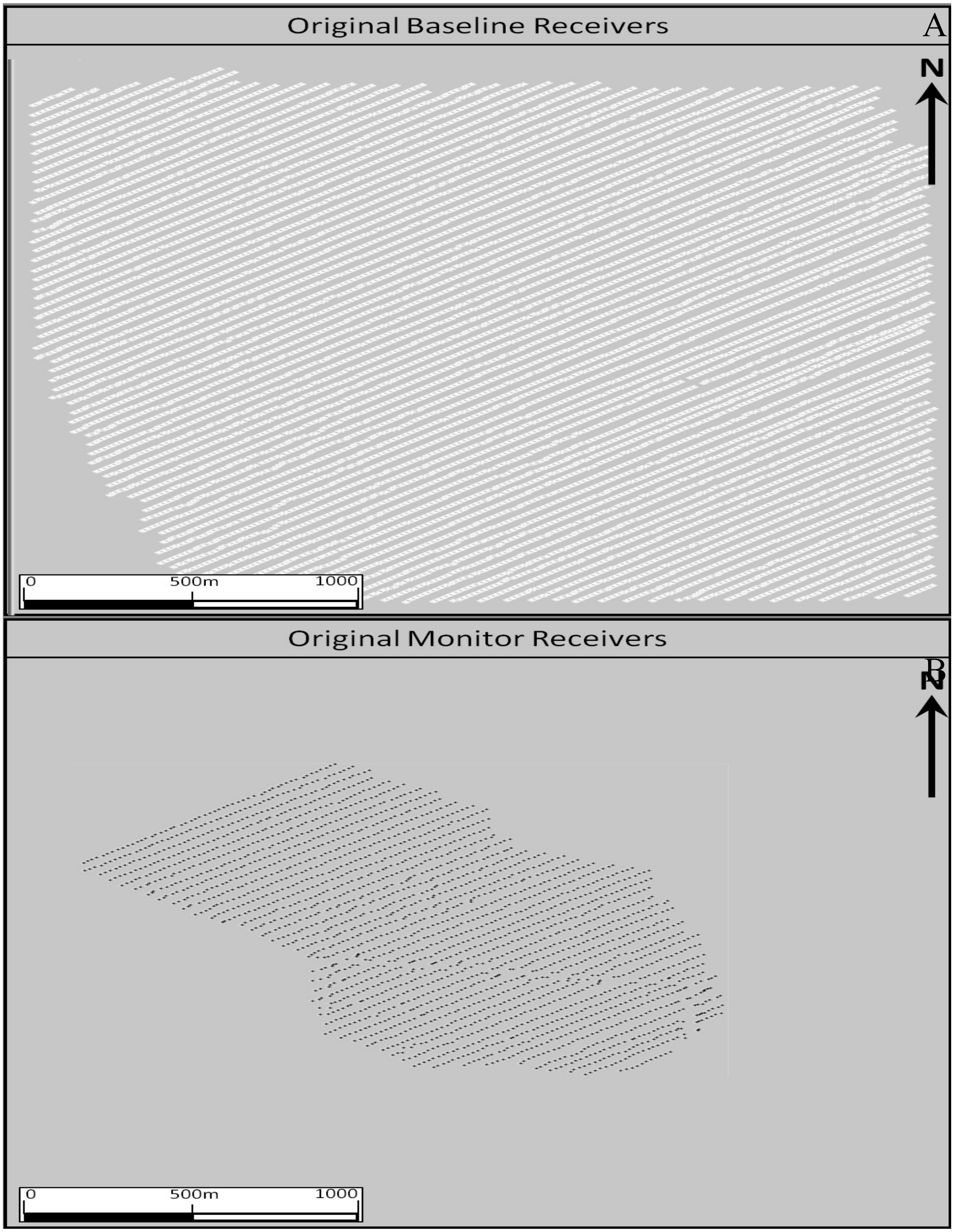

Figure 3-4 Original receiver locations for the 2002(a) and 2011(b) surveys

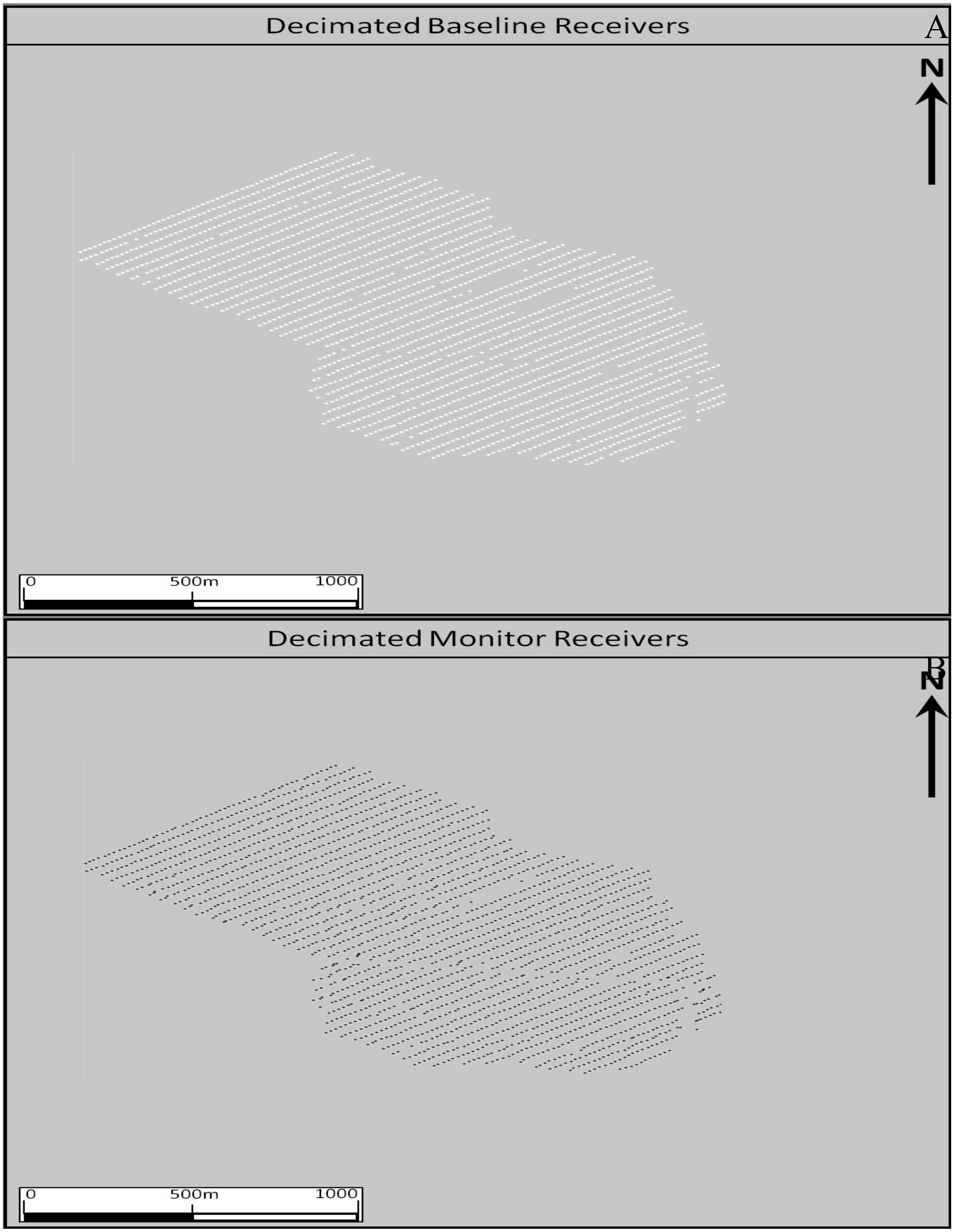

Figure 3-5 Decimated receiver locations for the (a) 2002 and (b) 2011 surveys

Furthermore, from examining Figure 3-8, it is evident that the 2002 data has higher S/N than the 2011data. I suspect that the elevated level of noise is due largely to surface noise contamination generated by ongoing reservoir production and other surficial activates that were not present during the recording of the 2002 data. To reduce noise, the raw event records were subject to conditioning techniques that were was carried out in three steps; (1) balancing amplitude contributions in a surface consistent manner, (2) attenuating coherent noise, and (3) balancing amplitudes on a trace-by-trace basis.

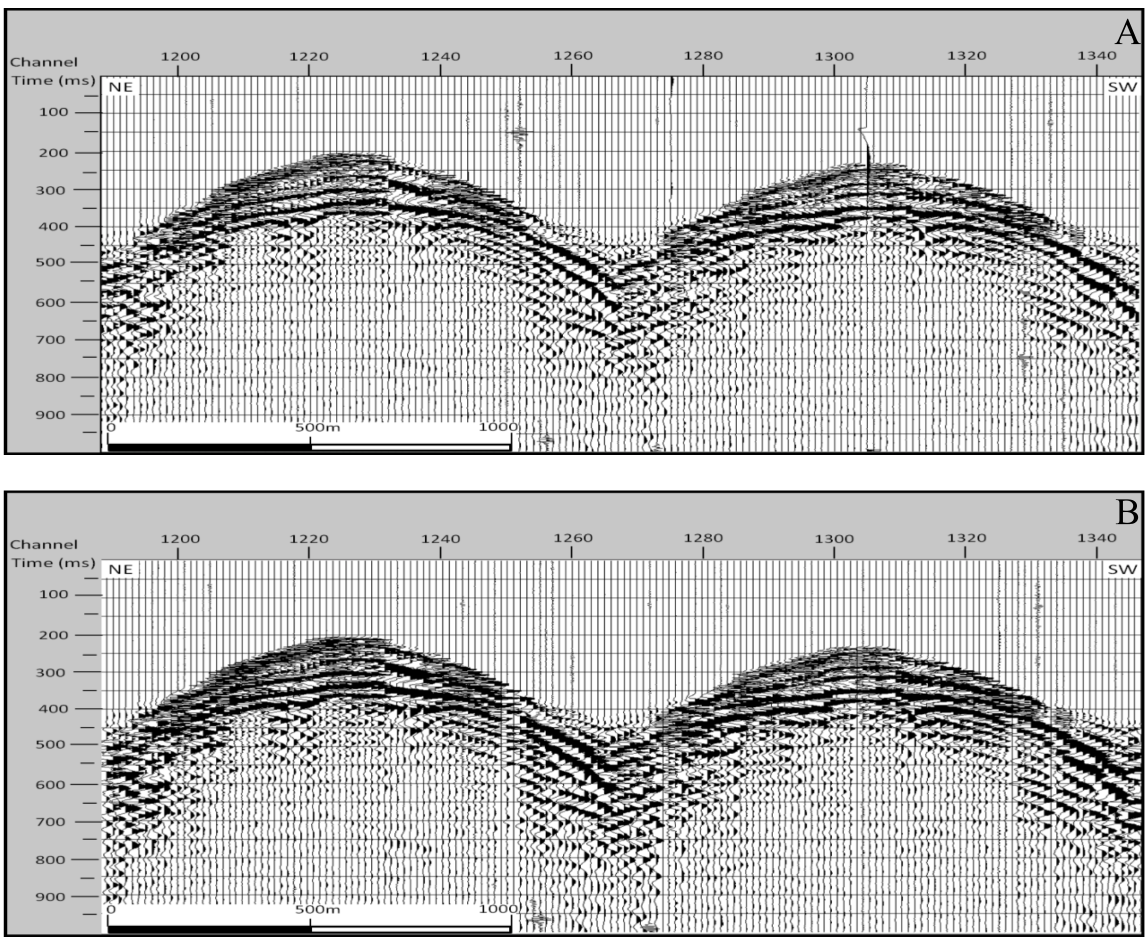

Figure 3-6 (a) Raw shot record from the 2011 survey displaying noisy traces. (b) Same record after removal of noisy traces

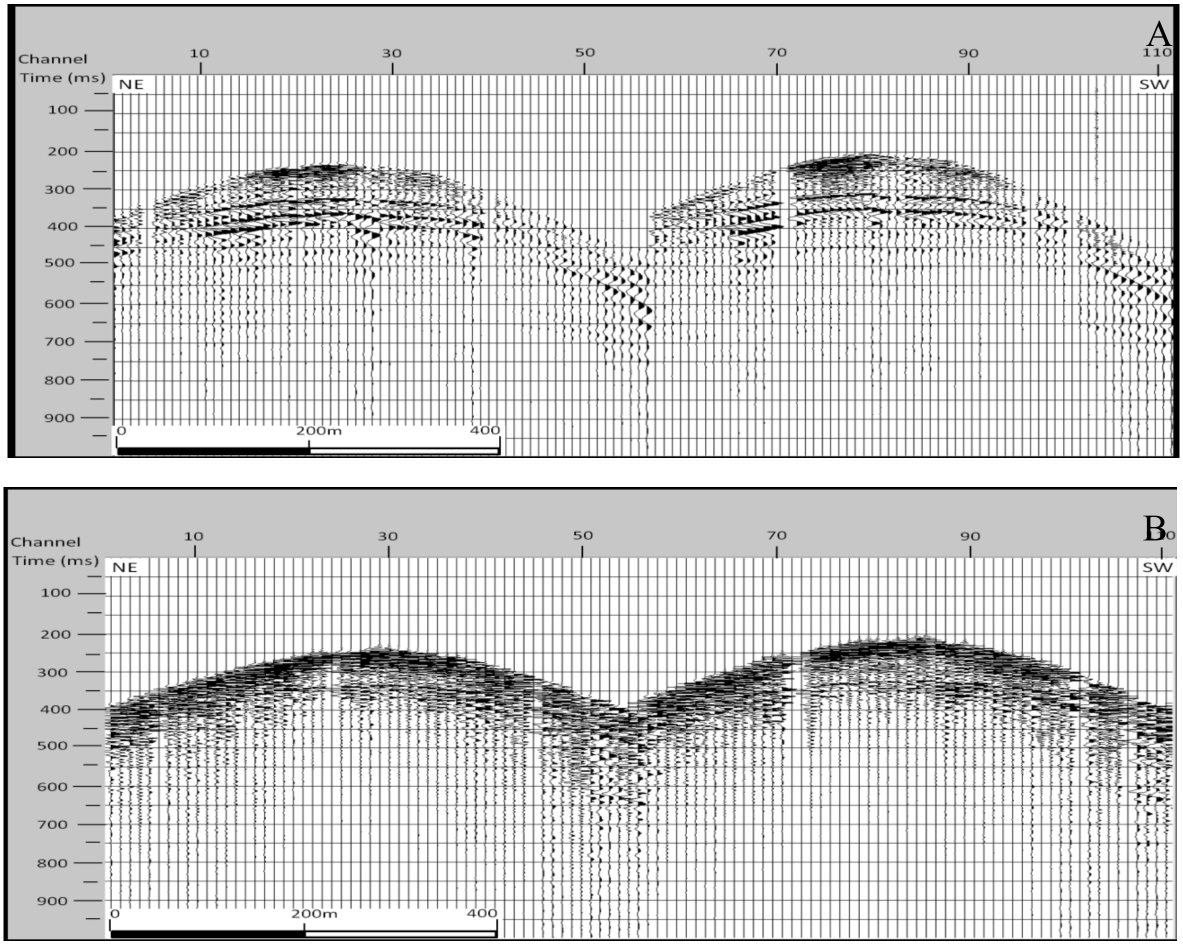

Figure 3-7 Comparison of raw traces from (a) 2002 and (b) 2011 equivalent record

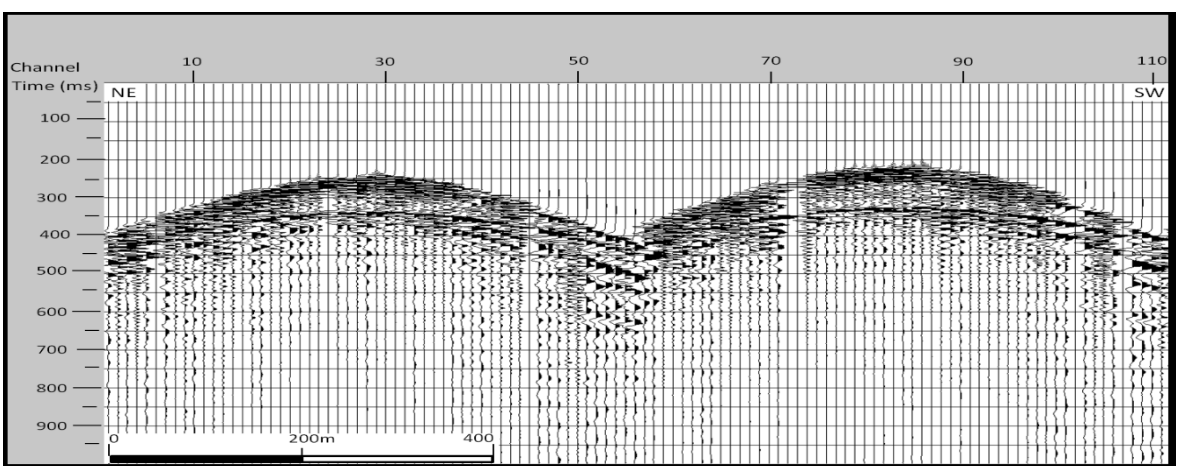

Figure 3-8 Same shot record as in Figure 3-8 (b) after integration from acceleration to velocity

3.2.1 Surface Consistent Amplitude Correction

The surface consistent amplitude correction estimated and adjusted the relative amplitude contributions from sources, receivers, offsets bins, CMP's and channels, applied on a surface consistent basis. The need to balance amplitudes stems from the need to reduce amplitude variations due to acquisition and near-surface effects, including receiver coupling and source strength variations. Through a surface-consistent processing technique, near-surface factors affecting amplitude contributions can be approximated and corrected (van Vossen, 2006; Taner, 1981).

The amplitude of a trace is a sum of the contributions from the source, receiver, source-receiver offset, density and velocity of reflecting horizon, and ambient noise. Statistically, using a large number of traces, these contributions were estimated as an ensemble and a correction was applied to accommodate for higher or lower amplitude values. The surface consistent amplitude correction statistically estimated amplitude contributions through a Hilbert transform and used a Gauss-Seidel inversion method to decompose amplitude contributions to the desired components (source, receiver, etc) through an iterative process (Young, 1971). Figure 3-9 is a shot gather after amplitude balancing though the surface consistent amplitude technique (in comparison to before, Figure 3-7 (b)).

3.2.2 Coherent Noise Attenuation

Coherent noise attenuation removed coherent noise with linear moveout through the application of an F-K filter. Noise estimates were calculated as a function of frequency and offset, and subtracted from the raw traces to yield filtered data. Coherent linear noise in land data is present in the form of ground roll, characterized by low group velocity, large amplitudes and low frequencies. Figure 3-10 is an example of raw data contaminated with ground roll, masking the presence of reflections due to the high amplitude of the ground roll (Yilmaz, 2001). Thus, linear energy was removed through F-K filtering, where coherent linear event can be separated in the F-K domain on the basis of event dip

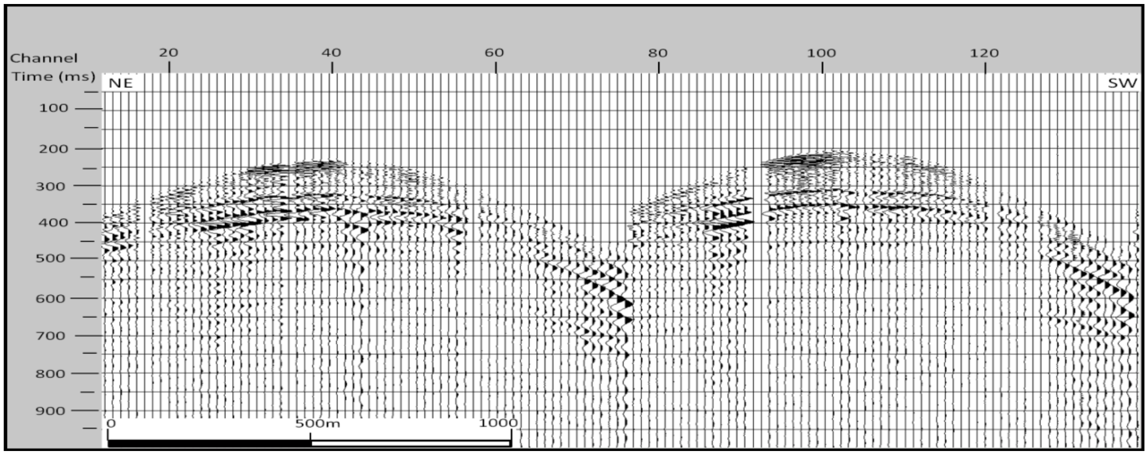

Figure 3-9 2002 shot record after surface consistent amplitude correction

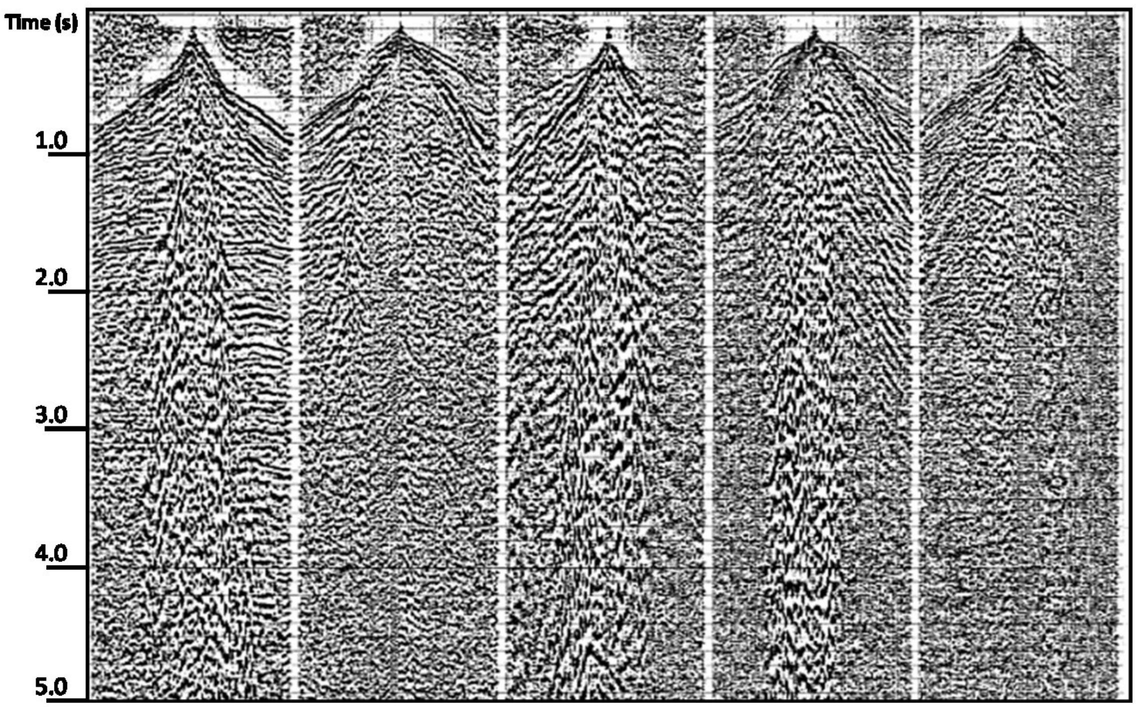

Figure 3-10 An example of raw data contaminated with ground roll. High amplitude of the ground roll masks the presence of reflectors (Yilmaz, 2001)

(Yilmaz, 2001). Events in the F-K domain are attenuated through a fan filter, defined on the basis of frequency and velocity pairs in the T-X domain. Fan filter frequency-velocity pairs were defined as follows: 2 Hz-1m/s, 4 Hz-100m/s, 13 Hz-1200m/s, 15 Hz-1400m/s.

3.2.3 Trace Equalization

Trace equalization is a scalar applied to balance amplitudes on a trace-by-trace basis in attempt to reduce anomalously high or low trace amplitudes. The scalar is defined as the mean amplitude value within a specified time gate. The time gate used was sufficiently large such that all of the data above and including the Devonian reflector were used to calculate the scalar; 0-600ms as applied to raw shot gathers. Figure 3-11 displays a shot gather after trace equalization.

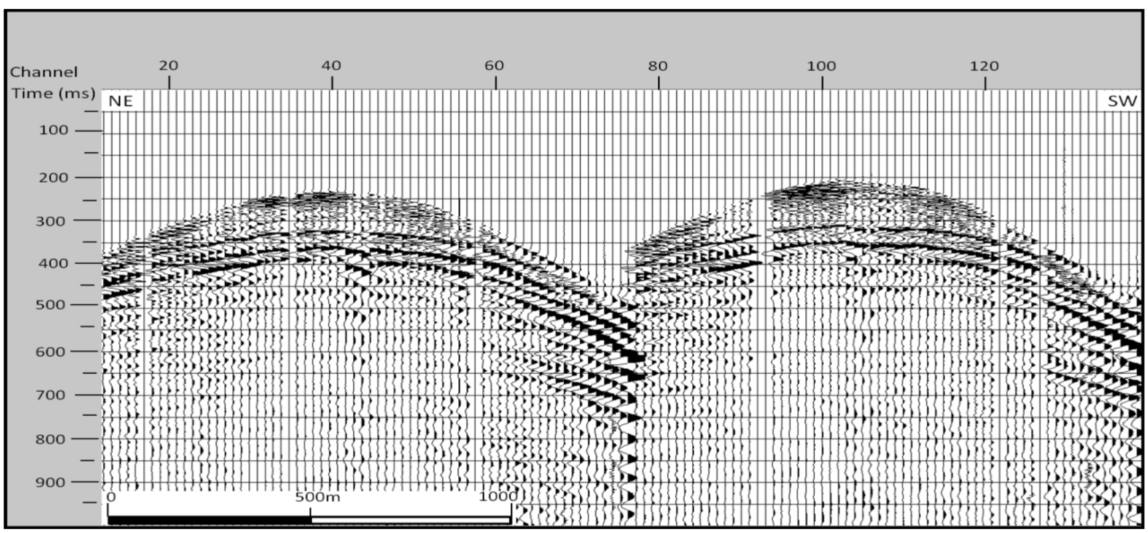

Figure 3-11 2002 shot record after trace equalization in comparison to before (Figure 3-9).

3.3 Gabor Deconvolution

A recorded seismogram is the convolution of a source signal with the time reflectivity of the earth. Often, this response includes a variety of undesirable effects including reverberations and attenuation. Deconvolution is a method which estimates these effects through linear filters, and then applies an inverse filter to remove the approximations of such effects (Wiener-Levinson filter) (Yilmaz, 2001). The deconvolution operator convolves the inverse filter with the seismic traces in an attempt to reproduce the earth's reflectivity.

There are a variety of deconvolution operators that are valid for removing the undesirable effects of attenuation and reverberations, including spiking deconvolution, predictive deconvolution. The deconvolution operator chosen for this thesis was the Gabor Deconvolution, which can be run in either spiking or predictive mode.

Gabor Deconvolution, as ran in spiking mode, is a nonstationary operator which extends the stationary Wiener spiking deconvolution to include nonstationary signal. It aims to remove both source signatures and earth attenuation effects by transforming the data into the Gabor- domain and performing a time-frequency decomposition of a seismic trace (Margrave, 2011). This nonstationary approach provides advantages over stationary algorithms, for a typical seismic trace is often non-stationary due to effects including inelastic absorption and source-generated noise contamination (Henley, 2001).

The Gabor operator decomposes a seismic trace by implementing overlapping Gaussian windows, and taking the Fourier transform of each window (Henley, 2001). The deconvolution operator is applied through the division of the Gabor transform by an estimated amplitude spectrum, producing a deconvolved Gabor transform from which the seismic trace can be reconstructed (Henley, 2001).

The window size chosen for the Gabor deconvolution operator is the most critical parameter affecting the quality of the output data, where the size of the time window largely influences the sensitivity of the deconvolution (Henley, 2001). Choosing the size of the window was a less than trivial task. The high amplitude peak of the Devonian

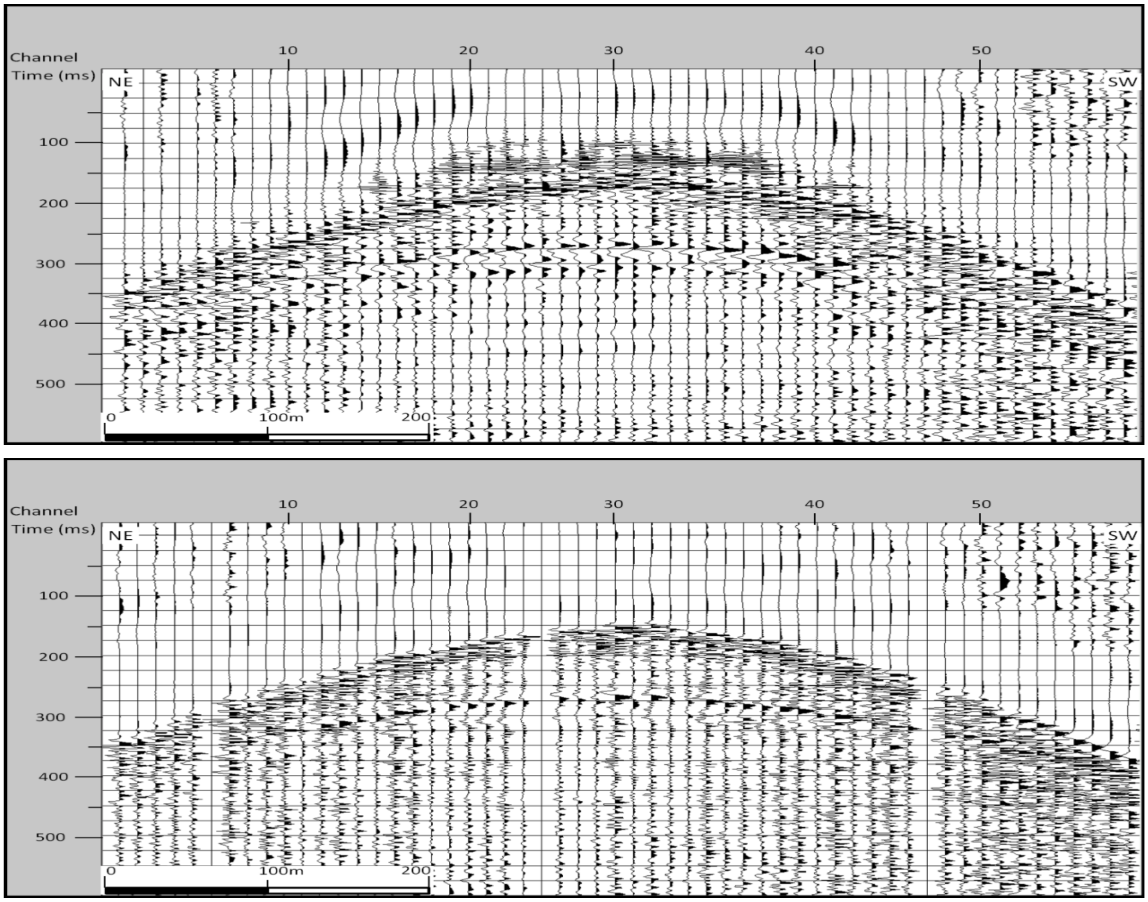

Figure 3-12 2002 shot record after Gabor deconvolution with (a) 800ms window and (b) 100ms window

carbonate dominates shot gathers, often being the only easily recognizable reflector on unstacked Sections (Figure 3-11). The high amplitude nature of the Devonian reflector negatively affected the deconvolution, where the frequency content of the shallow data was reduced through the involvement of the Devonian peak in the deconvolution calculation. To combat any frequency degradation, the Gabor deconvolution was applied with a very short time window of 100 ms. This short window allowed the operator to adapt to the frequency content of the signal both above and below the Devonian reflector, effectively enhancing the frequency content of the reservoir, retaining frequencies as high as 160 Hz. A comparison of the short window Gabor deconvolution data to the same data processed with a more typical 800 ms deconvolution operator yielded an improvement in both image quality and frequency content (Figure 3-12). Following the application of the Gabor Deconvolution, the data was bandpass filtered to reduce the whitening of the high frequency noise (above 160 Hz).The remainder of the parameters were largely left to default; a more detailed explanation of the workings of the Gabor transform can be found in Henley and Margrave (2001).

3.4 Velocity Analysis and Stack

The next step in the processing flow was to determine root-mean-squared (RMS) velocities for the normal moveout (NMO) correction. The NMO correction is a RMS velocity based correction to compensate for traveltime delays in a reflection arrival with increasing time and offset from a source location. By determining the RMS velocity of the subsurface, the NMO corrections were calculated and applied to the data.

3.4.1 Supergathers

Before the RMS values for the NMO correction were determined, the data was rearranged to form common offset supergathers. Supergathers are a summation of CMP's into a single large gather for input into a velocity analysis algorithm to aid in the determination of RMS velocity values. Supergathers sum a specified number of CMP's in 3D through the denotation of inline and crossline numbers, increments and ensemble size, all located within a specified grid. Figure 3-13 is an example of a supergather, in which 15 CMP's are summed into a single gather. For our processing, 9 CMP's were summed into a single gather. Figure 3-14 is a representation of the supergather grid generated for the 2002 and 2011 surveys.

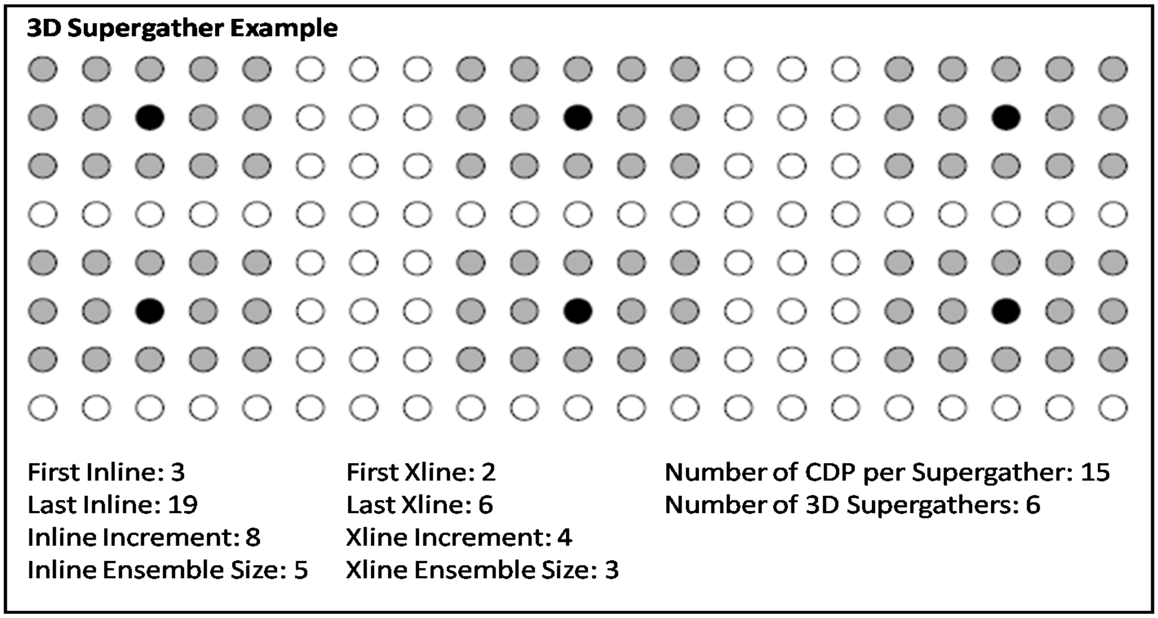

Figure 3-13 3D supergather example

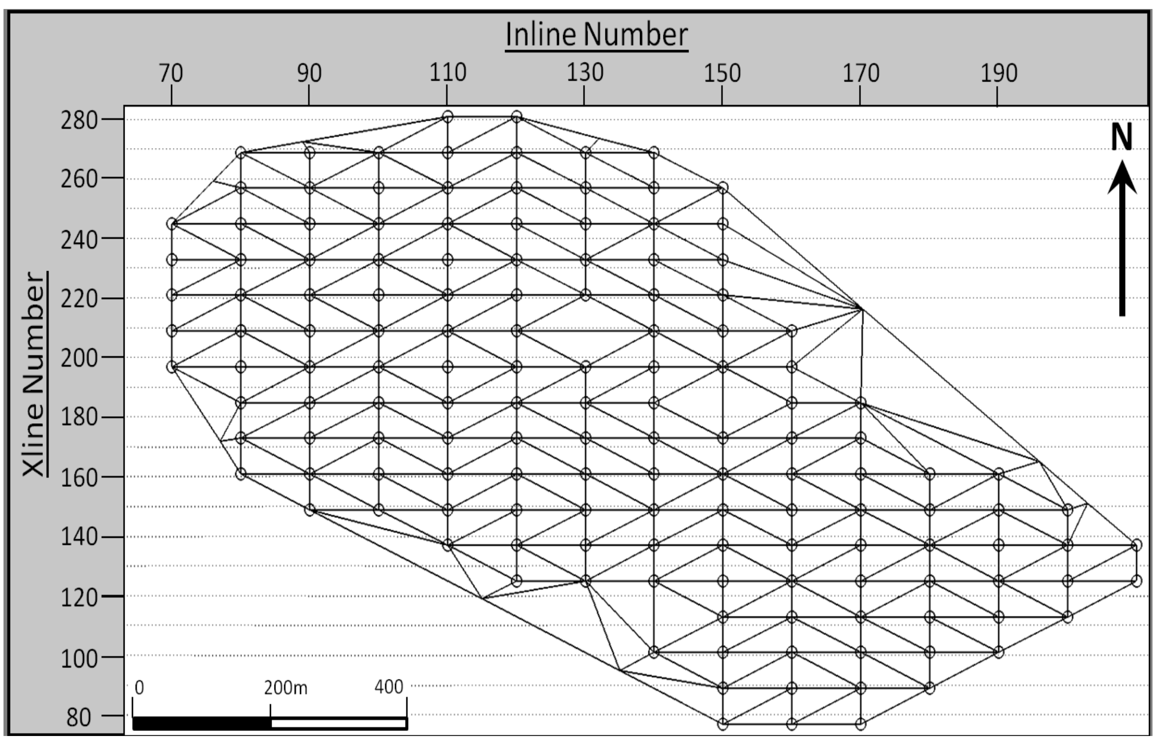

Figure 3-14 Supergather grid. Each circle represents the summation of 9 CMP's into a single gather, which will be analyzed for NMO RMS velocities.

3.4.2 Velocity Analysis

The RMS velocities for the NMO correction were determined through an interactive semblance display in conjunction with a supergather display of the data (Figure 3-15). Semblance is a measure of the coherency of traces across multiple channels. Quantitatively, it is the energy of a stack normalized by the energy of all the traces within the stack (Sheriff, 2002). A semblance plot analyzes each supergather, computing values on the basis of applying an NMO correction over a range of constant velocities within a defined minimum and maximum value. Semblance plots are a graphical representation of the measurement of similarity of each NMO correction, where a velocity value providing an appropriate NMO correction would display a high semblance value, while a velocity value providing a poor correction would be represented as a low semblance value. Semblance values were contoured for easier identification of highs and lows.

The selection of a semblance value will impact the gather display. The gather display represents the supergather, stacked and NMO corrected as a function of the selected RMS velocity. By selecting different velocities on the semblance panel, the gather display interactively changed to reflect this velocity. Thus, the semblance plot and the gather display were used in conjunction with each other. Hence, one can determine accurate RMS values for the NMO correction.

Figure 3-15 is a display of the semblance plot and stacked gather panel used to pick velocity values for the 2002 P-wave data. In the region of unconsolidated bitumen sands (150-250 ms) low RMS velocities were observed in the range of 1400 m/s to 2200 m/s, increasing with depth. Moving to later times, a sharp increase in RMS velocity was observed, associated with the Devonian carbonates at 250 ms, where RMS velocity values increase to 2500-3000 m/s. This sudden increase is attributed to the sharp change in lithology, as we move from the low velocity and attenuative bitumen reservoir sands, across the Paleozoic uncomformity and into the older and higher velocity Devonian carbonates. Beneath the carbonate reflector, semblance values become harder to select due to the loss of resolution with depth. Final RMS values for the deepest portion of the data are set to 5000m/s.

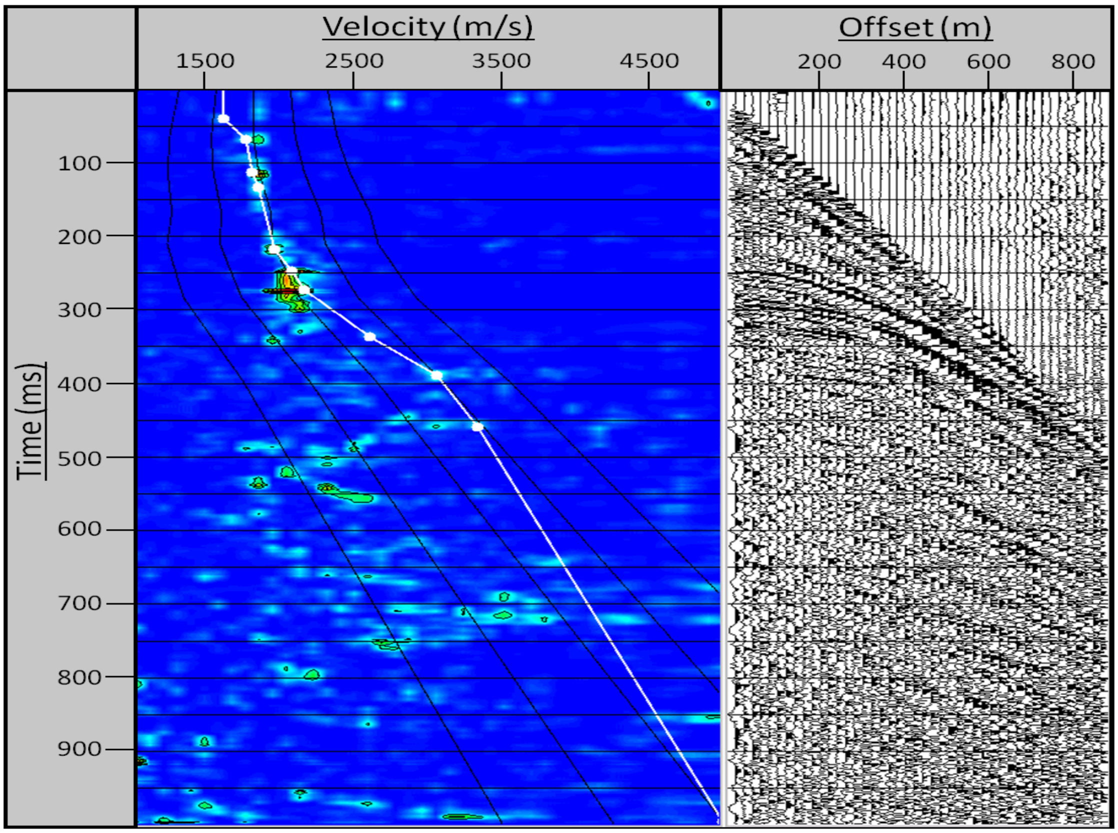

Figure 3-15 Semblance plot and supergather panel. White circles are RMS velocities selected to best correct NMO on the supergather panel. Semblance maxima observed at 500 – 600 ms are interpreted to be multiples of the primary energy at 300 – 350 ms.

To provide some quality control measurements for the velocity analysis, RMS velocity values were converted to interval velocities via a smoothed Dix Equation and cross-referenced against velocities provided from well logs. The interval velocities showed a strong correlation with well log values, with interval velocities of 2000m/s within the shallow Section, 2400m/s within the reservoir above the McMurray-Devonian interface, and 5000m/s beneath the Devonian reflector.

Figure 3-16(a) is a comparison of RMS velocities to interval velocities along an inline running N-S through the center of the 2002 data.

3.4.3 NMO Correction and Mute

Following the selection of RMS velocities, the NMO correction was applied. The NMO correction, as previously described, is a velocity based correction to compensate for traveltime delays with increasing time and offset. However, this correction introduces NMO stretch, a frequency distortion which degrades the image quality of shallow events at long offsets (Yilmaz, 2001; Trickett, 2003). This frequency distortion lowers the dominant frequency via a stretching of the dominant period (Yilmaz, 2001). Because the stretch affects large offsets, the imaging of shallow events will be particularly affected where shallow events rely on the stacking of longer offsets to produce robust images. The degradation of the long offsets greatly impacted the shallow imaging, an issues particularly pertinent to our data. Figure 3-18 is a CMP gather after the application of the NMO correction. Notice the long offset image degradation due to the NMO stretch.

To retain the highest amount of non-contaminated data the NMO stretch was removed via a surgical mute, specified in terms of a stretch mute percentage. The use of a stretch mute percentage allowed for the repeatable application between data sets. The alternative option, a manual mute, was designed on a selected number of CMP's and then extrapolated to the remaining. This introduced some variations when extrapolated between CMP's of different offsets, reducing the repeatability. A stretch mute percentage is more consistent between both CMP gathers and datasets, hence more repeatable.

Figure 3-18c shows a gather after the removal of the NMO with a 50% stretch mute. The shallow reflectors are now limited to short offsets. Figure 3-21 is a stacked Section produced using the 50% stretch mute. Comparing this to a stack produced from a more typical stretch mute percentage of 30% (Figure 3-22) it was observed that an increase in image quality provided by the longer offset mute. A 50% stretch mute was applied to all NMO corrected data.

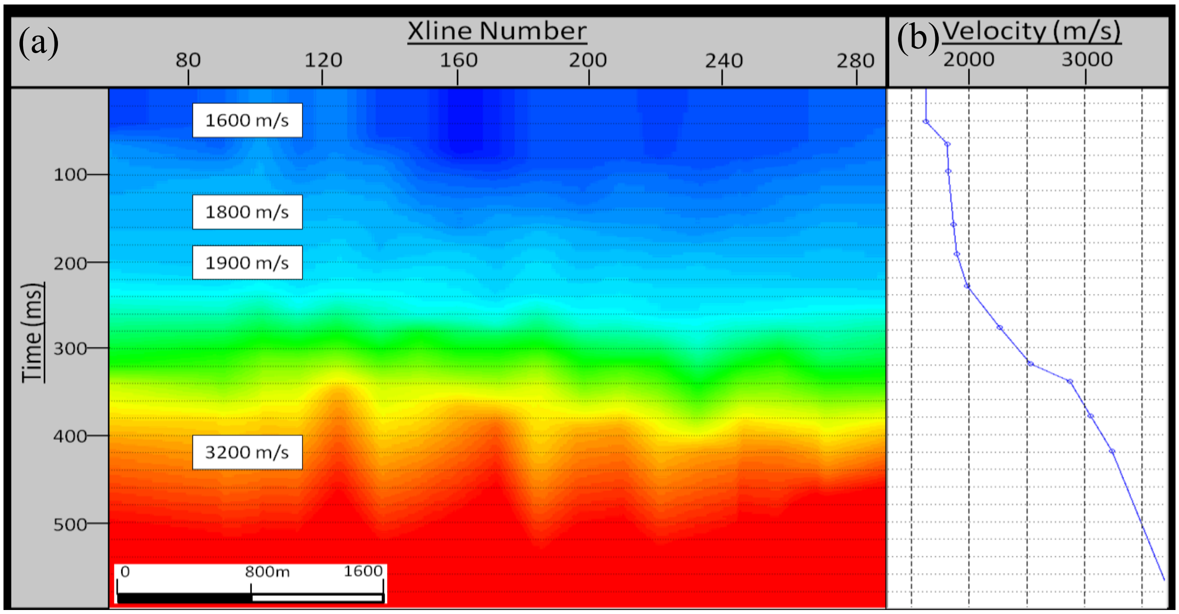

Figure 3-16 (a) RMS velocity profile for an inline running through the center of the 2002 survey (b) Velocity curve along Xline 160, middle of above profile.

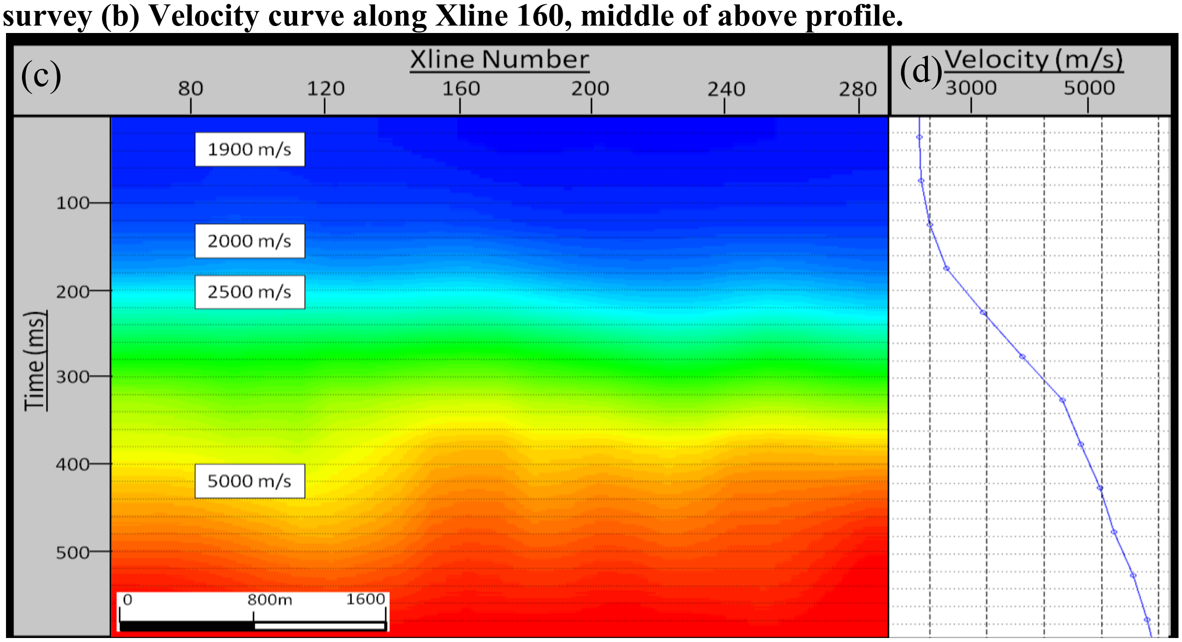

Figure 3-17 (c) Interval velocity profile estimated from the smoothed Dix equation and the RMS velocities (d) Interval velocity curve along inline 160, middle of above profile.

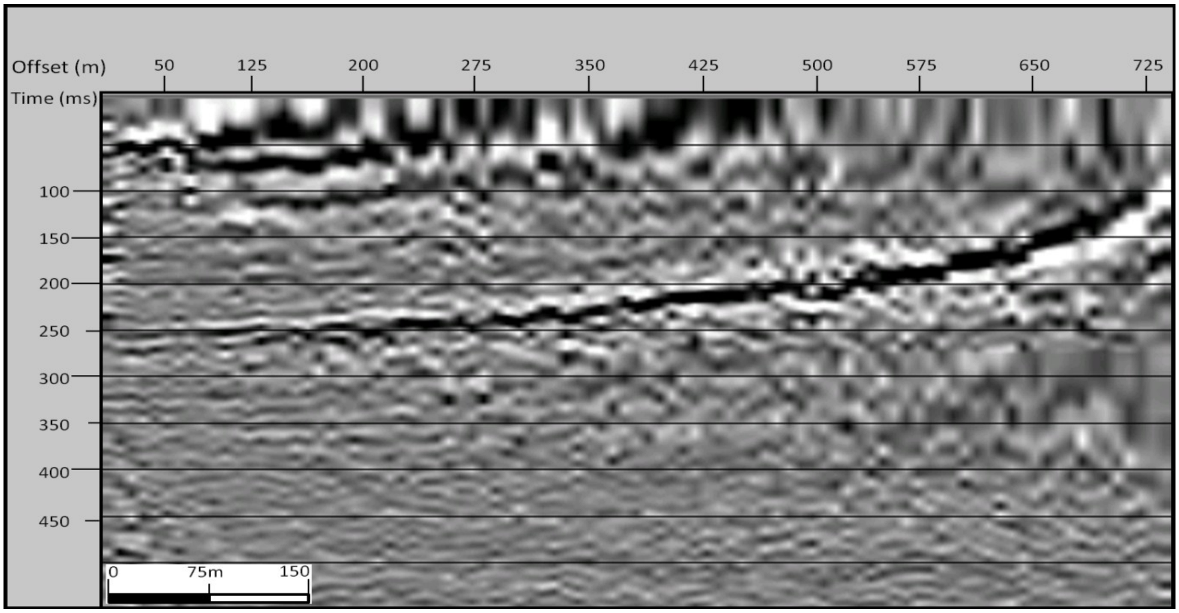

Figure 3-18 CMP gather after NMO correction. NMO stretch has contaminated the long offsets.

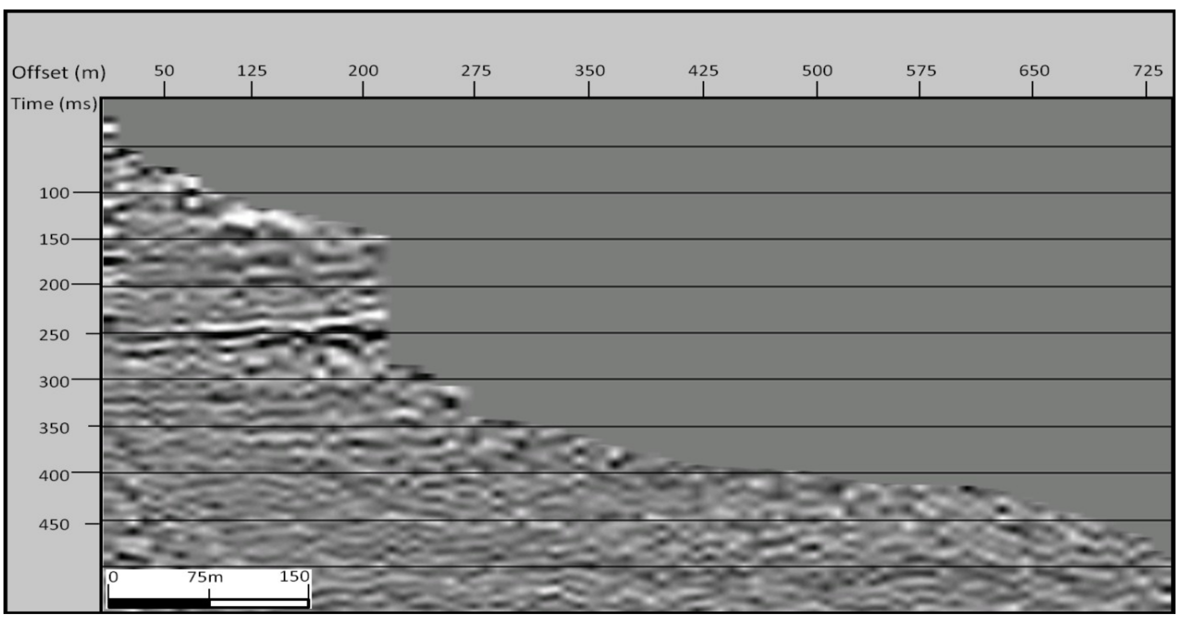

Figure 3-19 CMP gather after NMO correction and 50% stretch mute

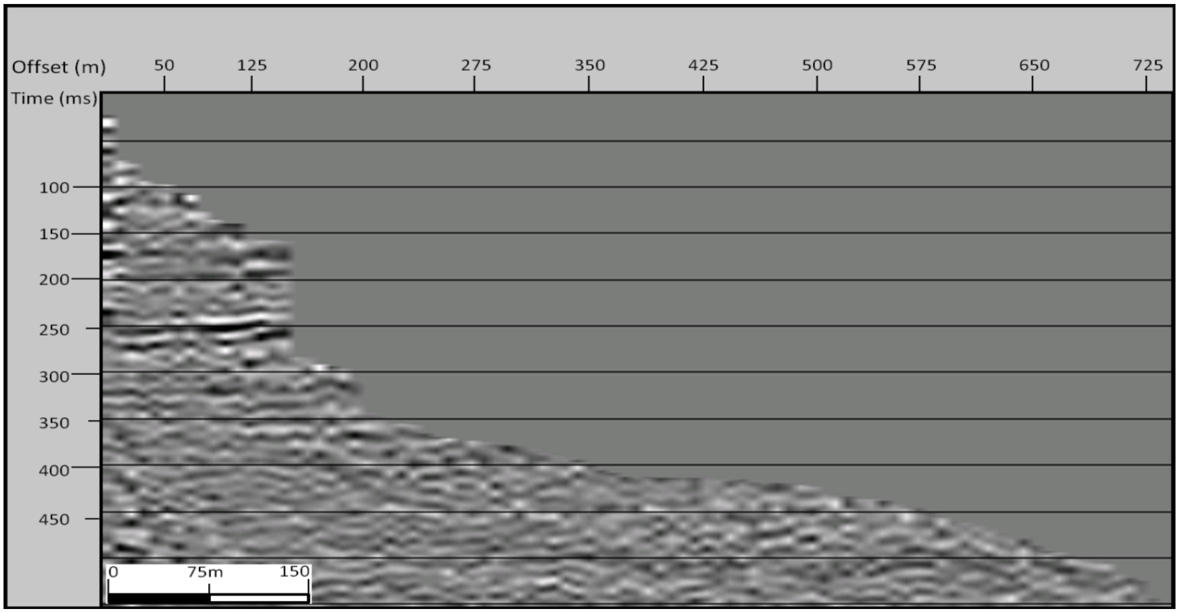

Figure 3-20 CMP gather after NMO correction and a 30% stretch mute

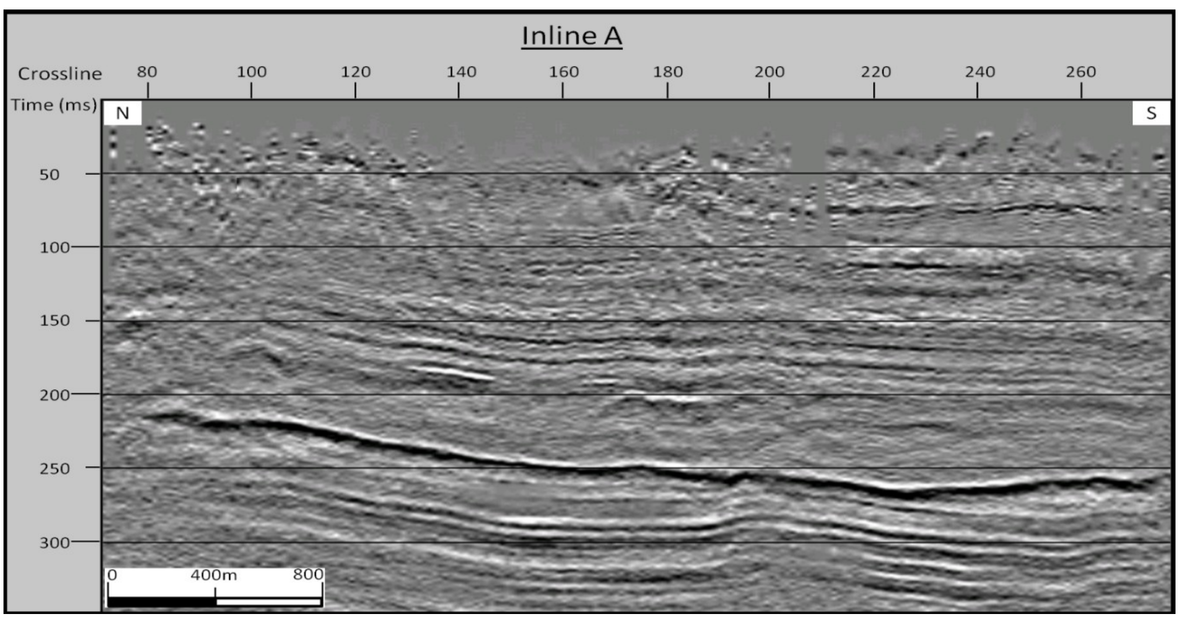

Figure 3-21 Stacked Section using a 50% stretch mute. Some residual statics have been applied (see Section 3.4.3)

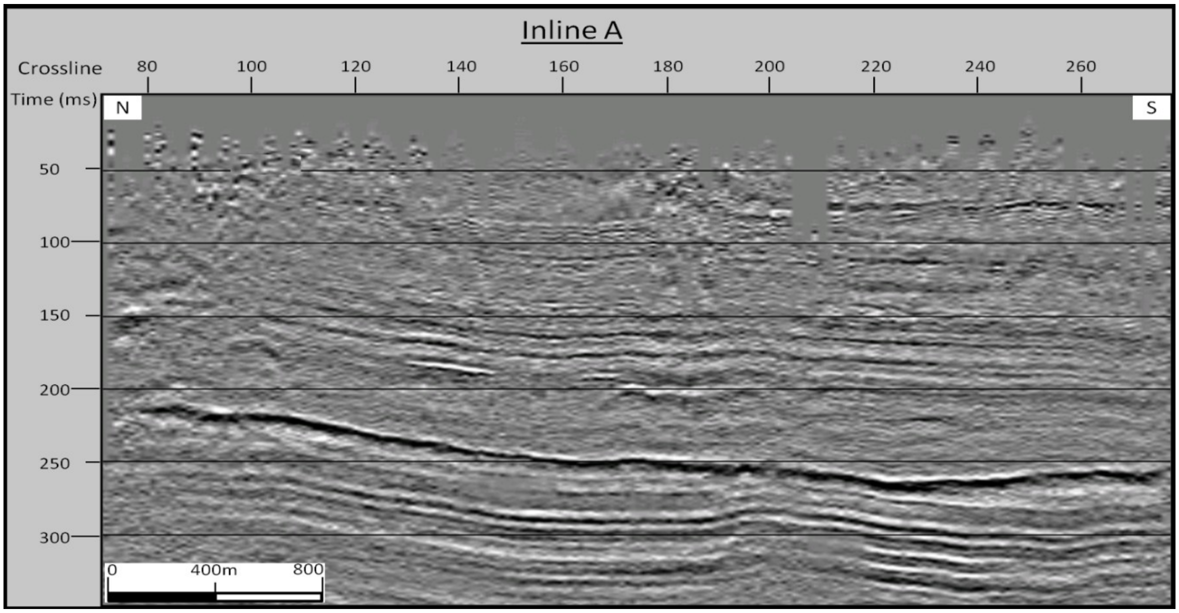

Figure 3-22 Stacked Section using a 30% stretch mute. Some residual statics have been applied (see Section 3.4.3)

3.4.4 CMP Stack

Following NMO corrections the data were stacked to increase the signal to noise ratio. Stacking refers to the summation of traces within CMP gathers. Traces from different shot records with a common midpoint are added together to form a single trace, creating pseudo zero-offset traces (zero-offset from a source) (Yilmaz, 2001). The stacking procedure significantly increased the signal to noise ratio, where in-phase signal added while random noise was out of phase and therefore canceled, improving the signal to noise ratio by a factor of the $\sqrt{n}$, where n represents the number of samples (Telford, 1990).

Prior to CMP stacking, NMO corrected traces were whitened through time-variant spectral whitening (TVSPW). TVSPW applies differential gains to individual frequency bands, varied as a function of time within the frequency domain. TVSPW was applied to boost the high frequency content of the data prior to stacking (8-10-150-160 Hz), improving the sharpness of the shallow events.

3.5 Static Correction

Static corrections are time shifts applied on a trace-by-trace basis to compensate for the effects of surface elevation variations, near surface weathering layer velocity and thickness variations. The main objective of static corrections are to calculate reflection arrival times representing a survey consisting of a flat plane (datum) on which all arrival times are no longer affected by low near surface velocities or a weathering layer (Cox, 1999; Sheriff, 2002).

Static corrections are computed and applied through a variety of techniques, each contributing to the total static solution while correcting for different factors. The following static corrections were applied: (1) elevation statics to compensate for differences in source and receiver surface elevations, (2) refraction statics to compensate for low near surface velocities and irregular thickness of the weathering layer, (3) residual static corrections to fine tune small inaccuracies within the near surface model, and (4) trim statics as a final cosmetic correction (Cox, 1999).

3.5.1 Elevation Statics

Elevation statics are corrections applied to the data to compensate for the effect of different source and receiver elevations (Cox, 1999; Sheriff, 2002). Through computation, the elevation of all sources and receivers were moved to a common floating datum, positioned somewhere below the lowest source or receiver elevation. Statics were calculated for each source-receiver pair using source-receiver geometry, elevations and a specified replacement velocity. Replacement velocity values are typically estimated from prior knowledge, or determined from uphole traveltimes or refracted arrivals from the sub-weathering layer. For our computations, the processing datum applied was 550 m and the replacement velocity was 2000 m/s. Elevation statics were applied to the data prior to data conditioning (Section 3.2).

3.5.2 Refraction Statics

Refraction statics are corrections applied to the data to compensate for traveltime differences due to the presence of a low velocity near surface layer(s). Often, this near surface layer will be comprised of weathered and/or unconsolidated sediments, containing lateral variations in both thickness and velocity (Farrell, 1984). Lateral variations in thickness and velocity, if not corrected via static solutions, can produce artificial time structures within the data and often lead to incorrect interpretations (Cox, 1999).

Refraction statics were calculated through the modeling of the near surface by estimating velocities and thicknesses on the basis of uphole time, source/receiver depths, elevations, offset values and first break picks for a desired number of layers. Modeling can be as complex as 5 layers, but typically a lower number is desired and in the case of our data set, a 1 layer refraction model was used.

Refraction static corrections compute refractor velocities and delay times, applying shot and receiver corrections on a trace-by-trace basis. Refraction statics were calculated and applied after the application of elevation statics (Section 3.5.1). The ProMAX refraction statics module calculated static corrections in a six step process as follows:

1. Input weathering layer velocity (600 m/s), and convert first-break picks into surface to surface traveltimes for delay time estimation
2. Compute refractor velocities for the desired number of layers to be modeled on CMP's
3. Compute source and receiver delay times using computed CMP velocities
4. Compute depth model for both source and receivers using computed refractor delay times and refractor velocities
5. Compute source and receiver statics using refractor velocities and depths, applied to a specified datum (550 m).
6. Smooth and apply source and receiver statics, and move to final datum. Also removes low frequency trend from the source and receivers.

3.5.3 Residual Statics

After refraction statics and NMO corrections, CMP traces may still exhibit some misalignment of reflection events in time due to slight errors in previous static routines. These errors are referred to as residual statics, characterized as trace-by-trace time variations not related to subsurface structure or stratigraphy (Gadallah, 2005). Typically, residual statics are caused by shallow near surface velocity errors in the NMO correction. Figure 3-23 is an example of such variations across a selection of CMP traces.

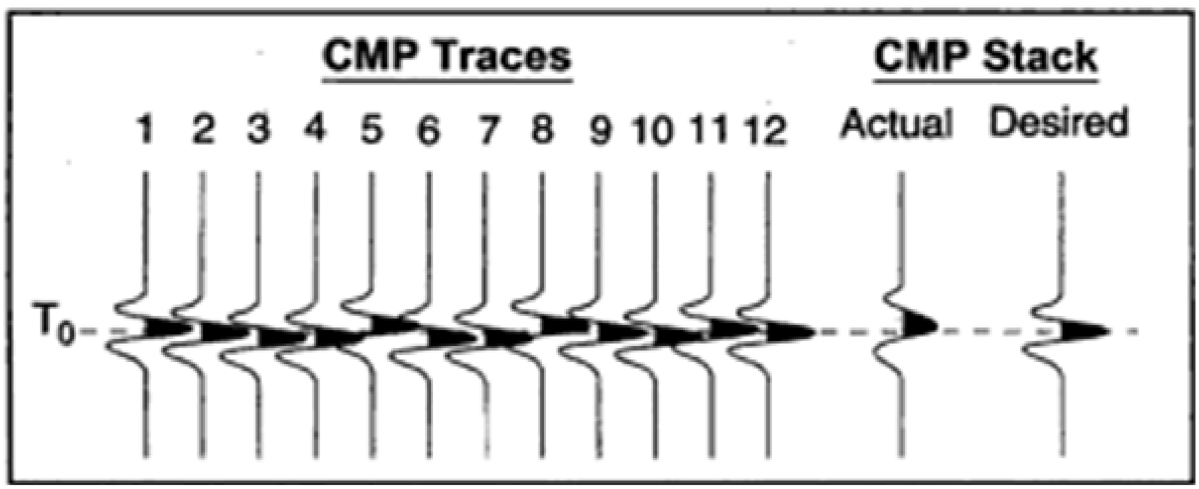

Figure 3-23 Static variations across CMP traces (Gadallah, 2005)

Residual statics are short wavelength surface-consistent statics applied to NMO corrected data. An analysis window is designed on a reflector which is coherent throughout the entirety of the data set and absent of significant dip. Through a cross-correlation of the input traces against a scaled and smoothed model of the data, time shifts are calculated to improve the alignment of the traces in time (Gadallah, 2005). Calculated time shifts are then applied to the NMO corrected data, and stacked to yield an improved image. Residual static corrections can also be applied to the data prior to velocity analysis such that new velocities can be picked and an updated velocity model can be used to calculate NMO corrections. The processing of the 4D P-wave data involved four iterations of residual statics and updating of the velocity field before a final stacked section was produced.

Figure 3-24 is a comparison of a stacked Section before and after the application of residual statics. A significant improvement in the coherency of the shallow reflections is evident.

3.5.4 Trim Statics

After residual statics had been applied to the data, a final pass of non-surface consistent CMP trim statics were applied to the data to enhance trace-by-trace alignment in time. As with residual statics, a time window was selected along a coherent reflection free of significant dip. Traces within the window were crosscorrelated against a smoothed model of the data and corresponding time shift values were computed. Trim static corrections were applied to the NMO corrected data after the application of the final iteration of residual statics.

Trim static solutions were calculated using the Devonian reflection, the most robust and coherent reflection within the data set. Due to the very high amplitude of the Devonian reflection, a 50 ms AGC was first applied to the data. Trim static values were calculated on the AGC'ed data and then applied to the data without AGC. This effectively suppressed the high amplitude Devonian event, allowing a more accurate calculation of trim statics. Figure 3-26 displays an inline Section after the application of trim statics.

3.6 Post Stack Migration

Images displayed through CMP Sections are observations of seismic reflections positioned with respect to midpoints, obtained through the previously described CMP based processing techniques. In order to accurately delineate subsurface reflection locations, the data must be repositioned in terms of true reflection points. The process of changing the positioning from CMP to subsurface reflection imaging is termed migration (Telford, et al., 1990; Robinson, 1983).

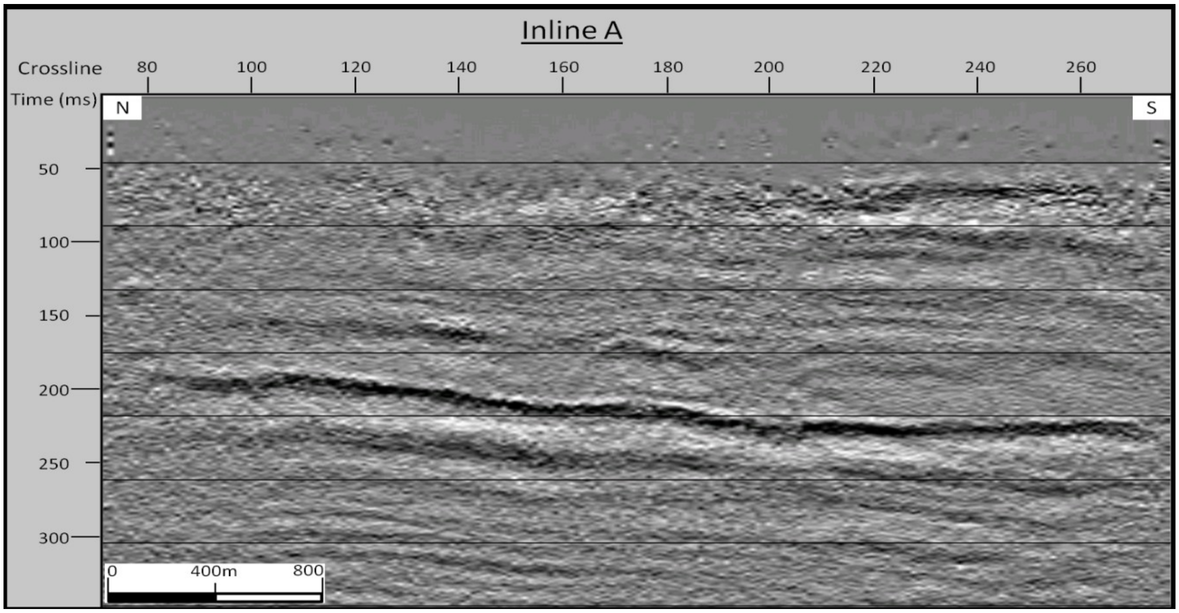

Figure 3-24 Stacked Section without residual static corrections

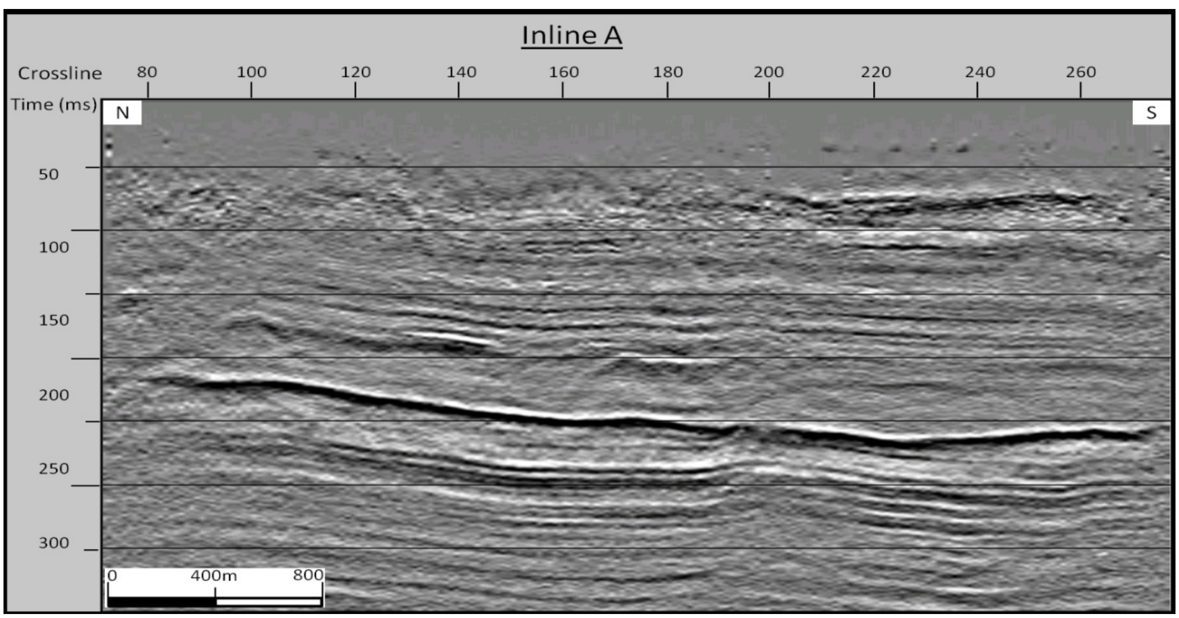

Figure 3-25 Stacked Section after 4 iterations of residual statics

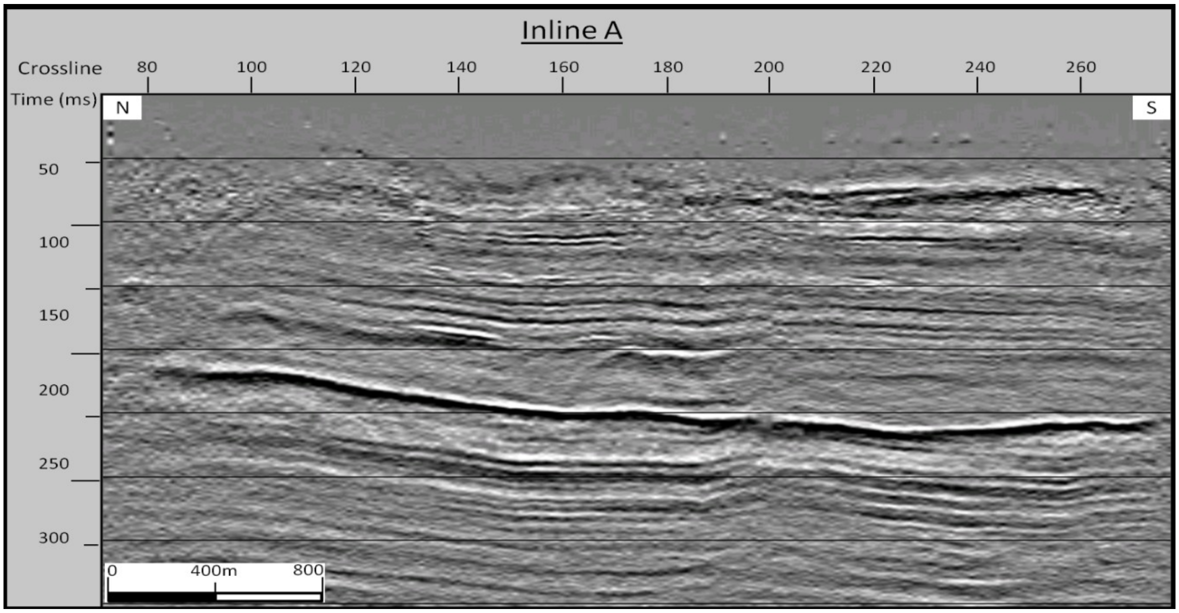

Figure 3-26 Stacked Section after residual statics and trim statics

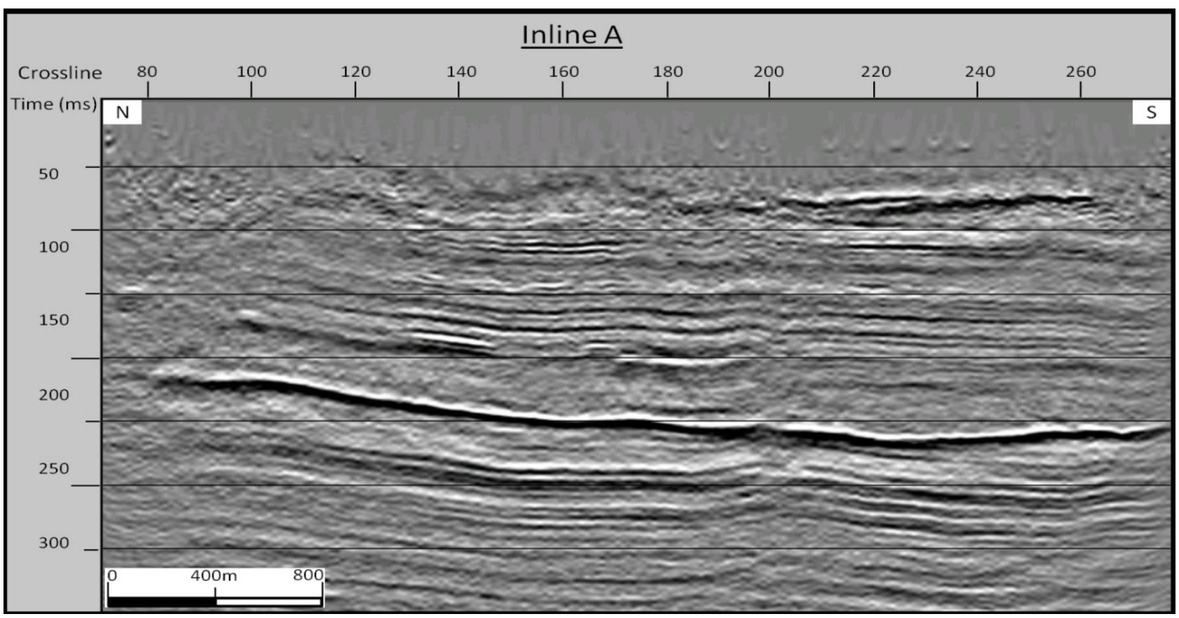

Figure 3-27 Inline A after the Phase-Shift migration

A seismic signal recorded via a geophone is a superposition of a wave originating from the subsurface. Migration is the focusing of such energy from its observation location to its reflection location through the backward projection of diffractions or primary reflections to their correct spatial position (Gazdag, 1984). Migration repositions dipping reflectors to their true spatial location and collapses diffraction energy, effectively increasing spatial resolution and enhancing the imaging of areas of complex geology and steep dips (Gazdag, 1984; Yilmaz, 2001). Migration requires knowledge of the subsurface velocity, often derived from RMS velocities obtained during the NMO correction, and modified to some extent (Section 3.4.2).

There are an assortment of migration techniques, each with its own set of advantages and drawbacks, including but not limited to, Kirchhoff migration, Finite Difference migration, Stolt F-K migration and Hagedoorn migration (Telford, 1990; Yilmaz, 2001; Gadallah, 2005; Bancroft, 2007). The migration algorithm applied to our data is a variation of Gazdag's Phase Shift Migration (Gazdag, 1978).

3.6.1 Phase-Shift Migration

The Phase-Shift migration is a technique in which the source and receiver positions are lowered into the subsurface through a phase rotation of the Fourier coefficients (Gazdag, 1978). Through this technique, the subsurface can be approximated by a series of layers of some thickness and velocity. The transition from one layer to the next is computed via a phase shift, dependant on the RMS velocity across the layer of the interest (Gazdag, 1978).

The main advantages of this technique are its simplicity, stability, flexibility and high degree of accuracy, where dips as steep as 90^{O} can be accurately resolved. Phase-shift migrations can provide more accurate images of the complex velocity structures, as well as incorporate a full migration aperture and turning rays, providing advantages over Kirchhoff migrations when migrating a full volume. Computation times are relatively low in comparison to other techniques, and it has the ability to handle vertical velocity variations quite well (Gazdag, 1978; Dubrulle, 1979; Bancroft, 2007). Although the phase-shift migration assumes no lateral velocity variations, moderate variations can be accommodated, where modifications to the Phase-Shift migration have accommodated for through interpolation (PSPT).

The Phase-Shift migration is achieved through a 2-D Fourier transform, where the conversion from one layer to the next requires multiplication of a phase-shift value (Bancroft, 2007). More details regarding Phase-shift migrations can be found in Gazdag, 1978, Dubrulle, 1979 and Bancroft, 2007.

The Phase-shift migration was applied to the 4D data to yield high quality migrated Sections with relatively low computational times. Interval velocity values for the migration were derived from the NMO corrections, where RMS velocities were converted to interval velocities (see Section 3.4.2), modified slightly and moved to a final processing datum of 550 m (consistent with the final stack datum). Figure 3-27 is an inline Section through the volume after the Phase-Shift migration. Notice the improvement in the resolution of reflections within the reservoir, as well as within the shallow Section. After migration, some over migrated energy is evident in the Section due to migration artifacts encountered when migrating data near the end of the line (Figure 3-27). These migration artifacts introduce noise, and will be addressed in the post-migration conditioning Section (Section 3.7).

3.7 Post Migration Conditioning

To combat some of the migration artifacts and reduce the overall noise level of the migrated Sections, some post migration data conditioning was applied. Primarily, migration artifacts were removed from data, including strong diffractions from edge effects as seen in Figure 3-27. The data was bandpass filtered with a high cut off of 160 Hz, to remove any high frequency noise, and a low cut-off of 10 Hz, to remove any low frequency noise. Following the bandpass filtering, the data was run through an F-XY deconvolution algorithm.

3.7.1 F-XY Deconvolution

F-XY deconvolution is a prediction filter applied in the frequency domain to remove or reduce random noise. Signal is predicted through a complex prediction filter, and any difference between the predicted and actual signal is deemed noise and removed. F-XY deconvolution is employed in an effort to minimize edge effects from migration, reduce random noise, improve reflector character consistency, and reduce attenuation of steeply dipping events (Harrison, 1990).

F-XY deconvolution applies a Fourier transform to move the data into frequency and space (f, x, y), followed by a complex prediction filter in time and space (x, y) for each frequency plane within a specified range. The F-XY deconvolution then inverse transforms each frequency trace back into time, removing any non-predicted data (noise) (Gulunary, 1986). F-XY deconvolution can be performed over a specified frequency range and with a specified rate of adaptation. A frequency range of 10-160 Hz was used, with a moderately-low rate of adaptation for lesser noise removal. Figure 3-28 is a comparison of the migrated volume before and after F-XY deconvolution. Notice the large increase in coherency of the shallow reflectors due to the reduction in random noise and the removal of the migration artifacts.

Lastly, a final round of TVSPW was applied similar to that discussed in Section 3.3.4. Again, this whitening was applied to boost the higher frequencies as well as to enhance the sharpness of the shallow reflectors.

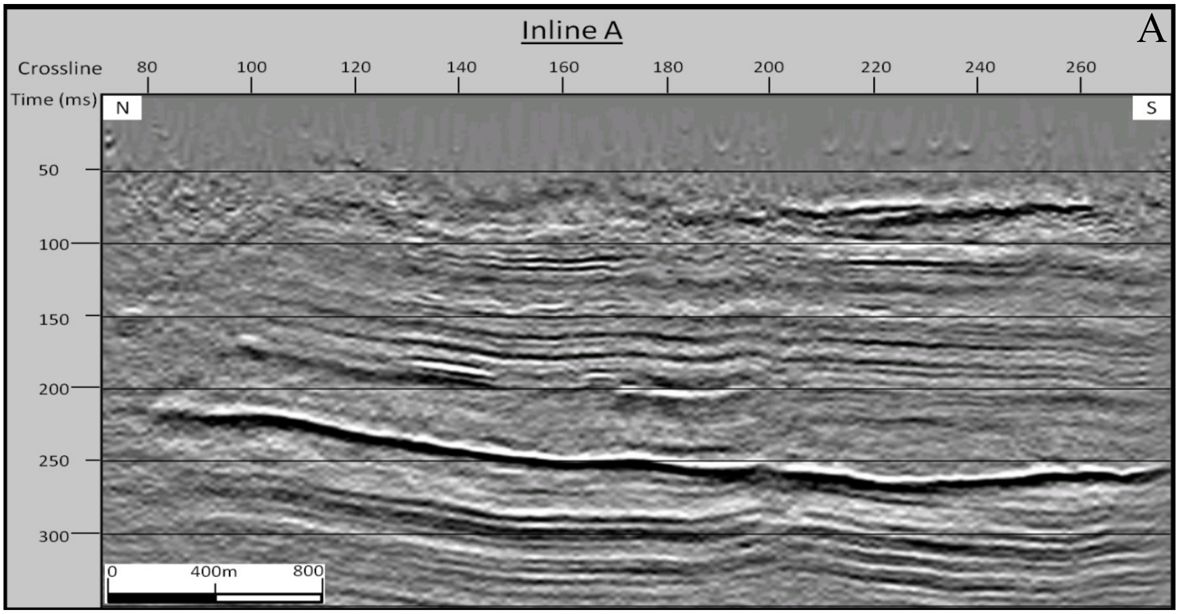

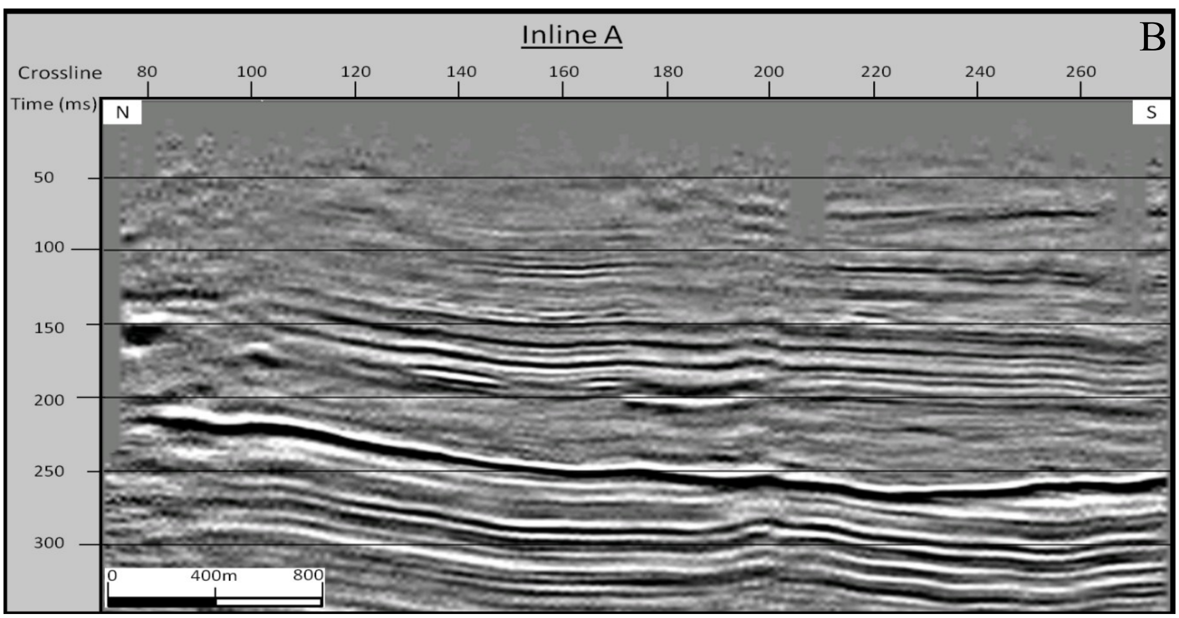

Figure 3-28 (a) Inline A after migration and (b) after F-XY deconvolution.

3.8 Discussion

The repeatable processing of the 4D P-wave data has increased our confidence that any time lapse differences observed can be more confidently attributed to production induced changes within the McMurray Formation reservoir and less likely due to differences from acquisition, processing or noise. Through the implemented processing routine I was able to effectively reduce both random and coherent noise, improve signal to noise ratio, and produce robust images of the shallow McMurray Formation reservoir as well as underlying and overlying strata. The effective processing of the data lead to a more accurate interpretation of time lapse changes within the reservoir, a topic discussed in detail in Chapter 4.

Figure 3-25a is a chair-cut display of the 2002 (baseline) data, providing an overview of the data quality in terms of crossline, inline and time-slices. Figure 3-29b is the equivalent view for the 2011 (monitor) data. Despite the identical processing routine, differences in the data quality in terms of S:N and coherency of the shallow reflections was observed, a point of consideration, which was addressed in Chapter 4 (Section 4.2).

Figure 3-30 to Figure 3-39 provide an overview of the 2002 and 2011 data, where various inlines and crosslines through the data are compared. High amplitude events are observed within the 2011 data which are not observed within the 2002 data, signifying the presence of steam induced anomalies within the McMurray Formation reservoir.

Lastly, Figure 3-40 to Figure 3-42 provide a comparison of the 2002 and 2011 data in terms of time slices for 100 ms, 200 ms, and 300 ms. Again, differences in the quality of the 2002 and 2011 data are apparent, primarily within the shallow reflections.

The compensation for survey differences and the investigation into the high amplitude events observed on the 2011 data is addressed throughout Chapter 4.

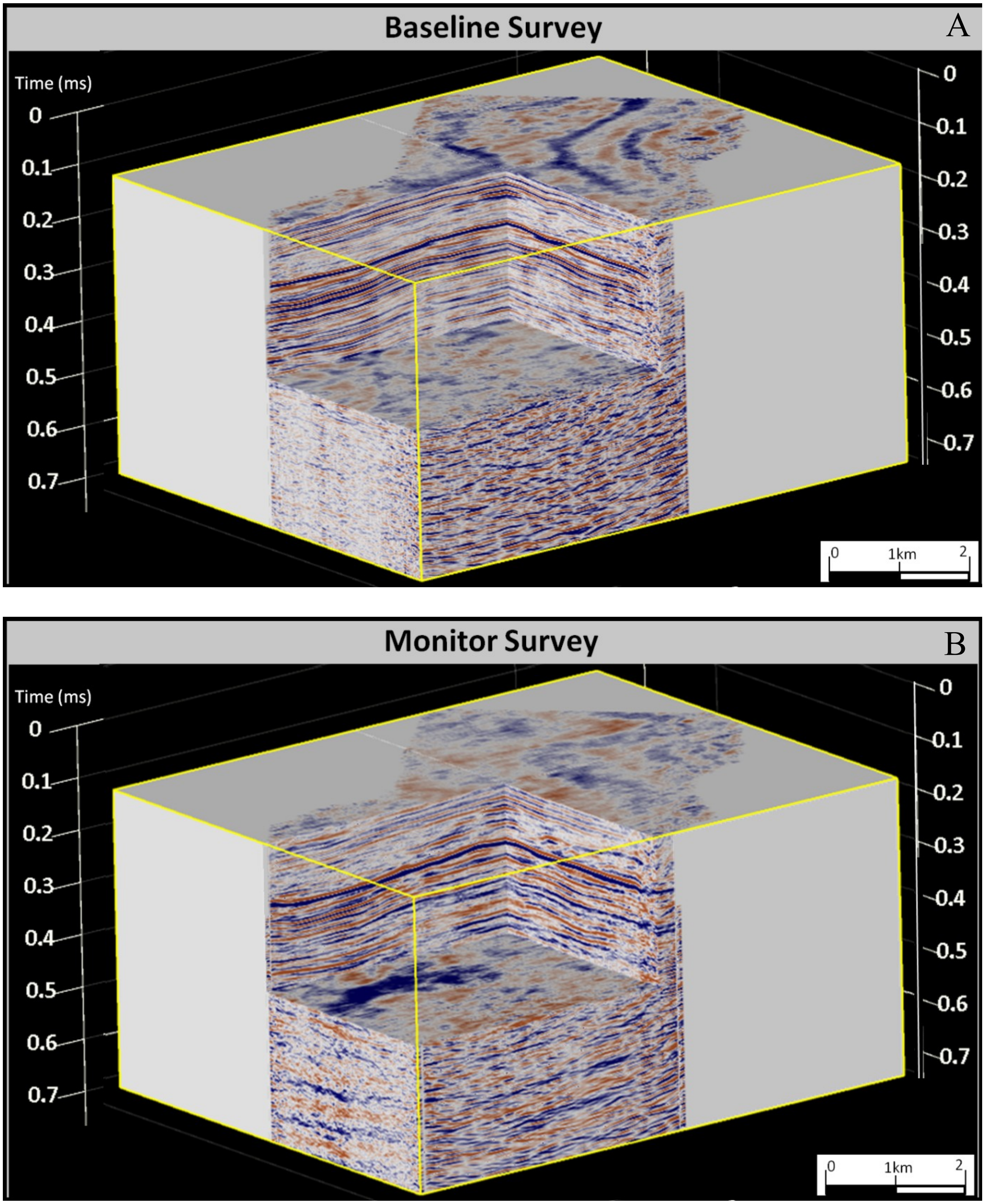

Figure 3-29 Chair-cut display of (a) baseline and (b) monitor datasets

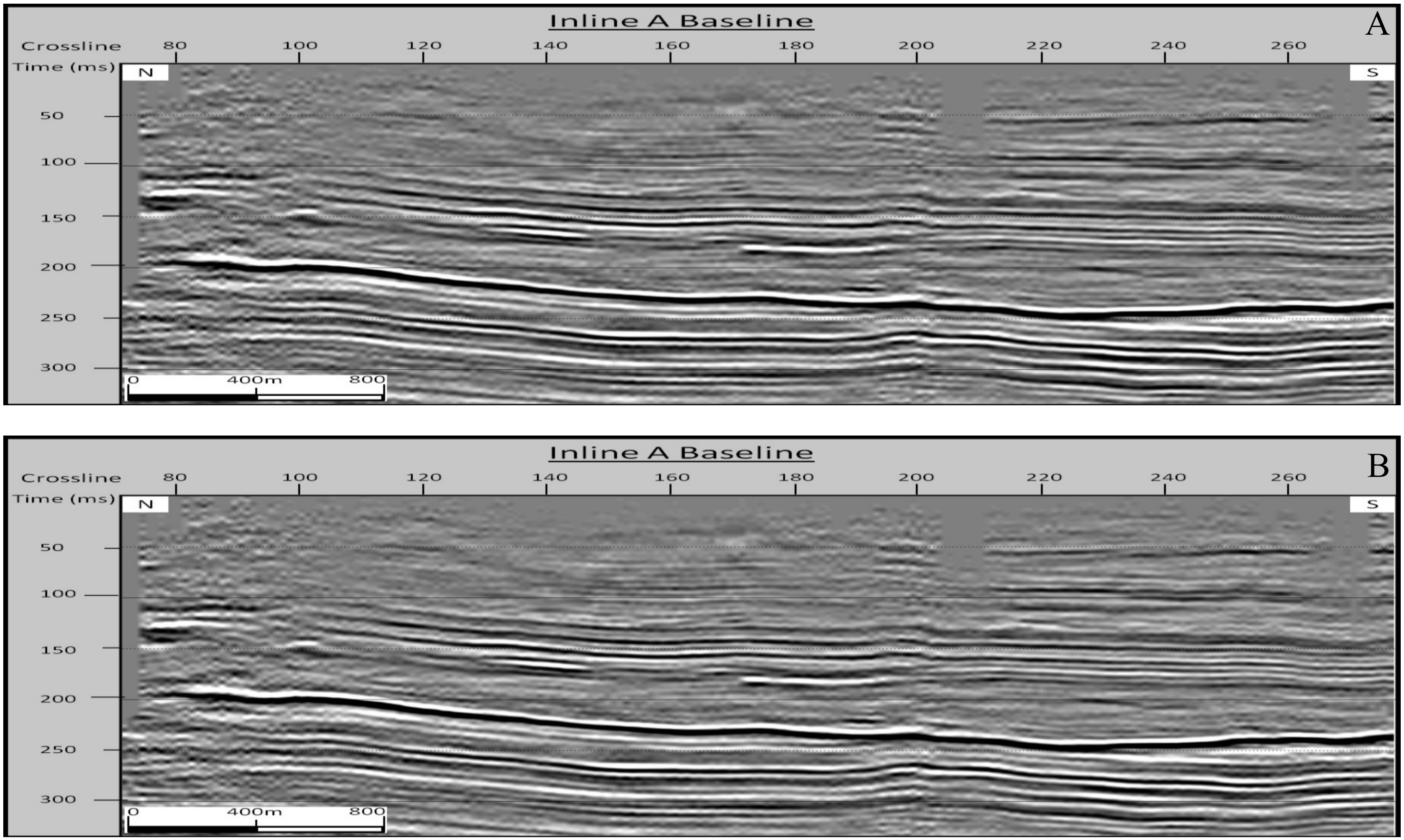

Figure 3-30 A comparison of Inline A through (a) Baseline and (b) Monitor survey after data processing.

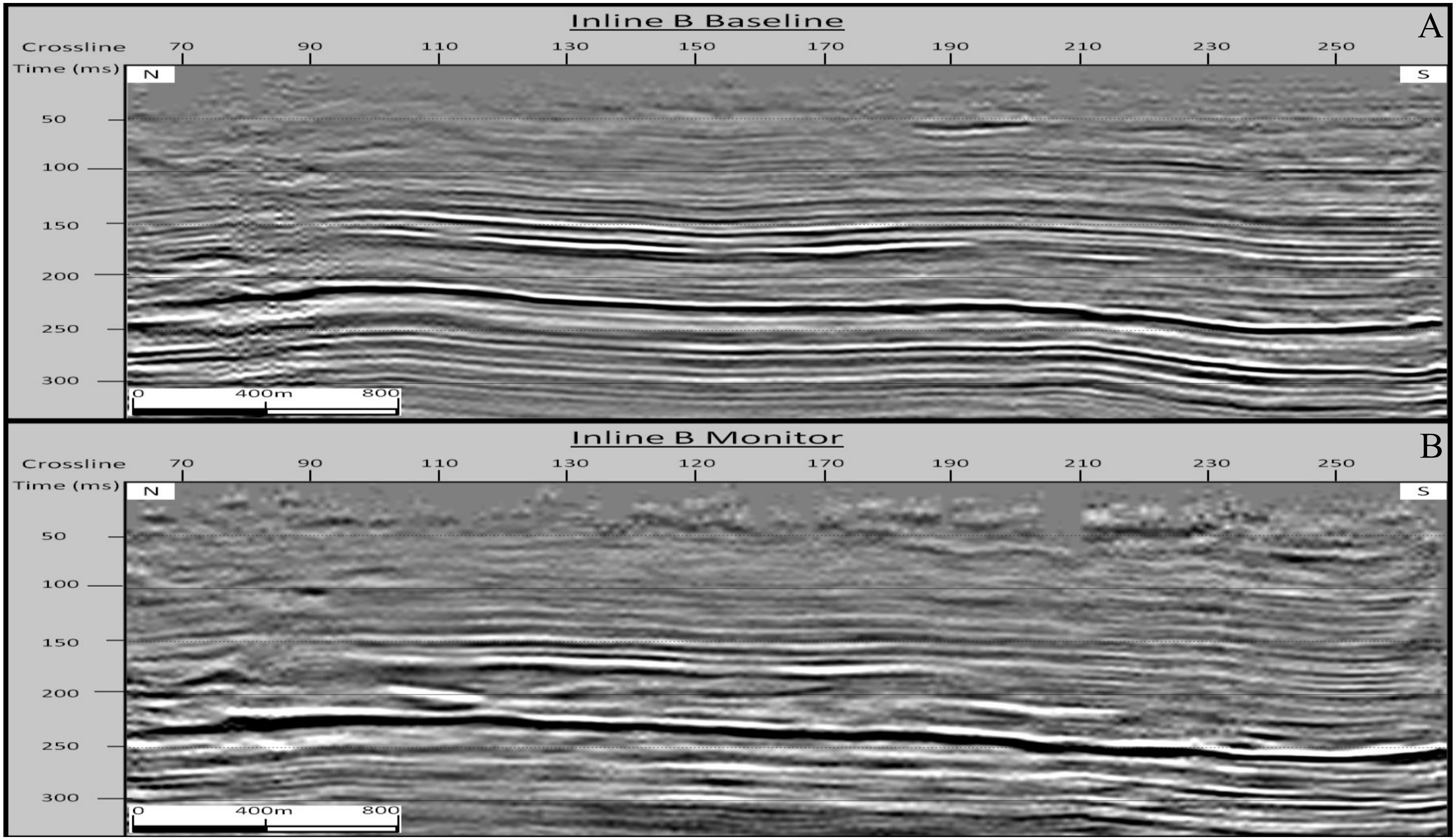

Figure 3-31 A comparison of Inline B through (a) Baseline and (b) Monitor survey after data processing. High amplitude events are observable on the monitor data that are absent on the baseline data.

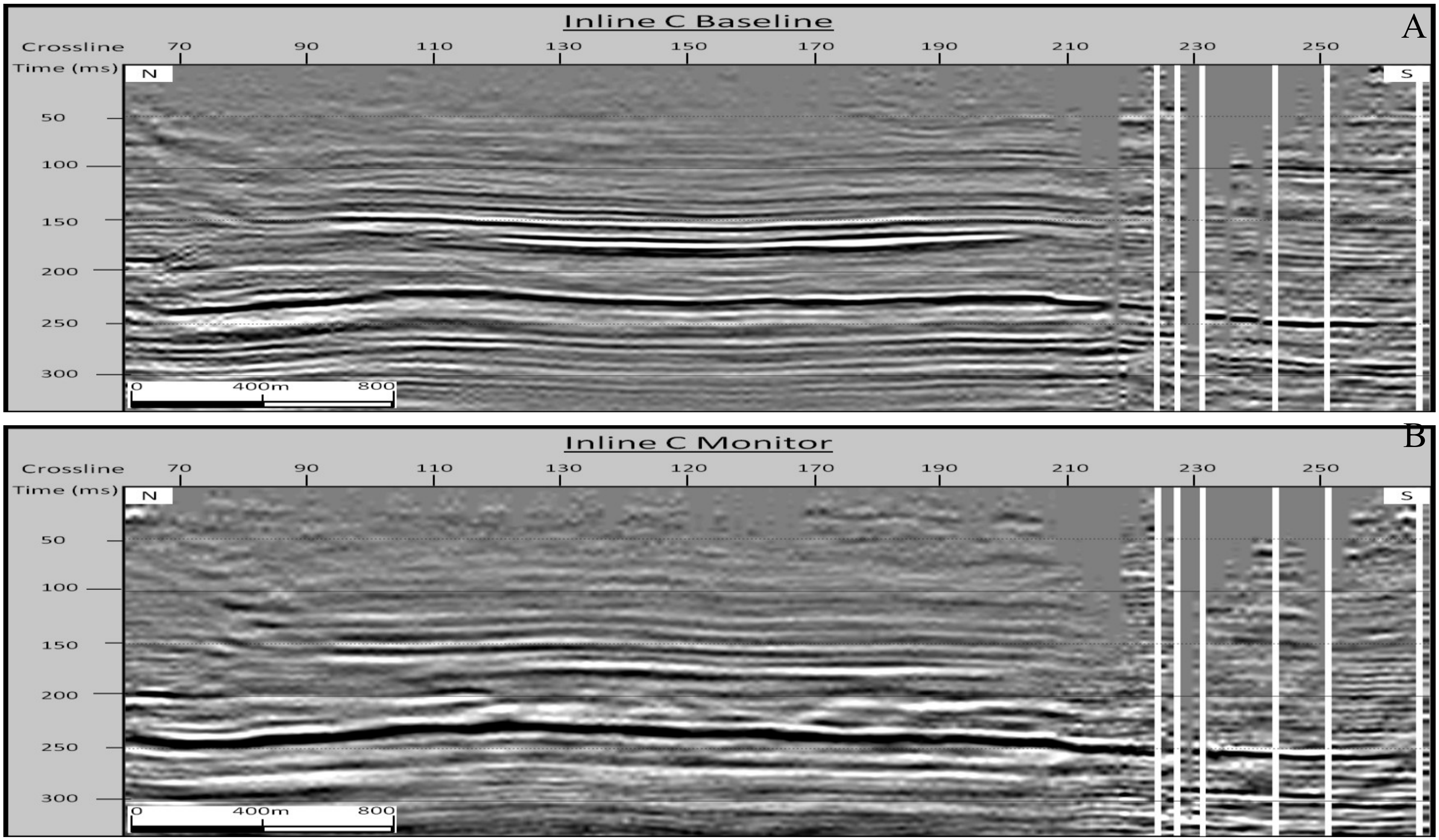

Figure 3-32 A comparison of Inline C through (a) Baseline and (b) Monitor survey after data processing. High amplitude events are observable on the monitor data that are absent on the baseline data. White vertical lines are gaps in the data.

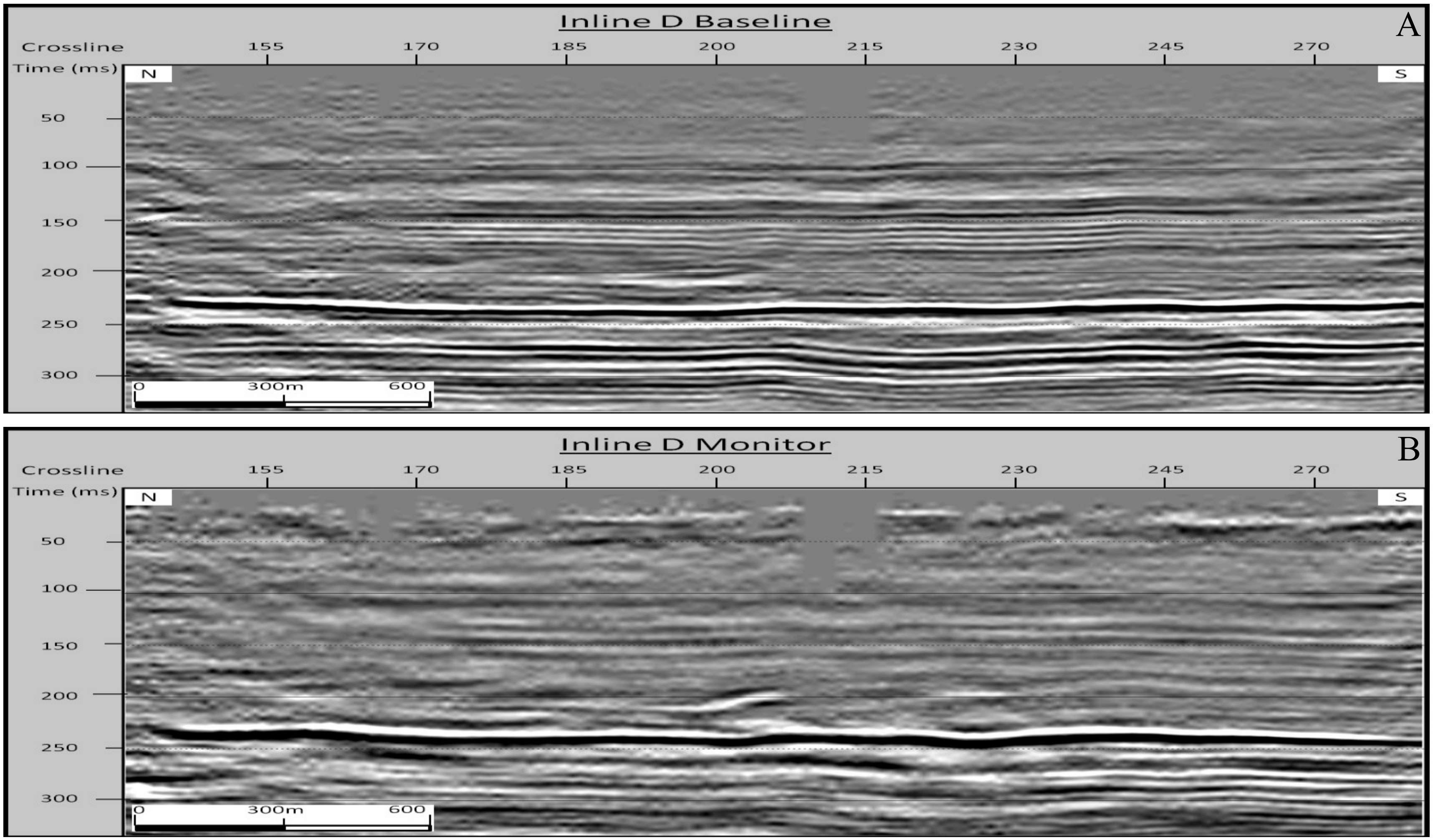

Figure 3-33 A comparison of Inline D through (a) Baseline and (b) Monitor survey after data processing. High amplitude events are observable on the monitor data that are absent on the baseline data.

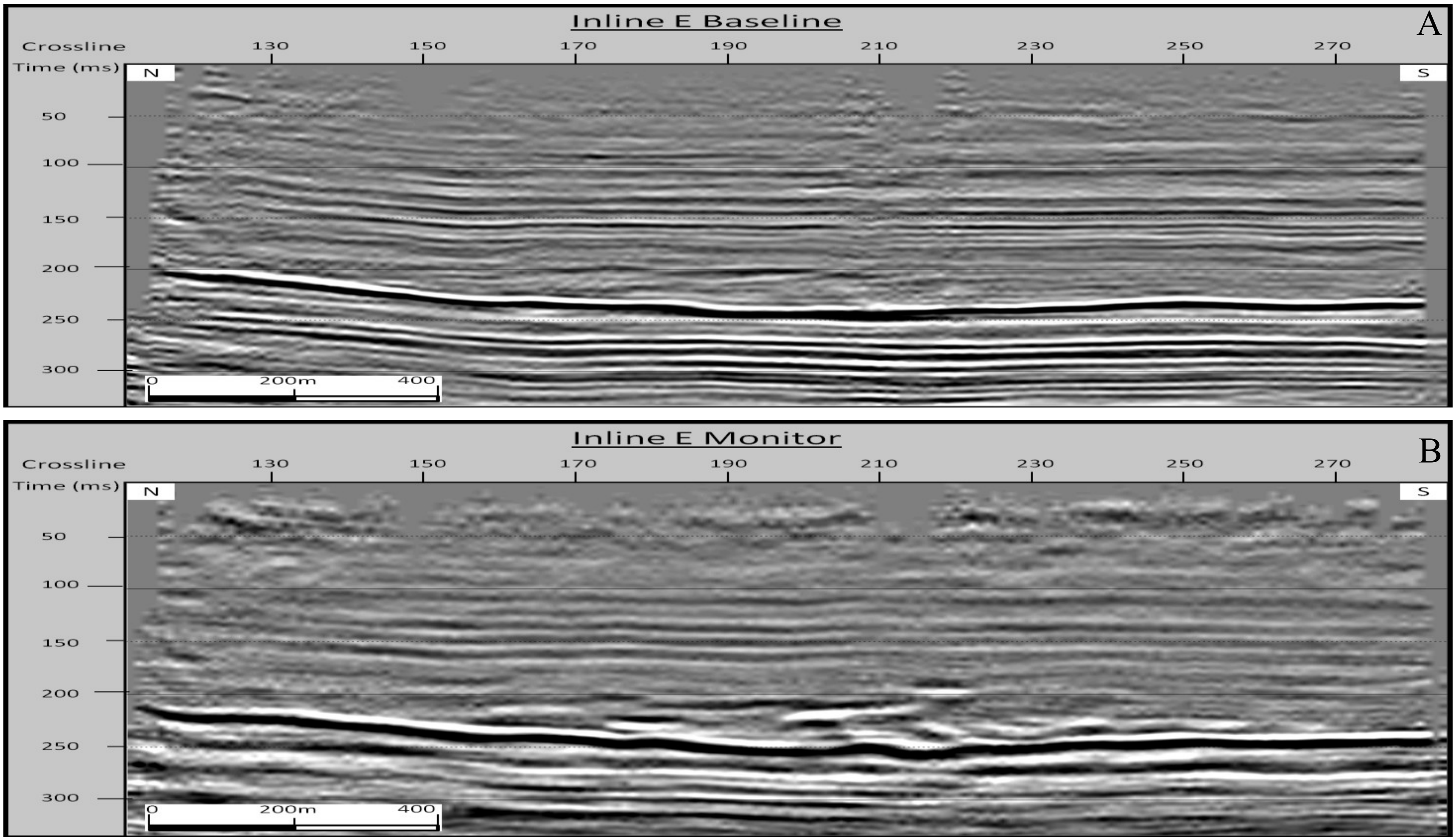

Figure 3-34 A comparison of Inline E through (a) Baseline and (b) Monitor survey after data processing. High amplitude events are observable on the monitor data that are absent on the baseline data.

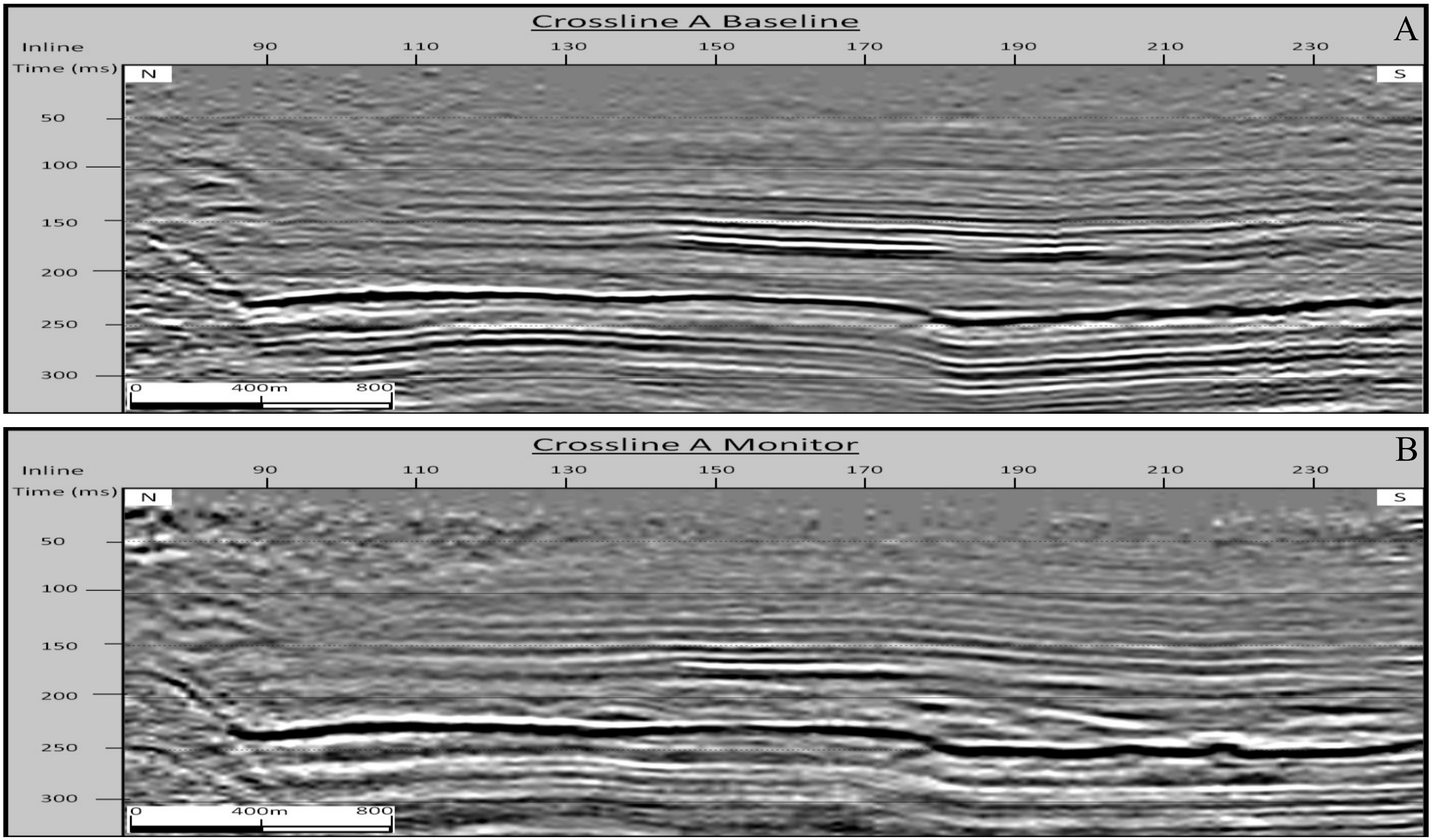

Figure 3-35 A comparison of Crossline A through (a) Baseline and (b) Monitor survey after data processing. High amplitude events are observable on the monitor data that are absent on the baseline data.

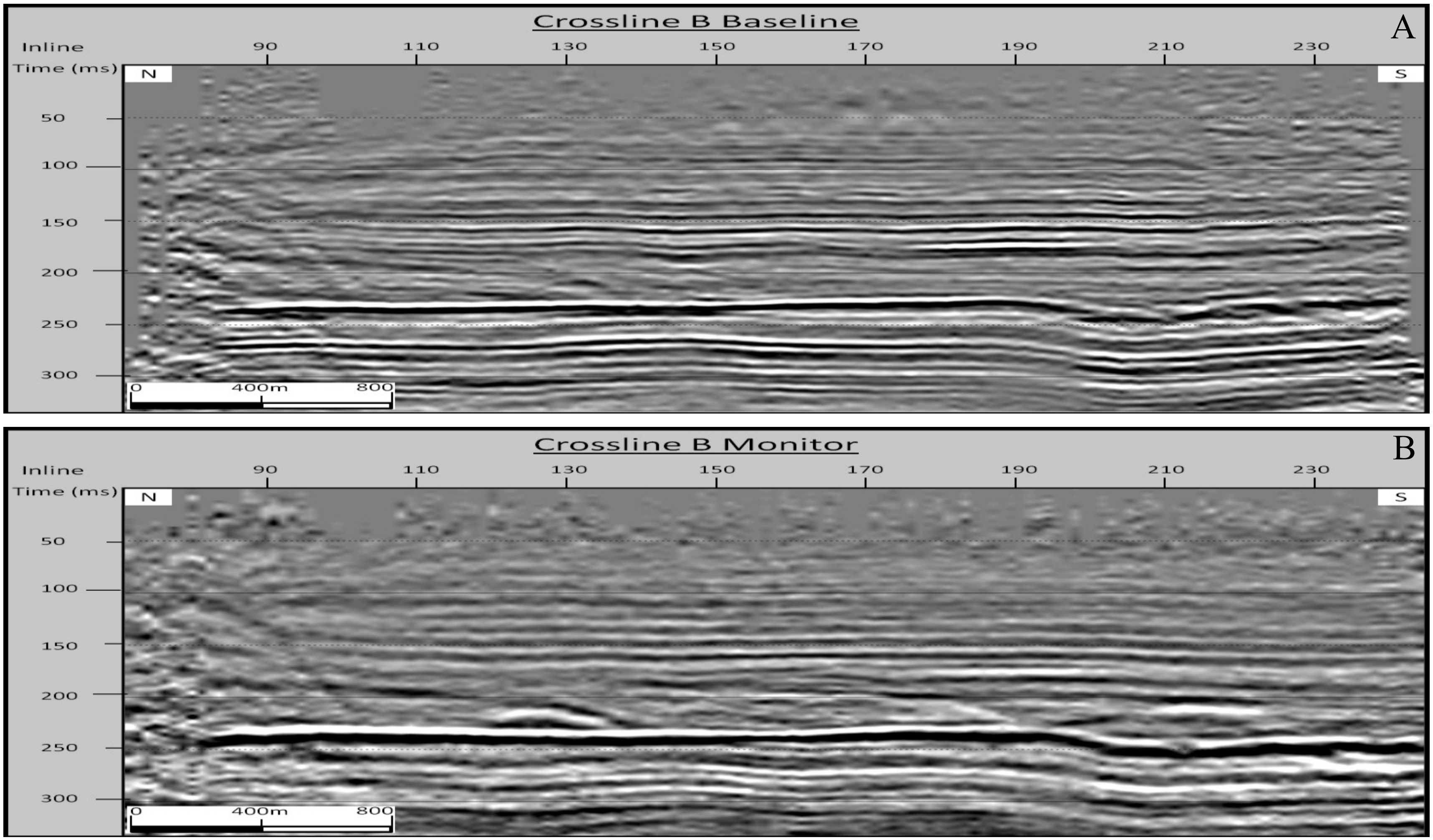

Figure 3-36 A comparison of Crossline B through (a) Baseline and (b) Monitor survey after data processing. High amplitude events are observable on the monitor data that are absent on the baseline data.

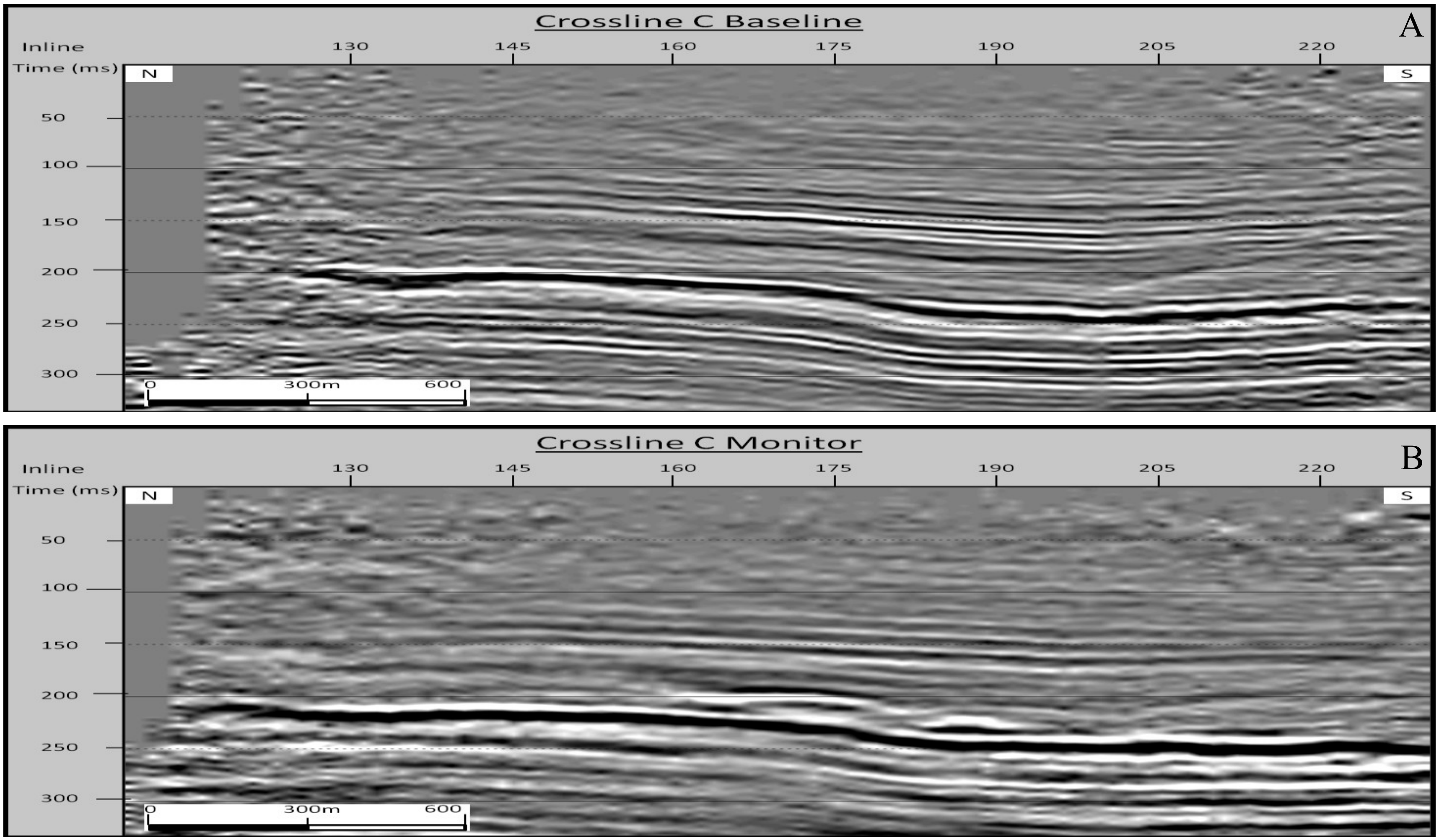

Figure 3-37 A comparison of Crossline C through (a) Baseline and (b) Monitor survey after data processing. High amplitude events are observable on the monitor data that are absent on the baseline data.

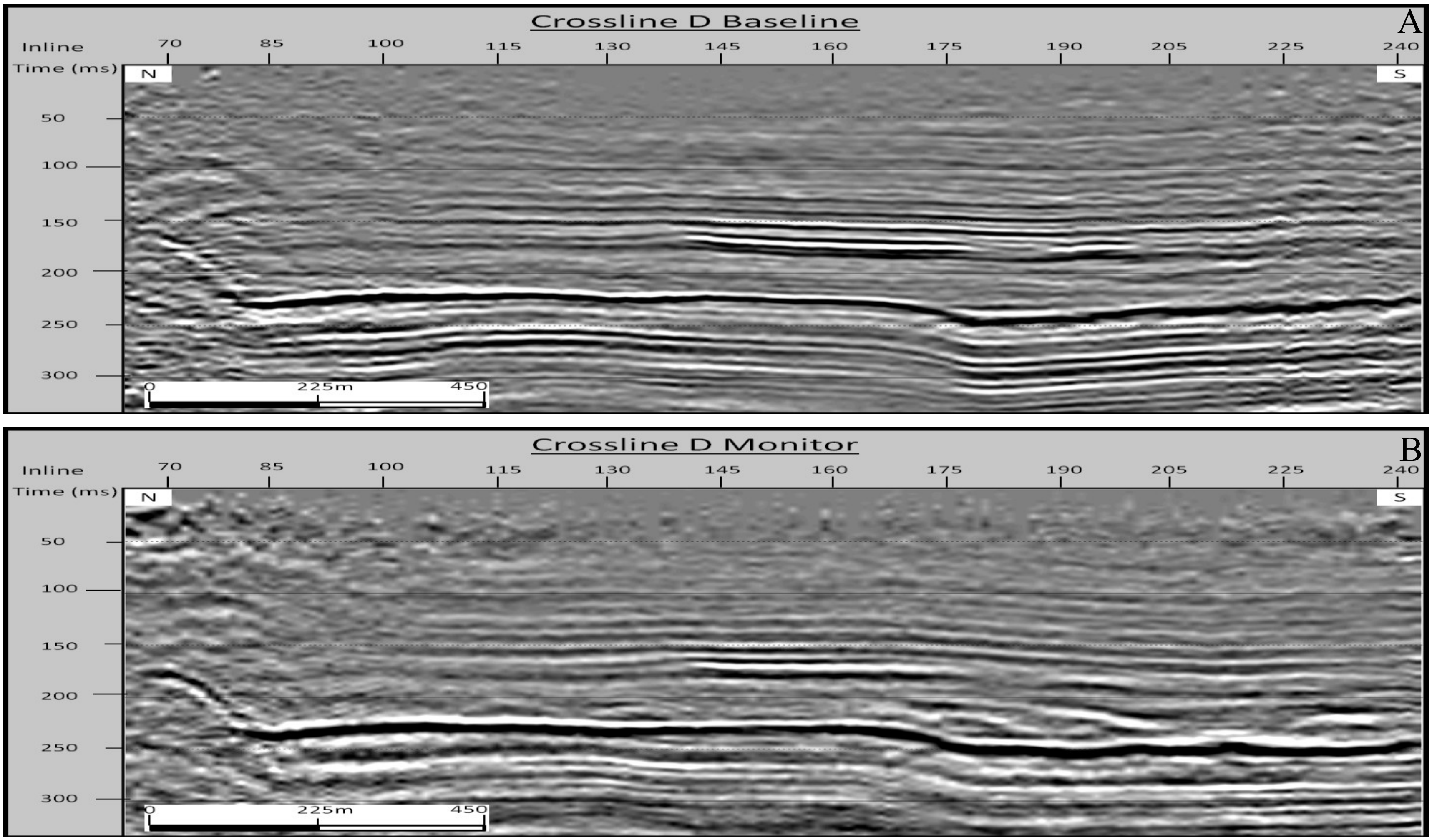

Figure 3-38 A comparison of Crossline D through (a) Baseline and (b) Monitor survey after data processing. High amplitude events are observable on the monitor data that are absent on the baseline data.

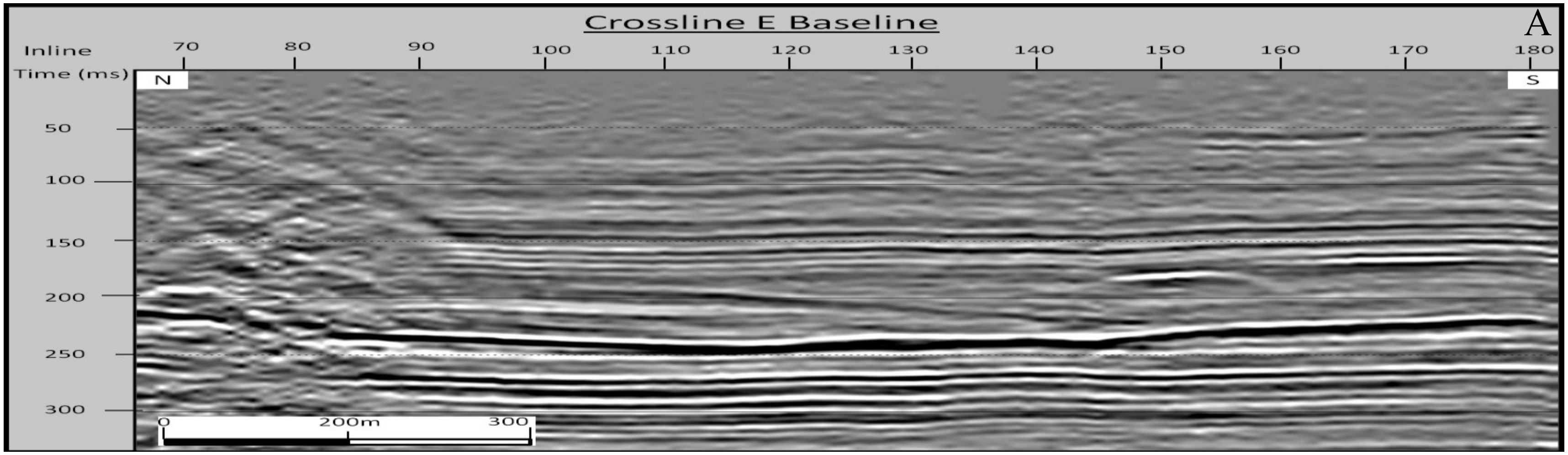

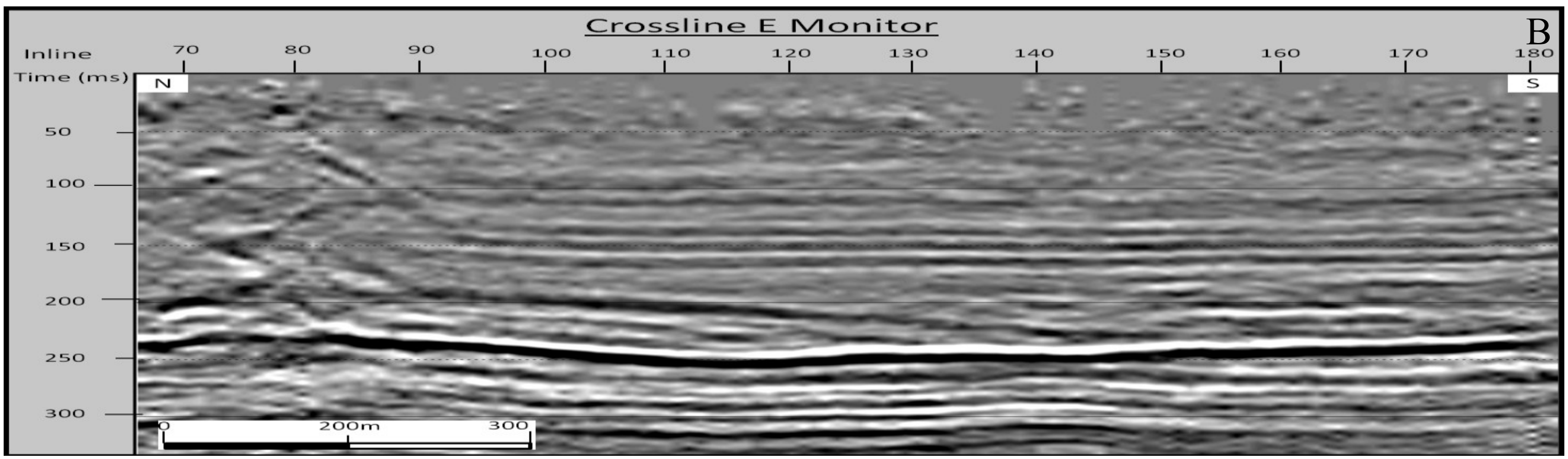

Figure 3-39 A comparison of Crossline E through (a) Baseline and (b) Monitor survey after data processing.

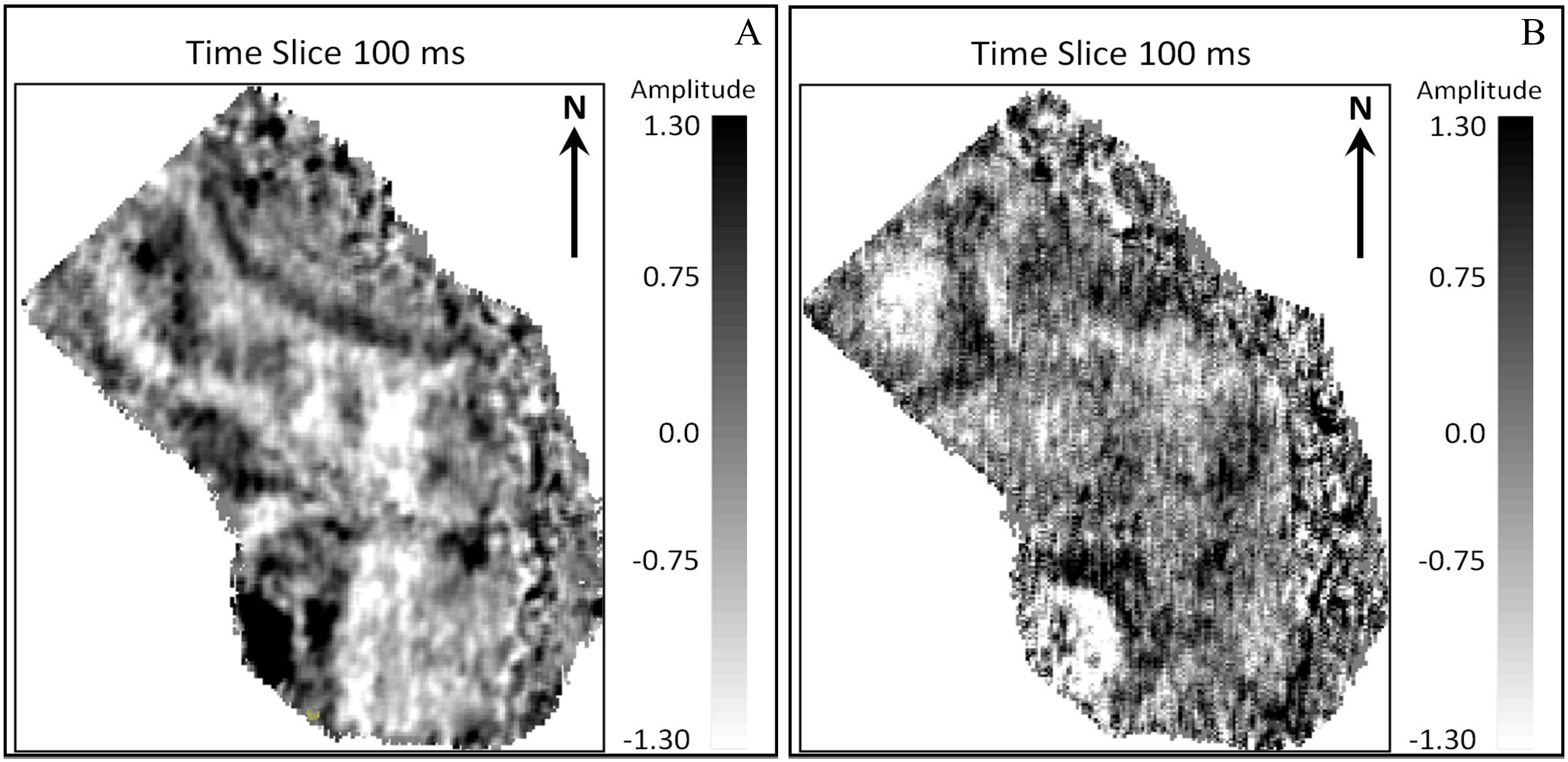

Figure 3-40 A comparison of time slices at 100ms through (a) Baseline survey and (b) Monitor survey after data processing. The S:N of the shallow data on the monitor survey is lower than that of the baseline data.

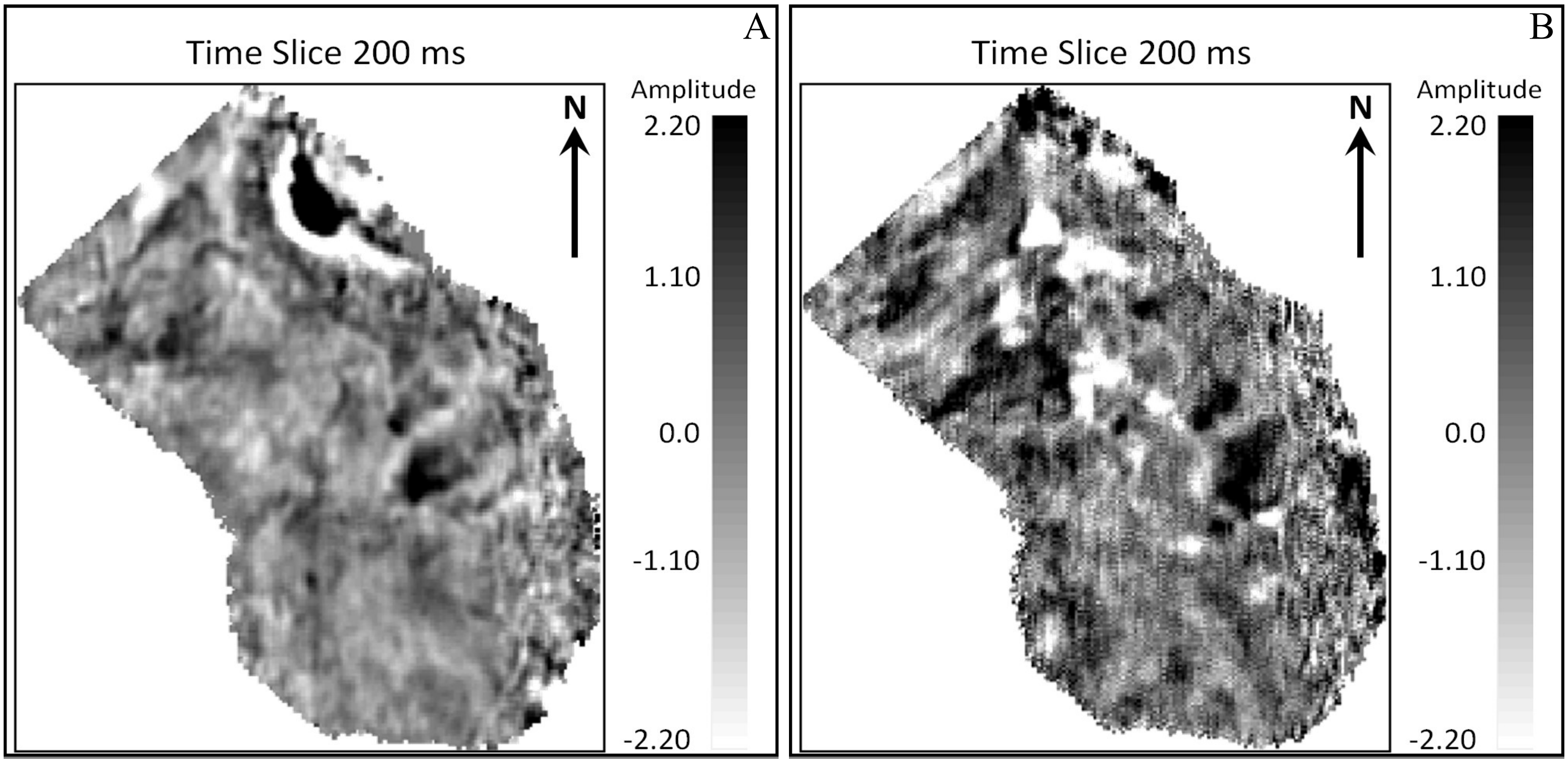

Figure 3-41 A comparison of time slices at 200ms through (a) Baseline survey and (b) Monitor survey after data processing. The S:N of the data on the monitor survey is still lower than that of the baseline data.

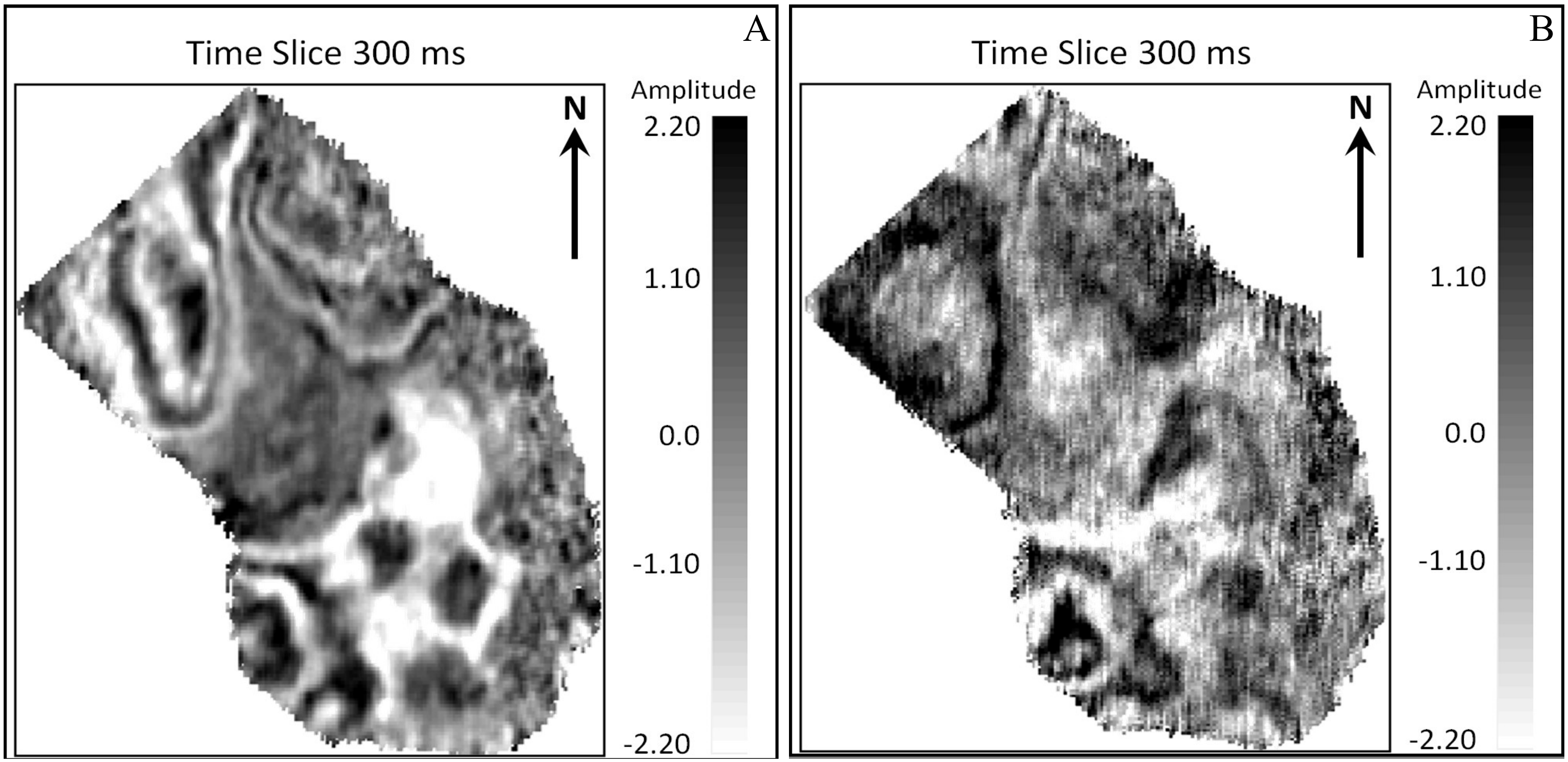

Figure 3-42 A comparison of time slices at 300ms through (a) Baseline survey and (b) Monitor survey after data processing. The S:N of the data on the monitor survey is still lower than that of the baseline data.

Chapter Four: **Time-lapse P-wave Data Interpretation**

Time-lapse monitoring is comprised of a baseline survey, ideally recorded before the onset of production, and a monitor survey recorded after a period of oil, gas or water production (Clifford, et al., 2003; Kalantzis, 1996). The objective of time-lapse seismic monitoring is to image production induced changes within the reservoir and to identify areas of bypassed reserves, or regions in which current steam injection is not optimally stimulating reserves. The analysis of monitor surveys may allow for the detection of both large and subtle changes within the reservoir (Johnston, 1997). To aid in the time-lapse interpretation, a difference volume was produced through the subtraction of the baseline data from the monitor data, producing a third dataset comprised of traces that are different between surveys. Difference volumes form the foundation for time-lapse seismic analysis, ideally integrated with reservoir characterization, geological modeling and reservoir production (Johnston, 1997).

The 4D dataset analyzed in this study was an ideal candidate for time-lapse interpretation. The baseline survey was recorded prior to production and possesses a high S:N, while the monitor survey was recorded after nine years of steam injection and production. The monitor data contains steam chambers and elevated temperatures within the reservoir zone, albeit a lower S:N due to noise contamination from production and surface activities. The strong contrast between the ideal baseline survey and a production influenced monitor survey has allowed for a detailed interpretation of reservoir changes due to production to be made.

However, observable time-lapse differences are a result of multiple factors, in which reservoir changes are one of many constituents. Differences in survey acquisition, processing, and near surface velocities during data acquisition can reduce the repeatability of a monitor survey, altering the phase, amplitude and static solution between surveys. The monitor survey was calibrated to match the phase, amplitude and statics to those of the baseline, effectively enhancing production-induced changes while suppressing differences created by other factors. Section 4.4 addresses the calibration procedure that was applied to the dataset.

Following calibration, the baseline, monitor, and difference volumes were interpreted for reservoir changes, identifying heated reservoir intervals and correlating these observations to well logs and production data.

4.1 Interpretation Overview

The interpretation of the 4D P-wave data was focused on production induced changes occurring within the McMurray Formation reservoir. The reservoir lies below the Clearwater C reflection (cap rock for the reservoir) and above the Devonian Carbonate reflection (Paleozoic unconformity). Time delays are observed along the Devonian reflection (monitor) due to a reduction in P-wave velocity of the heated bitumen sands in the overlying McMurray Formation reservoir (see Section 1.3, Chapter 1). These velocity anomalies, in combination with seismic attributes, reservoir isochrons, and amplitude anomalies, were the target of the P-wave 4D interpretation.

The interpretation of the time-lapse seismic did not include the data within the vicinity of the Quaternary channel. As discussed in Chapter 2 (Section 2.3), the Quaternary channel infill is highly attenuative, preventing coherent imaging of the Quaternary channel boundaries and the underlying reflections (Figure 2-7, Chapter 2). Thus, all seismic underlying the Quaternary channel was considered to be low quality and unreliable data, and was not considered during the time-lapse interpretation.

Prior to the interpretation of the time-lapse dataset, both the baseline and monitor data were bulk shifted to later times by 250 ms to tie the data into other interpretations and well logs. Although this thesis will not address these additional interpretations, it is important to take note of the bulk shift when comparing images of the data in this chapter to those in Chapter 3.

4.2 Data Comparison

Despite the best efforts to process the data in an identical manner, there are some differences in the baseline and monitor data. Figure 4-1 is a comparison of the baseline and monitor data, taken from the center of the survey within an area of known steam

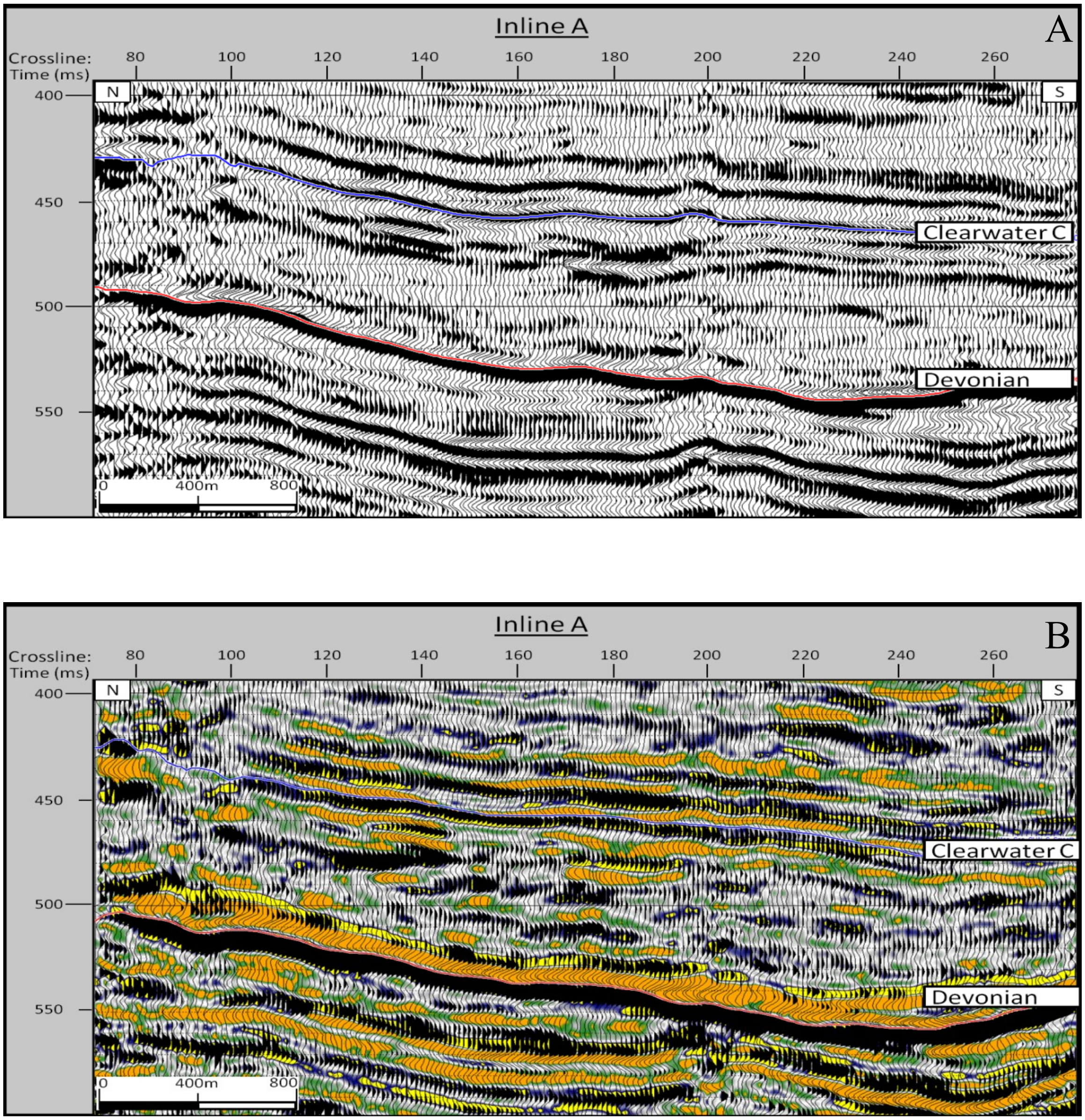

Figure 4-1 A comparison of (a) 2002 baseline survey to (b) 2011 monitor survey before calibration. The overlain color is the amplitude difference between the baseline and monitor data, calculated by subtracting the baseline data from the monitor data.

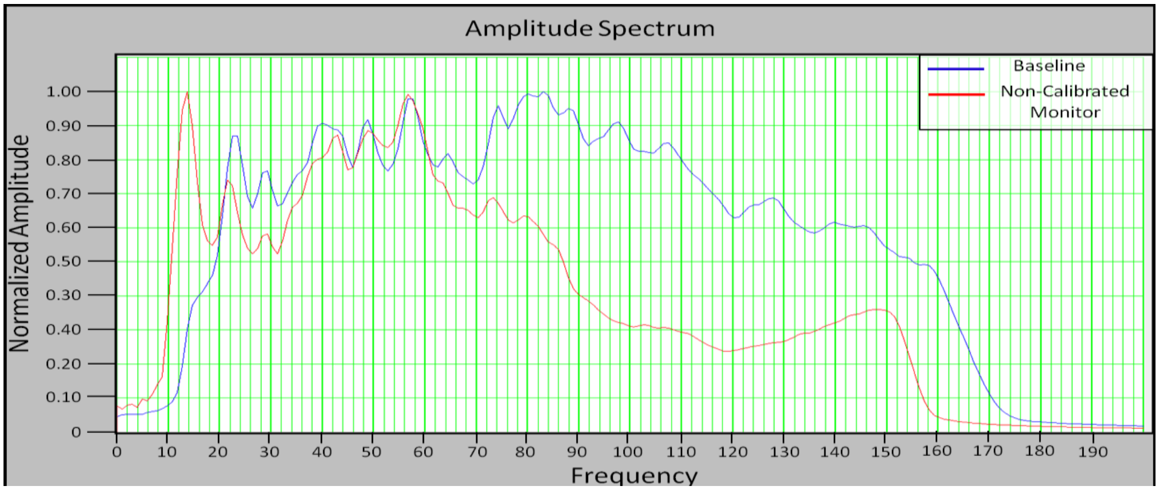

Figure 4-2 Amplitude spectrum for all traces in the baseline and monitor data before calibration. There is a large discrepancy in the amplitudes of the high frequencies (70-160 Hz).

injection. A comparison of the shallow reflections displays the large S:N and phase disparity between the baseline and monitor data. Globally, there is a phase difference of 34 degrees between the two datasets, as well as a discrepancy in the amplitudes of the higher frequencies (Figure 4-2). Overall, the baseline data is of higher quality than the monitor data.

The color overlay on the monitor data is the amplitude difference between the two datasets, calculated by subtracting the baseline data from the monitor data. Positive differences are yellow and negative differences are green-orange. There are a large number of differences that due to disparity in phase, statics and amplitudes, as well as differences within the reservoir due to production. Through the calibration procedure, Section 4.5, non-production induced differences will be reduced, while steam related anomalies will be preserved.

4.2.1 Normalized RMS

To provide a detailed understanding of the differences between the baseline and monitor survey, NRMS difference maps, crosscorrelation maps and time-shift maps of the reservoir interval were produced. NRMS difference maps are constructed by taking the difference between the two datasets on a sample-by-sample basis, with RMS equalization of the amplitudes prior to the difference calculation as follows:

$$\boldsymbol{NRMS} = \frac{\boldsymbol{2*RMS\ (B-A)}}{\boldsymbol{RMS\ (A)+\ RMS\ (B)}} \qquad \textbf{4-1}$$

where A is the baseline survey and B is the monitor survey, and where the RMS operator is defined as (Kragh & Cristie, 2002):

$$\boldsymbol{RMS} = \sqrt{\frac{\boldsymbol{\sum_{t1}^{t2}(x_t)^2}}{\boldsymbol{N}}} \qquad \textbf{4-2}$$

where N is the number of samples in the interval of t_1-t_2.

NRMS is a measure of the difference between the two surveys over a specified interval, normalized to a value ranging from 0-200 percent, where zero percent represent identical data and 200 percent represents totally uncorrelated data (Sheriff, 2002; Kragh & Cristie, 2002). NRMS is largely affected by small differences within the data, including noise, phase shifts and amplitude differences (Kragh & Cristie, 2002). Hence, NRMS provides a good display of the overall difference between two datasets.

Typical NRMS values are in the range of 10-30% after calibration, but may often exceed this due to acquisition and repeatability issues. For example, Koster, et al., (2000) displayed average NRMS values of 35% in the Draugen field, while Kommedal, et al., (2005) reported NRMS values of 14% and Eiken, et al., (2003) quoted NRMS values as low as 6-12%.

Figure 4-3a is an NMRS map taken above the Clearwater C horizon within an area free of reservoir production. The NRMS map displays areas of relatively lower value (80 percent) as well as areas of higher NRMS value (1.80 percent). Overall, the NRMS value is high, signifying that considerable differences exist between the two surveys that are not related to production. Through the calibration procedure, (Section 4.5), the overall NRMS value is reduced through adjustments made to the monitor survey in terms of phase, statics (time shifts) and amplitudes.

4.2.2 Crosscorrelation

Crosscorrelation maps provide an understanding of the correlativity of two datasets, where similar or identical events will have a high correlation value and dissimilar or unique events (i.e. events only observed on the monitor survey) will have a low correlation value. Crosscorrelation is a simple signal processing technique where a stationary or reference trace (baseline) is matched to a corresponding sliding trace from the input (monitor) over a specified time window. The process of crosscorrelation can be describes as a "shift, multiply, add" operation:

$$(\mathbf{f} * \boldsymbol{g})[\boldsymbol{n}] = \sum_{-\infty}^{\infty} \boldsymbol{f}^{*}[\boldsymbol{m}]\, \boldsymbol{g}[\boldsymbol{n}+\boldsymbol{m}] \qquad \textbf{4-3}$$

Computed crosscorrelation maps are interpreted in conjunction with computed time-shift maps, where time-shift maps display the shift (or lag) in ms required to produce the corresponding crosscorrelation values. Crosscorrelation and time-shift values are computed in conjunction; the amplitude value for two traces (baseline and monitor) are multiplied together and summed to produce a total value for the initial lag, following which the trace is shifted down one sample and a new value is computed (dot product). Using the initial alignment as the zero lag position, a plot of the lag vs. dot product displays the best time shift required to produce the maximum dot product, or the highest normalized crosscorrelation value (Figure 4-4) (Yilmaz, 2001; Gadallah, 2005). These time-shift values provide an understanding of the static adjustments required to better align the reflections in time, where negative values suggest that monitor traces are lower in time than the baseline, while positive values suggest that monitor traces are higher in time. Examples of the application of crosscorrelation are given by Eastwood et al., (1998) and Drijkoningen et al., (2012).

Figure 4-3b is a crosscorrelation map produced over the same interval as the NMRS map and Figure 4-3c is the corresponding time-shift map. The overall crosscorrelation value is high for this interval (70 – 90 percent), indicating that the cap

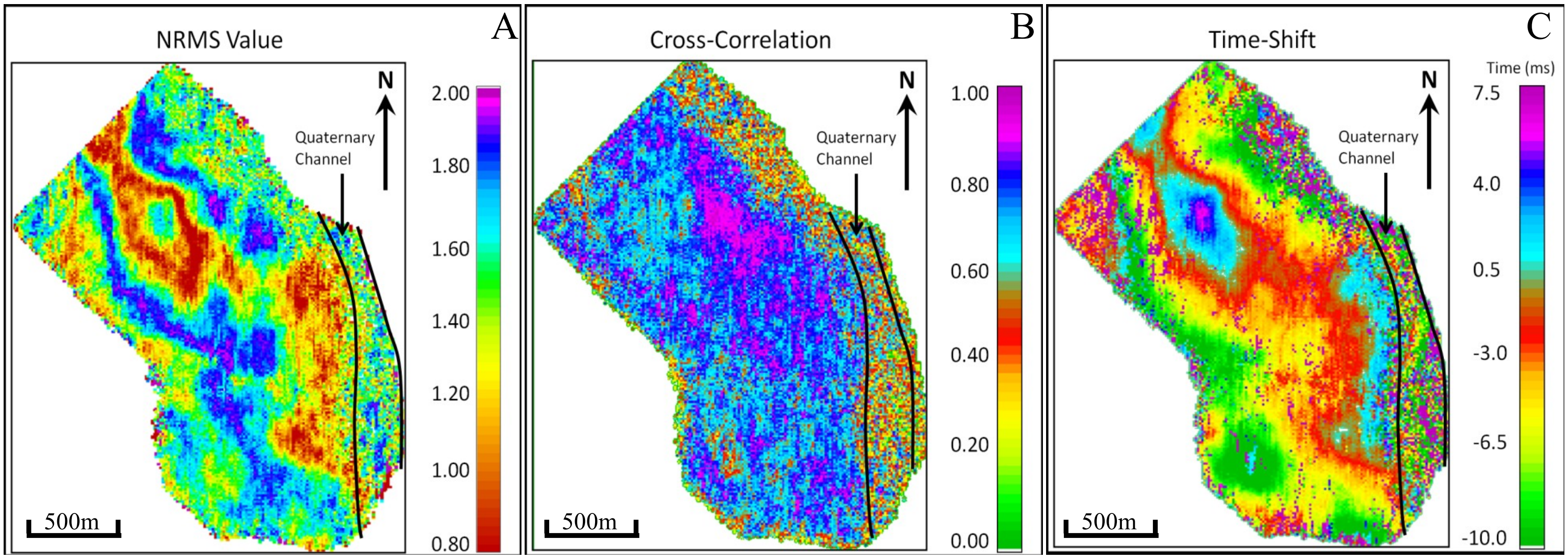

Figure 4-3 (a) NRMS error map of the Clearwater C interval, an area free of reservoir production (35ms window beginning 35ms above the Clearwater baseline horizon) (b) Crosscorrelation map and (c) Time-shift map of the same interval. The NRMS map displays areas of relatively low NRMS value (80 percent) and areas of high NRMS value (1.80 percent), suggesting that considerable differences exist between the baseline and monitor survey in terms of phase, amplitudes and statics. The crosscorrelation map shows overall high correlation values (0.70 - 0.90) which correspond to time-shift values of -8.0 to +6.0 ms. The high correlation paired with large time-shift values suggests that significant time-shifts are required to align the cap rock reflections of the monitor survey with those of the baseline, which would produce an overall high correlation. The outlined quaternary channel to the east represents a region of unreliable data due to signal attenuation from the Quaternary channel infill.

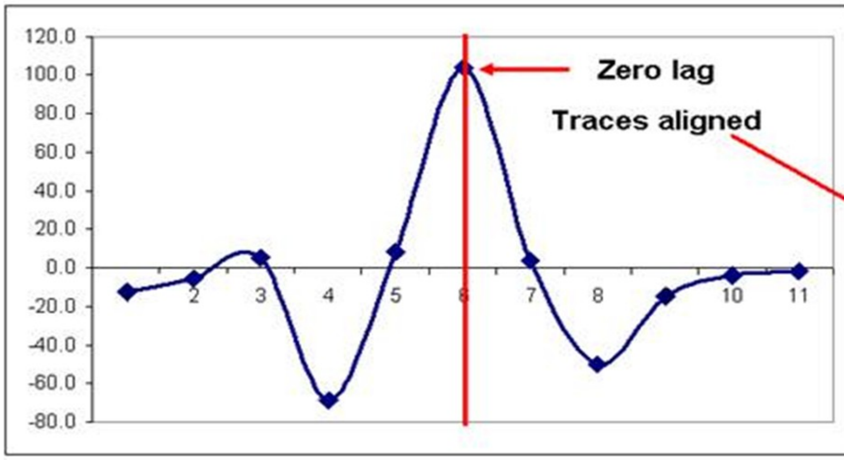

Lag	Dot product
-10	-12.3
-8	-5.1
-6	5.4
-4	-68.2
-2	8.2
0	103.6
2	3.8
4	-50.1
6	-14.3
8	-4.1
10	-1.2

Figure 4-4 Plot of lag vs. dot product for some theoretical set of traces. In this example, a time-shift of 0 ms is required to produce the maximum crosscorrelation value (Taken from Hampson-Russell's Pro4D guide).

rock reflections of the monitor survey correlate well with those of the baseline survey. However, to produce this high correlation, each trace must be shifted by a corresponding time-shift value as displayed in Figure 4-3c, ranging from -8.0 to 6.0 ms. These time-shifts were later corrected through the calibration procedure (Section 4.5) as both a global correction and as a trace-by-trace correction.

4.3 Horizon Interpretation

Prior to interpretation, the temporal positioning of the reservoir and reflectors of interest was determined. The main geological units of interest, as discussed in Chapter 2 (Section 2.2), are represented as seismic horizons corresponding to the Devonian Carbonates of the Beaverhill Lake Group, the Clearwater B Formation, and the Clearwater C Formation (cap rock). Each horizon was identified within the seismic data through the correlation of seismic reflections with geological units, where geological well tops identified on sonic logs were related to seismic reflectors via synthetic seismograms. The synthetic seismograms were generated by the convolution of the reflectivity series with an Ormsby wavelet containing a frequency range representative of that within the data. Figure 4-5 is an example of a synthetic seismogram tie for well A displaying well log tops for the Devonian, and Clearwater C Formations, and their relationship to the seismic data.

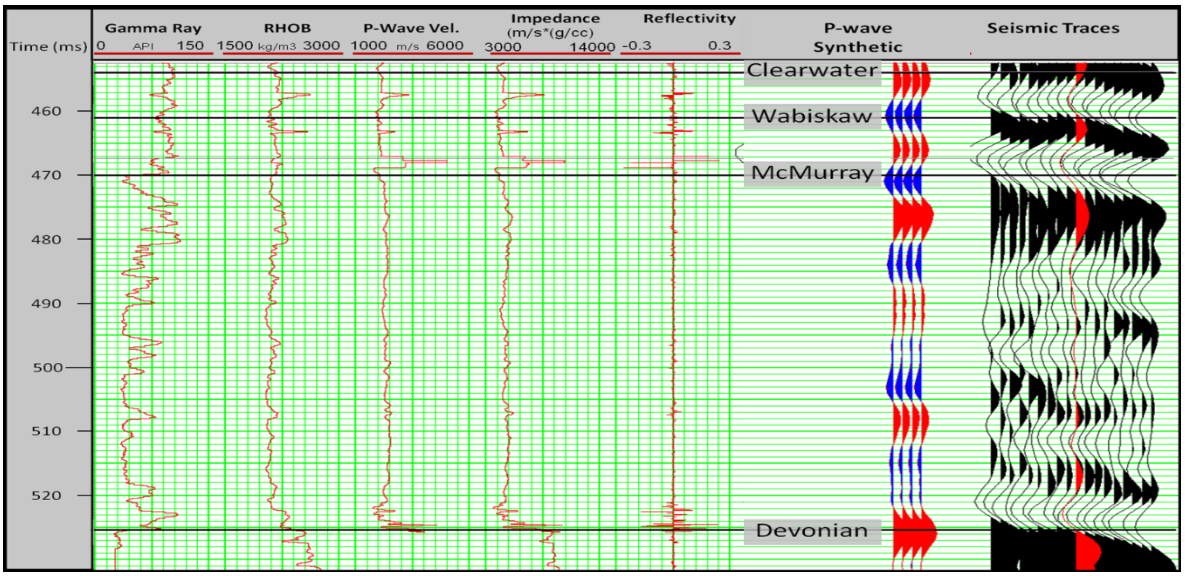

Figure 4-5 Synthetic seismogram for well A from the center of the survey area, including the calculated impedance and reflectivity for the Clearwater and Devonian reflections. The red trace is the reference trace from the seismic data.

Following the well tie, seismic horizons were picked on the zero crossing for each reflector of interest. Horizons were initially picked on the baseline survey and non-calibrated monitor survey, and after data calibration, repicked on the monitor survey (see Section 4.4.4). For more information about the seismic characteristic of each reflector of interest, refer to Section 2.2 (Chapter 2).

4.4 Preliminary Interpretation

Before data calibration, a preliminary interpretation of the baseline and non-calibrated monitor survey was performed to gain an understanding of amplitude anomalies observable within the reservoir interval. The interpretation of this time-lapse dataset was focused on the McMurray Formation reservoir, lying between 450-550 ms, bound above by the Clearwater C horizon and below by the Devonian horizon.

Figure 4-6 is a seismic cross Section taken along an arbitrary line running NW to SW through both the baseline and non-calibrated monitor data, focused on the McMurray Formation reservoir. Between inlines 160 and 180, at a time of 500 - 510 ms on the monitor survey, a high amplitude event is observed which is not observed on the baseline survey. This high amplitude event coincides with a velocity pushdown along the Devonian reflection of 6 ms. Overlaying gamma ray logs onto the baseline and non-calibrated monitor data demonstrates that the high amplitude anomaly intersects a low gamma ray value, representing a channel sand within the Lower McMurray Formation. The inter Section of an amplitude anomaly with reservoir channel sands is interpreted to be indicative of a steam induced anomaly.

A second high amplitude event is observed on the non-calibrated monitor data between inlines 100 and 120, at a depth of 530 – 540 ms, which is also not present on the baseline data. This event coincides with a Devonian time delay of 8 ms, and intersects a Lower McMurray channel sand, as indicated by the low gamma ray values on the overlain log. Again, this amplitude anomaly is interpreted to be due to steam injection.

Both of the amplitude anomalies are bounded by a mud or shaly unit, as indicated by a high gamma ray value overlying each anomaly. This muddy or shaley interval is a baffle to steam flow, preventing the steam from migrating upward in the reservoir to earlier times. The combination of channel sand with an overlying impermeable unit is representative of a flow conduit for steam within the reservoir. Injected steam will preferentially flow along the pours and permeable channel sands, migrating laterally throughout the reservoir while being bound to lower times due to the overlying baffle. This steam migration will bypass bitumen reserves in overlying channel sands, as steam cannot transfer significant heat through the shale/mud to the overlying channel sands.

To provide further support for the presence of channels within the McMurray Formation reservoir, the baseline data was transformed into a semblance volume. Semblance is a seismic attribute, used to analyze data for changes in the seismic character, computed by comparing the amplitude of a single trace to that of an adjacent trace.

Semblance is calculated over a 3D analysis window, with a defined dip and azimuth for each point in the data volume (zero dip for a flattened volume) (Marfurt, et al., 1999; Chopra & Marfurt, 2007). Semblance is defined as the ratio of energy of the average trace to the average energy of all the traces along a specified dip, averaged over a specified analysis window. Semblance, S(t, p, q) is defined as follows:

$$\boldsymbol{S(t,p,q)} = \frac{\sum_{k=-k}^{K}\left[\frac{1}{J}\sum_{j=1}^{J} u_{j}\left(t+k\Delta t-px_j-qy_j\right)\right]^2}{\sum_{k=-K}^{K}\frac{1}{J}\sum_{j=1}^{J}\left[u_j\left(t+k\Delta t-px_j-qy_j\right)\right]^2} \qquad 4\text{-}4$$

where x_j and y_j denote the x and y distances of the jth trace from the center trace, summed over 2K + 1 samples. P and q are the apparent dips measured in milliseconds per meter and t is the time in milliseconds (Chopra & Marfurt, 2007).

Semblance values range from 0 (low) to 1 (high), where traces exhibiting a semblance of 0 have extremely different amplitudes and traces with a semblance of 1 have the same amplitudes. Effectively, semblance is a quantitative measure of the coherency of seismic data across a set of traces (Chopra & Marfurt, 2008). The semblance attribute is effective at delineating discontinuities that would cause a change in the seismic signal, such as faults or channel edges (Chopra & Marfurt, 2008). Hence, the semblance analysis can be used to identify channels within the McMurray Formation reservoir.

Figure 4-7a is a time slice through the semblance volume displaying low semblance values (white). These low semblance values are interpreted to be channels within the McMurray Formation reservoir. Figure 4-7b is a semblance time slice from the lower McMurray Formation, overlain onto the 3-dimensional Devonian time structure map. The semblance time slice is interpreted to show a McMurray Formation channel, deposited within a low of the Devonian unconformity surface.

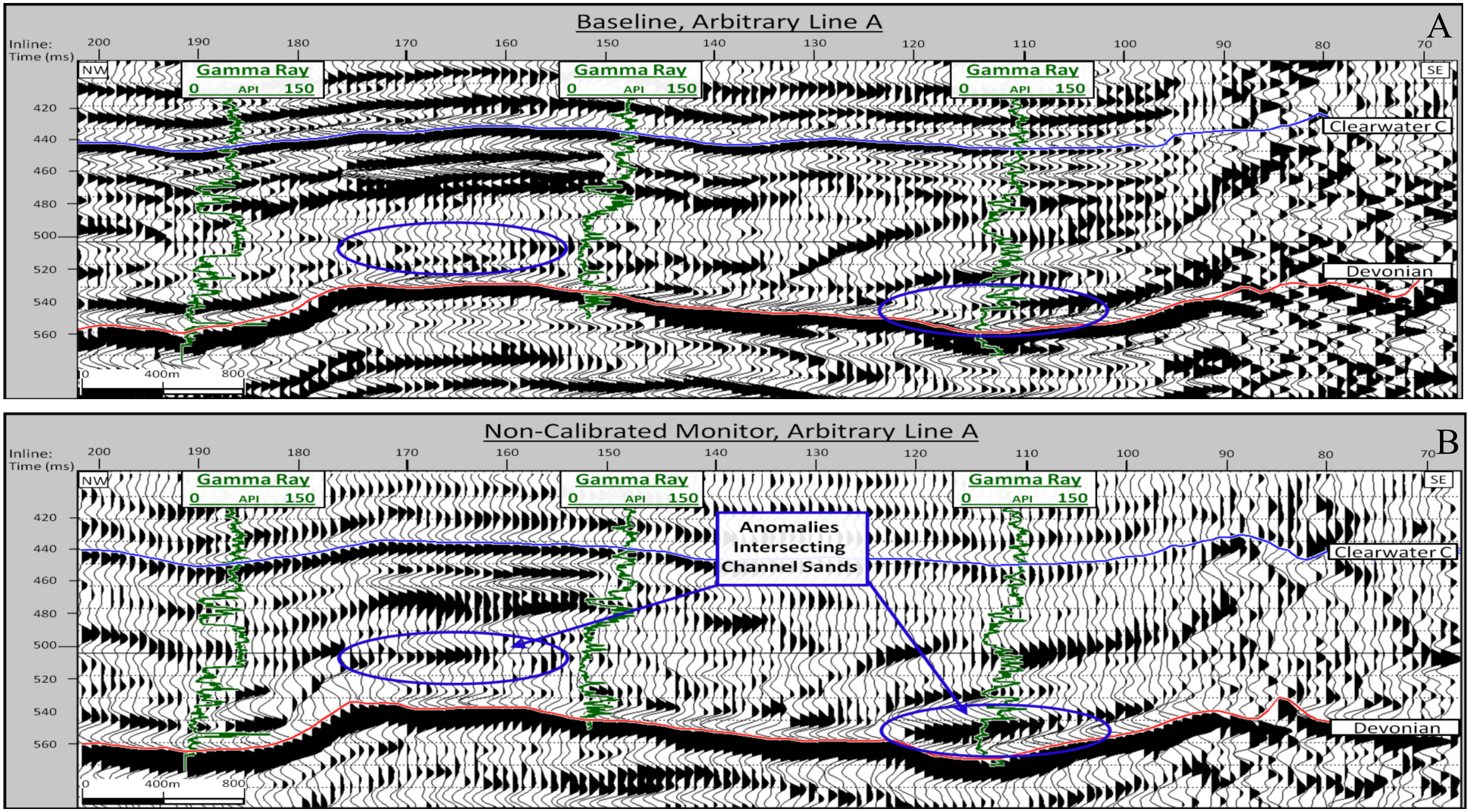

Figure 4-6 Arbitrary Line A running NW - SW through (a) baseline and (b) non-calibrated monitor data. Two amplitude anomalies are observed on the non-calibrated monitor data. Gamma ray logs indicate the inter Section of the anomalies with Lower McMurray Formation channel sands. The anomalies are interpreted to be indicative of steam injection into the McMurray Formation reservoir. Data on the SE end of the line is low quality due to signal attenuation from the Quaternary channel.

4.4.1 Frequency Attenuation

The analysis of the frequency content of the data may be indicative of reservoir steam zones. The attenuation of frequency beneath a steam induced anomaly has been discussed by Hickey, et al., (1991), Isaac (1996) and Yuwen (1998), attributing the attenuation of higher frequencies to a decrease in the viscosity of reservoir pore fluids. Velocity and viscosity are largely influenced by temperature, decreasing considerably during steam injection in conjuction with elevated reservoir temperatures above ambient values. These decreases may lead to high-frequency attenuation, where the frequency content of the reflections underlying steam zones may be characterized by low-frequency shadows (Taner, et al., 1979; Isaac, 1996; Macrides & Kanasewich, 1987). Hence, the non-calibrated monitor data was analyzed for the presence of low-frequency zones underlying observed amplitude anomalies.

Complex seismic trace analysis was employed to generate an instantaneous frequency volume to aid in the investigation of low-frequency zones. Instantaneous frequency is the temporal measurement of the rate of change of the instantaneous phase, with respect to time (the time derivative of instantaneous phase; see Appendix A) (Taner, 2002; Barnes, 2007). Instantaneous frequency is defined as (Barnes, 2007):

$$\boldsymbol{f(t) = \frac{1}{2\pi}\frac{d\theta(t)}{dt}} \qquad \text{4-5}$$

where Θ(t) is the instantaneous phase (Barnes, 2007):

$$\boldsymbol{\theta(t) = \mathbf{arctan}\left[\frac{y(t)}{x(t)}\right]} \qquad \text{4-6}$$

and where x(t) is the seismic trace and y(t) is the seismic trace rotated by -90 degrees (see Section 4.6.3 or Appendix A).

The baseline and non-calibrated monitor data were transformed to instantaneous frequency volumes using Hampson-Russell's Pro4D software. The two amplitude anomalies observed in Figure 4-6 correspond with a decrease in frequency content of the events underlying each anomaly. Figure 4-8 is a comparison of the baseline and non-calibrated monitor instantaneous frequency volumes. There is a low frequency shadow observed at 510 ms on the monitor data between inlines 110 and 150, located on the Devonian reflection underlying the amplitude anomaly. To display the spatial distribution of the frequency attenuation, a time slice was taken through the baseline instantaneous frequency volume and the non-calibrated monitor instantaneous frequency volume (Figure 4-9). These time slices display the instantaneous frequency values, averaged over a 20 ms window, beginning 510 ms beneath the anomaly observed between inlines 110 and 150. A comparison of the baseline and non-calibrated monitor frequency values displays the attenuation of higher frequencies on the non-calibrated monitor data, where instantaneous frequency values are significantly lower than those on the baseline data. The blue circle represents of the location of the amplitude anomaly on the time slices.

Other areas of the reservoir displayed significant frequency attenuation, as observed on the non-calibrated monitor instantaneous frequency volume time slice. Overlaying the horizontal SAGD well pairs onto the time slices displays the high correlation of horizontal wells with areas of frequency attenuation. These areas of reservoir frequency attenuation are interpreted to be representative of steam within the Lower McMurray Formation.

4.5 Data Calibration and Differencing

The time-lapse seismic surveys were loaded into Hampson-Russell Pro4D to perform reflectivity differencing of the two datasets. Prior to subtraction of the two volumes, I compared and calibrated the data to match phase, amplitude and statics between the surveys in an effort to reduce differences that are not production related. The calibration used the baseline survey as a reference, and altered the phase, statics and amplitudes of the monitor survey to match those of the baseline.

The calibration procedure is a comparison of two datasets, where differences are observed and correction factors are calculated and applied to the monitor survey on the basis of dissimilarity with the baseline data, specified within a windowed segment of the data. Typically, the calibration is windowed on reflections above the reservoir that have

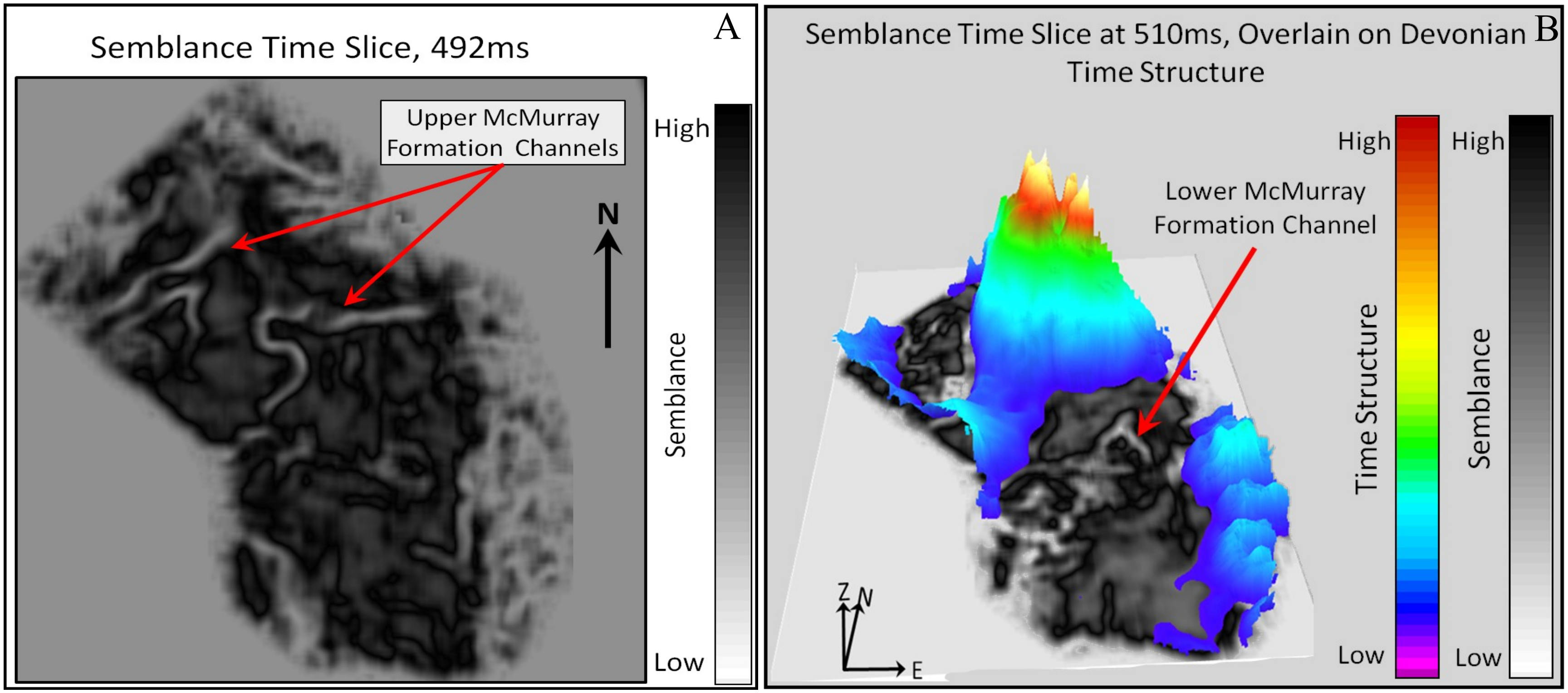

Figure 4-7 (a) Time slice at 492ms through the semblance volume, displaying channels within the Upper McMurray Formation. (b) Semblance time slice overlain on a 3D view of the Devonian time structure, displaying a McMurray Formation channel within a low along the Devonian surface.

not undergone reservoir production to ensure that correction factors do not remove production induced changes (Watson, 2004; Nakayama, 2005; Johnston, 1997). However, due to the very shallow nature of our reservoir, coupled with the low S:N and low event coherency of the shallow data (above the Clearwater C horizon), the shallow portion of the monitor survey was ill-suited for calibration. Instead, the calibration of the time-lapse data was windowed on the Devonian reflection. This reflection was chosen on the basis that (1) it is the most coherent and repeatable reflection within the survey due to its high amplitude nature, and (2) it marks the base of the reservoir. This modification allowed for a robust calibration of the monitor data. The calibration was performed in five steps as follows: (1) phase matching (2) shaping filter (3) static corrections (4) amplitude matching and (5) construction of a difference volume.

4.5.1 Phase Matching

Phase matching computed and applied a phase rotation and bulk time shift to the monitor survey to compensate for phase and time differences from the baseline survey. The phase matching was calculated over a 70 ms window, beginning 2 0ms above the zero crossing Devonian event. The calculation was restricted to a maximum time shift of 30 ms, and a crosscorrelation minimum of 70 %. Phase and time corrections were applied to the entire monitor survey on a global basis, where calculated phase and time corrections were 34 degrees and +7.28 ms, respectively. Figure 4-10b is an inline section through the monitor survey after the phase and time correction. The color overlain on the section is the amplitude difference when the baseline survey data was subtracted from the monitor survey data after the phase and time correction. The reduction in difference bright spots after the application of the phase and time correction (in comparison to the non-calibrated monitor data, Figure 4-1b), is due to the removal of the phase difference, and the alignment of reflections in time. The phase and seismic character of the Devonian reflection after the correction more closely resembles that of the baseline survey.

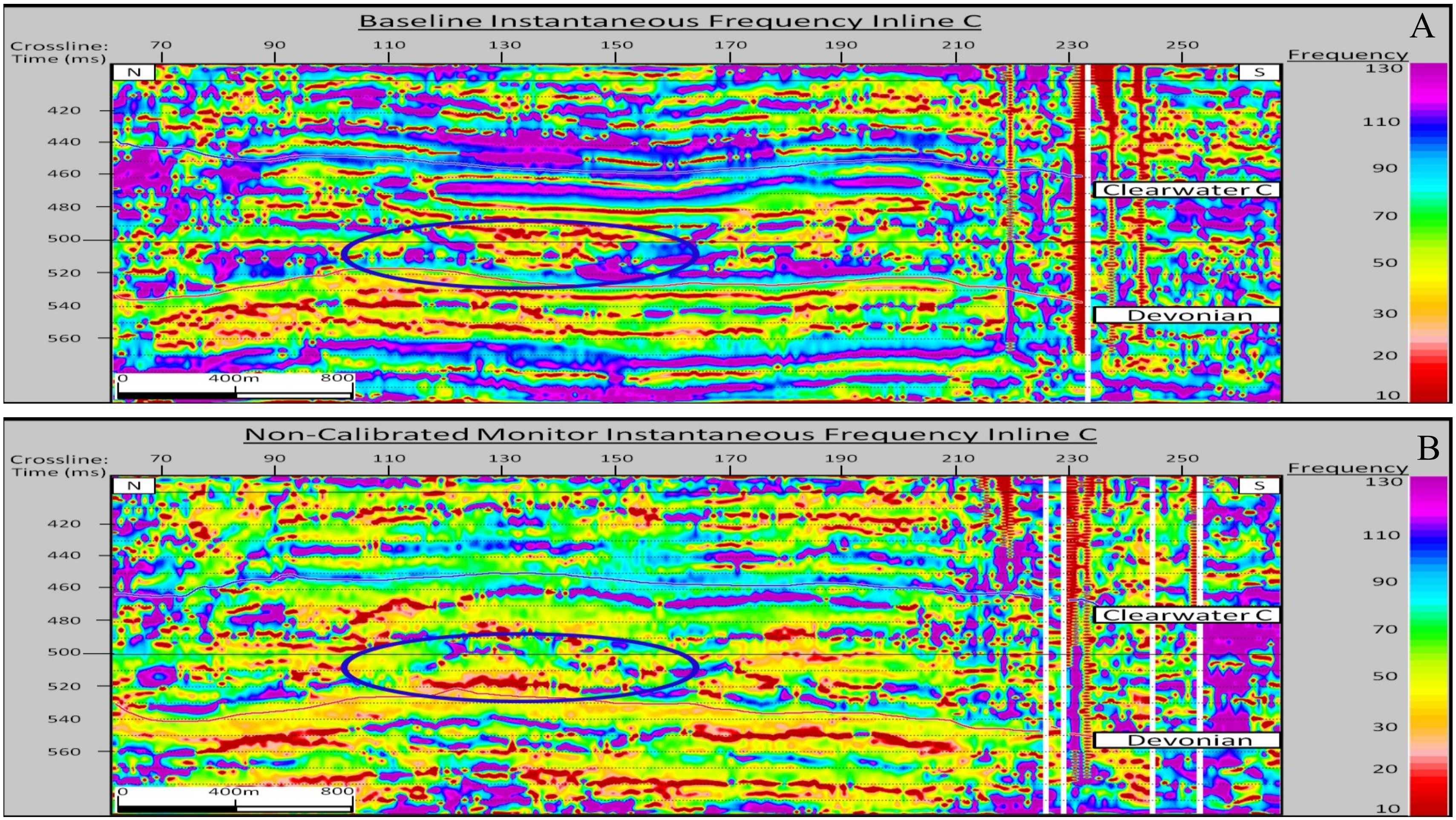

Figure 4-8 Inline C through the instantaneous frequency volumes for (a) baseline and (b) non-calibrated monitor displaying a lower frequency value on the monitor data than on the baseline data between crossline 110 and 150 at a time of 510 – 530 ms. The attenuation of high frequencies is attributed to steam injection. The red vertical lines represent errors in the frequency calculation due to gaps in the data.

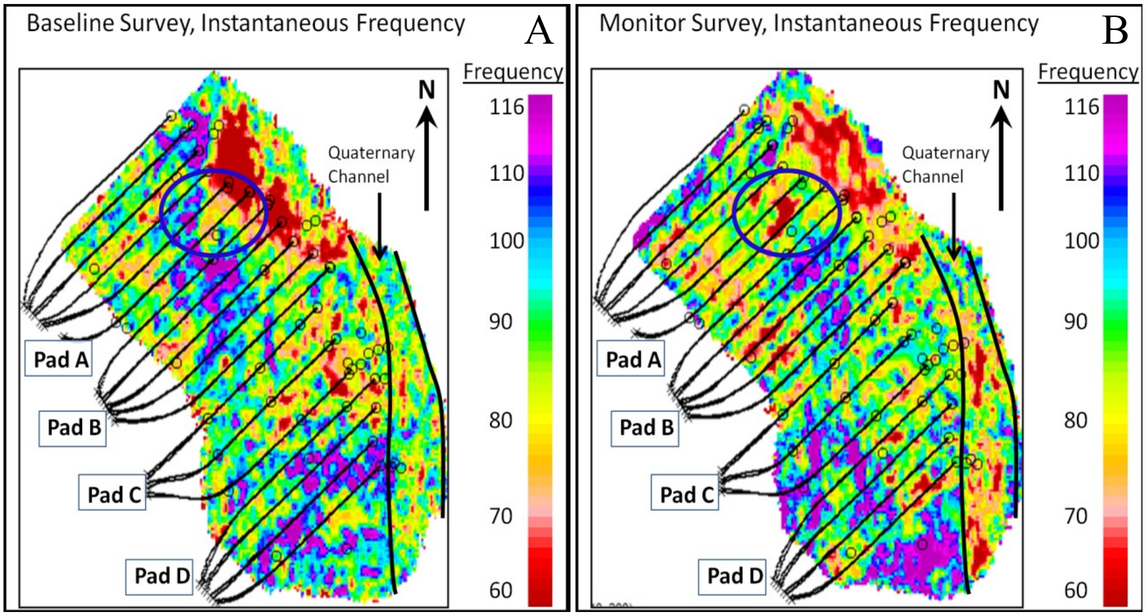

Figure 4-9 Instantaneous frequency slices calculated from 507 - 527ms for (a) baseline and (b) non-calibrated monitor displaying lower frequency values on the monitor survey than on the baseline survey, which correspond to horizontal well locations. The attenuation of high frequencies on the monitor survey is interpreted to be indicative of steam injection.

Figure 4-11 displays the crosscorrelation, time-shift and NRMS map above the reservoir after the phase and time correction. In comparison to earlier results (Figure 4-3), NRMS values have decreased overall, with high NRMS values remaining within the central region of the data. Crosscorrelation values have increased on average, due to the better alignment of reflections in time between the baseline and monitor data. Some small regions of low correlation exist, reflecting the low repeatability of the cap rock interval between the baseline and monitor data. Lastly, the time-shift values have been significantly altered to reflect the increased correlation. Regions in which the cap rock exhibits a high correlation, time-shift values are low (-2 to +2 ms) while areas where the cap rock is less repeatable and has a higher correlation (central region and edges of the data) the time-shift values are anomalously high. Due to the generally low S:N of the shallow reflections, the calibration procedure was focused on the McMurray Formation reservoir and underlying Devonian reflection, and not the shallow reflections above the Clearwater C horizon.

Figure 4-12 shows the crosscorrelation maps for the reservoir interval (Clearwater C reflection to the Devonian reflection) before and after the phase and time correction. Overall, the reservoir crosscorrelation map exhibits an increase in correlation in areas that are not expected to have steam, with crosscorrelation values of 80 – 100 percent. Areas exhibiting low values are observed, one in the north and a second in the south, which lie within areas of known steam injection. Hence, these low values are interpreted to be due to steam injection into the McMurray Formation reservoir. Figure 4-13 displays the time-shift values required to produce the crosscorrelation values.

Figure 4-14 shows the crosscorrelation maps for the Devonian interval (10ms above the baseline Devonian horizon zero-crossing to 25 ms below), displaying a high overall increase in correlation due to phase matching, with the majority of values approaching 100 percent. The corresponding time-shift maps (Figure 4-15) indicate that there are considerable static difference between the baseline and monitor that must be accounted for to produce the high correlation values observed in Figure 4-14. These statics are a function of the time-delays created by the overlying heated McMurray Formation sands (Section 4.1) which are addressed by trace-by-trace static corrections in Section 4.4.3.

Lastly, the NRMS maps of the Devonian interval shows a strong overall decreases in NRMS values, primarily within the central region, with overall values of 0.40 to 0.60 NRMS. This significant reduction in NRMS value displays the effectiveness of the phase and time correction, where the corrected monitor Devonian reflection more closely resembles that of the baseline in terms of phase and temporal position (Figure 4-16).

4.5.2 Shaping Filter

Finally, to best match the wavelet and amplitude spectrum of the two surveys, a shaping filter was applied to remove spectral and phase differences through a Wiener-Levinson least-squares filter (Rojas, 2008; Sheriff, 2002; Yilmaz, 2001; Robinson & Treitel, 2000). The shaping filter adjusted the wavelet of the monitor survey to best match

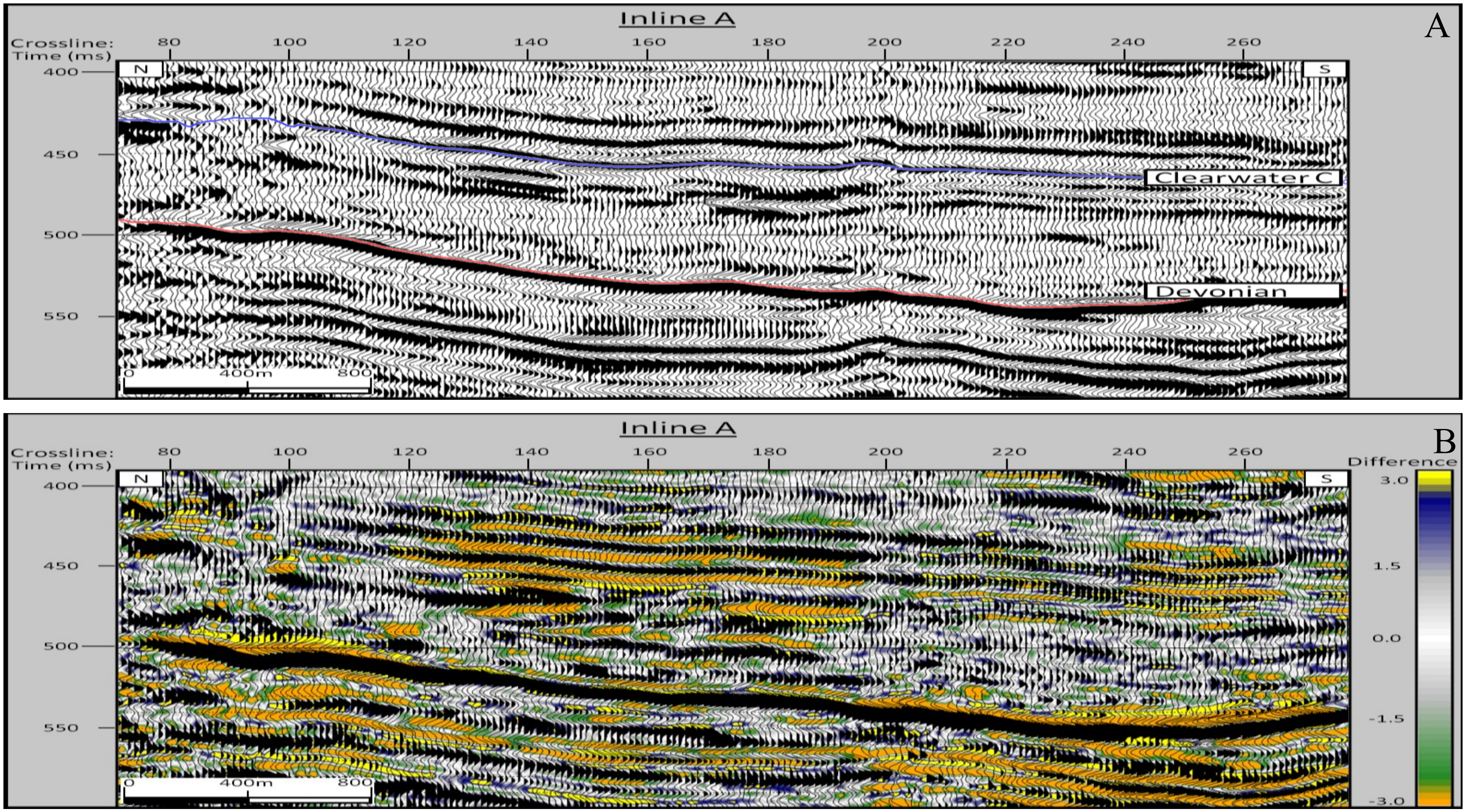

Figure 4-10 (a) Inline A through the baseline survey (b) Inline A through the monitor survey after the phase and time correction. The color overlay is the amplitude difference between the baseline and monitor survey, calculated by subtracting the baseline data from the monitor data. Notice the reduction in amplitude differences due to the correction (in comparison to Figure 4-1b).

that of the baseline survey in a least-squared sense (Yilmaz, 2001; Rojas, 2008). This is accomplished by using the autocorrelation of the monitor wavelet with the cross correlation of the baseline wavelet and the monitor wavelet to calculate and apply a shaping filter as displayed in equation 4-6.

$$\begin{pmatrix} \boldsymbol{r_0} & \boldsymbol{r_1} & \dots \boldsymbol{r_{n-1}} \\ \boldsymbol{r_1} & \boldsymbol{r_2} & \dots \boldsymbol{r_{n-2}} \\ \dots & \dots & \dots \dots \\ \boldsymbol{r_{n-1}} & \boldsymbol{r_{n-2}} & \dots \boldsymbol{r_0} \end{pmatrix} \begin{pmatrix} \boldsymbol{a_0} \\ \boldsymbol{a_2} \\ \dots \\ \boldsymbol{a_{n-1}} \end{pmatrix} = \begin{pmatrix} \boldsymbol{g_0} \\ \boldsymbol{g_1} \\ \dots \\ \boldsymbol{g_{n-1}} \end{pmatrix} \qquad \textbf{4-7}$$

where r_i is the autocorrelation of the monitor wavelet, a_i are the elements of the shaping filter, and g_i is the crosscorrelation of the baseline with the monitor wavelet (Yilmaz, 2001; Rojas, 2008).

The shaping filter estimates a function that matches the frequency, time and average power of the baseline and monitor datasets. The shaping filter process then calculates the crosscorrelation of the baseline and monitor data and the autocorrelation of the baseline data, which is fed into the matrix (equation 4-6) to calculate the desired filter. The filter is then applied to the monitor data to yield a filtered dataset that approximates the baseline data. This process is a global application, and is zero phase due to the previously applied phase rotation in Section 4.5.1 (Robinson & Treitel, 2000; Yilmaz, 2001).

The shaping filter was calculated over a 70 ms window, beginning 20 ms above the zero crossing of the Devonian horizon and restricted to contain only traces exhibiting greater than a 79 % correlation between surveys. The shaping filter is a global correction, applied to all of the data within the monitor survey.

Figure 4-17 is a comparison of the baseline wavelet to the monitor survey wavelet before and after the shaping filter, and Figure 4-18 shows its amplitude spectrum. After the shaping filter, the frequency spectrum of the Devonian event of the monitor data more closely resembles that of the baseline data. The monitor data shows a significant increase in the amplitudes of the high frequencies, 80-150 Hz, and a relative reduction of amplitudes in the low frequencies, 10-70 Hz.

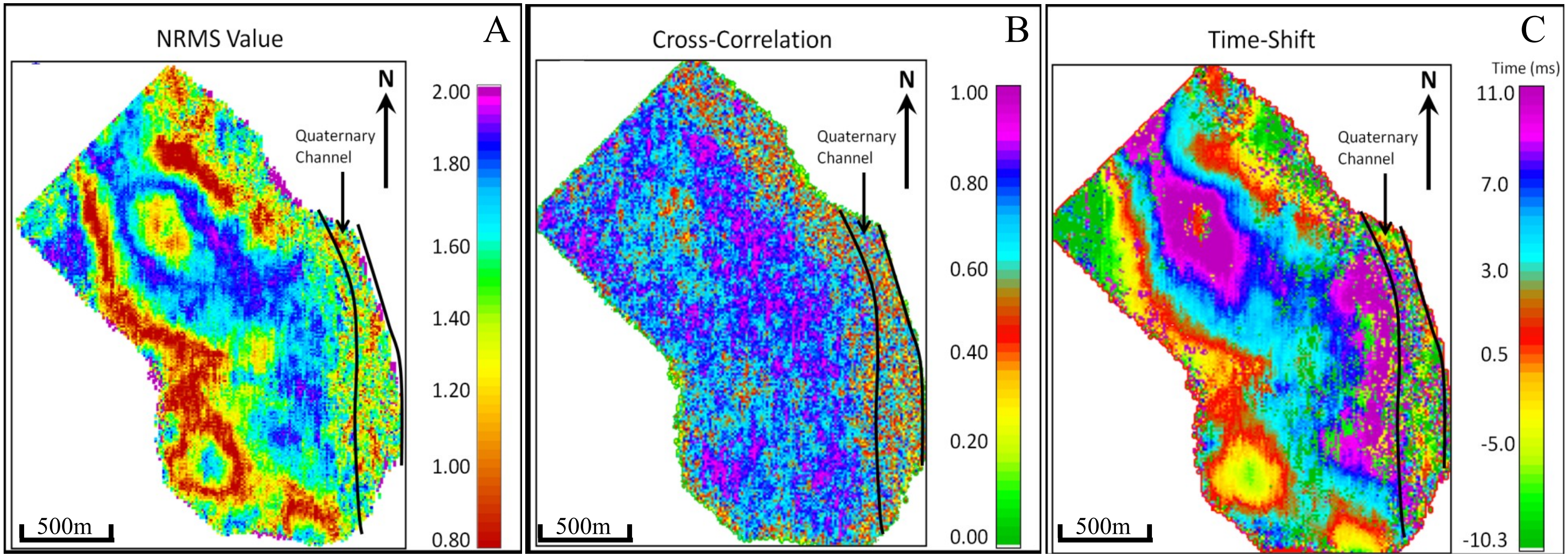

Figure 4-11 (a) NRMS value (b) crosscorrelation and (c) time-shift maps of the cap rock interval after the phase and time correction. In comparison to before (Figure 4-3), there is an overall decrease in NRMS value, while the central region remains relatively high. Cross correlation values have increased overall, however, the central region displays low values, reflecting the low repeatability of the cap rock interval on the monitor data. Time-shift values reflect this low repeatability, where regions corresponding to the low correlation values have anomalously high time-shift values.

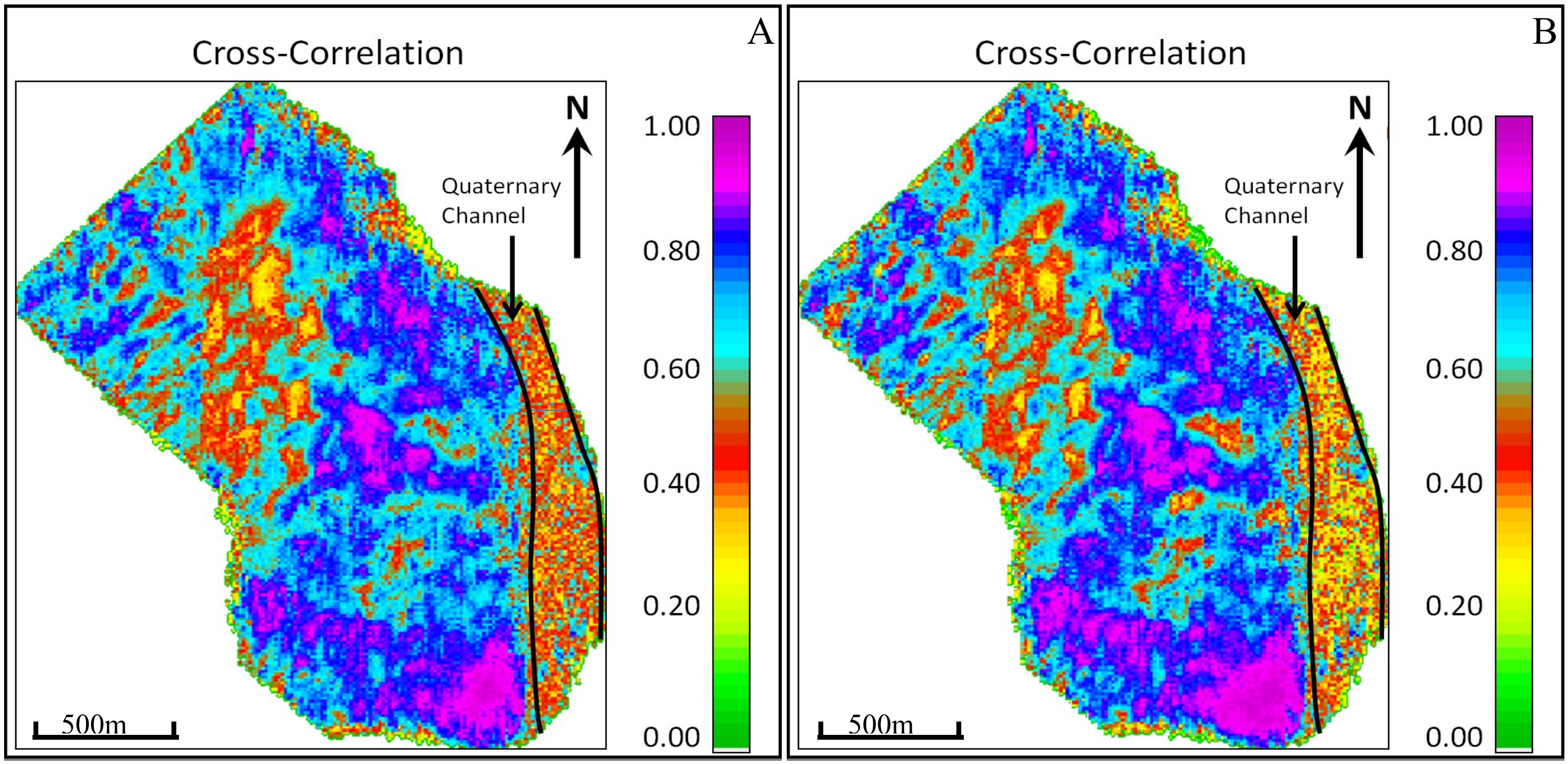

Figure 4-12 A comparison of the crosscorrelation values within the McMurray Formation reservoir interval (a) before and (b) after the phase and time correction. Two areas of low correlation can be observed, which are more defined after the phase and time correction. These values corresponded to known injection locations, and thus are interpreted to be due to steam injection into the McMurray Formation reservoir.

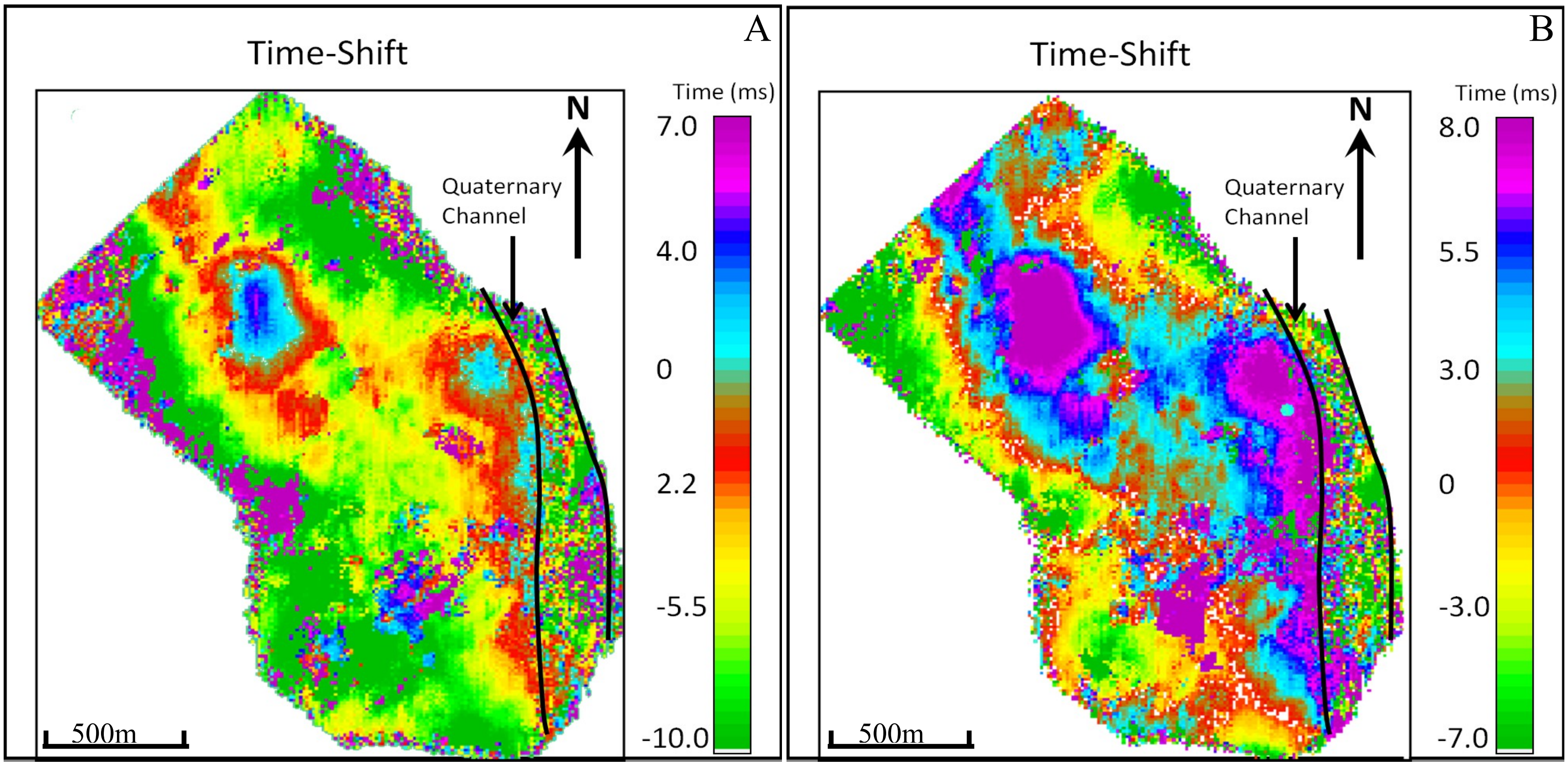

Figure 4-13 Time-shift map of the McMurray Formation reservoir interval (a) before and (b) after the phase and time correction. Regions exhibiting large time-shift values after the phase and time correction correlate with reservoir steam injection, as identified through the observation of lower crosscorrelation values (Figure 4-12).

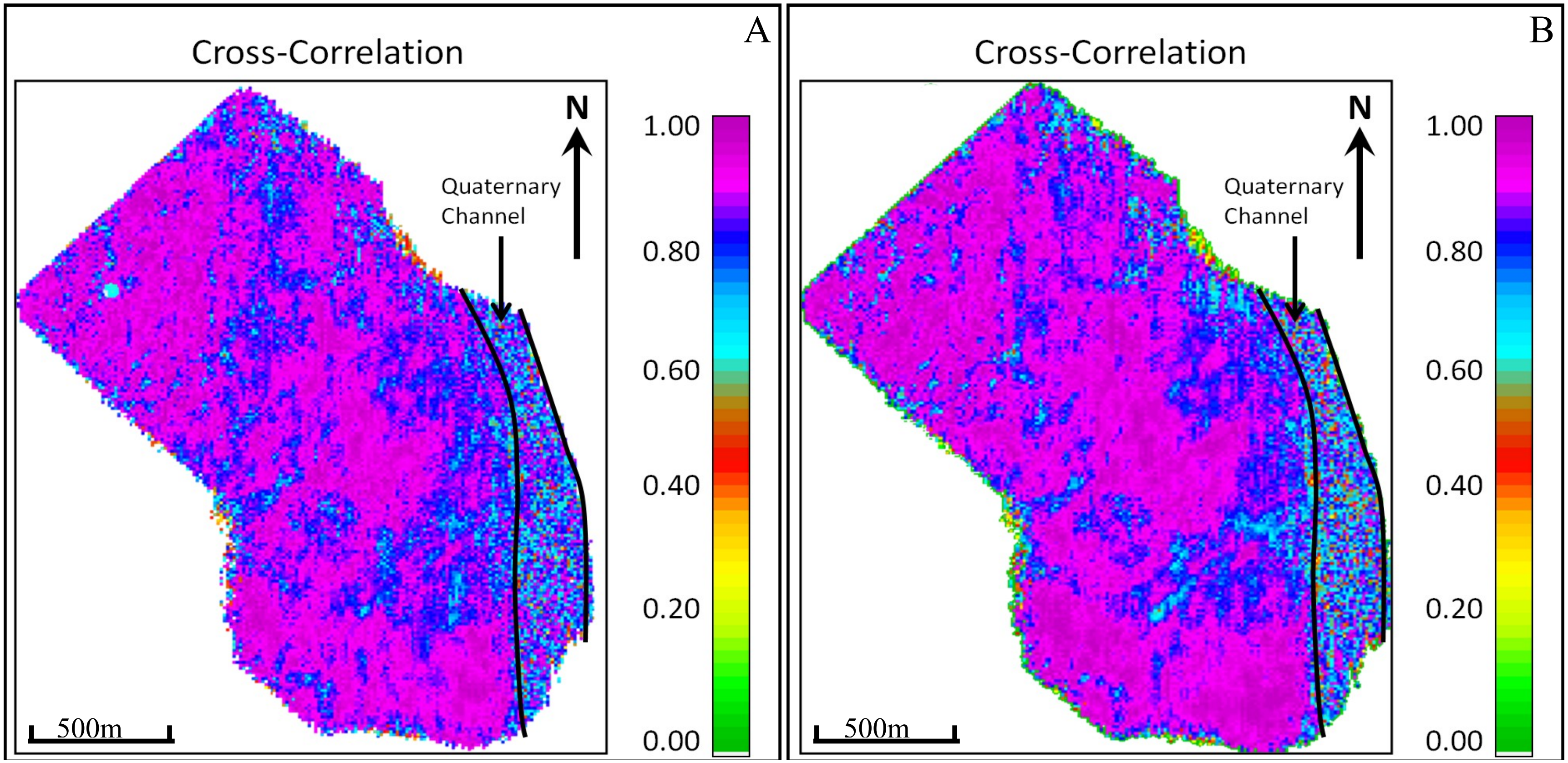

Figure 4-14 A comparison of crosscorrelation values for the Devonian interval (a) before and (b) after the phase and time correction. Overall, crosscorrelation values increase after the phase and time correction, while corresponding time-shift values (Figure 4-15) are significantly different from before and after the phase and time correction.

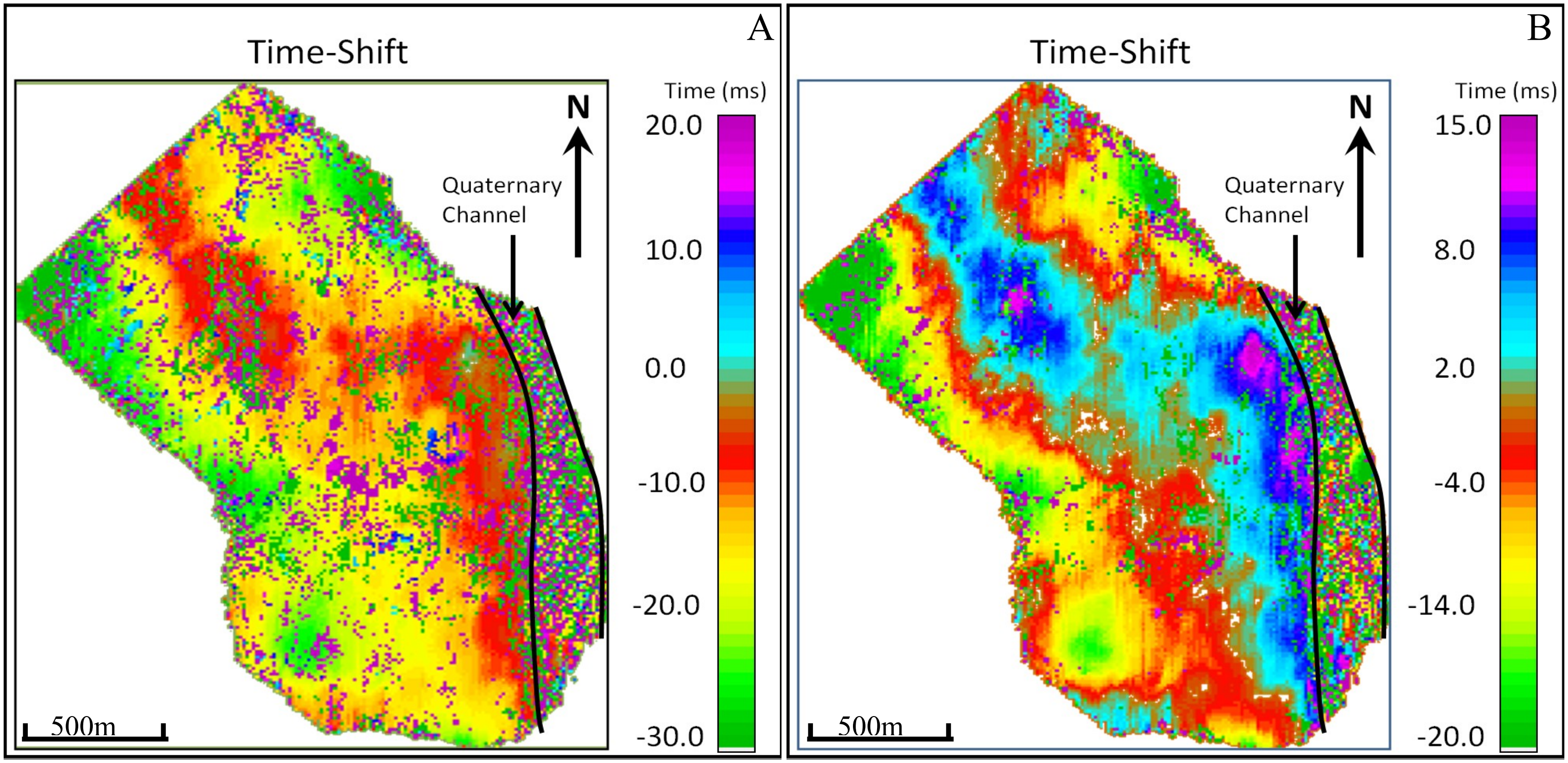

Figure 4-15 A comparison of time-shift values for the Devonian interval (a) before and (b) after the phase and time correction. The phase and time applied a global time correction of +7.28ms, moving the Devonian reflection of the monitor data upward in time to better align with the Devonian reflection of the baseline data. Time-shift values displayed on (b) reflect the static corrections required to compensate for the time-delays created by the low velocity heated bitumen sands overlying the Devonian reflection on the monitor data. Areas of ~0ms (light red-brown) are regions in which the Devonian reflection of the monitor already aligns with the Devonian reflection of the baseline in time due to the global time shift.

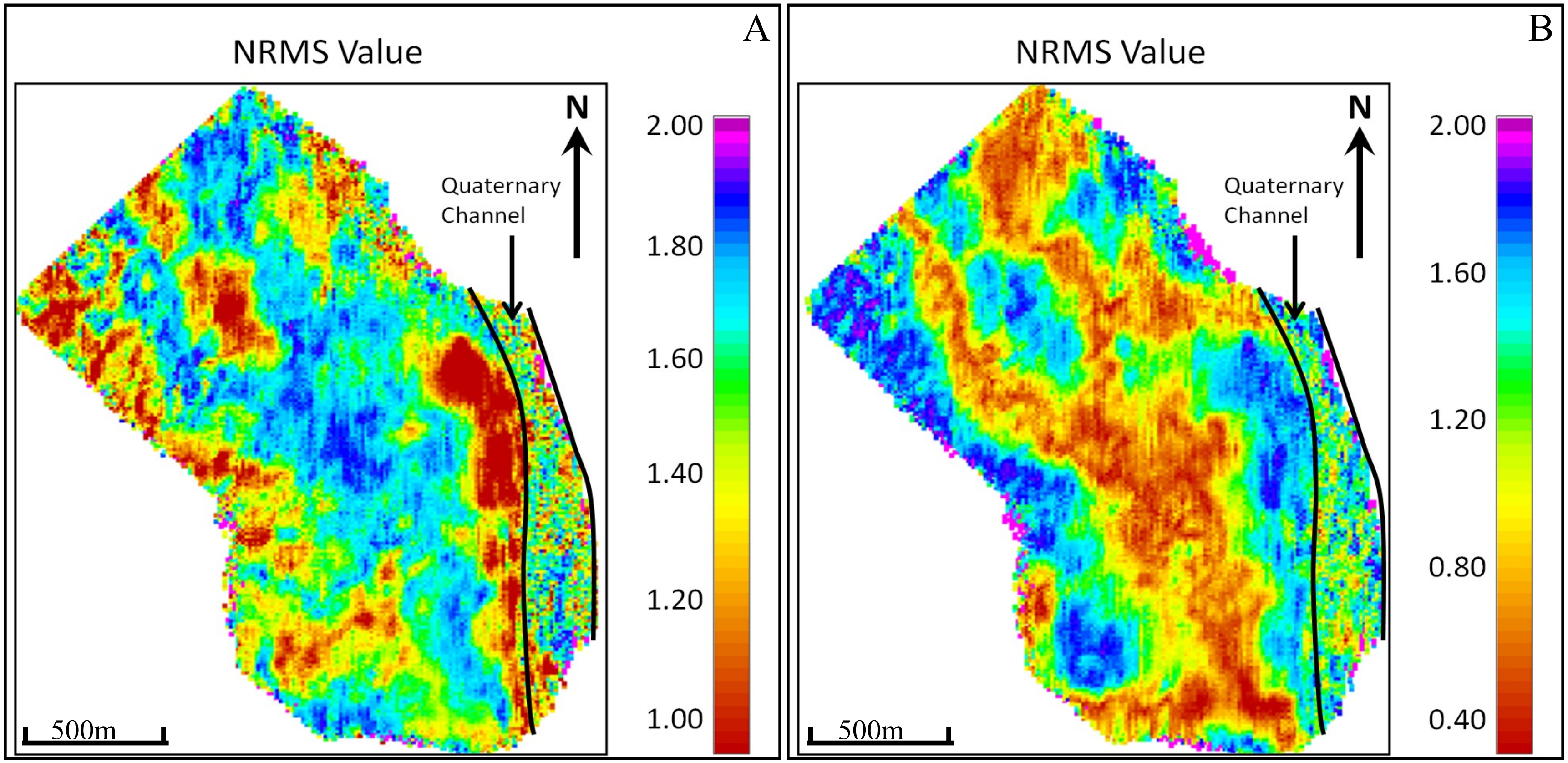

Figure 4-16 A comparison of NMRS maps of the Devonian interval (a) before and (b) after the phase and time correction, displaying a large overall decrease in NRMS values, primarily within the central region.

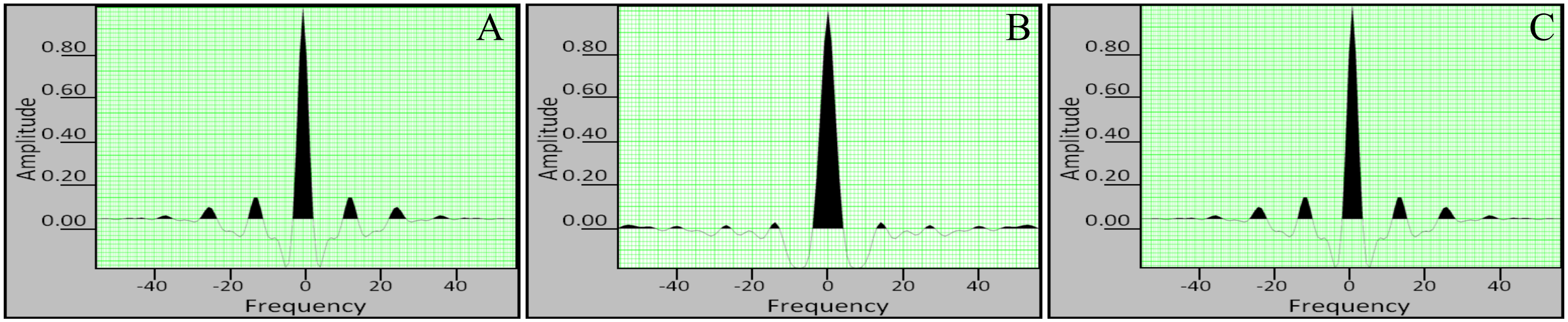

Figure 4-17 (a) The baseline wavelet, which was used as a reference for the shaping filter (b) monitor wavelet and (c) calibrated monitor wavelet. The wavelet is zero phase because a phase correction was previously applied (Section 4.5.1).

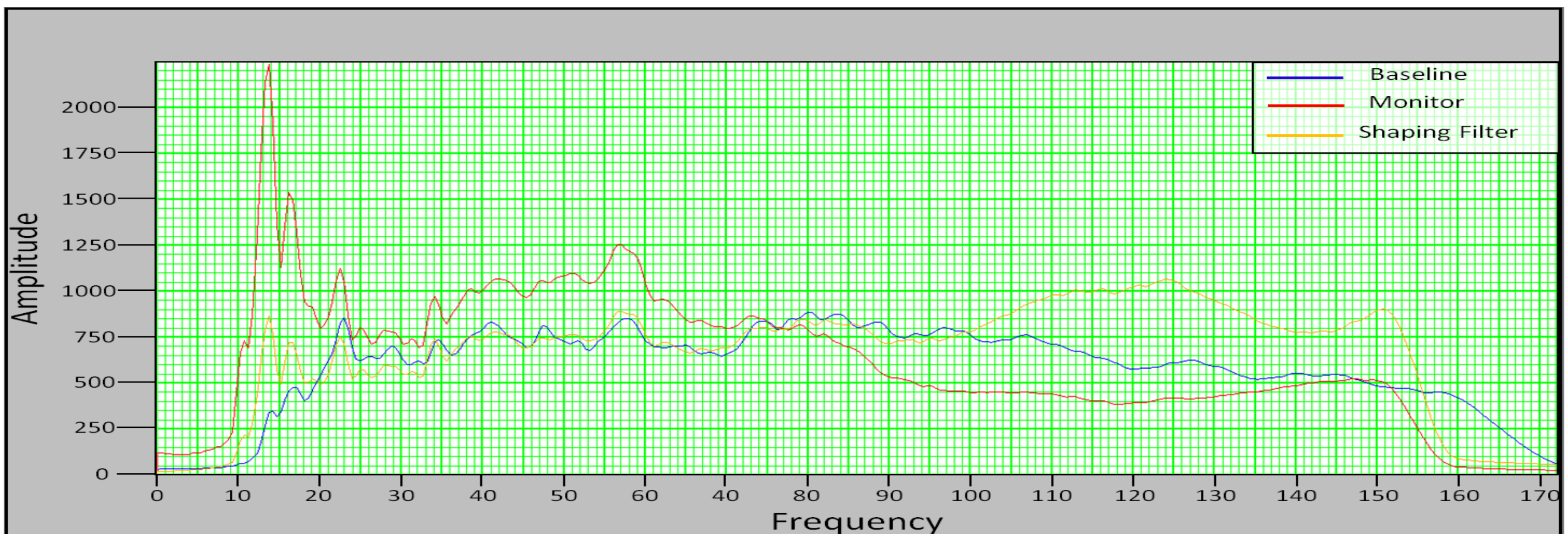

Figure 4-18 Amplitude spectrum for the baseline (blue), monitor (red) and calibrated monitor after shaping filter (orange). The monitor data after the shaping filter shows a significant increase of the high frequency amplitudes (80-150 Hz) and a reduction of the low frequency amplitudes (10-70 Hz).

4.5.3 Static Corrections

Despite the best efforts to process both surveys in an identical fashion, dissimilar static solutions were applied to the baseline and monitor survey. Although a global time shift has been applied to the monitor data to align reflections in time with those of the baseline data, small differences in the static solution still existed between surveys after the phase and time correction. Disparities in survey acquisition such as seasonal variations or altered ground conditions can lead to small changes in the static solution. To compensate for a different static solution between surveys, the baseline and monitor datasets were crosscorrelated to determine trace-by-trace static adjustments required to align reflections in time with respect to the baseline survey. Corresponding time-shift values for each trace are displayed in Figure 4-15b.

The crosscorrelation static analysis was run over a 35ms window, beginning 15ms above the Devonian horizon zero-crossing. Maximum allowable time shifts were set to 18ms to prevent cycle skipping. Figure 4-19 is an inline Section through the monitor survey after static correction. The time profile of the Devonian reflection is significantly altered, matching that of the baseline Devonian. Prior to static corrections, the Devonian of the monitor survey was subject to velocity pushdowns. Through trace-by-trace static corrections, I matched the time structure of the monitor Devonian reflection to that of the baseline, effectively pushing these velocity anomalies upward into the reservoir and overlying strata. This upward propagation is best observed through an analysis of the crosscorrelation maps through the cap rock interval (Clearwater C reflection to 50 ms above the Clearwater B reflection) (Figure 4-20a). Low correlation values represent the velocity anomalies that were pushed up in time into the cap rock event and overlying reflections through the static correction.

An analysis of the crosscorrelation map within the McMurray reservoir interval exemplifies the effectiveness of the static correction (Figure 4-21). In comparison with the crosscorrelation map produced prior to the static correction (Figure 4-12), I have improved the definition of the low correlation values and have increased the correlation in areas where steam has not been injected. This allowed us to delineate the spatial location of the heat within the reservoir, as well to identify sections that have not been influenced by heat. The corresponding time-shift values display an average shift of -1.0 to +1.0 ms, with higher values of 1.5 to 2.5 ms in regions of observed heat.

The crosscorrelation map of the Devonian reflection displays high overall correlation values of 90 to 100 percent, signifying the very close matching of the baseline and monitor Devonian reflections. However, these high values are not significantly increased over those from before the static correction, where previous correlation values were also in the 90 to 100 percent range (Figure 4-14). The effectiveness of the static correction is instead observed on the time-shift map (Figure 4-22b), where average time-shift value approach 0 ms. In comparison to before the static correction (Figure 4-15), time-shift values are significantly decreased, displaying the effectiveness of the static correction in matching the time structure of the monitor Devonian reflection to that of the baseline reflection.

Figure 4-23 is a comparison of NRMS values before the calibration procedure and after the static correction for the Devonian interval. Overall, NRMS values have decreased from 140 percent to 20 percent. In regions where NRMS values were the highest before calibration (180 to 190 percent), the reduction is on the order of 150 percent. This large overall improvement in NRMS values signifies the effectiveness of the calibration procedure. The monitor Devonian matched that of the baseline reflection in terms of statics, phase and time structure. The only remaining discrepancy between the two surveys is in terms of amplitudes, which will be equalized via a cross-normalization scalar as discussed in Section 4.5.4.

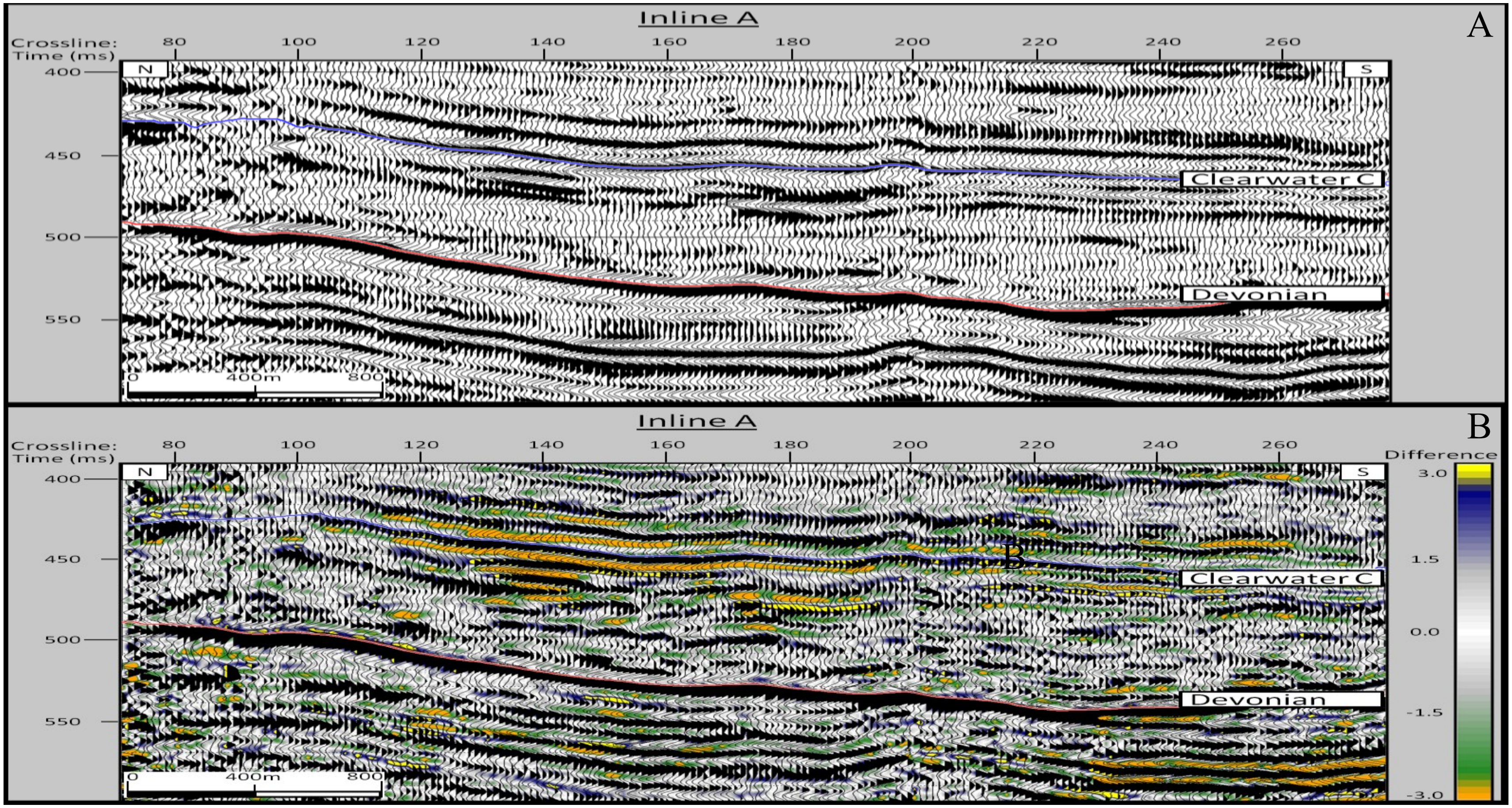

Figure 4-19 (a) Inline A through the baseline survey. (b) Inline A through the monitor survey after static corrections. The Devonian event of the monitor data now matches the Devonian event of the baseline due to the static corrections. Also, the caprock and overlying strata are largely similar, expect for the time-delay difference that have been propagated upward through the calculation process. The color overlay is the amplitude difference between the baseline and monitor survey, calculated by subtracting the baseline data from the monitor data. Notice the reduction in amplitude differences due to the correction (in comparison to Figure 4-10b).

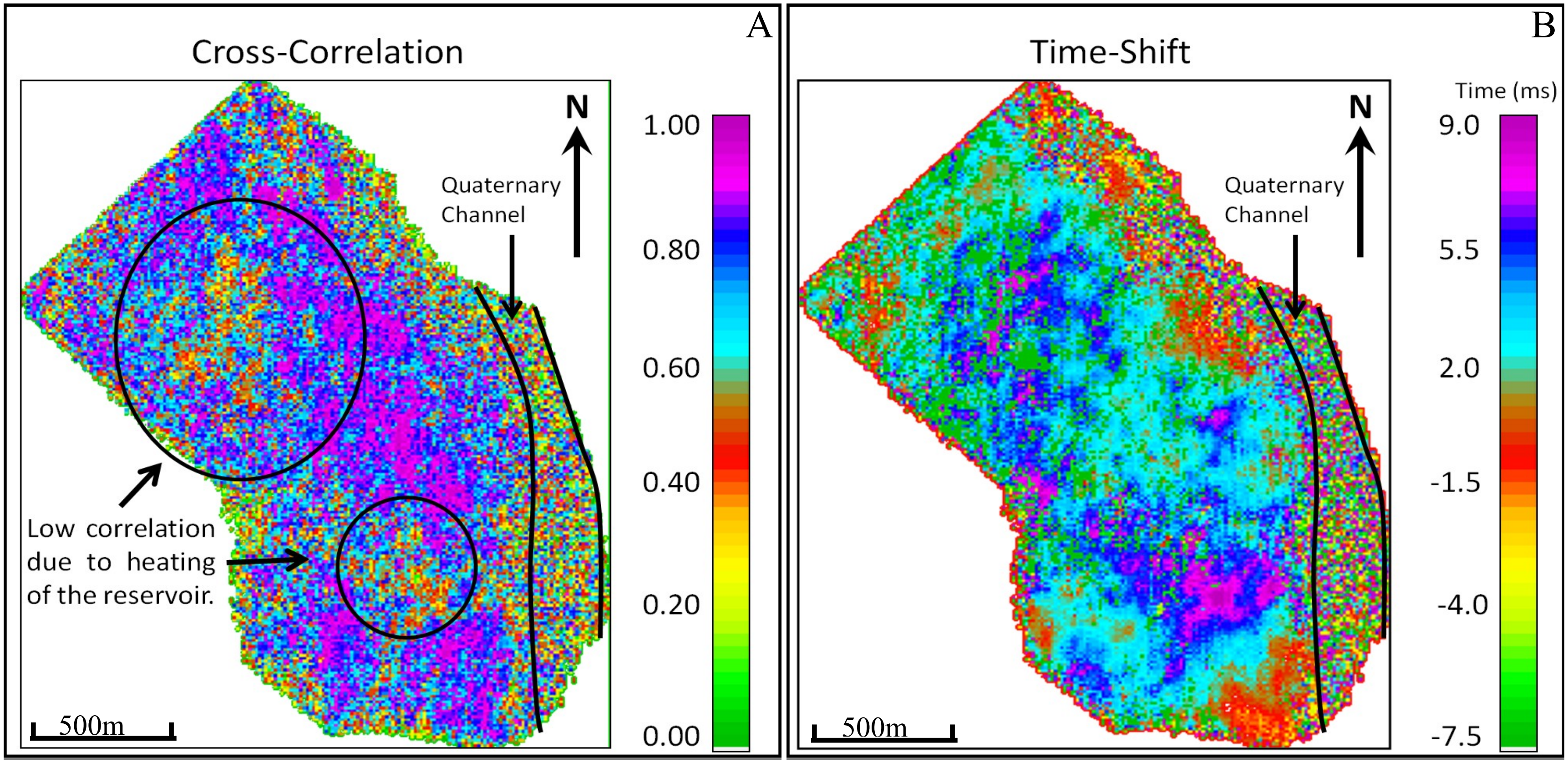

Figure 4-20 (a) Crosscorrelation map for the caprock interval, showing two areas of low crosscorrelation corresponding to the upward propagated reservoir anomalies through the static correction. (b) Corresponding time-shift values, displaying an overall low value of 0 – 2 ms. Two regions of high time-shift values are observed (7 – 9 ms), which correspond to low crosscorrelation values in (a). The combination of low correlation and high time-shift values is consistent with observations made within the McMurray Formation reservoir for steam induced anomalies (Figure 4-21).

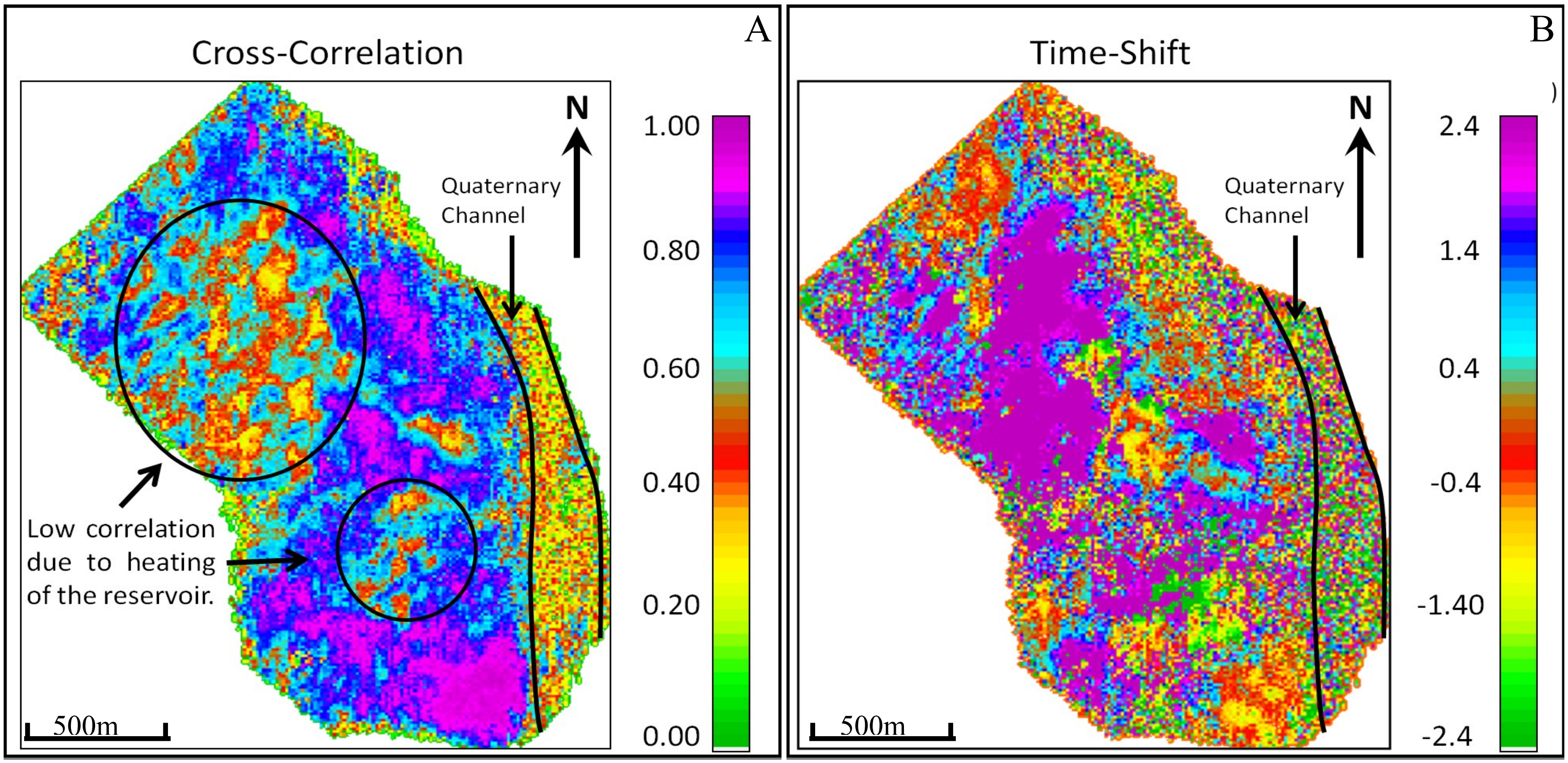

Figure 4-21 (a) Crosscorrelation map for the McMurray Formation reservoir interval after static correction displaying a low correlation value of 40-50 percent in areas of known steam injection and a high value of 80-100 percent areas not expected to have steam. The spatial definition of the low and high correlation values have improved in comparison to those after the phase and time correction (Figure 4-12b). (b) Corresponding time-shift values for the McMurray Formation interval. High time-shift values of +2.0 to 2.4 ms coincide with low crosscorrelation values representing steam injection. Average time-shift values range from -1.0 to +1.0ms (excluding time-shifts for the steam zones).

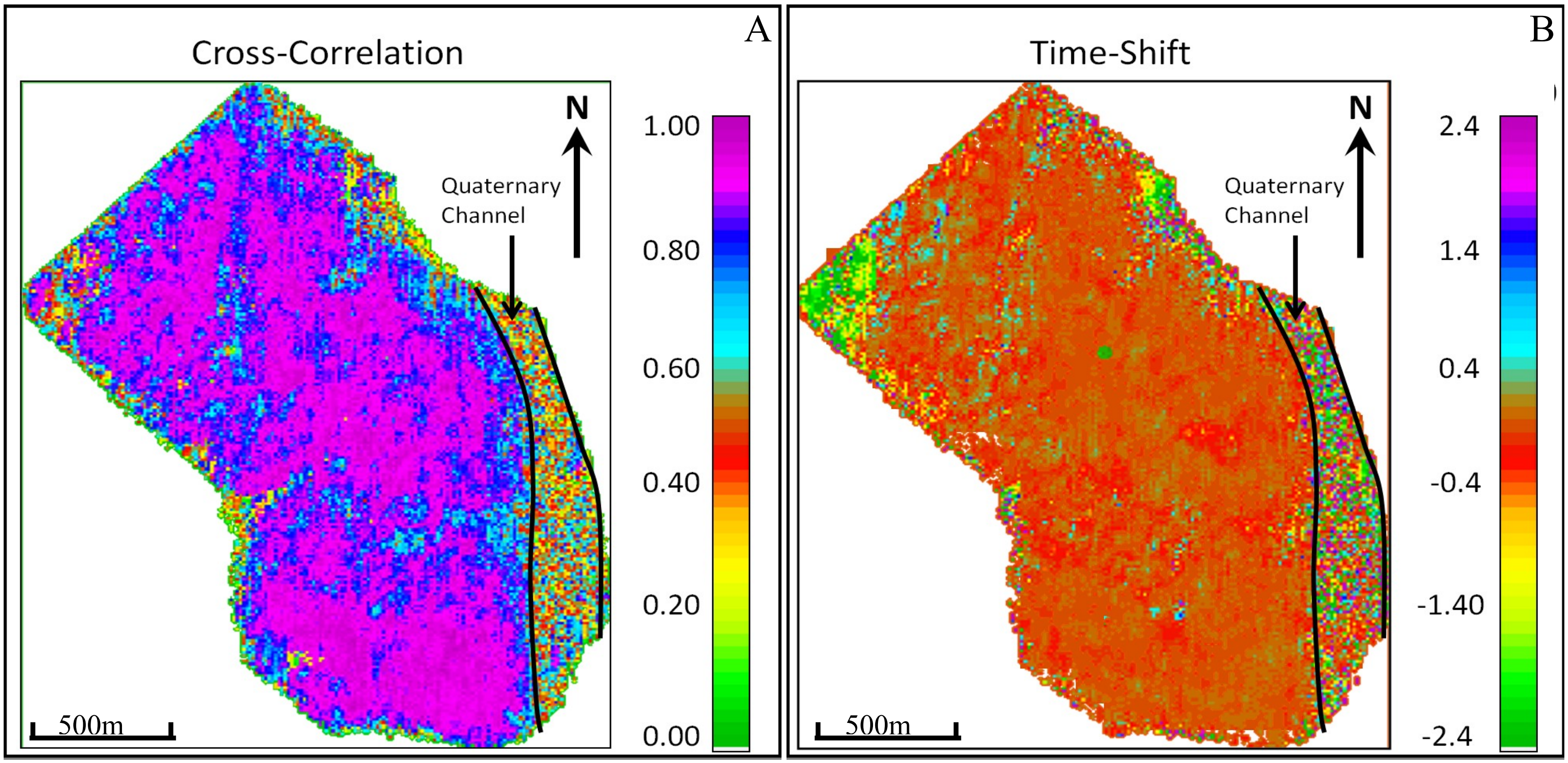

Figure 4-22 (a) Crosscorrelation map for the Devonian interval after the static corrections showing a high overall correlation between the baseline and calibrated monitor data between 90 - 100%. In comparison to before the static correction (Figure 4-14), values are not significantly increased. However, the time-shift map (b) for the Devonian interval displays a time-shift values of 0 ms for the corresponding crosscorrelation values of 90 to 100 percent, a significant increase over the time-shift values before the static correction (Figure 4-15). This signifies the effectiveness of the static correction in matching the time structure of the Devonian reflection.

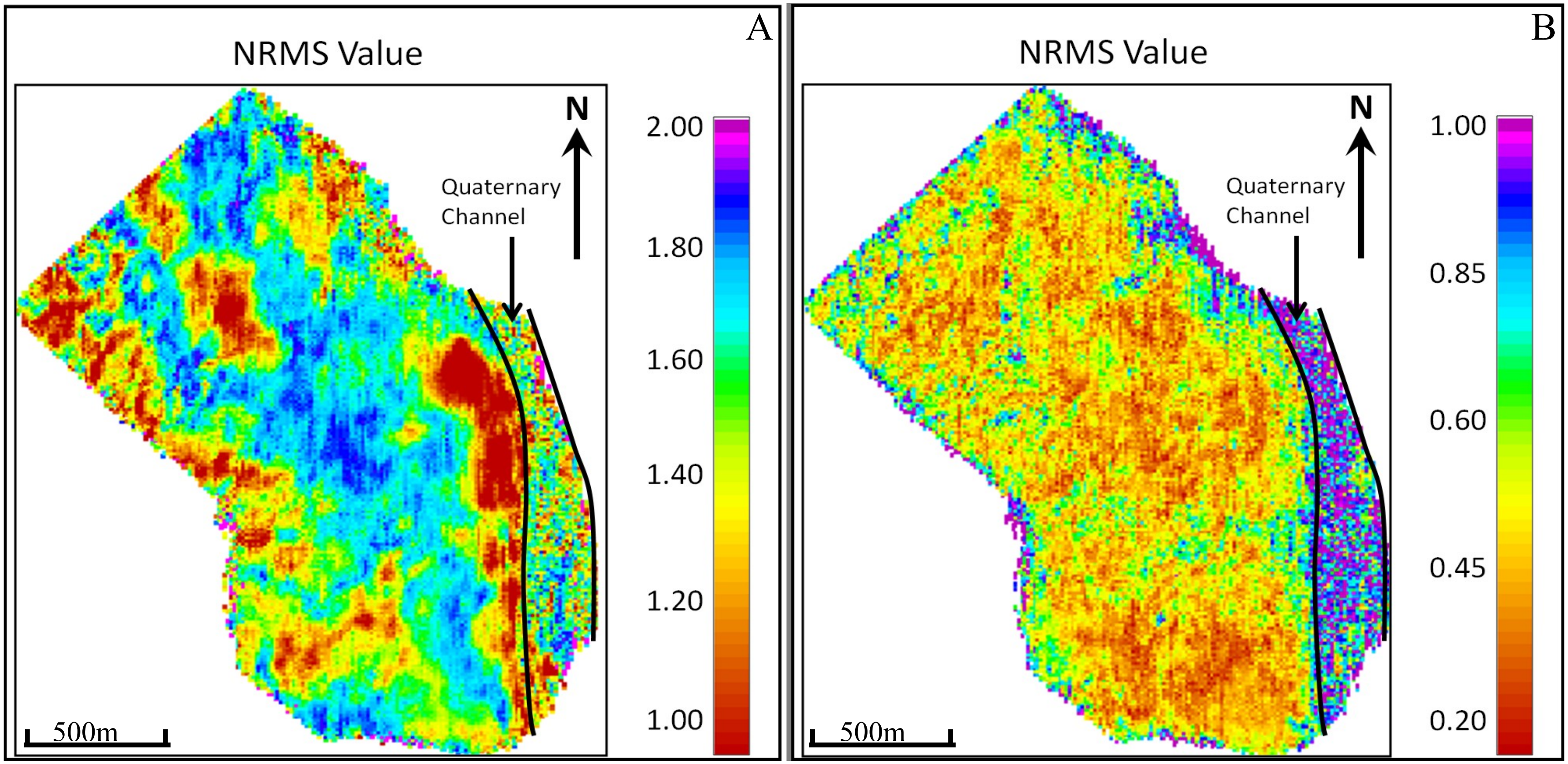

Figure 4-23 A comparison of (a) NRMS values across the Devonian event before calibration and (b) NRMS values across the Devonian event after the static corrections. The final NRMS values are consistent across the entire survey area (except for the Quaternary channel region) and display values as low as 18 – 20 percent, with an average NMRS value of 30percent. In comparison, average NRMS values prior to calibration were 140.

4.5.4 Amplitude Matching

Amplitude differences are present between the baseline and monitor survey due to scaling differences, influenced by a combination of factors including differences in survey acquisition, data processing, and variations in near surface conditions. Amplitude differences may be characteristic of steam injection within the reservoir (an increase in amplitude or the observation of an amplitude anomaly within a difference volume) as well as a source of error when producing a difference volume (subtraction of two events with differing amplitudes will result in an amplitude anomaly on a difference Section). To more accurately identify differences that are due to production and not related to other factors, the RMS amplitude of the two surveys were matched via an amplitude scalar, identified through cross normalization of the monitor data to the baseline data to statistically balance the amplitudes. The amplitude scalar is defined by calculating the RMS amplitude values of the baseline and monitor data within a defined analysis window (see equation 4-2, Section 4.2.1). The ratio of the RMS values within the window defines the scalar to be applied to the monitor data.

The cross normalization was calculated over a 20 ms window, beginning 2 ms above the Devonian reflection zero crossing. Scaling factors ranged from 0.10 to 4.7 RMS, where the overall amplitude of the baseline survey was greater than that of the monitor for all frequencies. All RMS amplitudes in the monitor survey were changed to match those of the baseline survey on a trace-by-trace basis.

Figure 4-24 is the amplitude spectrum of the McMurray Formation interval showing the RMS amplitudes of the baseline, non-calibrated monitor, and calibrated monitor data. There is an amplitude discrepancy between the baseline and non-calibrated monitor survey at all frequencies. This discrepancy is reduced after the application of the RMS scaling factor, where the amplitudes of the low (10-40 Hz) and high (80-160 Hz) frequencies within the monitor data now match those of the baseline. However, frequencies in the range of 40-70 Hz exhibit a higher RMS amplitude value on the calibrated monitor survey than on the baseline. The elevated amplitudes of the midrange frequencies may be related to the injection of steam into the reservoir. The steam is observable as a high amplitude reflection on the monitor survey that does not exist on the baseline survey, with a dominant period of 0.014 seconds (frequency of 70 Hz) (Figure 4-25). As discussed in Chapter 1, Section 1.3.1, the injection of steam into a unconsolidated bitumen reservoir will result in a velocity decrease and an amplitude increase from changes in the acoustic impedance. Through amplitude normalization, the RMS amplitudes were scaled to higher levels, effectively enhancing the high amplitude anomalies within the reservoir.

After normalizing the amplitudes of the calibrated monitor data, event horizons were picked for the Clearwater B and Clearwater C reflections. Horizons were picked on the event zero crossing, and now represent the reflections after calibration of the monitor data. The Devonian horizon was not repicked; its time structure already matched that of the baseline data after the calibration of the monitor data.

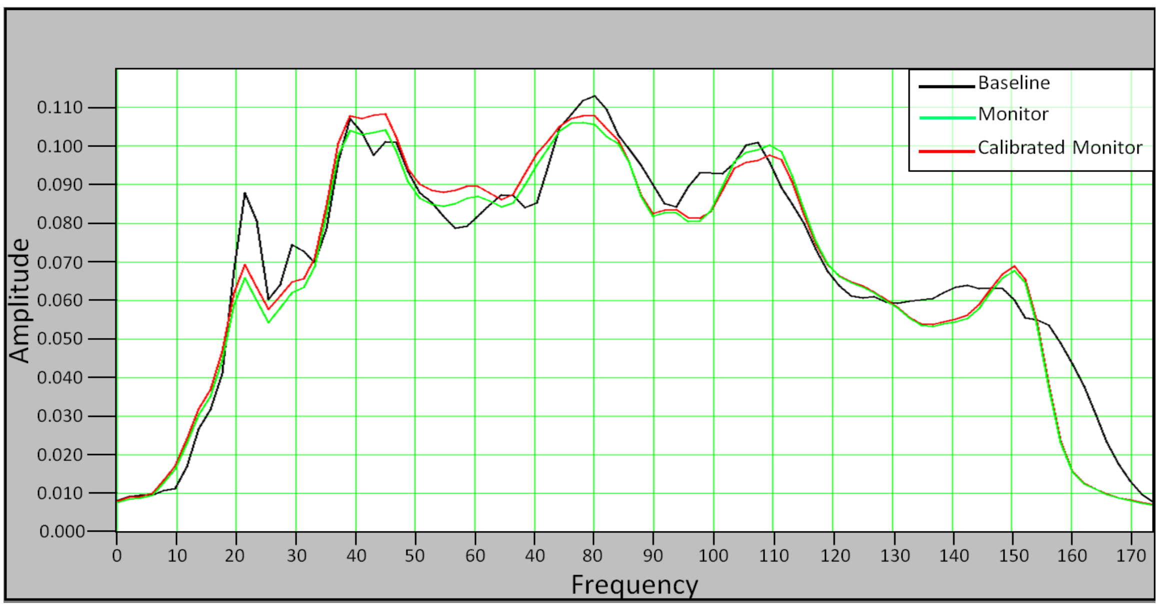

Figure 4-24 Amplitude spectrum displaying the RMS amplitudes of the Baseline (black), Monitor (green) and Calibrated monitor (red).

4.5.5 Difference Volume

After the calibration procedure, a difference volume was created, where the baseline survey data were subtracted from the monitor survey data. This difference volume removed all repeatable traces, leaving only the difference between the two surveys. The Devonian reflection is almost completely removed from the difference Section due to the matching of the Devonian event between surveys in the calibration procedure. All reflection differences overlying the Devonian event will remain, as well as any amplitude anomalies that are due to the injection of steam within the McMurray reservoir. The difference volume was flattened along the Clearwater C event to aid in interpretation. The two volumes will be referred to as (1) the difference volume and (2) the flattened difference volume throughout the remainder of this chapter.

Figure 4-26 is an inline Section through the flattened difference volume. From 470-500 ms, between crosslines 160 to 200, a large amplitude anomaly was observed, possibly representing a steam chamber. Taking a time slice though the flattened difference volume at 485 ms, and overlaying the horizontal well pairs, it was observed that the amplitude anomaly corresponds with the injection wells of pads B and C (Figure 4-27). Thus, this amplitude anomaly was interpreted to be related to steam injection. A second anomaly is observed between crosslines 120 – 140 at a time of 460 ms. Again, the time-slice displays the correlation of the anomaly with the horizontal well pairs, supporting the interpretation that the anomalies are due to steam injection into the McMurray Formation reservoir.

Observed amplitude anomalies within the difference volume appear to be located within the upper McMurray Formation, but are observed at later times on the monitor data prior to calibration. Following the global and trace-by-trace time shifts applied during calibration, the amplitude anomalies have been propagated to earlier times, and hence will be observed in the upper McMurray Formation on the difference volumes despite their original positioning within the Lower McMurray Formation on the non-calibrated monitor data (see Section 4.4 and Section 4.5).

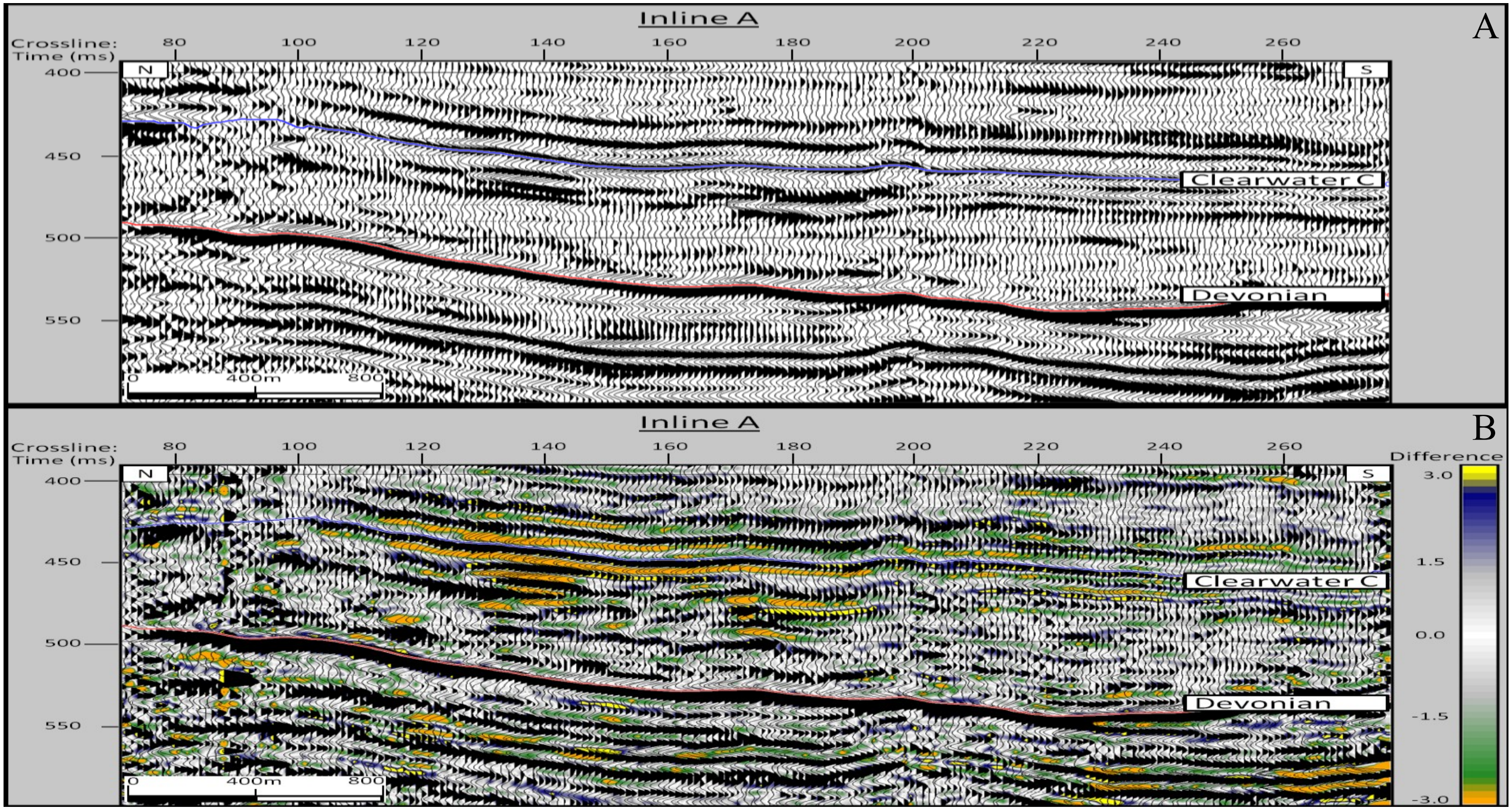

Figure 4-25 (a) Inline A through the baseline survey. (b) Inline A through the calibrated monitor survey, displaying high amplitude events within the McMurray reservoir that are not present on the baseline data. These amplitude anomalies represent steam injection into the McMurray reservoir. The color overlay is the amplitude difference between the baseline and monitor survey, calculated by subtracting the baseline data from the calibrated monitor data. Notice the reduction in amplitude differences due to the amplitude correction (in comparison to before Figure 4-19b

4.5.6 Data Calibration Discussion

NRMS, crosscorrelation and time-shift maps were used to understand the effectiveness of the calibration procedure, and for quality control purposes. Each step in the calibration process employed these tools before and after the application of a correction to ensure the accuracy and effectiveness of each process. Every correction increased crosscorrelation values and reduced time-shift and NRMS values calculated across the Devonian reflection.

Following calibration, crosscorrelation maps within the reservoir exhibited high values in areas without steam injection, and low values in areas where steam has created anomalies on the monitor survey. Corresponding time-shifts have been reduced to negligible values. Crosscorrelation values through the caprock interval displayed low values in regions where reservoir sourced anomalies were propagated to earlier times through the calibration procedure, and high values in areas free of reservoir induced anomalies.

The NRMS maps were significantly altered by the calibration procedure, where NRMS values were dependent upon the phase, static and amplitude difference between the two datasets (Sheriff, 2002; Kragh & Cristie, 2002). After these differences were corrected, NRMS maps exhibited low overall values across the Devonian interface of 20 percent (Figure 4-23b).

Calibrating the data using the Devonian reflection propagated the time-lapse anomalies to earlier times instead of later times, thus moving reservoir difference into the upper McMurray Formation, the Clearwater Formation and the overlying strata. Hence, reservoir anomalies were observed on difference volumes within the Upper McMurray Formation and overlying caprock and strata (Figure 4-26).

Due to the calibration procedure, time delays were removed from the Devonian reflection, shifted earlier in time through static corrections. Theses propagated time delays are observable in the cap rock region of the difference volume, where high amplitude, laterally continuous events are observed above the steam induced amplitude anomalies (Figure 4-26). These cap rock anomalies are created by subtracting the flat cap rock reflections of the baseline data from the reflection from the calibrated monitor survey that are no longer flat due to propagation of the time delays earlier in time. Hence, these anomalies represent heating of the reservoir, where elevated reservoir temperatures have reduced the velocity of P-waves traveling through the reservoir (Nur, 1982; Wang & Nur, 1988; Eastwood, et al., 1994). Reservoir temperature levels are elevated beyond the extent of the steam chambers, thus, time delays are observed to coincide with amplitude anomalies, but extend further than the lateral extent of the steam. Hence, anomalies in the cap rock region are more laterally continuous than the amplitude anomalies within the reservoir, and reflect heat distribution.

4.6 Time-lapse Interpretation

The time-lapse interpretation was focused on the identification of travel time shifts and amplitude anomalies within the reservoir, primarily observed within the difference volume. The observation of a significant time delay, coupled with an amplitude anomaly within the reservoir and the correlation to horizontal SAGD wells comprised the bulk of the P-wave time-lapse interpretation.

Other techniques were employed to further support the observation and interpretation of amplitude anomalies within the reservoir, including isochron analysis, amplitude anomaly distribution mapping, an instantaneous amplitude volume, and the integration of well log data.

4.6.1 Isochron Analysis

Isochron maps display time variations between two seismic events. Effectively, they can be thought of as time thickness maps, displaying the variation in traveltime between two events (Eastwood, et al., 1994; Isaac, 1996). Isochron maps are a quick, robust and effective technique for identifying areas of increasing or decreasing traveltime between a baseline and monitor survey. Because the reservoir thickness did not change over time, differences in isochron maps between the baseline and monitor data are representative of P-wave velocity decrease in the monitor data (Nakayama, et al., 2008).

Isochrons were built over the reservoir interval, bounded by the Devonian horizon and the Clearwater C horizon on both the baseline and calibrated monitor data. Figure 4-28 is a comparison of the baseline and monitor isochron maps. There is significant travel time thickening in areas of steam injection, due to the traveltime delay created by the lower velocity of heated bitumen. As discussed in Chapter 1, Section 1.3, the injection of steam into bitumen saturated reservoir reduces P-wave velocity up to 30 percent (Wang & Nur, 1988; Eastwood, 1993). A velocity reduction will create time thickening within the reservoir, represented as an increase in isochron thickness in a time-lapse sense. Taking the difference of two isochrons accentuates the time delays (Figure 4-29).

It is important to consider that the decrease in velocity signifies heating of the reservoir and not solely the presence of steam. The reservoir can be heated at a distance greater than that of the steam distribution. Thus, there are portions of the reservoir which do not contain steam but have elevated temperatures, creating a traveltime increase. Consequently, the isochron difference map is representative of the heat distribution and not of steam distribution.

4.6.2 Amplitude Anomalies

The flattened difference volume was analyzed for the presence of amplitude anomalies within the McMurray Formation reservoir. Figure 4-26 shows an inline though the center of the difference volume displaying two anomalies interpreted to be due to the injection of steam into the reservoir, with overlying anomalies in the cap rock due to heating induced time delays. Figure 4-30 is a chair cut display of the flattened difference volume, combined with an intersecting inline and crossline, displaying time delay anomalies within the cap rock interval, as well as steam amplitude anomalies within the McMurray Formation reservoir. As previously discussed, anomalies due to time delays were observed within the caprock interval, while anomalies due to steam injection were observed within the McMurray Formation reservoir.

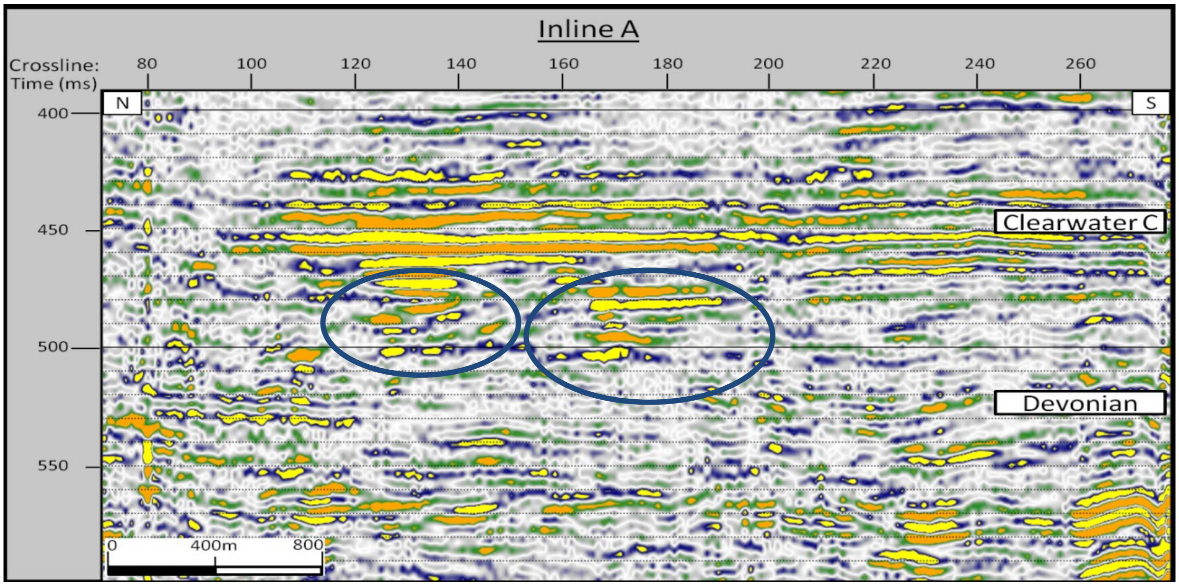

Figure 4-26 Inline A through the flattened difference volume. The two highlighted ellipses represent large amplitude anomalies within the McMurray reservoir due to steam injection. The laterally continuous anomalies overlying the steam anomalies are created from time delays due to heating, propagated upward into the cap rock reflections during the calibration procedure.

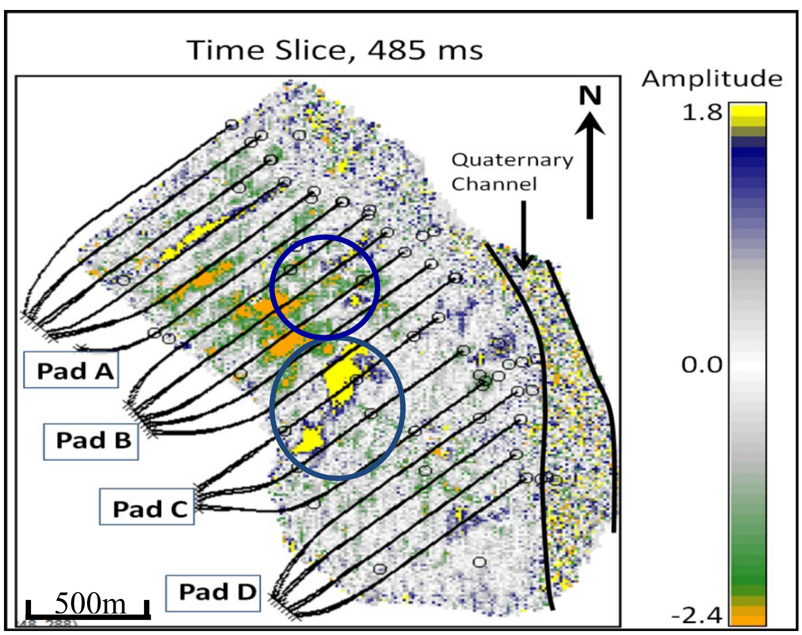

Figure 4-27 Time slice through the flattened difference volume at 485ms displaying amplitude anomalies and their correlation with horizontal well pairs. The circles represents the anomalies observed in Figure 4-26

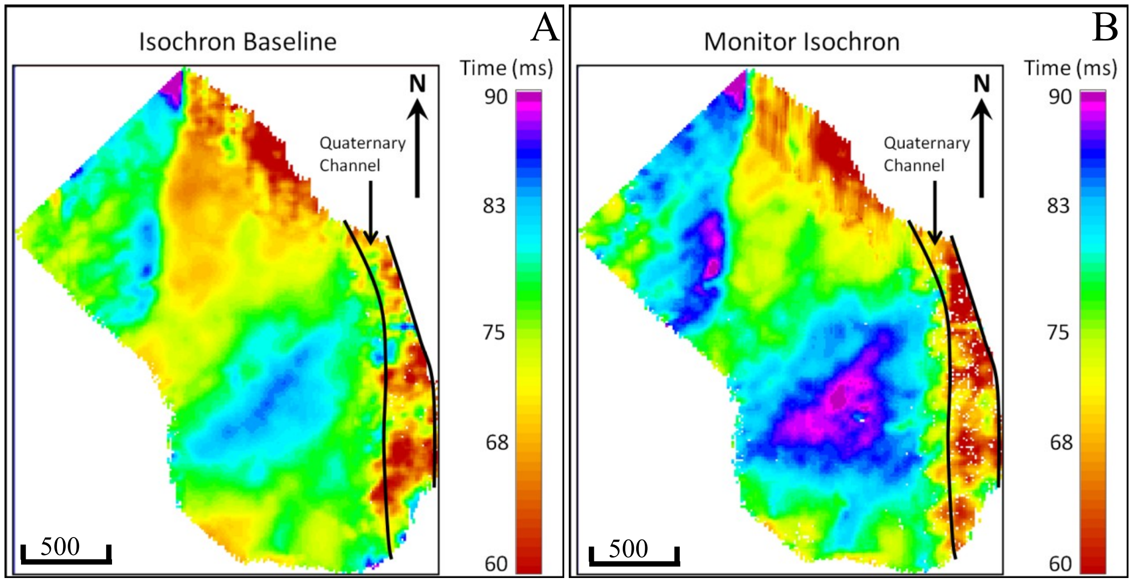

Figure 4-28 A comparison of (a) baseline isochron and (b) monitor isochron. Significant time delays are observable on the monitor isochron due to heating within the McMurray Formation reservoir.

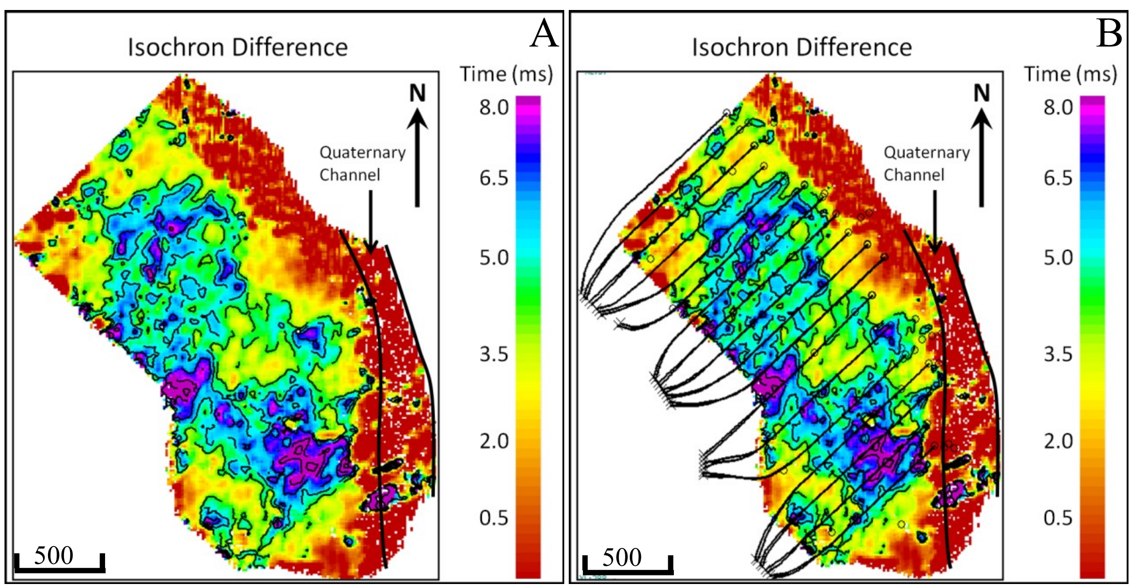

Figure 4-29 (a) Isochron difference map and (b) Difference map with horizontal wells overlain on time delays, highlighting their relationship. Contours highlight time delay difference between the baseline and monitor survey. Contours range from 4.0 ms to 8.0 ms in increments of 1.0 ms.

Reservoir amplitude anomalies were observed throughout the difference volume and largely correspond with locations of horizontal wells and also with isochron time delays (Figure 4-26 to Figure 4-29). This identification procedure was employed throughout the flattened difference volume, yielding multiple observations of amplitude anomalies within the McMurray reservoir.

To garnish our understanding of the distribution of amplitude anomalies throughout the entire reservoir, I adopted a technique developed by McGillivray (2005) for identifying the spatial distribution of heat within a reservoir. Using the flattened difference volume, the positive amplitudes were analyzed throughout the McMurray Formation reservoir. The reservoir interval was defined as the time interval 5ms lower than the flattened Clearwater C horizon to the Devonian horizon (Figure 4-31). The addition of 5 ms to the Clearwater C horizon ensured that the calculation of the amplitude anomalies did not include the anomalies present within the cap rock interval. Amplitude values were analyzed on a slice-by-slice basis, summed and displayed in map view, yielding the total distribution of the positive amplitude anomalies within the reservoir. This technique was also applied to the negative amplitude anomalies. Figure 4-31 is a map view of the positive and negative amplitude distributions. There are two large amplitude anomalies in the study area, one in the north corresponding to pads A and B and one in the south corresponding to pads C and D. Overlaying the well pairs onto the anomaly distribution maps highlights the correspondence of well placements with amplitude anomalies.

The anomalies on both the positive and negative distribution maps appear to follow the paths of the horizontal wells. From this, I interpret that the amplitude anomalies contained within the McMurray reservoir interval are likely a result of steam injection and thus are representing the reservoir heat and steam distribution in a spatial display.

The observed amplitude anomaly distributions coincide with areas of increased traveltime. Figure 4-32 is a comparison of the isochron difference map to the positive amplitude anomaly distribution map. A strong correlation between traveltime delays and amplitude anomalies were observed, thus supporting the interpretation that the increase in

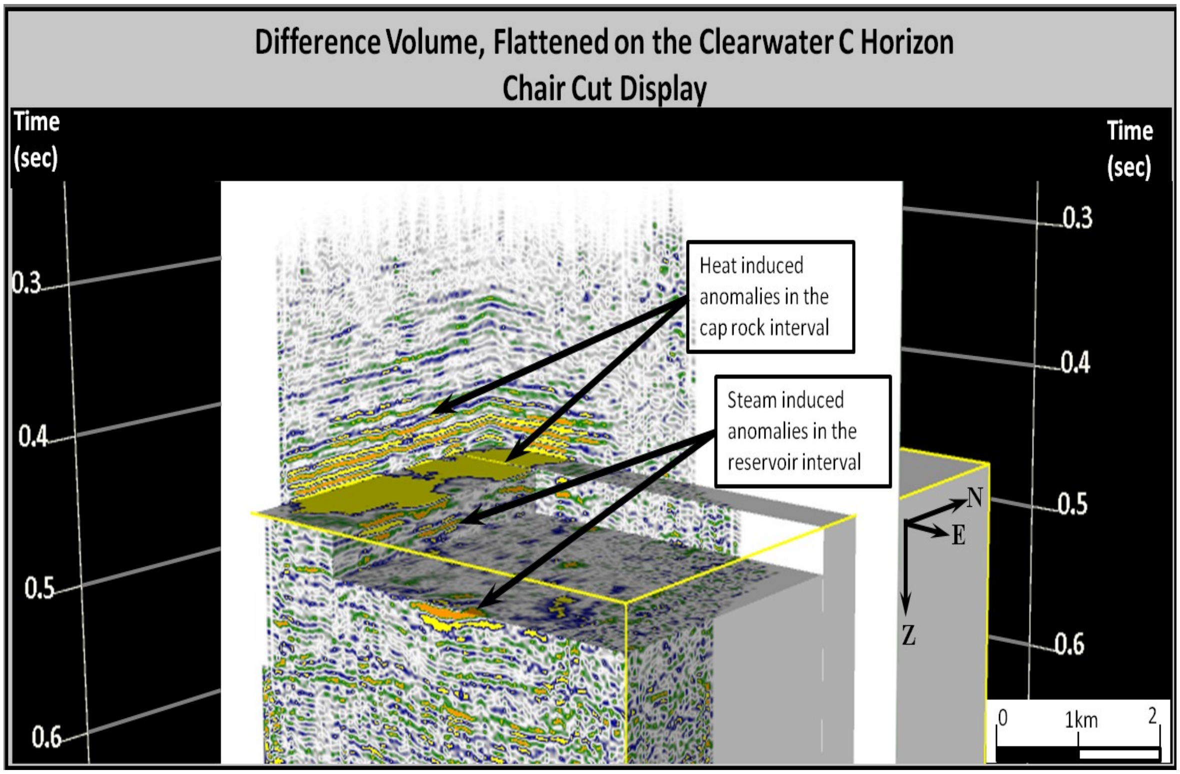

Figure 4-30 Chair-cut display of the flattened difference volume, combined with an intersecting inline and crossline. Amplitude difference anomalies are observed within the caprock interval, due to heating induced time delays, as well as within the reservoir due to steam.

traveltime within the McMurray Formation reservoir on the monitor survey is a result of reservoir heating, creating a time delay for waves propagating through the reservoir. However, the distribution of time-delays is greater than that of the amplitude anomalies. Reservoir temperatures levels are elevated beyond the extent of a steam chamber, creating time delays that are not associated with amplitude anomalies within the McMurray Formation reservoir (as discussed in Section 4.5.6). Thus, the isochron distribution map is representing the distribution of heat within the McMurray Formation reservoir, while the amplitude anomaly distribution map is representative of steam-induced anomalies (the amplitude anomaly distribution maps did not include the amplitude anomalies of the cap rock region that were created from the calibration procedure; Section 4.5.6).

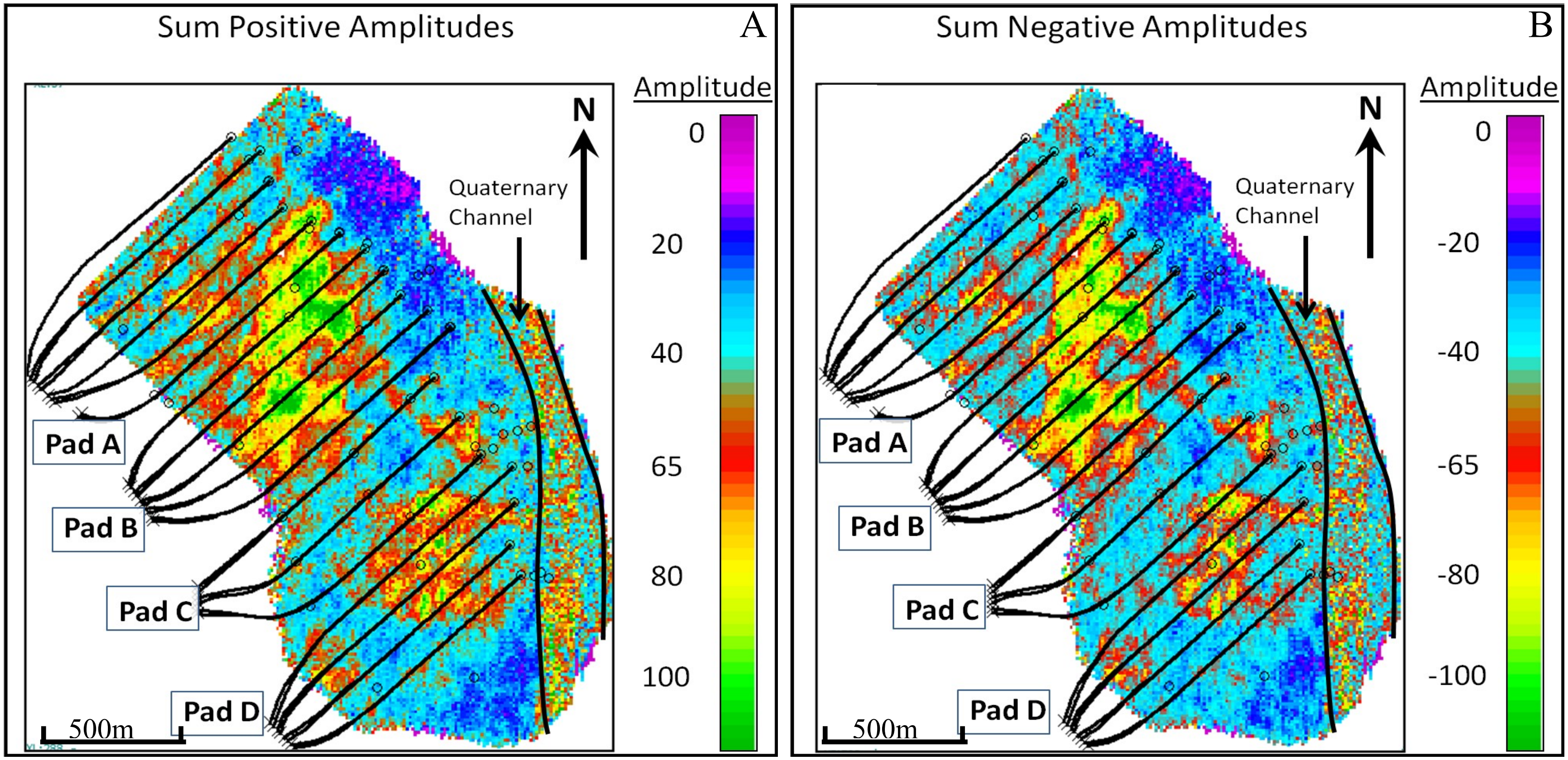

Figure 4-31 Amplitude anomaly distribution within the McMurray Formation reservoir for (a) Sum of positive amplitudes and (b) Sum of negative amplitudes. A northern and a southern anomaly are observed, representing heat distribution within the reservoir.

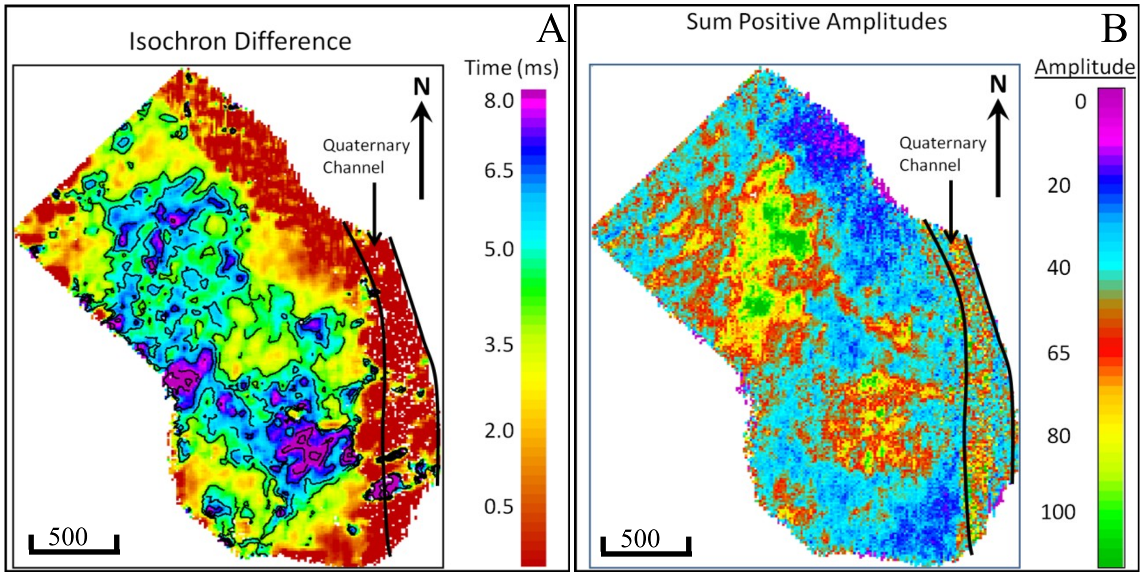

Figure 4-32 Comparison of (a) isochron difference map to (b) amplitude anomaly distribution map. Regions of high traveltime delay correlate with amplitude anomaly distributions. However, the time-delay distribution is larger than the amplitude anomaly distribution, suggesting the time-delay map is representative of heat distribution, while the amplitude anomaly map is representative of steam distribution.

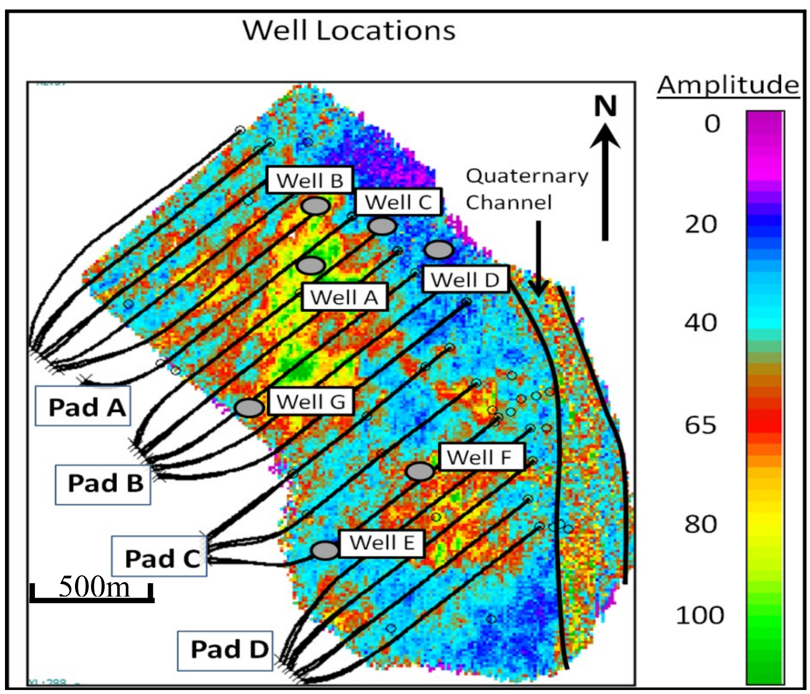

Figure 4-33 Amplitude anomaly map displaying the locations of wells A – G used in the well log cross Sections, Figure 4-34.

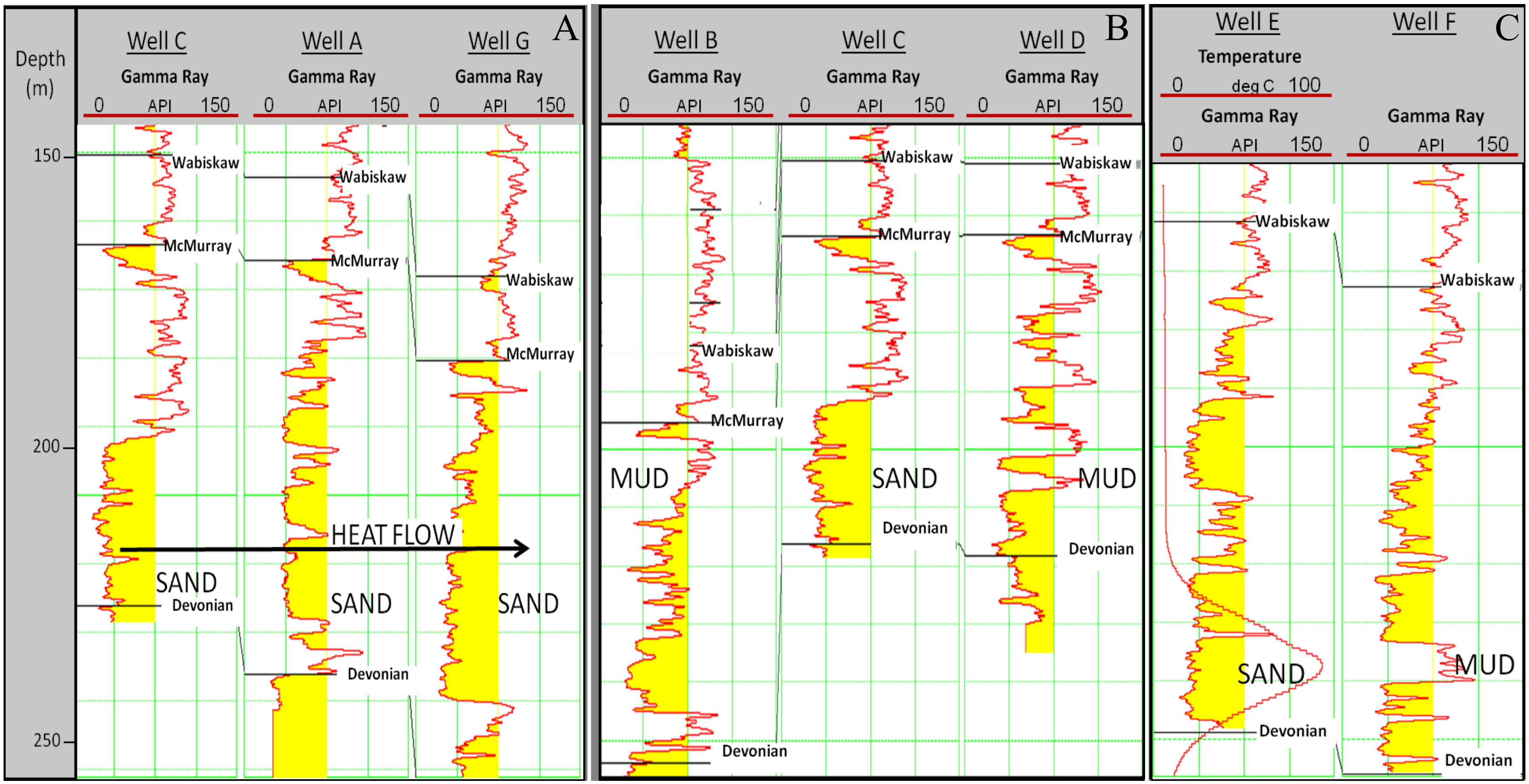

Figure 4-34 Well log cross Section constructed using Gamma Ray logs. (a) Cross Section through the northern anomaly displaying structurally equivalent channel sands, interpreted to be allowing heat flow between the horizontal wells of pads A and B (b) Cross Section through the northern anomaly displaying a large channel sand juxtaposing two muddy intervals to the east and west (c) Cross Section through the southern anomaly displaying a heated channel sand structurally equivalent to a thick mud. A temperature log is overlain on the gamma ray log, displaying elevated reservoir values within the McMurray Formation reservoir. Logs are recorded in depth as measured from the Kelly bushing, displaying the structural features of the McMurray Formation reservoir.

4.6.2.1 Northern Anomaly

A further point of interest is the asymmetry of the heat distribution. Although the amplitude anomalies tend to follow the horizontal well paths, the anomaly in the north also contains a northern trend, perpendicular to well orientation. The flow pathway of the heat appears to be between injection wells, connecting the well pairs of pad B to those of pad A. Pads A and B produced approximately 3.61 million barrels of oil from February 2008 to January 2011, the latter being the time of recording of the monitor survey.

Figure 4-34a is a well log cross Section running SW-NE along the northern amplitude anomaly. There is a very large succession of channel sands observed from on gamma ray logs, through which heat may flow from the wells of pad B and connect to the wells of pad A to the north.

The amplitude anomaly terminates along a NNE trend prior to the toe end of the wells, interpreted to indicate the inter Section of a muddy or silty unit and inefficient steam distribution. An E - W cross- Section along wells B, C and D displays a thick channel sand, bounded to the East and West by a large mud interval (Figure 4-33b).

The boundaries of the amplitude anomaly correlate with the channel boundaries observed within the semblance volume (Figure 4-7). Figure 4-35 displays the positive amplitude anomaly distribution map overlain onto the semblance time slice at 492 ms. The edges of the steam distribution show a strong correlation with the channel boundaries. This correlation is interpreted to representative of steam within a large sand-filled channel, which is bound to the east, west and northwest by muddy IHS bedding, restricting steam growth outside of the sand-filled channel. The semblance is displaying the edges of the sand filled channel.

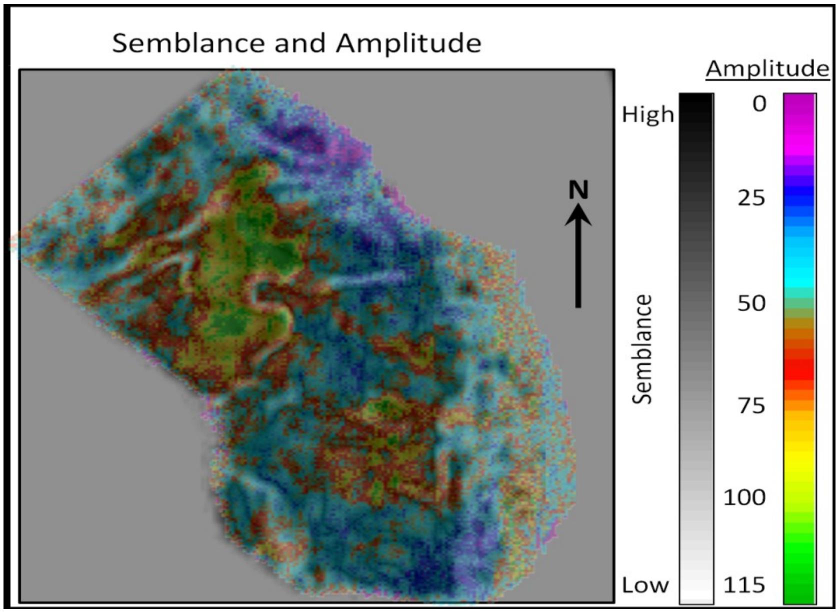

Figure 4-35 Sum of positive amplitudes (transparency 70%) overlain on semblance time slice at 492ms, displaying the correlation of northern amplitude anomalies with channel edges. Low semblance values are interpreted to be channel edges (Figure 4-7a).

4.6.2.2 Southern Anomaly

The southern anomaly is interpreted to show a more symmetrical heat distribution, flowing between the wells in pads C and D. This anomaly is more localized than its northern counterpart, where a significantly large area along the heel of pads C and D does not show any heating. Figure 4-34c is a well cross Section through the southern anomaly. Well E intersects the horizontal wells of pad D, and displays a large succession of channel sands with an elevated reservoir temperature of 80 degrees Celsius. Well F to the west intersects the heel of the same horizontal well, outside of the heat anomaly, and displays a mud or shale unit structurally equivalent with the heated sands of well E. This mud may be a baffle to steam flow, currently preventing the heat from reaching the overlying channel sands. The reservoir temperature recorded in well E (80 deg C) is relatively low considering the long period of injection (November 2007-January 2011) and the higher temperatures observed in other temperature logs of 200 ^{O}C and above. This low temperature suggests that there may be a nearby thief zone, which may be stealing injected heat and steam from the reservoir along the horizontal wells of Pad D (Figure 4-38).

Pads C produced approximately 1.68 million barrels of oil from May of 2003 through to January 2011 and pad D produced approximately 2.70 million barrels of oil from November of 2007 to January of 2011 for a total of approximately 4.38 million barrels of oil.

4.6.3 Instantaneous Amplitude and Instantaneous Phase

To provide further support for the distribution of heat within the reservoir, complex seismic trace analysis was employed to generate an instantaneous amplitude volume. The instantaneous amplitude (also known as amplitude envelope or reflection strength) is a measure of the total energy of a signal, or the maximum value of the seismic trace under a constant phase rotation (Schmitt, 1999; Barnes, 2007). Instantaneous phase is the phase angle required to rotate a seismic trace to its maximum value (Barnes, 2007). Thus, a seismic trace can be represented as a product of two independent functions, instantaneous amplitude and instantaneous phase. These two functions separate the phase and amplitude information in seismic data, and are the fundamental seismic attributes used to derive all other attributes (Barnes, 2007).

Instantaneous amplitude calculations are a measure of reflection strength, independent of polarity or phase of a reflection. Thus, its maximum value may be different from that of the largest peak or trough of a reflection (Taner, et al., 1979; Sheriff, 2002; Barnes, 2007). High amplitude envelope values are associated with abrupt lithological changes, gas accumulations, or in the case of SAGD, steam injection. Instantaneous amplitude is defined as follows (Taner, 2002; Barnes, 2007):

$$\boldsymbol{a(t) = \sqrt{x^2(t) + y^2(t)}} \qquad \textbf{4-8}$$

where x(t) is the seismic trace and y(t) is the seismic trace rotated by -90 deg, which is the Hilbert transformed trace. The phase rotation angel (angle required to rotate the trace to its maximum) is defined as (Taner, 2002; Barnes, 2007):

$$\boldsymbol{\theta(t)} = \mathbf{arctan}\left[\frac{\boldsymbol{y(t)}}{\boldsymbol{x(t)}}\right] \qquad \mathbf{4\text{-}6}$$

Instantaneous phase is a representation of the seismic data with the amplitude information removed. Its values represent the apparent position along a cosinusoid such that peaks have a 0 deg phase and troughs have 180 deg phase (Barnes, 2007).

Instantaneous phase and instantaneous amplitude have been employed in seismic interpretation to aid in the identification of features of interest. Schmidt (1990) used instantaneous amplitude to define porosity zones within the Casper Creek Field. Hein et al. (2010) used instantaneous amplitude and instantaneous phase to identify bottom simulating reflectors of gas hydrates in the Ulleung Basin. Riedel et al. (2011) used instantaneous amplitude to map gas hydrates within channel-levee systems in the Krishna-Godavari Basin. For this study, instantaneous amplitude was found to be more effective than instantaneous phase for enhancing the visibility of the amplitude anomalies within the reservoir.

Figure 4-36 is an inline Section through the calibrated monitor survey before and after the calculation of the instantaneous amplitude volume. There are large amplitude anomalies observed on the flattened difference volume, representative of steam injection into the McMurray reservoir. Through the transformation to the instantaneous amplitude volume, the phase content of the signal is removed, displaying a phase independent representation of the reservoir anomaly, characterized by positive amplitude values. The instantaneous amplitude volume enhances the representation of the anomalies within the Section, and suppresses the visibility of noise.

Applying the positive amplitude analysis technique (Section 4.7.1) to the instantaneous amplitude volume produced new heat distribution maps which account for both the positive and negative amplitudes of each event, represented as a single positive amplitude value. Figure 4-37 is the map view distribution of heat generated from the positive amplitude analysis technique. It correlates very well with the previous heat distribution maps (Figure 4-31), however displaying a larger heat distribution due to its representation of the positive and negative values as positive amplitude values.

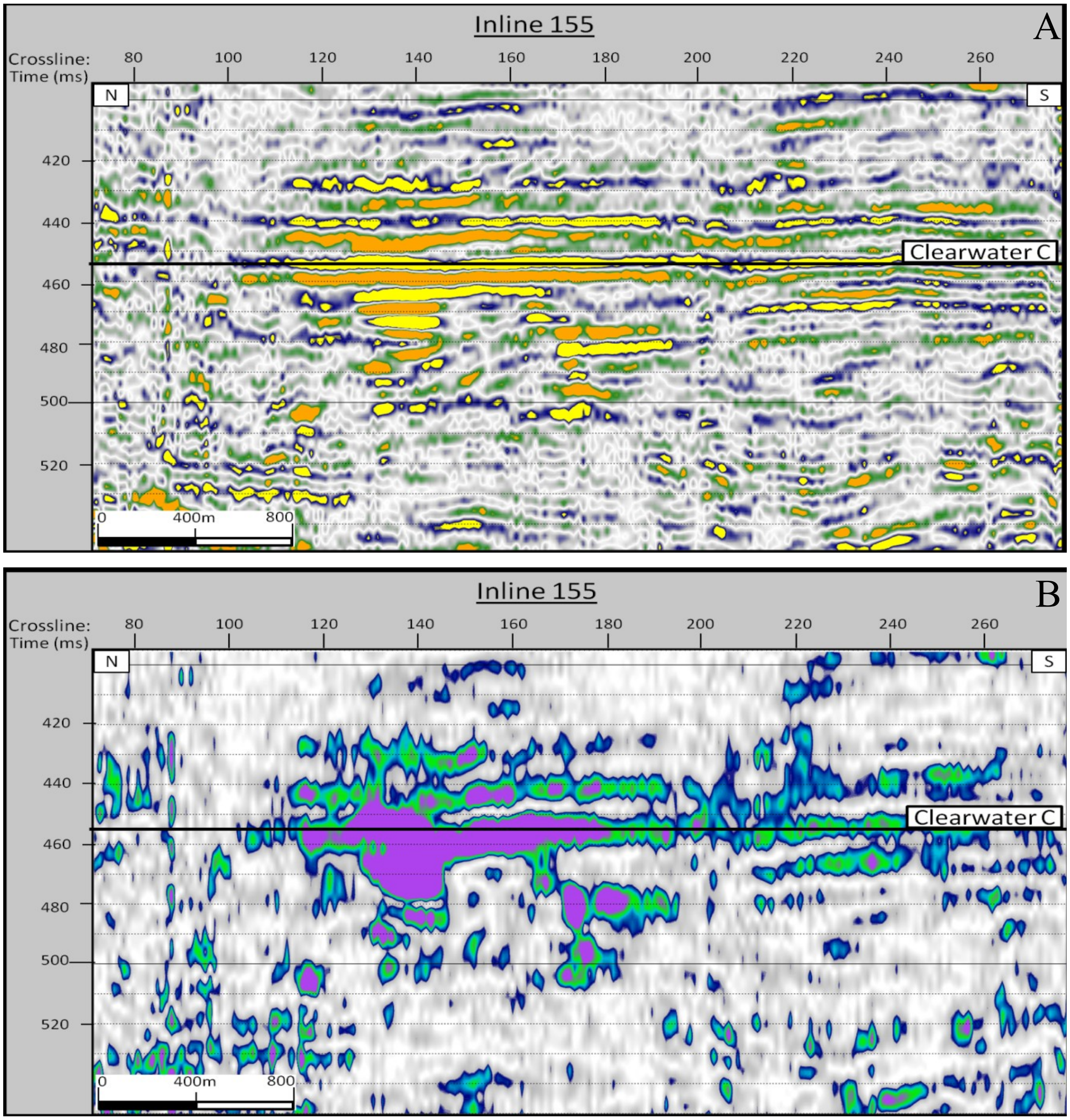

Figure 4-36 (a) Inline A through the flattened difference volume The highlighted ellipse represents large amplitude anomalies within the McMurray Formation reservoir due to steam injection (b) Inline A through the instantaneous amplitude volume. The instantaneous amplitude representation of the amplitude anomaly is independent of phase, representing the peaks and troughs as a single positive amplitude value.

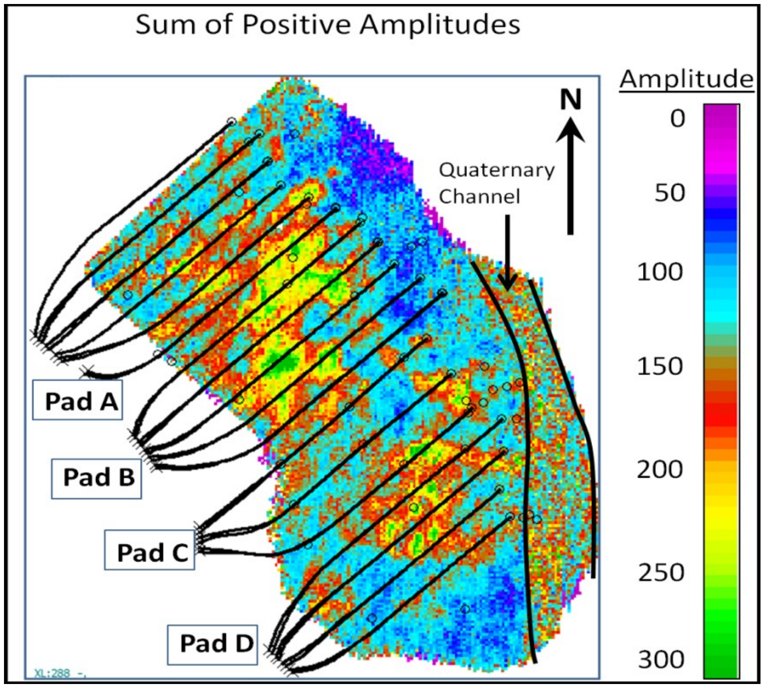

Figure 4-37 Sum of positive values through the McMurray reservoir, calculated on the amplitude envelope volume. The representation of the anomalies is free of phase, thus displaying peaks and troughs as a single positive amplitude value.

4.7 Discussion

Taking advantage of the strong contrast between the baseline survey and a production influenced monitor survey, a detailed interpretation of reservoir changes over time was carried out. Preliminary interpretation of the baseline and monitor survey identified seismic horizons of interest with the aid of synthetic seismograms and well ties, identifying the temporal location of the McMurray Formation reservoir.

Amplitude anomalies were observed within Lower McMurray Formation, which overlaid time delays and zones of frequency attenuation on the Devonian reflection. Lower and Upper McMurray Formation channels were identified within the data on semblance time slices.

NRMS and crosscorrelation maps were constructed, identifying differences between the baseline and monitor survey which were related to phase, amplitude, and time differences. These differences were corrected for through the detailed calibration of the monitor data to the baseline data.

Following the calibration, difference volumes were constructed to aid in the interpretation of observed amplitude anomalies. Amplitude anomalies were identified throughout the McMurray reservoir in conjunction with velocity anomalies within the caprock (upward propagated from the Devonian event after calibration).

McMurray Formation reservoir isochrons were built using the baseline and calibrated monitor surveys to provide a quick view of time thickening within the reservoir. The reduction in seismic velocity of the heated bitumen created significant traveltime delays, resulting in velocity pushdowns, identifiable as travel time increases on the reservoir isochrons. Taking the difference between the two isochrons accentuated these time delays, which correlate strongly with observed amplitude anomalies.

Amplitude anomalies were projected into map view, providing an examination of steam distribution within the McMurray Formation reservoir, which was contained within two main regions. Correlating these distribution maps with the SAGD injection and production well pairs provided strong support for the relationship of observed amplitude anomalies to steam injection. These maps provided a projected spatial distribution of steam within the McMurray Formation reservoir, as well as some information regarding heat flow, and steam connectivity between well pairs.

The amplitude anomaly distribution maps correlated well with the isochron difference map. However, difference between the amplitude anomaly maps and the isochron difference maps were observed. It was interpreted that the isochron difference map is representing the distribution of heat induced time delays within the McMurray Formation reservoir, while the amplitude anomaly distribution map is representing the distribution of steam anomalies within the McMurray Formation reservoir.

Combining the amplitude anomaly analysis technique with the instantaneous amplitude volume provided further support for the interpretation of steam distribution within the McMurray Formation reservoir. Correlating this data with the horizontal well pair locations supported the interpretation that the observed amplitude anomalies on both the difference volumes and the calibrated monitor volume are a result of the injection of high volumes of steam into the McMurray Formation reservoir.

Integrating the geological interpretations provided from the well log cross Sections to the geophysical observations, it was interpreted that the majority of the heat anomalies are located dominantly within two large McMurray channels which host the bulk of the McMurray sands (Figure 4-38). These two large channels trend towards the northeast, and are each comprised of a succession of smaller channels cross cutting one another. The southwest end of the southern channel may contain a thief zone, stealing steam and heat from the injection wells of pad D. The interpreted channels were further supported by combining the amplitude anomaly distribution map with semblance time slices. The northern anomaly was observed to coincide with Lower McMurray Formation channels, where the distribution of steam appeared to be bound by the edge of a mud-filled channel contained within the larger McMurray Formation channel feature.

The area outside of the two large McMurray Formation channels was interpreted to be dominantly mud and shale, with interspersed sand. These muds and shales create baffles to steam flow, preventing heat flow and thus bypassing sand units not contained within the two large channels.

Through each of the interpretation techniques employed, a detailed distribution of steam anomalies and time-delays were presented in a spatial display. The integration of geological well logs, and the co-integration of interpretation techniques (e.g. semblance time slices with amplitude anomaly distribution maps) provided robust interpretations for the distribution of steam anomalies. The anomalies were observed to be located within large channel features of the McMurray Formation, bound by muddy IHS and restricted in some regions by thief zones. Overall, the majority of the steam was observed within two large McMurray Formation channels, comprised of an amalgamation of smaller channel features.

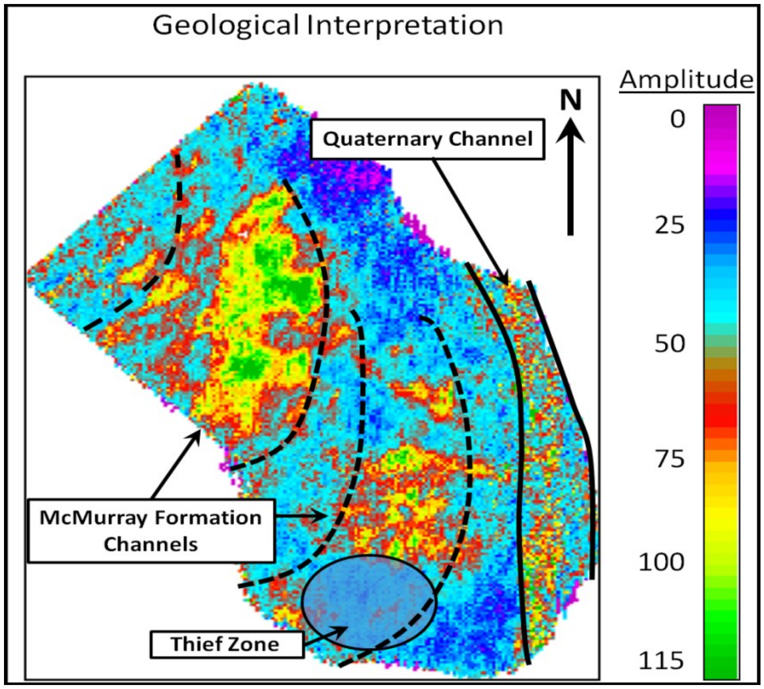

Figure 4-38 Combined geological and geophysical interpretation of two McMurray channels, with interpreted boundaries overlain on amplitude anomalies

Chapter Five: **Converted-Wave Data Analysis**

5.1 Introduction

Multicomponent seismic exploration has increasingly gained popularity for its applications to petroleum reserves. The integrated analysis of compressional- and shear-wave data has been applied rock property investigations concerning lithology, porosity, pore fluid content, and temperature where the ratio of compressional to shear velocity has been identified as a tool for both lithological and hydrocarbon identification (Tatham & Stoffa, 1976; Pickett, 1963; Domenico, 1984; Timur, 1977; Helbig & Treitel, 1985). Tatham and Stoffa (1976) showed that shear-waves are less sensitive to fluid content than compressional-waves, where the shear modulus of a rock should not be largely dependent its fluid content. Hence, the ratio of P to S velocities can be indicative of fluid content. Castagna et al. (1985) established Vp/Vs ratios for a range of siliciclastic rocks through laboratory measurements, while Domenico (1984) established that shear-wave velocities in sandstones are the most sensitive to porosity variations.

The application of multicomponent seismic to petroleum exploration has been well documented. Garotta et al. (1985) used P-S and P-P data to identify sand from shale within a Viking sand channel reservoir in the Winfeild oil field. Nazar and Lawton (1993) used P-S Sections to help image oil-saturated conglomerates in the Carrot Creek field. Chuandong (2004) used Vp/Vs maps for lithological discrimination of sand vs shale within the Ross Lake oil field. Dumitrescu (2006) used P-S data to characterize a heavy oil field, mapping oil sand reservoirs through Vp/Vs identification. Varga (2009) also employed P-S data to discriminate between reservoir sand and shale within a heavy oil reservoir, while identifying hydrocarbon saturated sands, manifested as low Vp/Vs ratios. For a further discussion on the applications of converted-wave seismic, refer to Stewart et al., 2003.

Multicomponent seismic takes advantage of the mode conversion that occurs at a reflection interface within the subsurface. As described Zoeppritz, at non-zero angles less than the critical angle, the downgoing compressional wave will reflect and transmit both compressional and shear-waves at a reflecting interface (assuming increasing impedance in the downward direction) (Isaac, 1996; Stewart, et al., 1999; Tatham & McCormack, 1991; Hardage, et al., 2011) (Figure 5-1). Four different wave types leave the interface, a reflected P-wave (PP_R), a reflected mode converted shear-wave (PSV_R), a transmitted P-wave (PP_T) and a transmitted mode converted shear-wave (PSV_T). The particle-displacement polarities are as assumed by Aki and Richards (1980) for P and SV modes; The P-wave particle motion is in the plane of incidence, so the shear-wave particle motion is restricted to be within this same plane (Tatham & McCormack, 1991). The mode conversion of a shear wave from a downgoing compressional wave forms the basis of P-SV subsurface imaging.

The method to derive Vp/Vs from P-SV data is typically calculated in terms of the traveltime thickness for P-waves and S-waves, using the traveltime ratio $\Delta T_S/\Delta T_P$ where ΔT_S is the traveltime required for the shear-wave to travel vertically across an interval of thickness ΔZ, and ΔT_P is the vertical traveltime required for the P-wave to travel the same interval. Hence, Vp/Vs is calculated as follows (Hardage, et al., 2011) (Figure 5-2):

$$\frac{Vp}{Vs} = \Delta \mathbf{T_S}/\Delta \mathbf{T_P} \qquad \textbf{(5-1)}$$

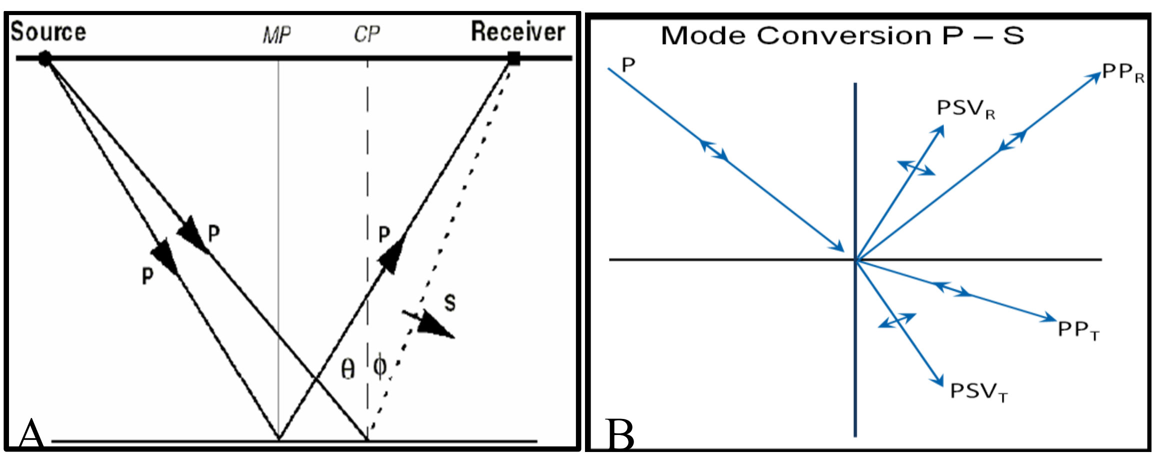

Figure 5-1 (a) A converted-wave reflection at its conversion point (CCP) compared to a compressional wave reflection at its midpoint (MP) (Stewart, et al., 1999) (b) Partitioning of energy into different wave types at an interface as governed by Snell's law (Tatham & McCormack, (1991).

5.2 Converted-Wave Applications to Heavy Oil

Converted-wave seismology has been previously employed to aid in the analysis of heavy oil reservoirs. As previously mentioned, work by Isaac (1996), Chuandong (2004), Dumitrescu (2006), and Varga (2009) each used P-SV data, in conjunction with P-P data to further reservoir analysis. In the terms of steam assisted gravity drainage (SAGD) recovery of a heavy oil reserve, production monitoring can benefit from the application of multicomponent seismic analysis, primarily through an analysis of the Vp/Vs.

The addition of steam into a reservoir alters elastic constants, reducing both the Vp and Vs, with a significantly large decrease in Vp (Watson, 2004). Aktan and Faroug Ali (1975) studied the effect of in-situ heating on the elastic constants of a range of sandstones, concluding that the young's modulus, bulk modulus and poisons ratio significantly reduced as a result of heating. Timur (1977) studied the temperature dependence of both Vp and Vs for a range of sedimentary rocks, concluding that the average decrease in velocity at 100°C was greater in Vp than in Vs.

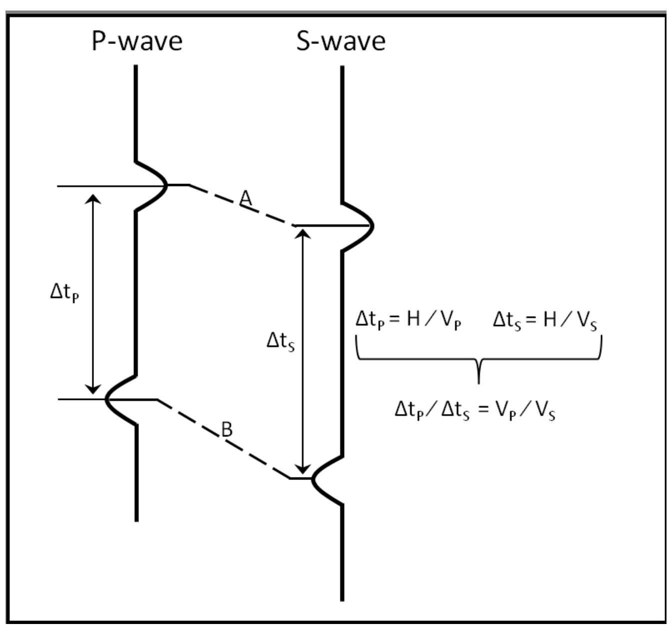

Figure 5-2 Schematic diagram of P- and S-wave response to the same interval, and derivation of traveltime ratio t_S/t_P and velocity ratio Vp/Vs (Tatham & McCormack, 1991).

Ito et al. (1979) furthered this work by analyzing water saturated sandstones, studying the compressional and shear velocities along the liquid-vapor phase transition. Their results showed an abrupt drop in Vp at the water-steam transition at 145°C, while Vs was largely unaltered. Poisson's ration increased significantly during the phase transition into steam, reducing the bulk modulus and therefore altering the compressional velocity. The shear velocity is insensitive to changes in the bulk modulus and is largely uninfluenced. The reduction of Vp resulted in a Vp/Vs difference for the steam vs. water saturated rocks, where the Vp/VS was the lowest during the steam phase.

In the Pikes Peak heavy oil field, Stewart et al. (1996) showed that the addition of steam into the reservoir decreased both the Vp and Vs, with a greater reduction in Vp than Vs. The larger reduction of Vp lead to a reduction in Vp/Vs due to the injection of steam, a reservoir change that can be observed through time lapse monitoring (Watson, et al., 2002). This characteristic of Vp/Vs can be used for the multicomponent monitoring of reservoir steam movements.

More recently, Vp/Vs analysis has been used to delineate reservoir sand bodies, map steam fronts and discriminate between shales and sands within heavy-oil reservoirs (Lines, 2008). Domenico (1984) and later Macrides and Kelamis (2000) estimated Vp/Vs ratios for lithology discrimination, estimated from time-thickness data. They proposed average Vp/Vs ratios of 1.6 for clean sandstones, 2.0 for limestones and 2.4 for silty or shaly sands. Pengelly (2005) used the traveltime method to determine reservoir Vp/Vs for the Jackfish heavy oilfield, while Dumitrescu (2006) used Vp/Vs from amplitude inversion to map sand and shale distribution within the Plover Lake oil field.

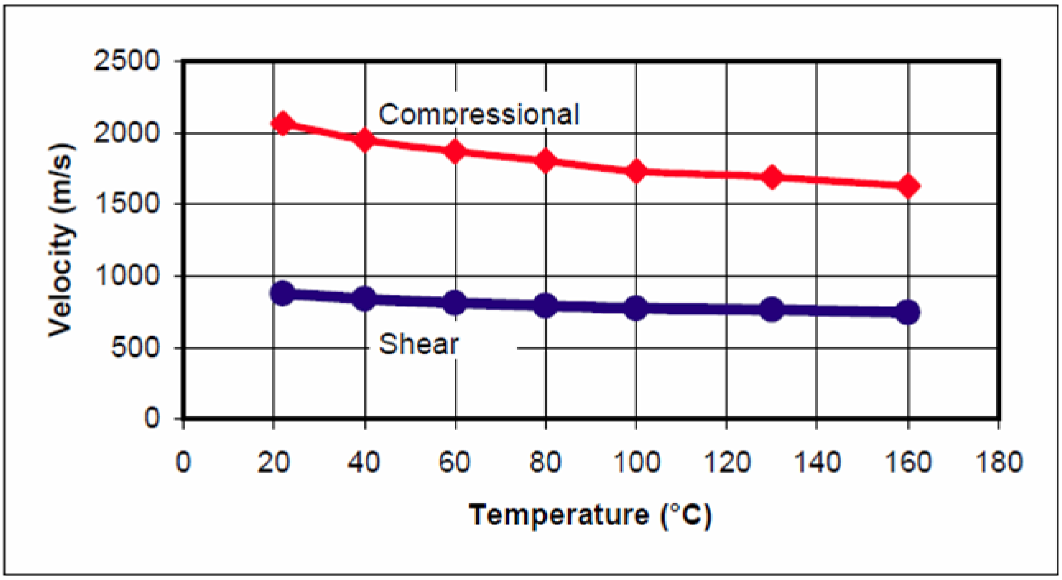

Figure 5-3 Temperature vs. velocity profile for P- and S-wave. A reduction in compressional and shear velocity is observed due to the injection of steam. The decrease in Vp is greater than Vs (Watson, et al., 2002).

5.3 Radial Component Processing and Analysis

The processing flow applied to the converted-wave data was similar to that of the P-wave data processing (see Chapter 3). Due to the duplicity of the processing flow, it will not be discussed in detail in this chapter. However, the processing of the mode converted data required the addition of a few processing steps, unique to mode-converted data and critical to the imaging routine, as described below.

5.3.1 Rotation Analysis

Azimuthal anisotropy within the subsurface has been shown to create shear-wave splitting of an upgoing mode-converted shear-wave into its fast and slow components (Nacille, 1986; Crampin, et al., 1986; Lynn & Thomsen, 1986; Harrison, 1992; Isaac, 1996). The presence of vertical birefringence can cause shear energy to be recorded on both horizontal components, leading to a decreased S:N on the radial component

(Harrison, 1992). Assuming the field coordinate system is known, the receivers were first rotated from field-coordinate space to the radial-transverse space, improving S:N on the radial data (Harrison, 1992; Hardage, et al., 2011) (Figure 5-4). The angle of rotation is unique for each source-receiver azimuth (Isaac, 1996). Figure 5-5 displays the rotation analysis of synthetic data from its field-coordinate space into the radial-transverse space.

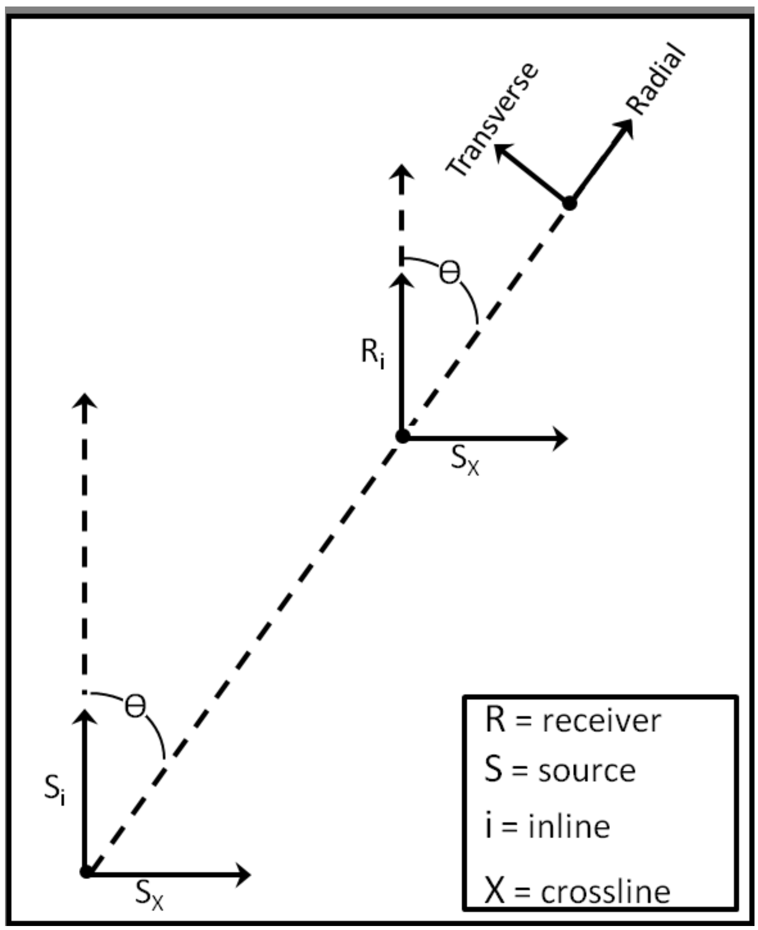

Figure 5-4 Schematic for the rotation from the inline-crossline coordinates to the radial-transverse coordinates (Hardage, et al., 2011).

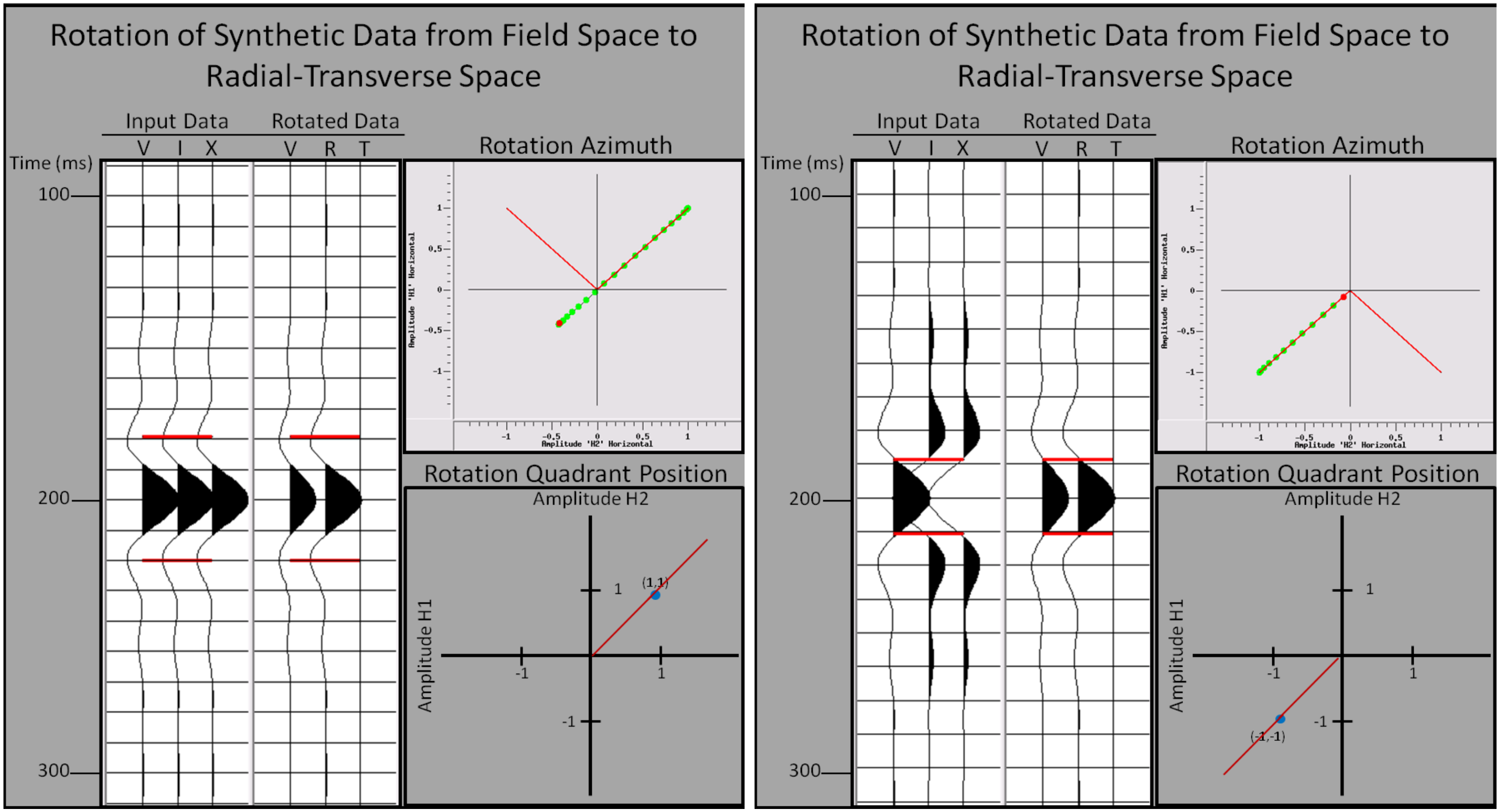

Figure 5-5 Rotation of synthetic data from field-coordinate space to radial-transverse space. Data recorded on geophones oriented at an angle to the source-receiver plane record energy from other source-receiver azimuths. The rotation from inline and crossline components to the radial and transverse component orients our receivers into the source-receiver plane (radial) and orthogonal to the plane (transverse). (a) Synthetic with positive amplitudes (b) Synthetic with negative amplitudes.

5.3.2 Common Conversion Point (CCP)

The common-midpoint concepts do not apply to multicomponent data when the velocity of the downgoing wavefield differs from that of the upgoing reflected wavefield, as is the case for the mode conversion of a downgoing P-wave into a reflected shear-wave (P-SV) (Hardage, et al., 2011). For converted-waves, the point of illumination does not occur at the common-midpoint location, but instead at the point of mode conversion (Figure 5-1). In P-SV imaging, the downgoing wavefield (Vp) has a faster velocity than the upgoing wavefield (Vs), and hence the point of reflector illumination is positioned closer to the receiver location than the source location (Hardage, et al., 2011). This subsurface location is also the point of mode conversion from the downgoing P-wave to the reflected shear-wave, referred to as the common-conversion point (CCP) (Tessmer & Behle, 1988; Hardage, et al., 2011) (Figure 5-6). CCP`s generated at different depths do not stack vertically, as is the case for CMP, but instead move towards the receiver as the depth is reduced or as Vp/Vs is increased (Hardage, et al., 2011; Stewart, et al., 2002).

Following the rotation of the inline and crossline data into radial-transverse space, the radial data was binned to CCP`s via a 3-D asymptotic CCP binning algorithm using an average Vp/Vs of 3.0.

5.4 Preliminary Data Analysis

5.4.1 2002 Converted-wave data

A preliminary analysis of the raw converted-wave data was performed to estimate Devonian moveout velocity and bulk Vp/Vs. The inline and crossline data was observed to be of high quality, with a relatively high S:N. Raw shot gathers taken from the center of the survey area displayed two high amplitude reflections, the latter corresponding to the Devonian interface at a time of 900ms (Figure 5-7). The Devonian event is characterized by a moveout velocity of 1500m/s. In comparison to the raw 2002 P-wave data, the converted-wave Devonian reflection lies at a time greater than the P-wave

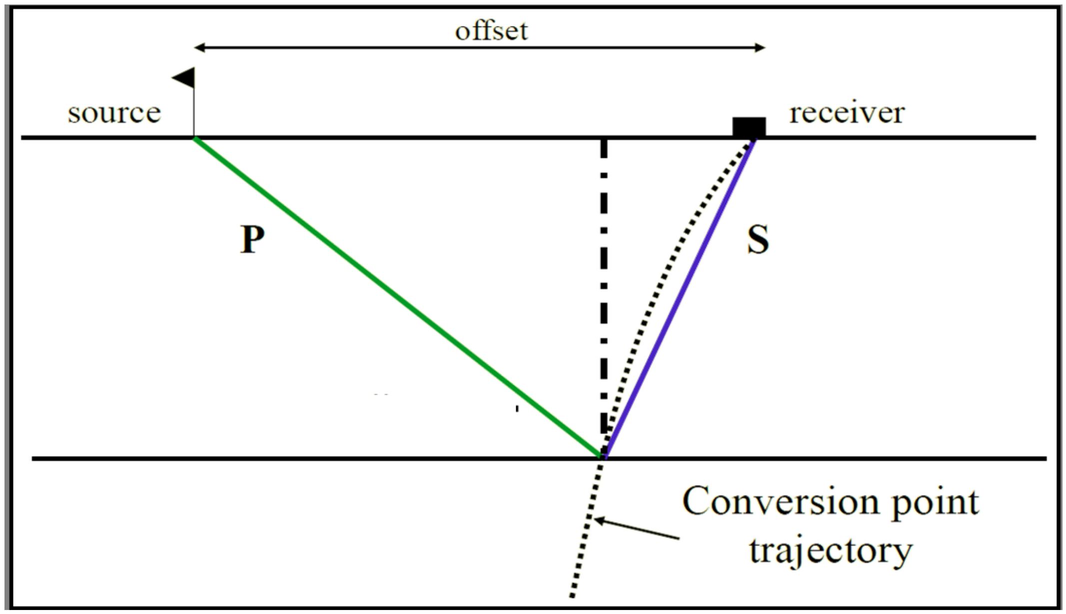

Figure 5-6 Illustration of subsurface CCP imaging and CCP trajectory.

equivalent (300ms), and it characterized by a slower velocity (1500 m/s vs. 2400m/s). Using the traveltime from the first-break to the Devonian reflection at zero-offset, the overall Vp/Vs ratio was estimated using equation 5-1. The bulk Vp/Vs ratio to the Devonian reflection is approximately 3.0.

Following the preliminary analysis, the converted-wave data was input into Halliburton's ProMAX processing software to perform converted-wave processing of the inline and crossline data. However, an assortment of problems plagued the dataset. For instance, the vertical traces of the 2002 dataset contained geometry information in the headers (source and receiver X and Y field-coordinates, etc) while the inline and crossline traces did not contain any geometry information. An attempt was made to copy the geometry from the vertical traces to the inline and crossline traces, matched by FFID number and channel number, but a discrepancy arose in the number of traces in each component of the dataset. The vertical traces contained approximately 10 million traces, while the inline data contained only 8.7 million traces, and the crossline data contained

15million traces, a discrepancy of 1.7 million traces in the inline data and an addition of 5million traces in the crossline data.

Furthermore, an investigation of the crossline data observed that each shot record contained duplicate traces for the crossline data, as well as a set of traces from the inline data (Figure 5-8). Reducing the crossline data to contain only one copy of the crossline trace reduced the number of traces to 5 million, a discrepancy of 5million traces with respect to the vertical data (10 million traces). The large discrepancy in the number of traces between crossline, inline and vertical data prevented the copying of the geometry information from the vertical data to the inline and crossline data. Without proper geometry information, the rotation from field-coordinate space to radial-transverse space was not possible, nor was the successive processing of the converted-wave data. Hence, the 2002 converted-wave data was not processed further.

5.4.2 2011 Converted-wave data

The 2011 inline and crossline data contained geometry information in the headers, allowing for the rotation to radial-transverse space, CCP binning, and successive processing of the converted-wave data. However, in comparison to the 2002 raw data, the 2011 converted-wave shot gathers contained very low S:N. Figure 5-9 is a shot gather taken from the center of the survey area. There were no strong converted-wave reflections observed corresponding to the Devonian event. Within the shallow Section, some P-wave contamination was observed, corresponding to the Devonian reflection as observed on raw P-wave shot gathers (Figure 3-6, Chapter 3). Rotating the data from the field-coordinate space to the radial-transverse space did not improve the S:N sufficiently. Again, shot gathers from the radial data did not display a strong coherent reflection from the Devonian interface (expected to be imaged at ~900ms, as was observed on the 2002 converted-wave data).

Following the rotation to the radial component, the data were binned to common-conversion point and subsequently fed through the same data conditioning routine as the

P-wave data (for more information, see Chapter 3). Because the data condition routine was the same as before, it will not be discussed in detail here.

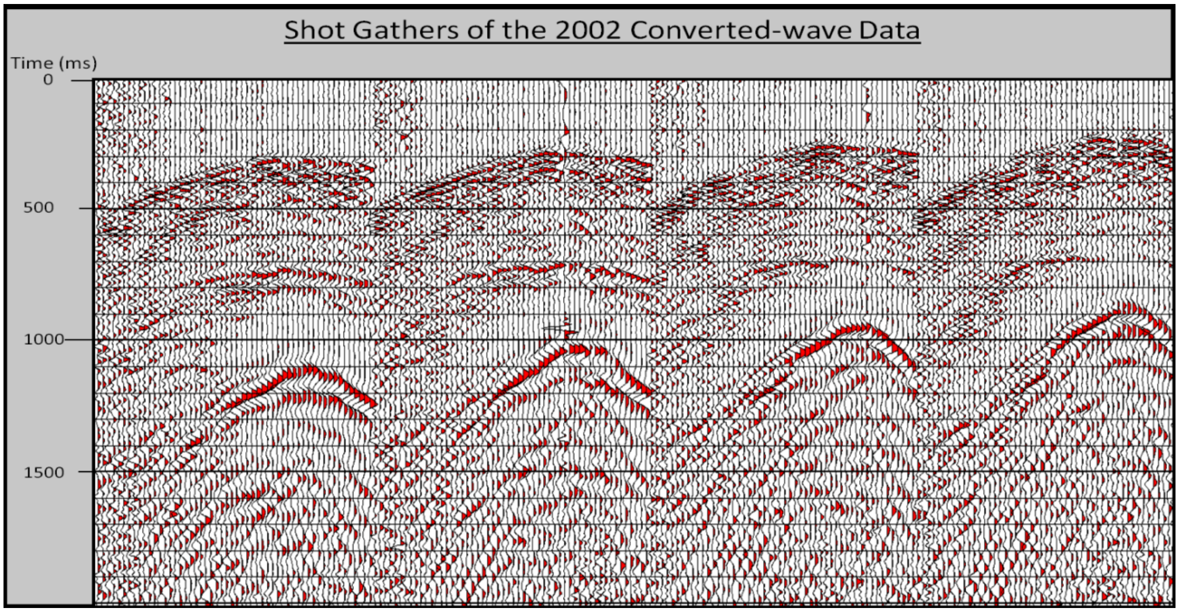

Figure 5-7 Raw shot gather from the 2002 converted-wave data with a 500ms AGC applied.

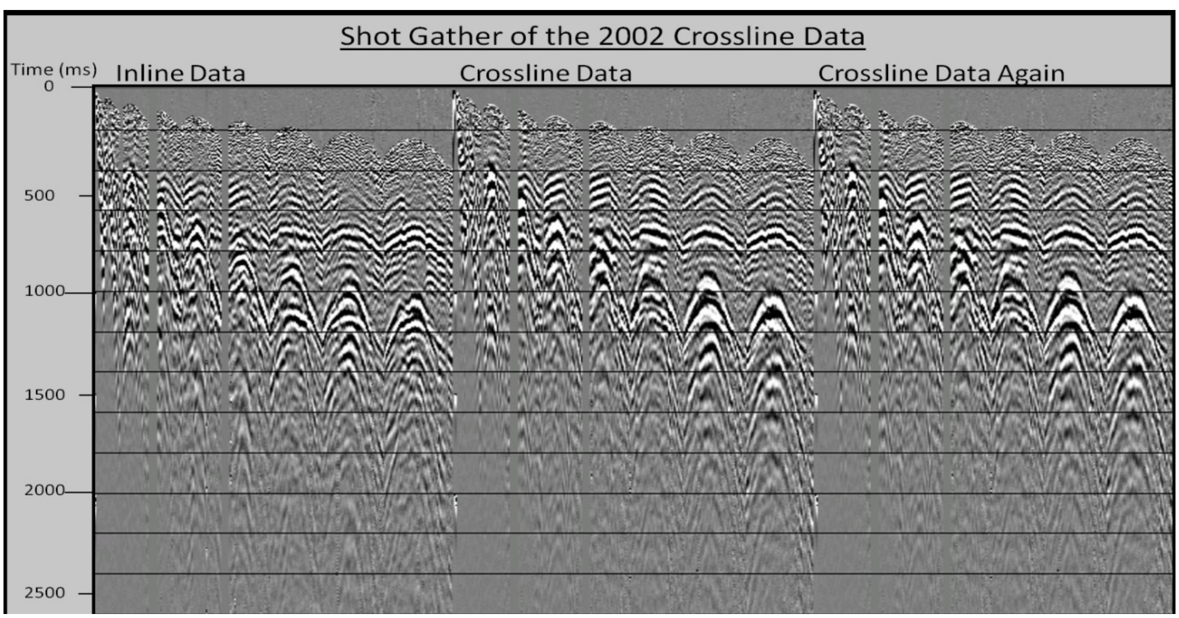

Figure 5-8 Raw shot gather from the 2002 Crossline Data. Duplicate Crossline data and a copy of the Inline data are visible on each shot gather.

In an attempt to confirm the absence of a coherent Devonian reflection, receiver stacks of the data conditioned radial data were constructed using a constant velocity equal to the normal-moveout velocity estimated on the 2002 raw shot gathers. Shot statics from the 2011 P-wave survey were applied to the 2011 converted-wave data. Assuming the presence of a strong and coherent reflection, receiver stacks were expected to show the Devonian reflection, with statics influenced only by those at the source location. Hence, a receiver stack of the dataset should display the P-SV Devonian reflection and enable receiver statics to be calculated. Figure 5-10 is an inline through the receiver stack. Again, a coherent reflection was not observed within the data set. Following these lack of observations, it was concluded that the 2011 data is of poor quality, and does not contain a strong reflection from the Devonian interface. Thus, the 2011 converted-wave data was not fully processed, nor determine a moveout-velocity or average Vp/Vs for the Devonian reflector.

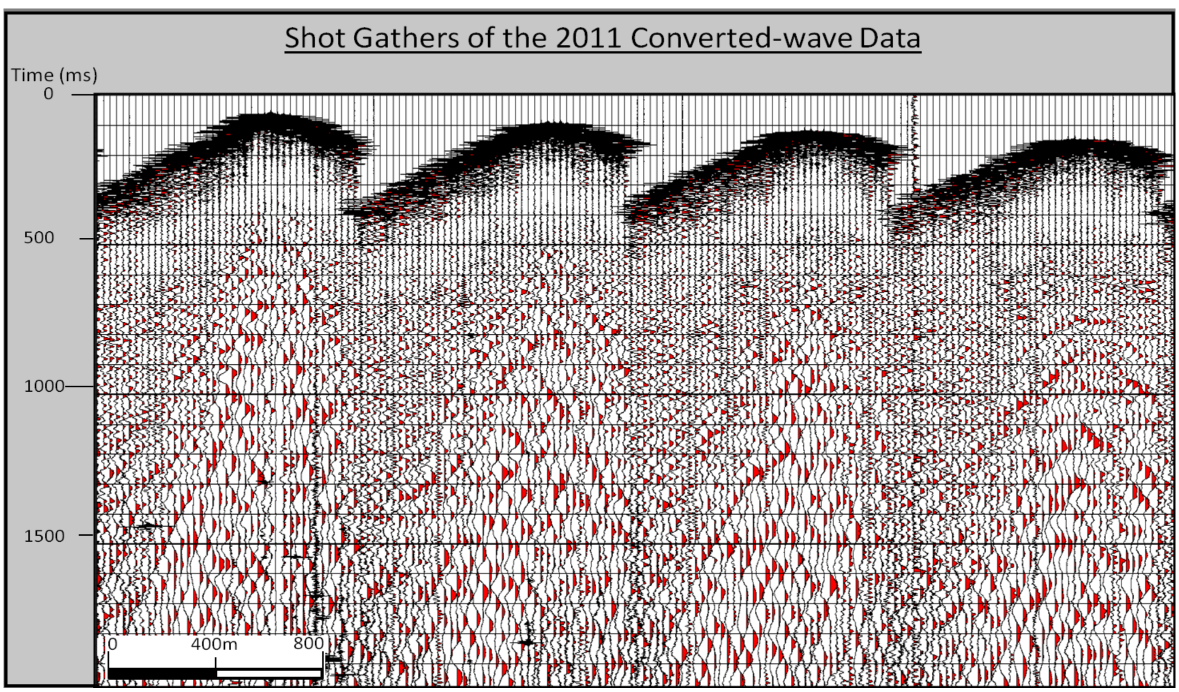

Figure 5-9 2011 raw converted wave data with a 500ms AGC applied. No reflections are observed at C-wave time. Some contamination from P-wave data is observed in the shallow data.

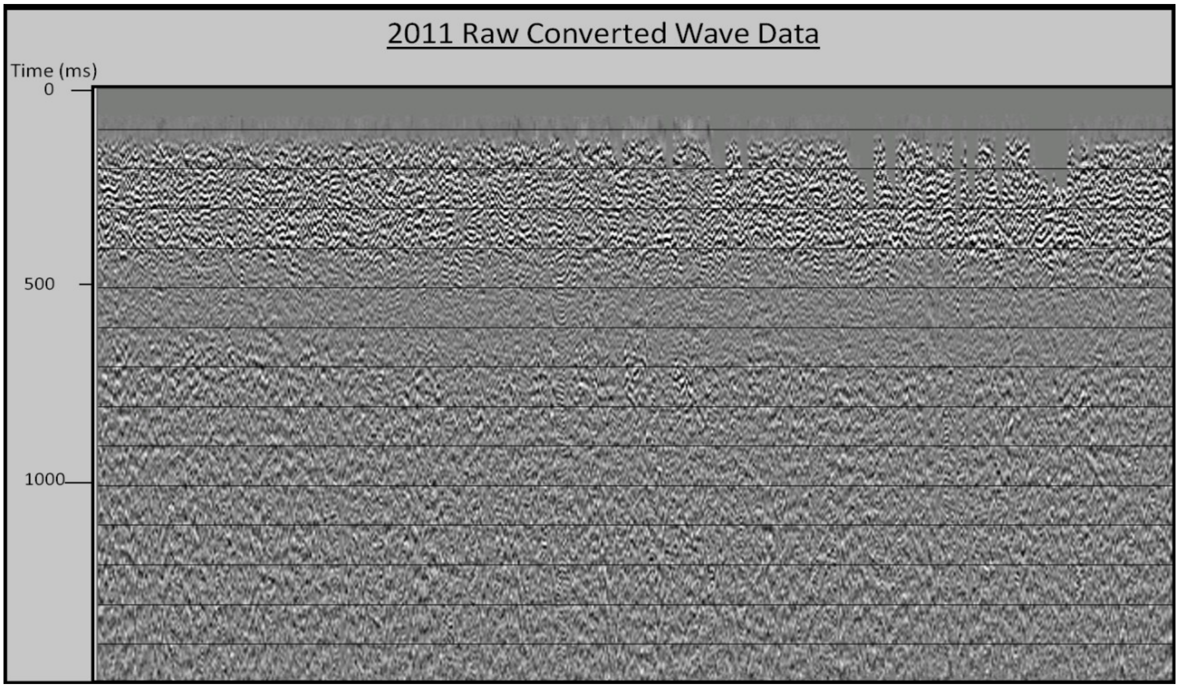

Figure 5-10 Receiver stack from the 2011 data after rotation, and data conditioning. No coherent reflections are observed.

5.5 Discussion

The 2002 converted-wave data was observed to be of high quality and showed great promise for generating high quality P-SV images. Using the raw data, a bulk estimate of the Devonian moveout velocity and Vp/Vs was calculated. However, due to the issues associated with the data set, a fully processed image could not be completed in a timely fashion. Hence, the 2002 converted-wave data was not used to its full potential. Future work for this dataset could involve the decimation of the 2002 data to common traces for the vertical, inline and crossline data, and subsequent processing; a non-trivial and time consuming task.

The 2011 raw converted-wave data did not show a high S:N as did the 2002 data. This overall low S:N limited the feasibility of the data, where a Devonian reflection was not observed on the raw shot gathers, nor the data conditioned receiver stacks. The lack of a reflection on the 2011 data may be related to the overall low S:N of the dataset; the 2011 P-wave data was significantly noisier than its 2002 equivalent. This disparity in data quality is further exemplified in the converted-wave data, where the 2011 data was apparently absent of converted-wave signal.

Overall, the converted-wave dataset was of limited use. The estimation of bulk Vp/Vs to the Devonian interface, and calculation of the moveout velocity of the Devonian reflection may prove to be useful information for further converted-wave studies of the McMurray Formation reservoir, but contributed limited value to this thesis.

Chapter Six: **Conclusions**

6.1 Heavy Oil Reservoir Monitoring

Heavy oil deposits in the Athabasca oil sand region are actively undergoing enhanced oil recovery processes, such as steam-assisted gravity drainage (SAGD), to aid in the production of bitumen reserves. To enhance the efficiency of SAGD recovery, the monitoring of steam injection over time is critical in order to track steam movements and to identify areas of bypassed reserves, or regions in which current steam injection is not adequately stimulating the reservoir. Time-lapse 3D seismic surveys are employed to monitor reservoir changes, ideally recorded before the onset of production (baseline survey) and repeated after substantial reservoir stimulation and production (monitor surveys).

Time-lapse seismic monitoring detects reservoir changes in terms of deviations in the seismic character of the reservoir, observed through a comparison of the baseline data to that of the monitor survey data. Theoretical and experimental studies have shown that steam injection into a heavy oil reservoir may alter the elastic moduli of the rock, potentially decreasing the compressional wave and shear wave velocities. Seismic wave velocities also depend on porosity, pore fluid, consolidation, temperature and effective pressure. A variation in these parameters will result in changes in the seismic wave velocity through the rock, observable in reflection seismic data.

Time-lapse seismic monitoring has been utilized in various Canadian heavy oil fields to provide a detailed understanding of the changes in the seismic properties of a reservoir over time. The data for this thesis was acquired over a heavy oil reservoir from the Athabasca oil sands region. It is comprised of a time-lapse 3D - 3C survey, containing a baseline survey and a single monitor survey.

6.2 Data Processing and Calibration

The baseline survey was acquired in the 2002, covering an area of approximately 9.0 km^2 and was recorded prior to steam injection or other recovery processes. The monitor survey was acquired after nine years of steam injection and oil recovery. Acquired in 2011, it was recorded over only a subset of the baseline survey, covering 3.8 km^2 and overlying all active horizontal injection and production well pairs.

The processing of the baseline dataset followed a typical routine for a shallow, heavy oil reservoir. To aid in the time-lapse interpretation, all processes applied to the baseline data were also applied to the monitor data.. The consistency in the processing routine allowed for enhanced repeatability of the two surveys, so that time-lapse reservoir differences were not a factor simply of any processing discrepancies. To further enhance data repeatability, the time-lapse dataset was decimated to contain only source and receivers common to both surveys, identified in terms of surficial X and Y coordinate locations.

Despite the identical processing of the time-lapse dataset, discrepancies between the baseline and monitor data existed in terms of phase, amplitude and static solutions. Such differences were corrected for through the detailed calibration of the monitor survey to match the baseline data on reflection events outside of the McMurray reservoir. Plots of NRMS, crosscorrelation and time-shifts values were used to understand the survey differences, as well as to display the effectiveness of each step in the calibration routine. The calibration of the dataset was employed through five steps: (1) phase matching to match the phase of the two surveys (2) zero-phase shaping filter to match the wavelet of the monitor survey to the baseline data (3) static correction to align reflections in time on a trace-by-trace basis (4) amplitude matching via cross-normalization to equalize the rms amplitudes between the two surveys and (5) computing a reflectivity difference volume by subtracting the baseline data from the monitor data. The calibration procedure reduced non-production induced differences and preserved time-lapse reservoir changes that are due to SAGD operations.

6.3 Compressional-wave Data Analysis

The two processed 3-D seismic datasets and the difference volume were interpreted and analyzed to yield multiple observations of steam and heat distribution within the McMurray Formation reservoir. The bulk of the interpretation comprised of the observation of amplitude anomalies within the monitor and difference volumes, as well as utilizing seismic attributes including isochrons, instantaneous frequency and instantaneous amplitude.

The injection of steam into the McMurray Formation reservoir was observed on the 2011 monitor data as high amplitude anomalies and apparent time-thickening of the reservoir interval due to a decrease in the P-wave velocity. This decrease in velocity was interpreted to be due to an increase in reservoir temperature and decrease in differential pressure created from the injection of high temperature steam into the McMurray Formation reservoir.

High amplitude events observed on the monitor data were projected into map view by summing the positive and negative amplitudes within the McMurray Formation reservoir interval, analyzed within the difference volume. This technique provided a spatial display of steam distribution within the McMurray Formation reservoir, which correlated with horizontal well pair locations.

A reservoir isochron difference map displayed the time delays created by the injection of steam into the reservoir. The spatial distribution of the time- is larger than the lateral extent of the amplitude anomalies. The time delays are interpreted to be representative of the areal extent of heat within the McMurray Formation reservoir interval, which may extend beyond the bounds of the actual steam chambers.

Frequency analysis of the baseline and monitor data was performed using the instantaneous frequency attribute, displaying the attenuation of high frequencies beneath steam chambers within the monitor survey. The frequency attenuation was characterized by a reduction of the monitor frequency values in comparison to the baseline values, as well as low-frequency shadows, observable on the Devonian reflection underlying the amplitude anomalies. The low frequency zones correlated with horizontal well pairs, observed on time-slices through the instantaneous frequency monitor volume.

Geological well log information was integrated with the geophysical observations. McMurray Formation channels were observed within the seismic data through the analysis of the semblance attribute, as well as within the geological data as low gamma ray values on well logs. The channel sands were observed to intersect amplitude anomalies with the monitor volume. Outside of the amplitude anomalies, the channel sands are interpreted to be bound by muddy inclined heterolithic sequence (IHS) bedding, creating baffles to steam flow.

On a larger scale, it was interpreted that the steam distribution is contained within two McMurray Formation channels, each of which is comprised of an amalgamation of smaller channel features as well as impermeable beds of muddy / silty IHS. The area outside of the steam zones was interpreted to be dominantly comprised of mud and shale, with interspersed sand.

6.4 Converted-wave Data Analysis

Converted wave data for the baseline and monitor surveys were analyzed in attempt to track time-lapse reservoir changes in terms of Vp/Vs for the McMurray Formation reservoir interval. The 2002 converted-wave data was observed to be of high quality and showed great promise for generating high quality P-SV images. Using the raw data, a bulk estimate of the Devonian moveout velocity was calculated to be 1500m/s and the bulk Vp/Vs was estimated to be 3.0, calculated over the interval spanning all events downto the Devonian reflection. However, due to complications with the dataset, a fully processed image could not be completed and thus was not pursued further for this thesis.

The 2011 multicomponent data were significantly lower in quality than its 2002 counterpart. Raw shot gathers of the 2011 data were contaminated with high levels of noise, and did not display any strong or coherent converted-wave reflections. It was interpreted that the lack of a converted-wave signal in the 2011 data may be related to the generally lower S/N of the 2011 dataset. Due to this lack of signal, P-SV images of the McMurray Formation reservoir could not be generated.

Overall, the converted-wave dataset was of limited use. The estimated bulk Vp/Vs from the 2002 data, and calculated moveout velocity of the Devonian reflection, provided some basic analysis of the converted-wave signal for this heavy-oil reservoir. Nevertheless, the converted-wave data remains an area of recommended future work, where the time-lapse analysis of P-SV images can potentially provide useful information for further characterizing the McMurray Formation reservoir.

Bibliography

Aki, K, and P G Richards. *Quantitative Seismology - Theory and Methods.* W. H. Freeman and Co., 1980.

Atkan, T, and S M Fargou Ali. "Effect of cyclic and in situ heating on the absolute permeabilities, elastic constants and electrical resistivities of rocks." *Society of Petroleum Engineering* 5663 (1975).

Bancroft, J., C. *A practical understanding of pre- and poststack migration techniques.* . Tulsa: Society of Exploration Geophysics, 2007.

Barnes, Arthur, E. "A tutorial on complex seismic trace analysis." *Geophysics* 72, no. No. 6 (2007): W33-W43.

Bianco, V, S Kaplan, and D Schmitt. "Seismic rock physics of steam injection in bitumonous oil reserves." *The Leading Edge,* , 2008: 11332-1137.

BP Global. "BP Statistical Review of World Energy 2012." June 2012. http://www.bp.com/assets/bp_internet/globalbp/globalbp_uk_english/reports_and_publications/statistical_energy_review_2011/STAGING/local_assets/pdf/statistical_review_of_world_energy_full_report_2012.pdf.

Britton, M. W., W. L. Martin, R. J. Leibrecht, and R. A. Harmon. "Street Ranch pilot test of fracture-assisted steamflood." *Jouranl of Petroleum Technology* 35 (1983): 511-522.

Buschkuehle, B. E. "Sedimentology and stratigraphy of Middle and Upper Devonian carbonates in northern Alberta: A contribution to the carbonate-hosted Pb-Zn (MTV) targetd geosicence initiative." *Alberta Geological Survey*, 2003.

Castagna, J P, M L Batzle, and R L Eastwood. "Relationship between compressional-wave and shear-wave velocities in clastic silicate rocks." *Geophysics* 50, no. No. 4 (1985): 571-581.

Chalaturnyk, Rick. "Obeservations on SAGD caprock integrity." *Recovery CSEG Annual Convention*, 2011.

Chen, Q. "Assessing and improving steam assisted gravity drainage: Reservoir heterogeneities, hydraulic fractures and mobility control foams." *PHD Thesis, Standford University*, 2009.

Chopra, Satinder, and Kurt J. Marfurt. *Seismic attributes for prospect identification and reservoir characterization.* Tusla, Oklahoma: Society of Exploration Geophysicists, 2007.

Chopra, Satinder, and Kurt Marfurt. "Detecting stratigraphic features via crossplotting of seismic discontinuity attributes and their volume visualization." *The Leading Edge* 28, no. No. 12 (2009): 1422 - 1426.

Chopra, Satinder, and Kurt Marfurt. "Gleaning meaningful information from seismic attributes." *First Break* 26 (2008): 43 - 53.

Chou, Queena. "Clearwater formation natural fracture characterization from cores and image logs, Athabasca oil sands, Alberta." *Recovery CSEG Annual Convention Abstracts*, 2011.

Chuandong, Xu, and Robert R Stewart. "Delineating a sand channel reservoir using 3C-3D seismic data: Ross Lake, Saskatchewan." *CREWES research report* 16 (2004).

Clifford, Peter J, et al. "Integration of 4D seismic data into the management of oil reservoirs with horizontal wells between fluid contacts." *Society of Petroleum Engineers 83956*, 2003: 1-10.

Collins, Patrick M. "Geomechanical effects on SAGD process." *Society of Petroleum Engineers International* 97905 (2005).

Cox, M., J., G., Scherrer, E., F., and Chen, R. *Static Corrections for Seismic Reflection Surveys.* Tulsa: Society of Exploration Geophysicists, 1999.

Crampin, S., E. M. Chesnokov, and R. G. Hipkin. "Seismic anisotropy - the state of the art: II." *Geophysical Journal International* 76 (1986): 1-16.

Dix, C., H.,. "Seismic velocities from surface measurments." *Geophysics, vol. 20*, 1955: 68-86.

Domenico, S. N. "Rock lithology and porosity determination from shear and compressional wave velocities." *Geophysics* 49 (1984): 1188-1195.

Domenico, S. N. "Rock lithology and porosity determination from shear and compressional wave velocity." *Geophysics* 49, no. No. 8 (1984): 1188-1195.

Drijkoningen, Guy, Guss van Noort, Rob Arts, Joren Bullen, and Jan Thorbecke. "Seismic time-lapse effects of solution salt mining - a feasibility study." *Geophysical prospecting* 60 (2012): 239-254.

Dubrulle, a., A., and Gazdag, J. "Migration by phase shift - an alogrithmic description for array processors." *Geophysics, vol. 44, no. 10*, 1979: 1661-1665.

Dumitrescu, Carmen C, and Larry Lines. "Heavy oil reservoir characterization using Vp/Vs ratios and spectral decomposition." *SEG Annual Meeting Abstracts*, 2006: 1640-1643.

Eastwood, J E, D Johnston, X Huang, K Craft, and R Workman. "Processing for robust time-lapse seismic analysis: Gulf of Mexico example, Lean Field." *68th Annual International Meeting, Society of Exploration Geophysicists, Expanded Abstracts*, 1998: 20-23.

Eastwood, J. "Temperature-dependant propogation of P- and S-waves in Cold Lake oil sands: Comparsion of theory and experiment." *Geophysics* 58,, no. No.6 (1993): 863-872.

Eastwood, J, P Lebel, A Dilay, and S Blakeslee. "Seismic monitoring of steam-based recovery of bitumen." *The Leading Edge* 13, no. 4 (1994): 242-251.

Eiken, Ola, Geir Ultveit Haugen, Michal Schonewille, and Adri Duijndam. "A proven method for aquiring highly repetable towed streamer seismic data." *Geophysics* 68, no. No.4 (2003): 1303-1309.

Farrell, R., C., and Euwema, R., N. "Refraction Statics." *Proceedings of the IEEE, vol. 72, No. 10*, 1984: 1316-1335.

Flach, P. D. "Oil sands geology - Athabasca deposit north." *Geological Survey Department, Alberta Research Council*, 1984.

Gadallah, M., R., and Fisher, R., L. *Applied Seismology. A comprehensive guide to seismic theory and application.* Tulsa, Aklahoma: PennWell Corporation, 2005.

Garotta, R. "Observations of shear waves and correlation with P events , in Dohr, G., Ed., Seismic shear waves, Part B: Applications." *Geophysical Press* 15B (1985): 1-86.

Gazdag. "Wave equation migration with the phase-shift method." *Geophysics, vol.43, no.7*, 1978: 1342-1351.

Gazdag, J., and Sguazzero, P. "Migration of Seismic Data." *Proceedings of the IEEE, vol. 72, no. 10*, 1984: 1302-1315.

Gingras, M, and D Rokosh. "A breif overview of the geology of heavy oil, bitumen and oil sand deposits." *CSEG Convention Abstracts*, 2004.

Gulunary. "FXDecon and complex wiener prediction filter." *Society of Exploration Geophysics 56th Annual International Meeting Abstracts*, 1986.

Hardage, Bob A, Michael V DeAngelo, Paul E Murray, and Diana Sava. *Multicomponent Seismic Technology.* Tulsa, Oklahoma: Society of Exploration Geophysicists, 2011.

Harrison. "F-X linear prediction filtering of seismic images." *CREWES Research Reports*, 1990: 147-165.

Harrison, Mark Paul. "Processing of P-Sv surface-seismic data: anisotropy analysis, dip moveout and migration." *University of Calgary Dissertation, Department of Geology and Geophysics*, 1992.

Hein, Frances J, and Darrell K Cotterill. "The Athabasca oil sands - a regional geological perspective, Fort McMurray Area, Alberta, Canada." *Natural Resources Research, vol. 15, no. 2*, 2006: 85-102.

Helbig, Klaus, and Sven Treitel. *Handbook of Geophysical Exploration. Section 1. Seismic Exploration. Seismic Shear Waves. Part B: Applications.* London: Geophysical Press, 1985.

Henley, D., C., and Margrave, G., F. "a ProMAX implementation of nonstationary deconvolution." *CREWES Research Report, vol. 13*, 2001: 203-222.

Hickey, C, J Eastwood, and T J.T Spanos. "Seismic wave propagation in oil sands." *AOSTRA J. Res.7*, 1991: 67-81.

Hicks, Warren, and James Berry. "Application of continuous velocity logs to determination of fluid saturation of reservoir rocks." *Geophyscis* XXI, no. No. 3 (1956): 739-754.

Hien, Doan Huy, Seonghyung Jang, and Youngwan Kim. "Multiple seismic attribute analyses for determination of bottom simulating reflector of gas hydrate seismic data in the Ulleung Basin of Korea." *Marine Geophysical Researchers*, 2010: 121-132.

Hien, F. J., R. A. Marsh, and M. J. Boddy. "Overview of the Oil Sands and Carbonate Bitumen of Alberta: Regional Framework and Infulence of Salt-Dissolution Effects." *Search and Discovery Article. Alberta Energy and Utilities Board*, 2008.

Hughes, D. S., and J. L. Kelly. "Variation of elastic wave velocity with saturation in sandstone." *Geophysics* 17 (1952): 739-752.

Isaac, J H. "Seismic methods for heavy oil reservoir monitoring." *Ph.D thesis, University of Calgary, Dept of Geology and Geophysics*, 1996.

Isaac, Janet Helen. *Seismic methods for heavy oil reservoir monitoring.* Calgary: University of Calgary, Department of Geology and Geophysic, 1996.

Johnston, D H. "A tutorial on time-lapse seismic reservoir monitoring." *Journal of Petroleum Technology, 49(5), 473-475*, 1997: 473-475.

Johnston, D., H. "A tutorial on time-lapse seismic reservoir monitoring." *Offshore Technology Conference*, 1997: 141-146.

Kalantzis, F, Vadifis, A, Kanasewich, E R, Kostyukevich, A. "Seismic monitoring and modeling of an enhanced oil recovery project at Cold Lake, Alberta, Canada." *Canadian Journal of Exploration Geophysics, vol 32, no. 2*, 1996: 77-89.

Kendall, Rob. "Using time-lapse seismic to monitor the toe-to-heel-air-injection (THAI) heavy-oil production process." In *Heavy Oils: Reservoir characterization and production monitoring, Chapter 23*, 275 - 284. Tulsa, Oklahoma: Society of Exploration Geophysicists, 2010.

Kommedal, Jan, and Olav I Barkved. "4D repeatability beyond twice - using variance." *Society of Exploration Geophysicists Expanded Abstracts*, 2005: 2526-2529.

Koster, Klaas, Peter Gabriels, Matthias Hartung, and John Verbeek. "Time-lapse seismic surveys in the North Sea and their business impact." *The Leading Edge* v.19, no. No.3 (2000): 286-293.

Kragh, Ed, and Phil Cristie. "Seismic repeatability, normailized rms and predictability ." *The Leading Edge* 21, no. No.7 (2002): 640-647.

Li, G., Purdue, G., Webber, G., and Couzens, R. "Effective processing of nonrepeatable 4-D sesimc data to monitor SAGD steam flood at East Senlac, Saskatchewan, Canada." *The Leading Edge, 20. doi 10.1190/1.1438878*, 2001: 54-63.

Lines, L. R. "Elastic wave seismic interpretation of heavy-oil reservoirs." *CSPG CSEG CWLS Convention Abstracts*, 2008.

Lines, Larry, R Jackson, and J Covey. "Seismic velocity models for heat zones in Athabasca Tar Sands." *Geophysics* 55, no. No. 8 (1990): 1108-1111.

Lynn, H. B., and L. A. Thomsen. "Reflection shear-wave data along the principle axis of azimuthal anisotropy ." *56th Annual International Meeting, Society of Exploration Geophysicists Expanded Abstracts*, 1986: 473-476.

Macrides, C, and P Kelamis. "A 9-C, 2-D land seismic experiment for lithology estimation of a Permian clastic reservoir." *The Leading Edge* 19 (2000): 1109-1116.

Macrides, Costas G, and Ernest R Kanasewich. "Seismic attenuation and poisson's ratios in oil sands from crosshole measurements ." *Canadian Society of Exploration Geophysicists* 23, no. No. 1 (1987): 46-55.

Marfurt, K. J., V. Sudhakar, A. Gersztenkorn, K. D. Crawford, and S. E. Nissen. "Coherency calculations in the presence of structural dip ." *Geophysics* 64 (1999): 104-111.

Margrave, G., Lamoureux, M., P., and Henley, D., C. "Gabor deconvolution: Estimating reflectivity by nonstationary deconvolution of seismic data. ." *Geophysics, vol. 76, no. 3*, 2011: W15-W30.

Matthews, L W, N E Pullin, and W K Hirshe. "Techniques applied to obtain very high resolution 3-D seismic imaging at an Athabasca tar sands thermal pilot." *The Leading Edge* 6, no. 12 (1987): 10-15.

McGillivray, P. "Microseismic and time-lapse seismic monitoring of a heavy oil extraction process at Peace River, Canada." *Recorder*, 2005: 5-9.

Mossop, Grant D. "Geology of the Athabasca Oil Sands." *Science, vol. 207, 11*, 1980: 145-207.

Nacille, C. "Detection of anisotropy using shear-wave splitting in VSP surveys: requirements and applications." *56th Annual International Meeting, Society of Exploration Geophysicists Expanded Abstracts*, 1986: 391-394.

Nakayama, T, A Takahashi, and A Kato. "Oil sands reservoir monitoring using time-lapse 3D seismic in canda." *International petroleum technology conference* 12333 (2008).

Nakayama, T., Takahashi, A., Skinner, L., and Kato, A.,. "Monitoring an oil-sands reservoir in northwest Alberta using time-lapse 3D seismic and 3D P-SV converted wave datta." *The Leading Edge*, 2005: 1158-1175.

Nazar, B. D., and Don Lawton. "AVO analysis of a thin conglomerate deposit ." *Journal of Seismic Exploration* 2 (1993): 333-348.

Nur, Amos M. "Seismic imaging in Enhanced Recovery." *SPE/DOE 10680*, 1982: 1-11.

Nur, Amos, Carol Tosaya, and Dung Vo-Thanh. "Seismic monitoring of thermal enhanced oil recovery processes." *54th Annual SEG Meeting Abstracts*, 1984.

O'Rourke, Cameron, and Don Anderson. "An analysis of steam thief zone scale effects on horizontal and vertical SAGD wells." *Society of Petroleum Engineers Annual Meeting* 99-75 (1999).

Parks, Kevin P. "Tectonostratigraphy, water-source and water-injection potenital of the Clearwater Formation." *Rock the Foundation Convention Abstracts, Canadian Society of Petroleum Geologists*, 2001.

Paulsson, B. N. P., J. A. Meredith, Z Wang, and J. W. Fairborn. "The steepbank crosswell seismic project: reservoir definition and evaluation of steamflood technology in Alberta tar sands." *The Leading Edge* 13, no. No. 6 (1994): 737-747.

Pengelly, Karen Jean. "Processing and interpretation of multicomponent seismic data from the Jackfish heavy oil field." *University of Caglary Dissertation*, 2005.

Pickett, G. R. "Acoustic character logs and their applications in formation evaluation." *Journal of Petroleum Techonology* 15, no. No. 6 (1963): 6569-667.

Pooladi-Darvish, M, and L Mattar. "SAGD operations in the presence of overlying gas cap and water layer - effect of shale layers." *Journal of Canadian Petroleum Technology* 41, no. 6 (2002).

ProMAX. "ProMax Reference." ?

Riedel, M., T. S. Collett, and U. Shankar. "Documenting channel features associated with gas hydrates in the Krishna-Godavari Basin, offshore India." *Marine Geology* 279 (2011): 1-11.

Robinison, E., A.,. *Migration of Geophysical Data.* Boston: International Human Resources Co. , 1983.

Robinson, Enders A, and Sven Treitel. *Geophysicla signal analysis.* Society of Exploration Geophysics, 2000.

Rojas, N. "Spectral decomposition applied to time-lapse seismic interpretation at Rulison Field, Garfield County, Colorado." *Colorado School of Mines Dissertation*, 2008.

Schmidt, J. "Seismic detection of porosity in the Tensleep sandstone reservoir, South Casper Creek, Wyoming." *Colorado School of Mines, Dissertation* , 1990.

Schmitt, Douglas R. "Seismic attributes for monitoring of a shallow heated heavy oil reservoir: A case study." *Geophysics* 62, no. No. 2 (1999): 368-377.

Schneider, Chris L, Shilong Mei, Matthias Grobe, and Kristine Haug. "Beneath the oil sands: stratigraphy and structural features of the Devonian of northeast Alberta." *GeoConvention 2012: Vision Abstracts*, 2012.

Sheriff, R., E. *Encyclopedic Dictionary of Applied Geophysics.* Tulsa: Society of Exploration Geophysicists, 2002.

Smith, R. J., and K. R. Perepelecta. "Steam conformance along horizontal wells at Cold Lake." *SEP International Thermal Operations and Heavy Oil Symposium and International Horizontal Well Technology Conference*, 2002.

Stewart, R R, James E Gaiser, R J Brown, and D C Lawton. "Converted-wave seismic exploration: a tutorial." *CREWES Research reports* 11 (1999).

Stewart, Robert R, James E Gaiser, R James Brown, and Don C Lawton. "Converted-wave seismic exploration: Applications." *Geophysics* 68, no. No. 1 (2003): 40-57.

Stewart, Robert R, James E Gaiser, R James Brown, and Don C Lawton. "Converted-wave seismic exploration: Methods." *Geophysics* 67, no. No. 5 (2002): 1348-1363.

Stewart, Robert, Robert Ferguson, Susan Miller, Eric Gallant, and Gary Margrave. "The Blackfoot seismic expirement: Broad-band, 3C-3D, and 3-D VSP surveys." *CSEG Recorder*, 1996: 7-10.

Subrahmanyam, D. "Seismic attributes - A review." *Hyderabad International Conference and Exposition on Petroleum Geology*, 2008: 398-403.

Sun, Z. "Seismic methods for heavy oil reservoir monitoring and characterization." *Ph.D thesis, University of Calgary, Dept of Geology and Geophysics*, 1999.

Taner. *Attributes revisited: Technical paper in rock solid images.* 2002. http://www.rocksolidimages.com/pdf/attribrevisited.htm.

Taner, M T, F Koehler, and R E Sheriff. "Complex seismic trace analysis." *Geophysics* 44, no. No.6 (1979): 1041-1063.

Taner, M., T., and Koehler, F. "Surface Consistent Corrections." *Geophysics, vol. 46, NO.1*, 1981: 17-22.

Tatham, R H, and M D McCormack. *Multicomponent Seismology in Petroleum Exploration.* Tulsa: Society of Exploration Geophysicists, 1991.

Tatham, Robert H, and Paul L Stoffa. "Vp/Vs - A potential hydrocarbon indicator." *Geophysics* 41, no. No. 5 (1976): 837-849.

Telford, W., M., Geldart, L., p., and Sheriff, r., E. *Applied Geophysics, Second Edition.* Cambridge: Press Syndicate of the University of Cambridge, 1990.

Tessmer, G, and A Behle. "Common reflection point data-stacking technique for converted waves." *Geophysical Prospecting* 36 (1988): 671-688.

Timur, A. "Temperature dependence of compressional and shear wave velocities in rocks." *Geophysics* 42, no. No. 5 (1977): 950-956.

Tosaya, C, A Nur, P Atonstam, and G DaPrat. "Monitoring of thermal EOR fronts by seismic methods." *SEP Californian regional meeting* , 1984: 12744.

Tosaya, C, A Nur, V Dung, and G Da Prat. "Laboratory seismic methods for remote monitoring of thermal EOR." *SPE Reservoir Engineering* , 1987: 235-242.

Trickett, S., R.,. "Stretch-Free Stacking." *CSEG/CSPG Joint Annual Convention Abstracts*, 2003.

Uwiera-Gartner, M. M.E, M. R. Carlson, and C. T.S. Palmgren. "Evaluation of Clearwater Formation caprock for a proposed, low pressure, steam-assisted gravity-drainage pilot project in northeast Alberta." *Society of Petroleum Engineering International 147302*, 2011.

van Vossen, R., Curtis, A., and Trampert, J. "Surface-consistent amplitude corrections for single or multicomponent sources and receivers using reciprocity and waveform inversion." *Geophysics Journal International, 165*, 2006: 311-322.

Varga, Roxana M, and Robert R Stewart. "Delineating sand channels using 3C-3D seismic data: Manitou Lake Heavy Oilfield, Saskatchewan." *CSPG CSEG CWLS Convention Abstracts*, 2009: 211-214.

Wang, Z, and A Nur. "Effect of temperature on wave velocities in sands and sandstones with heavy hydrocarbons." *Borehole Geophysics* 1 (1988): 3-5.

Warren, G Hicks, and James Berry. "Application of continuous velocity logs to determination of fluid saturation of reservoir rocks." *Geophysics* XXI, no. No. 3 (1956): 739-754.

Watson, A, I. *Integrated geological and geophysical analysis of a heavy-oil reservoir ar Pikes Peak, Saskatchewan.* Calgary, Alberta: M.Sc Dissertation, University of Calgary, 2004.

Watson, Ian A, Laurence R Lines, and Katherine F Brittle. "Heavy-oil reservoir characterization using elastic wave properties." *The Leading Edge*, 2002: 736-739.

Watson, Ian Anderw. *Integrated geological and geophysical analysis of a heavy-oil reservoir at Pikes Peak, Saskatchewan.* Calgary: University of Calgary, 2004.

Wyllie, M. R. J., A. R. Gregory, and L. W. Gardner. "Elastic wave velocities in heterogeneous amd porus media." *Geophysics* 21 (1956): 41-69.

Yilmaz. *Seismic Data Analysis. Processing, Inversion and Interpretation of Seismic Data.* Tulsa, Oklahoma: Society of Exploration Geophysics, 2001.

Yilmaz, O. *Seismic Data Analysis. Processing, Inversion and Interpretation of seismic data. .* Tulsa, Oklahoma: Socienty of Exploration Geophysics. , 2001.

Young, D., M.,. *Iterative Solution of Large Linear Systems.* New York: Academic Press, 1971.

Yuwen, C., Tongshu, P., Lisheng, W., and Yinghui, L. "Monitoring steam injection performance in shallow heavy oil reservoirs." *Proceedings - UNITAR International Conference on Heavy Crude and Tar Sands, 7, No. 1998.108*, 1998: 1-9.

APPENDIX A: COMPLEX SEISMIC TRACE ANALYSIS

The analytic seismic trace, F(t), can be defined as follows:

$$\boldsymbol{F(t) = f(t) + ig(t)} \qquad \boldsymbol{A-1}$$

where f(t) represents the real part (seismic data) and g(t), the imaginary part of the complex trace, is the Hilbert transform of f(t) defined as (Hien, et al., 2010; Barnes, 2007; Taner, 2002):

$$\boldsymbol{g(\mathrm{t}) = \frac{1}{\pi}\int_{-\infty}^{\infty}\frac{f(T-t)}{T-t}dT} \qquad \boldsymbol{A-2}$$

where T is the delay time.

Then, the envelope is the modulus of the complex function (Taner, 2002):

$$\boldsymbol{a(t) = \sqrt{[f^2(t) + g^2(t)]}} \qquad \boldsymbol{A-3}$$

where a(t) represents the total instantaneous energy, with a magnitude equal to that of the input traces. The envelope is independent of polarity and phase, and relates directly to acoustic impedance contrasts (Taner, 2002). The envelope (instantaneous) amplitude is a measure of the total energy of a signal, or its maximum value of the seismic trace under a constant phase rotation (Barnes, 2007). The phase angle $\boldsymbol{\theta(t)}$ required to rotate the trace to its maximum is defined as (Taner, 2002):

$$\boldsymbol{\theta(t) = \mathrm{arctan}\left[\frac{\mathrm{f}(t)}{g(t)}\right]} \qquad \boldsymbol{A-4}$$

The phase angle, or instantaneous phase, is a representation of the seismic data without amplitude information, with peak values representing the apparent position along a cosinusoid such that peaks have a 0 deg phase and troughs have 180 deg phase (Barnes, 2007).

The temporal measurement of the rate of change of the instantaneous phase with respect to time is the instantaneous frequency (the time derivative of phase divided by 2π) defined as (Barnes, 2007; Hien, et al., 2010):

$$f(t) = \frac{1}{2\pi}\frac{d\theta(t)}{dt} \qquad \textbf{\textit{A - 5}}$$

with units of Hertz.

The instantaneous frequency can be related to wave propagation, as well as a direct hydrocarbon indicator through the identification of a low frequency anomaly.